The Effects of Radiative Feedback on Star Cluster Formation and the Galactic Interstellar Medium

The Effects of Radiative Feedback on Star Cluster Formation and the Galactic Interstellar Medium

By

Corey S. Howard, B.Sc, M.Sc

A Thesis

Submitted to the School of Graduate Studies

in Partial Fulfilment of the Requirements

for the Degree

Doctor of Philosophy

McMaster University

Doctor of Philosophy (2017) McMaster University

(Physics and Astronomy) Hamilton, Ontario

TITLE: The Effects of Radiative Feedback on Star Cluster Formation and the Galactic Interstellar Medium

AUTHOR: Corey Howard, B.Sc, M.Sc (McMaster University)

SUPERVISOR: Ralph E. Pudritz

CO-SUPERVISOR: William E. Harris

NUMBER OF PAGES: xxix, 245

Abstract

The majority of stars form in clusters which are themselves birthed in Giant Molecular Clouds (GMCs). The radiation produced by clusters during their formative phase heats and ionizes the surrounding gas and drives outflows via radiation pressure. The combination of these processes, referred to as radiative feedback, is a proposed mechanism for limiting the star formation efficiency (SFE) in molecular clouds. In this thesis, we use 3D numerical simulations of turbulent GMCs, completed using the code FLASH and a sophisticated radiative transfer scheme, to explore the effects of radiative feedback on cluster formation and the larger scale interstellar medium (ISM). We present suites of simulations that vary the initial GMC mass from 10^4 to 10^6 $M_\odot$ and consider both gravitationally bound and unbound clouds. We find that clusters form within the highly filamentary clouds where they can undergo subsequent merging. Radiative feedback only plays a minor role in lowering the SFE of 10^6 $M_\odot$ GMCs. However, it completely disrupts intermediate mass clouds ($\sim 10^5$ $M_\odot$), reducing the SFE by a factor of two. We then examine the escape fraction of UV photons from GMCs — a quantity relevant to the structure of the ISM and cosmic reionization. We show that the escape fraction is dynamic and can vary by factors of two over short timescales because of the rapid growth and collapse of HII regions. The escape fractions from massive GMCs are typically low ($\sim$5%) while intermediate mass models are characterized by escape fractions nearing 100%. We combine our GMC models to represent the escape fraction from a population of clouds in dwarf starburst and spiral-type galaxies. We successfully reproduce the star formation rates in these galaxies and find typical escape fractions of 8% in all

cases. These results place important constraints on galactic-scale models studying the ISM and cosmic reionization.

Co-Authorship

Chapters 2, 3, and 4 of this thesis are original works written by myself. Chapter 2 is a published article which appeared in the peer-reviewed journal Monthly Notices of the Royal Astronomical Society (MNRAS). The full reference is: *Howard, Corey S., Pudritz, Ralph E., Harris, William E. 2016, MNRAS, Volume 461, Issue 3, p.2953-2974.* My co-supervisors are the second and third authors of this paper. Chapter 3 also appeared in MNRAS with my co-supervisors as the second and third authors. The reference to this work is: *Howard, Corey S., Pudritz, Ralph E., Harris, William E. 2017, MNRAS, Volume 470, Issue 3, p.3346-3358.* The fourth chapter has been published in the peer-reviewed Astrophysical Journal (ApJ). My co-supervisor Dr. Ralph Pudritz is the second author and Dr. Ralf Klessen is the third author. Dr. Klessen contributed to the development of the paper and aided in the editing process. The reference for this article is: *Howard, Corey S., Pudritz, Ralph E., Klessen, Ralf S. 2017, ApJ, Volume 834, Issue 1, article id. 40, 8 pp.*. All previously published articles have been reformatted to be consistent with the McMaster thesis guidelines. I hereby grant an irrevocable, non-exclusive license to McMaster University and the National Library of Canada to reproduce this material as part of this thesis.

Acknowledgements

This thesis has been a long time in the making and it would not have been possible without the help of friends and family. I cannot thank everyone here due to the limited space, and my thesis-addled brain has little motivation left for writing, so if I forget to express my gratitude, please accept my apologies.

First and foremost, I'd like to thank my supervisors, Dr. Ralph Pudritz and Dr. Bill Harris. Your insight and direction, from the smallest details to the ever important 'big picture', have been invaluable during my time at McMaster. You instilled in me a true passion for astrophysics and a drive to succeed at it. Moreover, you have always placed an emphasis on getting me to the right places and making lasting connections with the right people — a fact I will never forget. I am proud of the work we achieved together.

To my supervisory committee, Dr. James Wadsley and Dr. Christine Wilson, thank you for your helpful advice. Your individual perspectives, both numerical and observational, have been instrumental in guiding my research.

I'd like to thank my collaborator, Dr. Ralf Klessen, for the time and effort he has put into the papers we published together. You were kind enough to invite me to ITA for an extended stay and opened up your group to me. The fruits of this visit make up a large portion of this thesis.

None of this would have been possible without the companionship of my office mates, both past and present. Between the office pranks, the awful puns, the brainstorming, the death-rays, and the dealing with "Comps Corey", I never once did not look forward to coming into the office. Most importantly, I'd like to thank Mikhail Klassen. You were

always there to lend a helping hand when I struggled with FLASH. I hope I've adequately filled your shoes in the back corner desk.

To my parents, Mark and Gina, your never-ending support has meant so much to me. You have always placed a strong emphasis on the importance of education and, without that, I would not be where I am today. Thank you for *believing* and I love you both.

Sarah, I would be completely lost without you. You've said before that my work ethic inspires you but, in truth, it's your passion and dedication in everything you do that inspires me. Thank you for taking this journey with me and I love you to the star clusters and back. You're up next (pre-)Dr. Fiander!

To Jeannine

"I believe a leaf of grass is no less than the journey-work of the stars."

Song of Myself

Walt Whitman (1819-1892)

Table of Contents

Descriptive Notes ii

Abstract iii

Co-Authorship v

Acknowledgements vi

List of Figures xv

List of Tables xxix

Chapter 1 Introduction **1**

1.1 Star Cluster Formation 5

1.2 Radiative Feedback 23

1.3 The Effects of Cluster Formation on Global Scales 34

1.4 Thesis Outline 39

Chapter 2 Simulating Radiative Feedback and Star Cluster Formation in GMCs: I. Dependence on Gravitational Boundedness **45**

2.1 Abstract 45

2.2 Introduction 46

2.3 Numerical Methods 51

2.3.1 Subgrid model for cluster formation: Cluster sinks 53

2.3.2 Initial Conditions 59

2.4 Results 61

2.4.1 Global Evolution and Gas Properties 61

2.4.2 Formation Efficiencies and Particle Evolution 72

2.4.3 Radiative Feedback Effects 78

2.4.4 Cluster Formation Thresholds 84

2.4.5 Cluster Properties 88

2.4.6 Stellar Content 95

2.4.7 Star Formation Rates 97

2.5 Comparison to Observations 101

2.5.1 Mass Distributions 101

2.5.2 Star Formation Rates in Molecular Clouds 103

2.6 Conclusions 107

2.7 Acknowledgments 111

Chapter 3 Simulating Radiative Feedback and Star Cluster Formation in GMCs: II. Mass Dependence of Cloud Destruction and Cluster Properties **113**

3.1 Abstract 113

3.2 Introduction 114

3.3 Numerical Methods 119

3.3.1 Initial GMC Conditions 122

3.4 Results 124

3.4.1 Global Evolution and Cluster Properties 124

3.4.2 The role of radiative feedback 133

3.5 Observational Comparisons 141

3.5.1 The Initial Cluster Mass Function 141

3.5.2 Cloud Mass - Maximum Cluster mass Relation 142

3.5.3 Combined Cluster Mass Function 145

3.5.4 Star Formation Rates 148

3.6 Discussion and Conclusions 150

3.7 Acknowledgements 153

Chapter 4 Ultra Violet Escape Fractions from Giant Molecular Clouds During Early Cluster Formation 155

4.1 Abstract 155

4.2 Introduction 156

4.3 Method 160

4.4 Results 163

4.5 Discussion and Conclusions 175

4.6 Acknowledgements 177

Chapter 5 Simulating the UV Escape Fractions from Star-forming Dwarf and Spiral Galaxies 179

5.1 Abstract 179

5.2 Introduction 180

5.3 Numerical Methods 185

5.3.1 Simulation Details 185

5.3.2 Escape Fraction Calculation 187

5.4 Individual GMC Escape Fractions 189

5.5 Escape Fraction from GMC Populations 194

5.6 Comparison with Observations of Galactic Star Formation Rates . . . 205

5.7 Discussion and Conclusions 208

Chapter 6 Conclusions 212

6.1 Thesis Summary 212

6.2 Broader Implications for Cluster Formation 217

6.3 Future Work 221

List of Figures

1.1 A view of the Trapezium cluster as seen by the Hubble Space Telescope. The bright stars in the center of the image are O-stars of masses 15-30 $M_{\odot}$. While the cluster itself is molecular gas free, it is still shrouded by the gas of the Orion Molecular Cloud complex that surrounds it. *Credit: C.R. O'Dell and S.K. Wong (Rice University) and NASA/ESA.* 6

1.2 The measured virial parameters as a function of GMC luminous mass for the MW (grey) and M31 (black). The dashed line represents the uncertainty-weighted, mean value of the virial parameter for M31. *Figure adapted from Rosolowsky (2007) ©AAS. Reproduced with permission.* 11

1.3 Column density maps of the Aquila (left) and Polaris (right) sub fields displaying the filamentary nature of these regions. The figure was produced using SPIRE/PACS data. The location of Class 0 protostars and bound prestellar cores are over-plotted in green stars and blue triangles, respectively. *Credit: André et al., A&A, 518, L012, 2010, reproduced with permission ©ESO.* 12

1.4 A map of the column density of the Rosette Molecular Cloud where the location of filaments, as identified using the DisPerSE algorithm, have been over-plotted as white lines. The locations of young, star-forming clusters are indicated by blue stars, grey triangles represent dense cores, and white stars are the locations of O-stars. Star clusters are clearly associated with the locations of the filaments, particularly at the regions they join. *Credit: Schneider et al., A&A, 540, L12, 2012, reproduced with permission ©ESO.* 14

1.5 Centroid velocity measurements from N_2H^+ in the Serpens South star-forming region. Contours trace the dust emission, and the dashed line shows the peak ridge of the filament. The locations of young stars are shown as points. The colours show a clear velocity gradient of 1.4 km/s/pc in the southern part of the filament which extends to the grouping of stars in the center of the image. The flow rate of the filament is found to be 30 $M_\odot Myr^{-1}$. *Figure adapted from Kirk et al. (2013) ©AAS. Reproduced with permission.* 17

1.6 A collection of proposed forms of the IMF. The Chabrier (2005) IMF, corresponding to Equation 1.6, is shown by the magenta dashed line. *Figure reproduced with permission from Offner et al. (2014).* 22

1.7 A view of the 30 Doradus star-forming region in the LMC. Shown in blue is hot, ionized gas indicative of a giant HII region. The infrared emission from cold gas, shown in orange, has been carved out by these hot bubbles. *Credits: X-ray: NASA/CXC/PSU/L.; Infrared: NASA/JPL/PSU/L.* 27

1.8 Column density images of simulations with ionizing feedback (bottom panel) and without ionizing feedback (top panel). The low density voids are filled with hot, ionized gas (ie. an HII region). The locations of stars are marked by the white dots. *Figure reproduced with permission from Boneberg, D.M., Dale, J.E., Girichidis, P., & Ercolano, B., Turbulence in giant molecular clouds: the effect of photoionization feedback, 2014, MNRAS, 447, Issue 2, 1341* 31

1.9 The wavelength dependence of the UV background up to 13.6 eV. Equation 1.7, expressed in terms of energy rather than wavelength, is plotted as a solid black line and is meant to represent the best fit to the previous theoretical and observational estimates shown by the points. *Figure adapted from Draine (1978) ©AAS. Reproduced with permission.* 36

2.1 The Mach numbers corresponding to the initial virial parameters. 61

2.2 A three-dimensional view of the $\alpha_0 = 1$ simulation. The density contours are shown in yellow, green, and blue and the ionized regions are shown in red. The black circles represent cluster particles. Rows show two different views at the same time and columns show the state of the simulation at 0.97, 2.68, and 3.65 Myr from top to bottom. 62

2.3 Density slices through the centre of the z-axis (left) and column density projections (right) for the simulation with $\alpha_0 = 1$. Cluster locations are projected onto the viewing plane and are plotted as black circles for the slice plots and blue circles for the column density plots. 65

2.4 Density slices through the centre of the z-axis (left) and column density projections (right) for the simulation with $\alpha_0 = 3$. Cluster locations are projected onto the viewing plane and are plotted as black circles for the slice plots and blue circles for the column density plots. 66

2.5 The corresponding temperature slices to Figure 2.3 (left) and Figure 2.4 (right). Cluster particles are now shown in white for ease of viewing. 67

2.6 Mass components in 5 simulations with different α_0's. The dashed lines show the total mass in cluster particles. The dotted lines show the total gas mass in the simulation volume. The total mass in the simulation is the sum of gas and particles and is shown by the solid lines. Note that mass is lost from the simulations, particularly in the unbound cases, because outflow conditions are present. 69

2.7 Left: Evolution of the virial parameter over time including both gas and particles. Right: Individual contributions to α from the gas (dashed) and the cluster particles (dotted). See text for more detail on how the virial parameter was split. 70

2.8 Top: The evolution of the total mass for the two most massive cluster particles that survive until the end of the simulation. Discrete jumps in total mass are due to cluster particle merging. Bottom: Solid lines represent the total mass contained in cluster particles and corresponds to the left axis. Dashed lines represent the dense clump formation efficiency, ϵ_{cl}. Dashed-dotted lines represents the star formation efficiency, ϵ_{sf}. 73

2.9 The total number of cluster particles as a function of time. The total number can increase via forming new particles, and decrease via mergers or particles leaving the simulation volume. 77

2.10 The dense clump formation efficiency (left) and the star formation efficiency (right) for simulations with radiative feedback included, shown by solid lines, or not included, shown by the dashed lines. 79

2.11 Mass components in the $\alpha_0 = 3$ simulations (similar to Figure 2.6). Red lines represent the RHD simulations including radiative feedback, while the black lines represent the HD simulations not including radiative feedback. 82

2.12 Left: The number of cluster particles as a function of time for RHD simulations, shown by the solid lines, and HD simulations, shown by the dashed lines. Right: The maximum and median mass cluster particles for simulations with different α_0 values. 83

2.13 The effects of radiative feedback on ϵ_{cl} from varying the particle formation threshold in a bound ($\alpha_0 = 0.5$, left) and an unbound simulation ($\alpha_0 = 3$, right). As described in Section 2.3, the fiducial value we have used throughout is 10^4 cm^{-3}. 85

2.14 The number of cluster particles versus time for different formation thresholds. Simulations with an α_0 of 0.5 and 3 are shown by the solid and dashed lines, respectively. 87

2.15 Representative snapshots of the cluster mass function at various times (2, 3, and 4 Myr from left to right, respectively) for the simulation with an initial virial parameter of 3. 89

2.16 The final cluster particle mass distributions for all simulations. The initial virial parameter is shown an the top of each panel. The final panel shows the mass function for all of the data combined. The data is fit with a straight line for masses greater than log(M) > 2.4, following the work of Moore et al. (2015), and the resulting slope is shown in top right of each panel. 90

2.17 The particle gas mass fractions, defined as the total mass in the gas reservoir divided by the total cluster particle mass, of individual particles for simulations with different initial virial parameters, shown at 2 Myr (left) and 4 Myr (right). We only show three simulations for readability. Note that the gas reservoir refers to the gas which has been incorporated into the particle, and therefore resides within the particle radius of 0.325 pc. 92

2.18 The particle gas mass fractions as a function of cluster age for a bound ($\alpha_0 = 1$) and an unbound ($\alpha_0 = 3$) simulations. The colours are now used to represent different times. 94

2.19 The stellar mass distributions within the maximum mass cluster particle (left), the median mass cluster particle (middle), and the total cloud (right). See Table 2.1 for the masses of the cluster particles being shown. 95

2.20 The global star formation rates over time for the 5 simulations including radiative feedback. The curves were smoothed using a sliding average window for readability. 98

2.21 Stellar age distributions for the maximum mass cluster particle, median mass cluster particle, and the global age distribution from left to right, respectively. 100

2.22 The SFR of individual cluster particles at various times in simulations with an initial virial parameter of 0.5 (red), 2 (blue), and 5 (purple). The crosses represent the SFRs measured in local star forming regions from Lada (2010). The black triangles represent another dataset presented by Heiderman et al. (2010). The solid line is an extrapolation to smaller masses from extragalactic SFR measurements performed by Wu et al. (2005). 104

2.23 The fraction of total cluster particle mass obtained via merging events. Clusters with fractions greater than 0.5 have grown primarily through accreting other clusters. The legend shows the percentage of surviving particles that have undergone at least one merger in its history. . . . 107

3.1 Density slices through the center of the simulation volume for the 10^4 (left), 10^5 (center), and 10^6 (right) $M_\odot$ GMCs. Time, shown in the top left of each panel, increases from top to bottom. Cluster locations are projected onto this slice and shown by black circles. Note that the physical (xy) scales change with cloud mass (10x10 pc, 20x20 pc, and 40x40 pc from left to right). 125

3.2 The corresponding temperature slices to the panels shown in Figure 3.1. 126

3.3 The total mass contained in clusters (top) and the total number of clusters (bottom) in our five GMC models including radiative feedback. Note that the total mass contained in clusters can decrease over time due to clusters leaving the simulation volume, and the number of clusters can decrease both through escaping clusters and merging events. . . . 129

3.4 The merged mass fraction, defined as the total cluster mass that has participated in at least one merging event divided by the total mass contained in all clusters, versus time for the 5 GMCs including radiative feedback. 130

3.5 The total star formation rates (SFRs) for the 5 simulated GMCs which include radiative feedback. Note that this plot has been smoothed for readability (see text). 132

3.6 Left: The cluster particle formation efficiency (ϵ_{cl}, defined as the total mass in cluster particles divided by the GMC's initial mass) for our 5 RHD simulations (shown by solid lines) and the 5 HD simulations (shown by dashed lines). Right: Identical to the left panel except the star formation efficiency (ϵ_*, total mass of stars within clusters divided by the initial GMC mass) is plotted. 134

3.7 The fractional reduction of ϵ_{cl} (left) and ϵ_* (right) when including radiative feedback into a simulation, relative the HD formation efficiencies. 136

3.8 The ratio between the total internal energy of the gas to the global gravitational potential energy of the cloud. A lower ratio suggests a higher suppression of cluster and star formation. 138

3.9 The number of clusters as a function of time (as seen in Figure 3.3) including both RHD (solid) and HD (dashed) simulations. 140

3.10 The cluster mass function for the 10^4 (left), 10^5 (center), 10^6 (right) $M_\odot$ GMCs, plotted at 5 Myr. 142

3.11 The maximum mass cluster produced in our 5 RHD models (circles) and the 5 HD simulations (triangles) as a function of the initial cloud mass. The results are plotted at 3 Myr (gold) and 5 Myr (black). The slope of the distributions are shown at the top of the plot and are colored based on the times they represent. Fits to the HD data are shown by the dashed lines, and fits to the RHD data are shown by solid lines. . 143

3.12 The combined cluster mass function obtained from all 5 RHD simulations. The relative abundance of each parent cloud has been included via the GMC mass function in order to compare directly to observations. Fits to the mass range of observed embedded clusters (solid) and the high mass regime (dashed) are also included. 147

3.13 The SFR of individual cluster particles at various times for the 10^4, 10^5, and 10^6 $M_\odot$ GMCs. The squares are the observational results from Lada (2010) and the black triangles are a similar data set from Heiderman et al. (2010). 149

4.1 Maps of the ionizing photon flux across a spherical surface of radius 33.8 pc (corresponding to the initial GMC radius) shown at 6 different times. White circles represent the closest location of the 10 most luminous clusters to the sphere. More luminous clusters are shown by larger circles. The maps were produced using a Hammer projection, which is an equal area projection. 164

4.2 Top Left: The total UV escape fraction across the spherical surface presented in Figure 4.1. The vertical lines, shown in all panels, correspond to the times shown in Figure 4.1 (1.50, 2.51, 3.18, 3.31, 3.75, and 4.10 Myr). The horizontal line shows the average f_{esc} from 2.5 to 4.2 Myr. The escape fraction is defined here as the total number of photons crossing the surface divided by the total number of photons being produced by the clusters. Note that we only include clusters above the mass threshold described in Section 4.3, since clusters below this threshold are not included in the radiative transfer calculations. Top Right: The total ionizing photon rate produced by clusters above the mass threshold for radiation. Bottom Left: The fraction of gas, by mass, which has an ionization fraction of greater than 95%. Bottom Right: The mass evolution of the four most massive clusters, shown for reference. Discrete jumps in mass are due to cluster merging events. The complete mass evolution tracks can be found in Howard et al. (2016). 166

4.3 3d images of the density (shown in green) and ionized regions (shown in red) at 3.18, 3.31, and 3.75 Myr from left to right, respectively. These images correspond to the first peak in f_{esc} in Figure 4.2, the trough at 3.31 Myr, and the second peak at 3.75 Myr. The density contours represent densities of $\sim$30 cm^{-3} and the box side length is 80 pc. . . . 168

4.4 Top Left: A slice of density centered on the location of the most luminous cluster associated with the collapsing HII region at 3.25 Myr. Top Right: The same slice in the previous panel except the ionization fraction of the gas is displayed. Bottom Left: A Hammer projection of the neutral gas column density at a 20 pc spherical surface centered on the same cluster, plotted before the HII region collapses at 3.25 Myr. Bottom Right: The same but $\sim$35,000 yr after the Bottom Left panel. The HII region has collapsed by this time. 172

4.5 Left: The positions of all clusters plotted at 3.18 Myr. The stars represent the locations of the 10 most massive clusters and colours represent Z-position. Right: The escape fraction, f_{esc}, across a spherical surface of radius 25 pc. This is the smallest possible radius which contains 90% of the total ionizing luminosity within its volume and therefore minimizes the contribution to the flux across the surface from outside sources. 174

5.1 The flux of ionizing photons across the extracted spherical surface for the 10^4 (left) and 10^5 (right) $M_\odot$ GMCs. White circles represent the luminous clusters which are plotted at their closest location to the sphere and are scaled in size by their ionizing luminosity. 190

5.2 The escape fraction from our 5 GMC models of varying mass. The highest escape fractions are seen in the 5×10^4 and 10^5 $M_\odot$ clouds, both of which are nearly fully ionized at the end of the simulation. 192

5.3 The evolution of the mass reservoir out of which GMCs are drawn to determine Δt for the dwarf model with α = -1.5 (top left), α = -2.5 (top right), and the spiral-type model (bottom). We choose the time between GMC formation such that the gas is exhausted after one gas consumption time of $\sim$1 Gyr for dwarf and $\sim$2.35 Gyr for the spiral model. 200

5.4 The escape fraction for the two starburst dwarf models (top and middle) and the spiral-type galaxy model (bottom) as it evolves over time. Black circles represent the average over 100 Myr timescales. The histogram, plotted with the same vertical scale as the left plot, represents the distribution of f_{esc} over each galaxy's history. 201

5.5 The contributions to the total f_{esc} by each of the 5 cloud masses. Note that there can be many GMCs with the same mass at any given time. The sum of these curves represents the total f_{esc} presented in Figure 5.4. 203

5.6 The evolution of the star formation rate (SFR) for the dwarf starburst models and the spiral-type galaxy model. As in Figure 5.4, the black dots represent the average values in 100 Myr bins and the histogram shows the overall distribution of SFRs over each model's history. . . . 206

List of Tables

2.1 Particle masses in models with varying α_0 values. 97

3.1 Summary of parameters for each simulation. Note that two simulations were completed for every entry in the table — one including radiative feedback and one without radiative feedback. 123

5.1 Escape fraction results for individual GMCs of different masses. 193

Chapter 1

Introduction

Star clusters are the fundamental units of star formation. It is generally accepted that the vast majority of stars form in clusters (Lada & Lada, 2003) with $\geq$80% forming in clusters of more than 100 members (Porras et al., 2003). Since stars are a driver for a plethora of astrophysical processes — including generating the chemical seeds for life itself — studying their main mode of formation is a crucial undertaking.

With the recent advances in infrared (IR) and submillimeter astronomy over the past decades, a general picture of cluster formation has been established. Cluster formation takes place within Giant Molecular Clouds (GMCs) — massive, cold, and dense collections of molecular gas — which can vary over orders of magnitude in both size and mass. Internally, these clouds are supersonically turbulent leading to the formation of a network of dense filaments. These filaments can gravitationally fragment above a critical mass or potentially act as channels which funnel gas along their length. This gas then collects at the regions where filaments intersect resulting

in a dense clump of molecular gas that hosts cluster formation. An individual GMC can birth many such regions.

Despite the general acceptance of this scenario, several open questions related to the formation of star clusters remain. The low global star formation efficiency (SFE) in GMCs — defined as the ratio of the mass contained in stars to the unused gas mass, typically $\sim$2% (Evans, 1991) — is of particular importance. The mechanisms proposed to explain this observation generally fall into two categories; the physical conditions of the host GMC, or feedback from young stars.

The turbulence within GMCs is an example that falls into the first category. The pressure support provided by the turbulent motions of the gas can slow gravitational collapse and therefore limit the SFE (Mac Low & Klessen, 2004). This may be particularly relevant for the population of GMCs that are globally gravitationally unbound (Rosolowsky, 2007; Ward et al., 2016). While this is likely an important piece of the puzzle, turbulence can only slow the formation of star clusters. Given enough time, and no other mechanisms to disperse the cluster-forming gas, the SFE of a given GMC will become unphysically high (Klessen et al., 2000; Bate et al., 2003; Bonnell et al., 2008).

The injection of radiation into the gas surrounding cluster-forming regions — a process deemed radiative feedback — is another possible mechanism to limit the SFE. The absorption of UV photons by molecular gas results in the production of hot, ionized bubbles (HII regions) which thermally expand, sweeping up interstellar gas and thereby limiting the formation of stars and clusters. Furthermore, the

direct radiation pressure induced by the absorption of UV photons by dust grains can drive outflows from young protoclusters. Radiative feedback is argued by some authors to be the most important feedback mechanism for clusters hosting massive star formation (Murray et al., 2010).

The complex interplay among gravity, turbulence, and radiative feedback necessitates the use of numerical simulations. Previous simulations have attempted to quantify the role of radiative feedback (Dale et al., 2005; Offner et al., 2009; Bate, 2009; Peters et al., 2010a; Commerçon et al., 2010; Krumholz et al., 2010; Harper-Clark, 2011; Klassen et al., 2012b; Dale et al., 2012b). In general, it is found to reduce the SFE by up to a factor of 2. However, these simulations typically focus on low mass ($\leq 10^4$ $M_\odot$) clouds or only cover a subset of the observed GMC properties (eg. only considering gravitationally bound clouds). The role of GMC initial conditions, the effects of radiative feedback in those clouds, and the degree to which cluster properties are shaped by feedback are still yet to be understood.

The radiation produced by young stars also drives crucial astrophysical processes on scales larger than GMCs. The bulk properties of the Interstellar Medium (ISM) are largely determined by interactions with the UV portion of the Interstellar Radiation Field (ISRF). Since massive stars are significantly more luminous than low mass stars, they are thought to be an important contributor to the ISRF. However, massive stars have short lifetimes and are often still embedded in their host GMC when they explode as supernovae. The UV photons from massive stars must therefore escape their GMC, at least to some degree. The fraction of photons that escape from a GMC, however, is not well constrained.

On even larger scales, stellar photons are an important player in cosmic reionization (ie. the complete ionization of the Intergalactic Medium (IGM) by z$\sim$6). Again, this requires photons to escape their host galaxy. While several simulations have attempted to characterize the escape fraction of photons from galaxies (Gnedin et al., 2008; Razoumov & Sommer-Larsen, 2010; Paardekooper et al., 2013; Wise & Cen, 2009), the results often conflict. This is likely due to the differences in the treatment of dense, star-forming gas. Detailed and physically motivated numerical simulations including radiative feedback that model star and cluster formation at its source (ie. GMCs) can therefore provide important insights on both the ISRF and cosmic reionization.

In this thesis, I address the questions outlined above relating to GMC initial conditions, radiative feedback, cluster properties, and photon escape fractions via the use of numerical simulations. The introduction below provides further context for my work and is organized as follows.

Section 1.1 presents a top down overview of star cluster formation. The bulk properties of local GMCs are discussed followed by an examination of their internal structure. An emphasis is placed on the filamentary nature of molecular clouds and how this directly relates to cluster formation. I finish with a discussion of the observed properties of embedded star clusters.

Section 1.2 describes radiative feedback and the physical reasons why it is thought to be important in limiting the SFE of a GMC. A review covering previous simula-

tions involving radiative feedback is also included, with the goal of identifying gaps in the literature that this thesis addresses.

Section 1.3 introduces the ISRF, cosmic reionization, and the connection to cluster formation. This is followed by the thesis outline in Section 1.4 which contains a brief summary of each chapter and how it relates to the overarching themes presented in the introduction.

1.1 Star Cluster Formation

Clusters can generally be divided into three categories; embedded clusters, open clusters, and globular clusters. Embedded clusters are the youngest cluster type, actively star-forming, and are still highly obscured by the gas and dust out of which they are forming. Due to their young age, these clusters provide an important test bed of cluster formation theories. Open star clusters, typically associated with the galactic disk, are the gas free products of embedded cluster formation. Not all embedded clusters will become open clusters since an estimated $\sim$90% of embedded clusters are disrupted during the process of gas expulsion (Lada & Lada, 2003). The Trapezium cluster, a recently formed open cluster in the Orion Molecular Cloud complex hosting massive stars, is shown in Figure 1.1. The Trapezium is one of the most well studied, young clusters which contains $\sim$3500 stars — four of which are massive, OB stars — with mean ages of $\sim$1 Myr contained within a radius of 2.5 pc (Hillenbrand, 1997). Globular clusters constitute the oldest ($\geq$ 10 Gyr) and the most massive (10^{4-6} $M_{\odot}$) star clusters (Harris, 1991; Brodie & Strader, 2006). Since

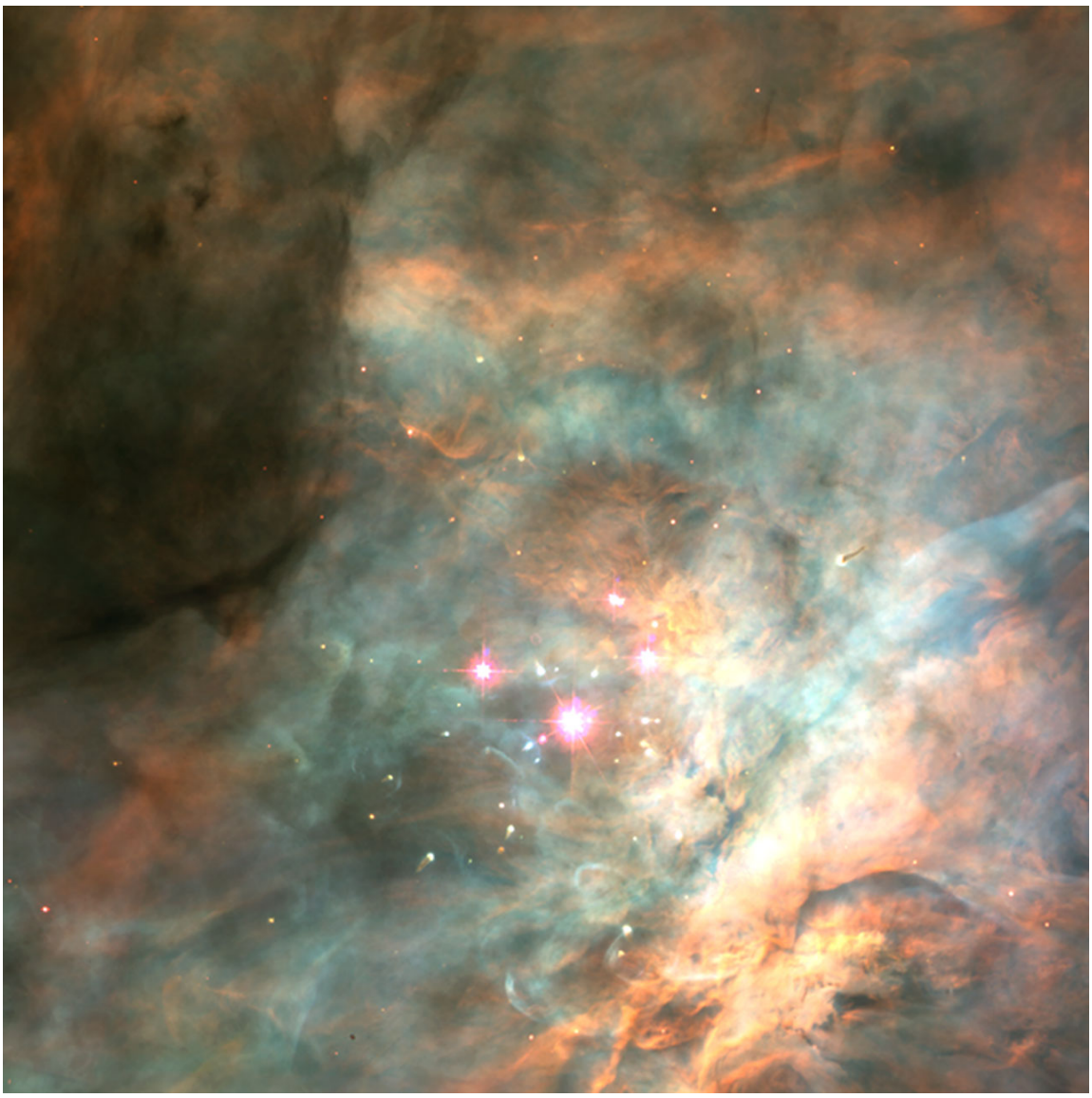

Figure 1.1: A view of the Trapezium cluster as seen by the Hubble Space Telescope. The bright stars in the center of the image are O-stars of masses 15-30 $M_{\odot}$. While the cluster itself is molecular gas free, it is still shrouded by the gas of the Orion Molecular Cloud complex that surrounds it. *Credit: C.R. O'Dell and S.K. Wong (Rice University) and NASA/ESA.*

the physical conditions present during the epoch of globular cluster formation are unknown, the exact mechanisms leading to their formation are debated.

GMCs are the nurseries of present day star cluster formation. GMCs typically have sizes in the range of 10-100 pc, masses of 10^{4-7} $M_{\odot}$, and average densities of $\sim$100 cm^{-3} (Fukui & Kawamura, 2010). These high densities, in combination with temperatures of around 10 K, lead to the formation of molecules of which molecular hydrogen (H_2) is the most common. The high column density of both gas and dust in GMCs make observational studies of their internal structure unfeasible using visual wavelengths. However, the most recent generations of telescopes using infrared and submillimeter wavelengths (eg. *Herschel* and *ALMA*) have the resolution and sensitivity to characterize the properties of molecular clouds.

The bulk properties of GMCs are found to vary significantly both within the Milky Way (MW) and other galaxies. The masses of GMCs, in particular, cover approximately three orders of magnitude. The exact distribution of GMC masses is important to constrain because the properties of newly formed stars and clusters depend on their host cloud. For example, observations of M51 by Hughes et al. (2013) indicate a relation between a GMC's mass (M_{GMC}) and the maximum mass cluster ($M_{cl,max}$) it produces of the form $M_{cl,max} \propto M_{GMC}^{0.5}$. This result, in combination with a similar relation between a cluster's mass and the most massive star it forms (Elmegreen, 2002; Pflamm-Altenburg et al., 2007), implies massive GMCs should preferentially host massive star formation. This has been confirmed by Kawamura et al. (2009) and Fukui & Kawamura (2010) via observations of the Large Magellanic

Cloud (LMC) that indicate HII regions — signposts of massive star formation — are more often associated with high mass GMCs.

The mass distribution of GMCs is commonly represented by a powerlaw of the form,

$$\frac{dN}{dM} \propto (\frac{M}{M_0})^{\gamma} \tag{1.1}$$

where M is the mass of the GMC, M_0 is an upper mass cutoff (typically the highest mass cloud in the observational sample), and dN/dM is the number of clouds with masses between M and $M + dM$ (Williams & McKee, 1997). The powerlaw index γ indicates where most of the molecular gas in GMCs is found. For $\gamma >$ -2, most of the molecular gas is contained in high mass clouds and vice versa for $\gamma <$ -2.

The mass distribution of GMCs in the inner MW was first characterized by Solomon et al. (1987) who found $\gamma \sim$ -1.5. Later, Williams & McKee (1997) used a collection of cloud catalogs from Dame et al. (1986), Solomon et al. (1987), and Scoville et al. (1987) and found best fitting parameters of $\gamma \sim$ -1.7 and $M_0 \sim 6{\times}10^6$ $M_{\odot}$. The majority of the mass contained in GMCs can therefore be found in the most massive clouds. Two other key results are inferred from this study. Firstly, the upper mass cutoff is not a statistical artifact but is indeed a reflection of the physical properties of the ISM. Secondly, the total mass contained in the catalogues used to fit the GMC mass spectra only account for $\sim$40% of the total observed CO emission in the inner MW. This deficit is attributed to cold clouds not associated with star formation that are too small to be accounted for in these surveys.

More recently, Rosolowsky (2005) reanalyzed the above data and used the catalogues of Heyer et al. (2001) and Brunt et al. (2003) for clouds in the outer MW as well as GMC catalogues of M33 and the LMC to characterize the GMC mass distribution in different environments. The results for the inner MW were consistent with Williams & McKee (1997) finding best fit values of $\gamma \approx$ -1.5 and $M_0 \approx 6{\times}10^6$ $M_\odot$. The slope of the powerlaw is found to vary significantly between different regions. For the outer MW, M33, and the LMC, γ is found to be -2.1, -2.86, and -1.71, respectively. All slopes are steeper than the inner MW. This may indicate that the physical conditions of the ISM are significantly different in these regions compared to the MW and these differences leads to a suppression of massive GMCs.

The virial parameter of GMCs is another property that is observed to vary between clouds. The virial parameter, α, is a dimensionless ratio of the kinetic energy to the gravitational potential energy of the cloud and is used to measure the degree to which a GMC is gravitationally bound. It is a natural consequence of the virial theorem and is mathematically defined as (Bertoldi & McKee, 1992),

$$\alpha = a\frac{2E_{kin}}{|E_{grav}|} = \frac{5\sigma^2 R}{GM} \tag{1.2}$$

where E_{kin} is the total kinetic energy of the cloud, E_{grav} is the gravitational potential energy, a is a parameter that accounts for non-homogeneous and non-spherical density distributions, σ is the velocity dispersion along the line of sight, and R is the cloud radius. In the case of a spherical and uniform density cloud, a is 1. If $\alpha = 1$, the cloud is said to be bound — the gravitational potential energy is greater than

the kinetic energy — and is in virial equilibrium (ie. "virialized"). Clouds with $\alpha < 2$ are also bound while clouds with $\alpha > 2$ are unbound. We note that the form of the virial parameter presented above neglects the contributions of magnetic fields — a source of pressure preventing collapse thereby increasing α — and an external pressurized medium that can exert a surface pressure on the cloud resulting in a more bound object. These additional terms are typically neglected in observational measurements of α and are not included in this work.

The seminal work by Larson (1981) led to the widespread notion that most molecular clouds are virialized. This is one of three so called "Larson's Laws" which are observed scaling relations that link the velocity dispersion, physical size, and masses of GMCs. Larson's first law, known as the size-linewidth relation, connects the observed, 3-dimensional velocity dispersion (σ) to the size of the cloud (L) via $\sigma = 1.1L^{0.38}$ (Larson, 1981). This relation was then updated by Solomon et al. (1987) who found $\sigma \propto L^{0.5}$. The second law states that the column density does not vary between GMCs. The combination of these two laws directly implies that molecular clouds are both bound and virialized.

More recent catalogues of GMCs obtained with higher resolution telescopes, however, have found evidence that α is not universally 1. The work by Solomon et al. (1987) instead indicates an average α of $\sim$1.5 and an overall range of 0.6 - 4. Therefore, GMCs are not solely virialized and can exist in both bound and unbound states. This has also been confirmed for GMCs in M31 (Rosolowsky, 2007) which cover a similar range of virial parameters. In Figure 1.2, we show the measured virial parameters for the MW and M31 which clearly demonstrate that GMCs can exist in

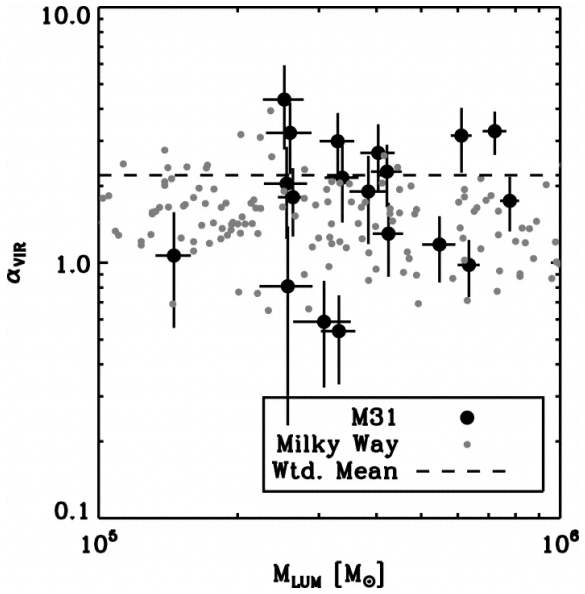

Figure 1.2: The measured virial parameters as a function of GMC luminous mass for the MW (grey) and M31 (black). The dashed line represents the uncertainty-weighted, mean value of the virial parameter for M31. *Figure adapted from Rosolowsky (2007) ©AAS. Reproduced with permission.*

various states of gravitational boundedness. Not only do observations cast doubt on Larson's third law, but simulations of GMC formation in galactic disks also naturally form unbound molecular clouds (Dobbs et al., 2011). As discussed below, the virial parameter of a GMC can have important implications for its star formation rate (SFR) and star formation efficiency (SFE), particularly if the cloud is unbound.

A striking feature of GMCs revealed by the latest generations of IR and sub-mm telescopes (eg. *Herschel* and *ALMA*) is that they are highly filamentary and have clumpy internal structure (Arzoumanian et al., 2011; Hill et al., 2011; Megeath et al., 2012; André et al., 2014). This feature appears to be ubiquitous in molecular clouds, regardless of the varying bulk properties described above. An example of this filamentary substructure can be seen in Figure 1.3. The discovery of these filaments,

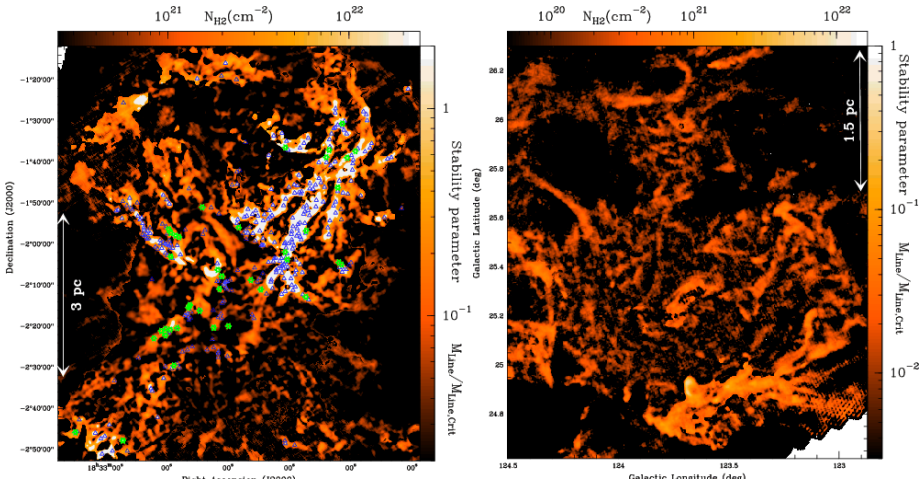

Figure 1.3: Column density maps of the Aquila (left) and Polaris (right) sub fields displaying the filamentary nature of these regions. The figure was produced using SPIRE/PACS data. The location of Class 0 protostars and bound prestellar cores are over-plotted in green stars and blue triangles, respectively. *Credit: André et al., A&A, 518, L012, 2010, reproduced with permission ©ESO.*

and their association with young stars and clusters, represents a paradigm shift in star formation theory.

The origin of this prominent filamentary structure is still debated, but turbulence likely plays a central role. It is this turbulence that determines the magnitude of E_{kin} in Equation 2 and counteracts, to some degree, the self-gravity of the molecular cloud. GMCs are observed to be supersonically turbulent with Mach numbers, the ratio between the root mean square velocity and the sound speed, of order 10 or higher (Mac Low & Klessen, 2004).

An important characteristic of supersonic turbulence in compressible media is its ability to produce density enhancements via shocks. The repeated interactions between shocks can naturally produce filamentary structure. This has been demon-

strated both theoretically and via numerical simulations (Klessen et al., 2000; Mac Low & Klessen, 2004; Ballesteros-Paredes et al., 2007; Pudritz & Kevlahan, 2013; Hennebelle, 2013). The strength of these density enhancements is shown numerically to depend on the mixture of solenoidal (divergence-free) and compressive (curl-free) modes in the adopted turbulent velocity field (Girichidis et al., 2011) with compressive turbulence leading to larger density enhancements. The turbulence within a GMC is typically assumed to be a 2:1 mixture of compressive to solenoidal modes (Girichidis et al., 2011). This convention is adopted throughout this work.

The turbulent motions within a molecular cloud are ultimately responsible for their column density probability distribution functions (PDF). The shape of the PDF was first predicted to be lognormal (Vázquez-Semadeni, 1994; Vázquez-Semadeni & García, 2001; Ostriker et al., 2001) by considering the density at any one point to be a random variable which is itself a product of multiple random processes (ie. the passage of turbulent shocks). The central limit theorem therefore applies and a lognormal column density distribution is the natural consequence. This was first confirmed observationally by Kainulainen et al. (2009) through near IR dust extinction mapping of $\sim$20 local molecular clouds. An important result of this study was that a purely lognormal PDF is only an appropriate fit for starless molecular clouds such as Infrared Dark Clouds (IRDCs). Clouds that host star formation are instead better represented by a lognormal at low column densities and a powerlaw tail extending to high column due to the local collapse of gas (Kritsuk et al., 2011). Turbulence is therefore an essential process which is responsible for setting the initial density structure out of which stars and clusters form.

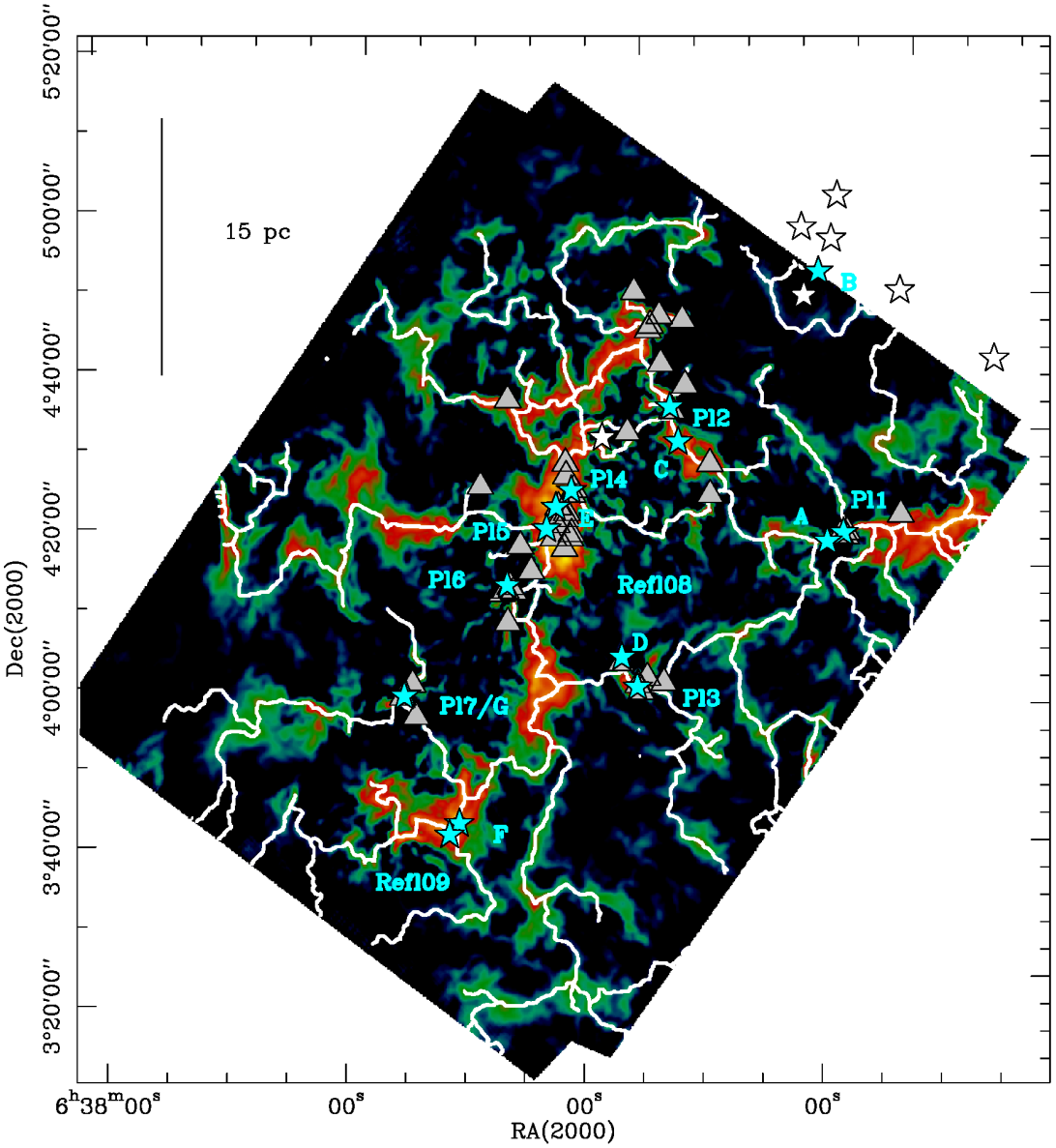

Figure 1.4: A map of the column density of the Rosette Molecular Cloud where the location of filaments, as identified using the DisPerSE algorithm, have been over-plotted as white lines. The locations of young, star-forming clusters are indicated by blue stars, grey triangles represent dense cores, and white stars are the locations of O-stars. Star clusters are clearly associated with the locations of the filaments, particularly at the regions they join. *Credit: Schneider et al., A&A, 540, L12, 2012, reproduced with permission ©ESO.*

The (potentially) turbulently formed filaments are inextricably linked with star and cluster formation. Due to the enhanced density in these filaments, they are the among the first objects to fragment gravitationally and collapse to form clusters of stars. Whether a filament is stable against gravitational collapse can be determined via its line mass defined as the mass per unit length. Assuming an isothermal, non-turbulent filament, there exists a critical line mass above which the filament is unstable to gravitational collapse given by,

$$(\frac{M}{L})_{crit} = \frac{2c_s^2}{G} \tag{1.3}$$

where c_s is the sound speed of the gas (Ostriker, 1964; Inutsuka & Miyama, 1997; Fiege & Pudritz, 2000; André et al., 2014). Filaments above this line mass will fragment to form stars unless otherwise supported by turbulent gas motions.

Filaments can not only directly fragment into stars but also act as channels which funnel gas into central hubs that act as the sites of cluster formation. This is demonstrated in Schneider et al. (2012) who compared the locations of young clusters with filaments identified through *Herschel* observations of the Rosette Molecular Cloud. As shown in Figure 1.4, young clusters, represented by the over-plotted points, are preferentially formed at the intersection of 2 or more filaments. The results from Liu et al. (2012) also support this notion. Combining various molecular spectral lines — tracers of high density gas — and millimeter dust continuum measured in the G33.92+0.11 cluster forming region, they found evidence of at least three filaments connected to a dense, central clump containing $\sim 3\times10^3$ $M_\odot$ of molecular gas. Free-

free continuum emission indicates the presence of an embedded OB cluster in the center of this clump.

These results imply that molecular gas is channeled into these hubs but do not provide direct evidence of this process. However, Kirk et al. (2013) fills this gap. Using observations of N_2H^+ (see Figure 1.5), they find velocity gradients along the main filament in Serpens South which are directed towards a central cluster forming region. The rate of filamentary flow is $\sim$30 $M_\odot Myr^{-1}$. Interestingly, this is roughly consistent with the inferred SFR in Serpens South. This places strong constraints on the process, and initial conditions, of cluster formation.

As discussed in length by Longmore et al. (2014), the initial conditions for cluster formation, particularly Young Massive Clusters (YMCs) of masses $\gtrapprox 10^4$ $M_\odot$, are not fully constrained. Two general modes for cluster formation have been considered; "in-situ" formation and "conveyor belt" formation. The former implies that all the gas required to form a cluster is collected into a clump before cluster formation is initiated. Given the densities required to form massive clusters, the resulting clump would have a short freefall time and therefore difficult to find observationally. The latter scenario is characterized by lower gas surface densities and SFRs at the onset of cluster formation, but accretion of gas from a region much larger than the size of the cluster-forming region sustains star formation. The filamentary accretion flows discovered by Kirk et al. (2013), and the similarity between the accretion rate and SFR, appear to favour the conveyor belt formation scenario.

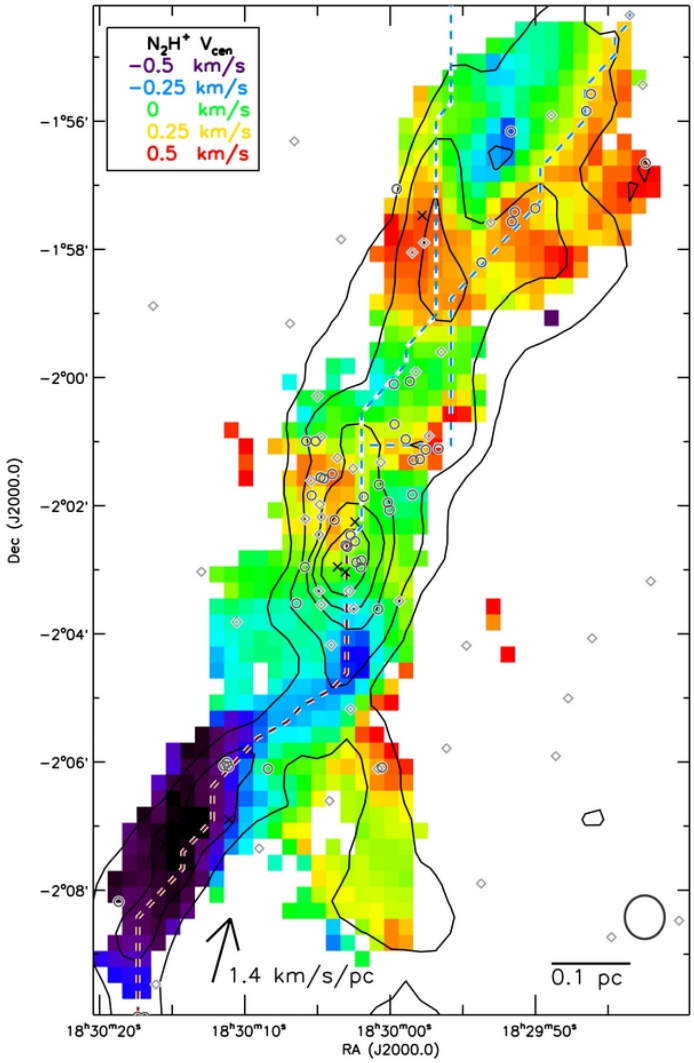

Figure 1.5: Centroid velocity measurements from N_2H^+ in the Serpens South star-forming region. Contours trace the dust emission, and the dashed line shows the peak ridge of the filament. The locations of young stars are shown as points. The colours show a clear velocity gradient of 1.4 km/s/pc in the southern part of the filament which extends to the grouping of stars in the center of the image. The flow rate of the filament is found to be 30 $M_\odot Myr^{-1}$. *Figure adapted from Kirk et al. (2013) ©AAS. Reproduced with permission.*

When sufficient mass is gathered into a clump, the gravitational potential exceeds its internal pressure support and it becomes unstable to collapse. For a non-turbulent region of uniform density, ρ, the condition for collapse can be expressed in terms of the Jeans mass,

$$M_J = \frac{\pi}{6} \frac{c_s^3}{G^{3/2} \rho^{1/3}}. \tag{1.4}$$

When the mass contained in the region exceeds the Jean mass, it is unstable to gravitational collapse. Regions containing multiple Jeans masses of material fragment into clusters of stars. The fragmentation of dense regions being the ultimate cause of cluster formation is well accepted and observationally supported. For example, Teixeira et al. (2006) finds that the separation between NGC 2264 protostars forming in dense filaments is consistent with the local Jeans length — the corresponding length scale to the Jeans mass — indicating that stars, and therefore clusters, form through the thermal fragmentation of gas.

The properties of the clumps that host cluster formation, and of the embedded clusters themselves, have been characterized for local regions. The pioneering work of Lada & Lada (2003) has laid much of the observational groundwork for our current understanding of cluster formation. The authors combined several catalogues of embedded clusters within 2 kpc of the sun (for a total of 76 clusters) in order to characterize the bulk properties of star-forming clusters. To be included in the sample, the clusters were required to show evidence of an embedded nature, either through the presence of HII regions or significant optical or IR extinction, and contain

at least 35 member stars. The masses of the resulting clusters range from ∼30-1100 $M_\odot$.

A particularly important result from this work is that embedded clusters are associated with the most massive and dense clumps within their host GMC. The clumps hosting cluster formation have typical masses of 100-1000 $M_\odot$. The density of these clumps is $\sim 10^4$ cm^{-3}, or approximately 2 orders of magnitude greater than the average GMC density, with physical sizes of 0.5-1 pc. The association of clusters with 10^4 cm^{-3} gas has been taken as evidence for a threshold density for cluster formation. Later work by Kainulainen et al. (2014), who derived the density PDF for 11 nearby GMCs, also finds a similar threshold density for cluster formation. When adopting the parameters typical of local GMCs, the analytic models of Krumholz & McKee (2005) and Padoan & Nordlund (2011) reproduce this density.

Another important contribution from Lada & Lada (2003) is the characterization of the Embedded Cluster Mass Function (ECMF). There are two notable features of this function. Firstly, the ECMF is well characterized by a powerlaw with the same form as Equation 1, except with γ = -2. This indicates that, while rare, the most massive clusters in their sample (∼1000 $M_\odot$) contribute a significant fraction of the total stellar mass contained in embedded clusters. Moreover, an estimated 90% of stars form in clusters with masses greater than 50 $M_\odot$ (or clusters with more than ∼100 member stars). The second notable feature of the ECMF is a peak at 50 $M_\odot$ and a drop off at lower masses. While the sample of embedded clusters is likely not complete at these low masses, the authors also examine the mass function of a subset of clusters from a sample of local GMCs where the measurements are

complete. This also results in a decreasing ECMF below 50 $M_\odot$ indicating that this is a robust feature.

Further work by Fall & Chandar (2012) provides evidence that the ECMF is a universal function. The same slope (-2) is found for young clusters of ages 1-10 Myr in the LMC, SMC, M83, M51, and the Antennae galaxy. Moreover, the same mass function characterizes open clusters with ages up to 1 Gyr. An understanding of the origin of this apparently universal function, and the processes that set it, is yet to be determined.

The connection between star/cluster formation and dense gas is elucidated further in Lada et al. (2010) who measured the SFRs in 11 local GMCs. To measure the SFRs in GMCs, the *Spitzer* telescope was used to directly count the number of Young Stellar Objects (YSOs) in each region. Assuming an average YSO mass and age, the SFR can be inferred. Since this method relies on resolving individual YSOs, it is inherently limited to nearby star-forming clouds. The resulting SFRs span two orders of magnitude from 3×10^{-6} to 7.15×10^{-4} $M_\odot yr^{-1}$. There is no apparent relation between the SFR per unit cloud mass, equivalent to the SFE, and the total cloud mass. Instead, a direct relation between the SFR and the total amount of *dense* gas is found. In this context, dense gas has a K-band extinction of 0.8 magnitudes or higher which is equivalent to number densities of $\gtrapprox 10^4$ cm^{-3}. When considering only this gas component (M_{dense}), a relation with little scatter of the form,

$$SFR[M_\odot yr^{-1}] = 4.6 \times 10^{-8} M_{dense} \tag{1.5}$$

is found, where M_{dense} is expressed in solar masses. This is consistent with similar relations found by Gao & Solomon (2004) and Wu et al. (2005) for extragalactic clouds that are several orders of magnitude more massive than local GMCs. These results taken together indicate that the total mass of a GMC does not control the star formation rate within it. Instead, it is the total amount of dense material in the GMC that sets the SFR.

The time frame over which an embedded cluster can sustain star formation is a fundamental, yet difficult, quantity to constrain. Quantifying the age, and spread of ages, of a young cluster relies on photometry coupled with theoretical pre-main sequence evolution models. The inferred stellar ages are found to sensitively depend on the details of the chosen evolutionary model. Moreover, cluster formation occurs within a larger star-forming complex which can have several distinct centers of star formation that may not be coeval. Projection effects can result in confusion when these distinct regions overlap.

Nevertheless, several measurements of age spreads in young clusters have been undertaken. One of the nearest and most well studied clusters is the Orion Nebula Cluster (ONC) which contains approximately 1100 $M_{\odot}$ of stars. Using the method described above, Da Rio et al. (2010) find an age spread of 2-3 Myr in the ONC. As pointed out by Alves & Bouy (2012), these results are likely contaminated by an older, foreground cluster and the actual age spread is smaller. Other studies of massive clusters in the MW favour smaller age spreads ($\lessapprox$1 Myr) that are significantly less than the age of the cluster (Massey & Hunter, 1998; Kudryavtseva et al., 2012). While it is more difficult to ascertain age spreads in more evolved clusters, most

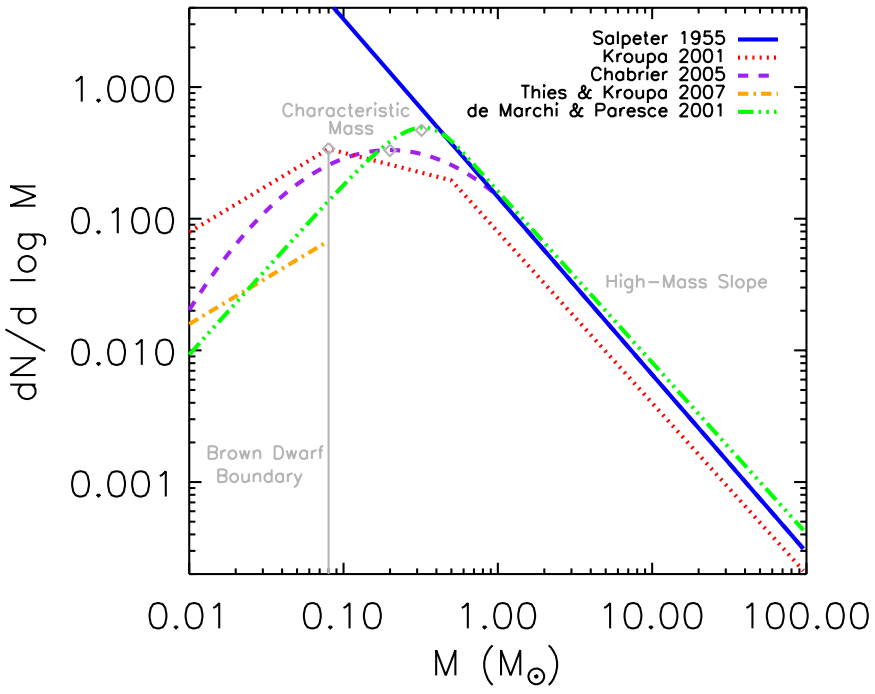

Figure 1.6: A collection of proposed forms of the IMF. The Chabrier (2005) IMF, corresponding to Equation 1.6, is shown by the magenta dashed line. *Figure reproduced with permission from Offner et al. (2014).*

studies find no evidence of large age spreads (Currie et al., 2010; Bastian & Silva-Villa, 2013). Taken together, these results show that cluster formation occurs over Myr timescales as opposed to tens or hundreds of Myr. This corresponds to up to ten freefall times of the host clump which is 0.36 Myr assuming a density of 10^4 cm^{-3}. The processes responsible for halting star formation in clusters, and removing the unused gas resulting in an open cluster, are discussed below.

The resulting stellar ensemble formed from an individual cluster forming event has been well characterized. First studied by Salpeter (1955) for stars greater than 1 M$_\odot$,

the distribution of initial main-sequence stellar masses for a population of stars — deemed the Initial Mass Function (IMF) — can be expressed as a powerlaw function (see Equation 1) with a slope of -2.35. More recently, the form of the IMF has been extended to lower mass stars. While several functional forms have been used to represent the IMF (see Figure 1.6), they share common elements. The slopes above 1 $M_\odot$ are consistent with Salpeter (1955) but the distribution flattens at lower masses. Some IMF fits also include a peak at $\sim$0.08 $M_\odot$. One popular parameterization of the IMF presented in Chabrier (2005), and the one used throughout this work, is a lognormal distribution for masses less than 1 $M_\odot$ and a powerlaw tail at higher masses. Mathematically, it is expressed as,

$$\xi(log\ m) = \begin{cases} 0.093 \times exp\{\frac{-(log\ m - log\ 0.2)^2}{2\times(0.55)^2}\}, & \text{m} \leq 1\ \ \text{M}_\odot \\ 0.041 m^{-1.35\pm0.3}, & \text{m} > 1\ \ \text{M}_\odot, \end{cases} \tag{1.6}$$

where $\xi(log\ m)$ is the probability of a star having a mass between $log\ m$ and $log\ m + d(log\ m)$.

1.2 Radiative Feedback

The processes described above — the collection of molecular gas into filaments and clumps and their subsequent conversion into clusters of stars — are well established but several fundamental questions remain. Firstly, the conversion of molecular gas into stars is an inherently inefficient process. The SFE of a GMC, defined here as

the ratio of the stellar mass to the original gas mass, is typically $\sim$2% (Evans, 1991) but can range from 0.2% to 20% (Murray, 2011). On smaller scales, however, the SFE can be higher. For example, the SFE of star-forming clumps is typically quoted as 10-30% (Lada & Lada, 2003) and dense cores hosting the formation of individual stellar systems have SFEs that can exceed 30% (André et al., 2014). Nevertheless, the vast majority of a GMC's mass does not participate in star formation.

Connected to the question of SFEs are the lifetimes of molecular clouds. Since most of the molecular gas in a GMC remains unused, some process must be responsible for dispersing a GMC and limiting star formation. The lifetimes of clouds, however, have been a matter of considerable debate. Estimates range from a single free-fall time, typically 10 Myr for an average GMC, to 10 or more free-fall times (Elmegreen, 2000; Hartmann et al., 2001; Scoville & Wilson, 2004). Recent estimates for massive GMCs favour 1-3 free-fall times (Murray, 2011). This estimate is consistent with observations of GMCs in M33 that suggest an average lifetime of 14.2 Myr (Corbelli et al., 2017). The lifetime of a single cluster forming event is also a poorly constrained quantity. As discussed above, cluster formation must be completed in $\lesssim$3 Myr but the processes responsible for this timescale are debated.

Since GMCs are observed to be turbulent, initial attempts at explaining the low SFEs of molecular clouds focused on this process since it provides a form of pressure support that can slow gravitational collapse. Simulations modeling the formation of stars using gravity and realistic turbulent velocity fields show that the SFE can indeed be reduced but, given enough time, 100% of the gas is converted to stars (Klessen et al., 2000; Bate et al., 2003; Bonnell et al., 2008). Reduced star formation

rates, and therefore SFEs, can also occur within unbound ($\alpha > 2$) clouds (Ward et al., 2016). However, only a subset of GMCs are unbound so turbulence alone cannot explain the star-forming properties of molecular clouds.

Magnetic fields also add an additional form of pressure support which slows the collapse of a cloud (Myers & Goodman, 1988; Tilley & Pudritz, 2007; Federrath & Klessen, 2012). More specifically, the presence of magnetic fields affects the structure of the filaments out of which clusters form. Compared to purely hydrodynamic filaments, magnetic fields result in broader, less centrally peaked filaments that are less prone to fragmentation (Kirk et al., 2015). The strengths of magnetic fields within molecular clouds, however, are not high enough to fully suppress star formation. Moreover, their presence can only delay star formation and cannot disperse a GMC.

Instead, feedback is a unifying process that can, at least in part, answer the open questions discussed above. In this context, feedback refers to the injection of energy and momentum from newly formed stars into the gas enveloping them. Feedback comes in many forms;

- **Protostellar Jets**: The twisting of magnetic fields within the rotating disk surrounding a protostar drives perpendicularly collimated outflows (Li & Nakamura, 2006; Pudritz et al., 2007; Maury et al., 2009; Federrath et al., 2014). The velocity of the jets depend on the mass of the host, but values of 100 km s^{-1} are typical. While the jets affect the accretion flow onto the forming protostar, they only drive turbulence on maximum scales of $\sim$1 pc and are probably not responsible for the large scale clearing of cluster gas.

- **Radiative Feedback**: The ionizing radiation released by young stars can heat and ionize the surrounding gas resulting in the production of HII regions (Dale et al., 2005; Peters et al., 2010a; Klassen et al., 2012b). Moreover, the direct radiation pressure from ultraviolet (UV) photons interacting with interstellar dust can drive outflows and blow bubbles in the ISM (Krumholz & Thompson, 2012; Murray et al., 2010).

- **Stellar Winds**: The high luminosities of O and B type stars result in a wind of charged particles being released from their surface. This is caused by radiation pressure acting on the absorption lines of heavy elements in their atmospheres. The velocities of these winds can exceed 10^3 km s^{-1} with mass outflow rates of 10^{-6} $M_\odot$ yr^{-1}. Such winds are capable of blowing bubbles in the surrounding GMC (Castor et al., 1975; Dale & Bonnell, 2008).

- **Supernovae**: Massive stars end their lives rapidly — $\sim$5 Myr for the most massive O stars — and explode as supernovae. The release of this energy may be sufficient to stop star formation and clear the remaining gas (Hensler, 2011).

Of particular importance for clusters hosting massive stars is radiative feedback. It is noted that throughout this work, radiative feedback is taken to be the combination of ionization feedback and direct radiation pressure. These processes are described in more detail below. Unlike Supernovae, ionization feedback and radiation pressure act during the entire lifetime of an O star and are therefore vital to the early evolution of a cluster. The combination of these processes is thought to be the key feedback mechanism for GMCs hosting massive clusters (Murray et al., 2010).

Figure 1.7: A view of the 30 Doradus star-forming region in the LMC. Shown in blue is hot, ionized gas indicative of a giant HII region. The infrared emission from cold gas, shown in orange, has been carved out by these hot bubbles. *Credits: X-ray: NASA/CXC/PSU/L.; Infrared: NASA/JPL/PSU/L.*

The absorption of UV photons by interstellar gas results in ionization and subsequent heating as the freed electrons interact with their surroundings. The absorption of UV photons by dust grains, which also release electrons into the gas via the photoelectric effect, is another significant heat source. The resulting HII region is composed of mainly ionized hydrogen gas at temperatures of ∼10,000 K. These elevated temperatures increase the gas pressure and the HII regions expands, sweeping up gas into a shell as it moves outwards. This process, and its effect on subsequent star formation, is referred to as ionization feedback. The size of an HII region depends on the local gas density and the population of massive stars creating it. Ultra compact HII regions can be less than 1 pc in size while Giant HII regions can span hundreds of parsecs. The largest HII region in the Local Group, known as 30 Doradus located in the LMC, is shown in Figure 1.7. The blue regions show the hot ionized gas which has carved bubbles in the cold, infrared emitting gas shown in orange. The diameter of the HII region is estimated to be 200 pc (Lebouteiller et al., 2008) and the massive cluster at its center (R136) hosts $\sim 4.5 \times 10^5$ $M_\odot$ of stars (Bosch et al., 2009).

The high temperatures brought on by photodissociation are the core reason radiative feedback can reduce the SFE in a GMC. The Jeans mass (Equation 3) increases with temperature as $T^{3/2}$. Increasing the temperature therefore limits fragmentation of the gas and can decrease the overall SFE.

Early analytic models attempted to quantify the role of ionization feedback in GMCs (Whitworth, 1979; Williams & McKee, 1997). These models consider a generalized setup in which an OB association has created an eroded cavity that bursts through one side of a uniform density GMC resulting in a "blister" HII region. Ra-

diation produced by the massive stars can either escape through this cavity into the lower density regions surrounding the cloud, or it can be released towards the cloud contributing to an ionization front that propagates into the GMC. By adopting densities typical of local clouds, Whitworth (1979) found that a GMC can be completely ionized, and therefore disrupted, in 3-5 Myr if only 4% of the initial cloud mass is converted to stars under the assumption of a Salpeter IMF. The updated model of Williams & McKee (1997) instead find that several generations of OB stars are required to completely ionize massive ($> 3{\times}10^5$ $M_\odot$) GMCs over a timescale of $\sim$30 Myr. Nevertheless, these works suggest that ionization feedback plays a central role in the destruction of molecular clouds. The assumption of a blister HII region in an otherwise uniform density cloud, however, does not capture the true nature of GMCs because, as discussed above, it ignores the clumpy and filamentary structure of observed clouds.

The absorption of UV photons exerts a direct pressure on the dust surrounding forming stars. At the densities typical of these regions, the dust is well coupled to the gas via collisions so a pressure is also exerted indirectly on the gas. In addition to the direct radiation pressure from UV photons, the emission and subsequent trapping of IR photons can also apply further pressure. The role of this additional pressure is argued to be small in typical MW GMCs (Murray et al., 2010) and is therefore neglected in this work. Theoretical considerations suggest direct radiation pressure plays a central role in controlling the SFE of massive protoclusters (Krumholz & Matzner, 2009; Fall et al., 2010; Murray et al., 2010).

Due to the complexity of radiative transfer, and the array of other physical processes involved in star formation, numerical simulations are required to understand the role of radiative feedback. The role of ionization feedback, in particular, has been studied in variety of works (Dale et al., 2005; Offner et al., 2009; Bate, 2009; Peters et al., 2010a; Commerçon et al., 2010; Krumholz et al., 2010; Harper-Clark, 2011; Klassen et al., 2012b; Dale et al., 2012b). A typical example of the effect of ionizing feedback is shown in Figure 1.8. These column density images of 10^4 and 10^5 $M_\odot$ GMCs show pronounced, low density voids in the simulations containing ionizing feedback (bottom panel) that are not seen in the purely hydrodynamic cases (top panel). These voids are the HII regions produced by young, massive stars. Despite the dramatic visual differences, including ionization feedback into star formation simulations generally only lowers the SFE up to a factor of 2. The large scale dispersal of cluster forming gas is typically not observed.

Many of these simulations, however, focus on the formation of individual clusters in an attempt to explain the origin of the IMF. The typical mass scale of these simulations is 100-1000 $M_\odot$ (Dale et al., 2005; Offner et al., 2009; Krumholz et al., 2010; Klassen et al., 2012b). The inclusion of ionization feedback is found to affect the IMF by limiting the fragmentation of low mass stars. However, its role in an entire GMC cannot be constrained in these types of simulations. An individual molecular cloud can host several centers of cluster formation and these distinct regions may be able to affect one another depending on their proximity. For example, Dale et al. (2007) shows that the presence of external UV radiation can dramatically affect the

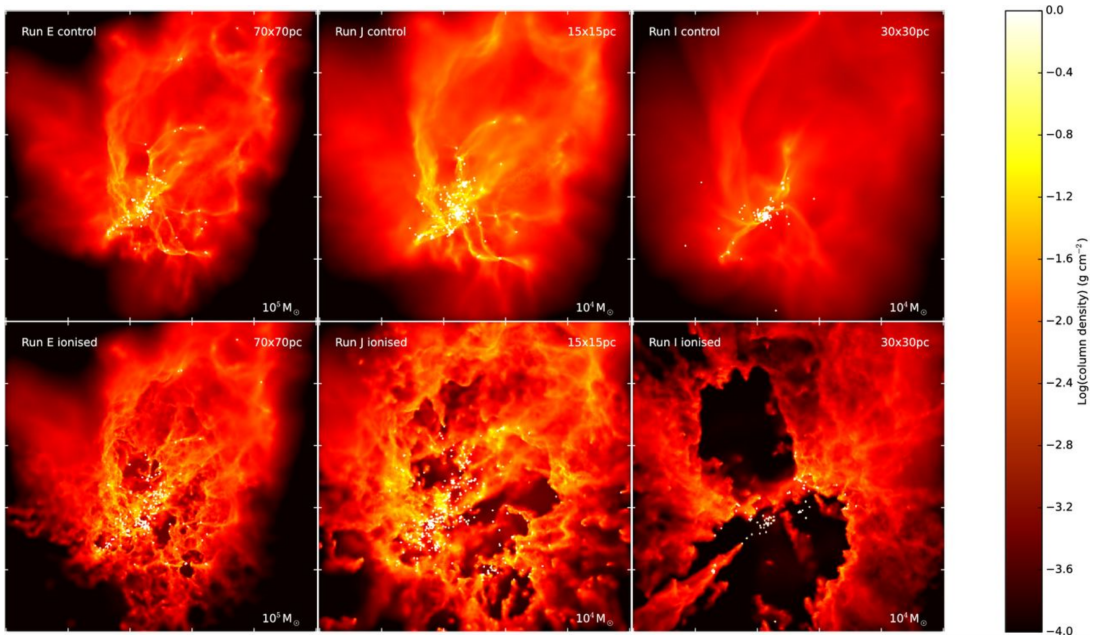

Figure 1.8: Column density images of simulations with ionizing feedback (bottom panel) and without ionizing feedback (top panel). The low density voids are filled with hot, ionized gas (ie. an HII region). The locations of stars are marked by the white dots. *Figure reproduced with permission from Boneberg, D.M., Dale, J.E., Girichidis, P., & Ercolano, B., Turbulence in giant molecular clouds: the effect of photoionization feedback, 2014, MNRAS, 447, Issue 2, 1341*

structure of a cluster forming region. Simulations of cluster formation within the context of an entire GMC are therefore required.

Such simulations have indeed been completed (Harper-Clark, 2011; Dale & Bonnell, 2011; Dale et al., 2012b). Because of the expense of the computations required, only a small number of models can be run and several approximations need to be made. Most notably, it is difficult to resolve the formation of individual stars when simulating an entire molecular cloud. Instead, these simulations rely on isolating regions that will eventually form clusters and prescribing how star formation proceeds within those clusters.

The different numerical methods used can lead to contradicting results. For example, Harper-Clark (2011) found that cluster formation can be entirely quenched by radiative feedback alone and the final SFEs are reduced by more than a factor of 3. However, these simulations do not model the growth and evolution of clusters. Instead, they are assumed to instantly appear with their luminosity determined by their formation masses. Moreover, only two realizations of the simulations are completed with masses $2{\times}10^5$ and $8{\times}10^5$ $M_\odot$. This is a small mass range compared to observed GMCs. Additionally, both models were assumed to be virialized.

Dale et al. (2012b), on the other hand, simulated a wider range of GMC masses (10^4, 10^5, and 10^6 $M_\odot$) and found no significant effect on the star formation efficiency in any cloud. To model star formation within clusters, the authors again do not model cluster growth and make the assumption that all the mass in the cluster is entirely contained in stars from which the massive stellar content can be approximated. The

explanation for the small effect on the SFE in these clouds is that the ionizing radiation is preferentially released into the low density voids naturally produced by turbulence. The dense filaments out of which the clusters formed are, therefore, not strongly affected.

Another possible reason for the small impact of radiative feedback on SFEs is pointed out by Peters et al. (2010a). The HII regions produced in their simulations of cluster formation do not systematically grow in size. Instead, the turbulent nature of the gas causes the HII regions to change both size and shape over short timescales — a process called flickering. Therefore, an ionized and hot region of gas may be able to form stars in the future after the HII morphology has changed. Flickering has also been seen in other simulations (Klassen et al., 2012b; Howard et al., 2014, 2016) and there is also recent observational evidence that suggests it is a real process (De Pree et al., 2014).

Despite the SFE not being heavily impacted by radiative feedback in Dale et al. (2012b), they do find indications that its effects vary depending on cloud mass. More specifically, the fraction of mass which becomes gravitationally unbound as a result of feedback is higher for low mass clouds. This is attributed to the lower escape velocities of these clouds. This study, however, only used three GMC masses and all models were initially gravitationally bound.

Nevertheless, these results hints at the exciting prospect that radiative feedback does not play a singular role in all environments. Instead, it may it may be a complex function of GMC properties. A more detailed exploration of the parameter space of

initial GMC conditions, and the role of radiative feedback in those environments, is a main aspect of this thesis.

1.3 The Effects of Cluster Formation on Global Scales

The radiation fields from massive star and cluster formation that escape their host GMCs drive several crucial processes on scales larger than the GMC out of which they form. Within a galaxy, light from newly formed OB stars contributes to the UV portion of the ISRF — the pervading radiation field that interacts with the ISM and has peak energy densities at optical and UV wavelengths (Draine, 2011).

The importance of the ISRF has been recognized for nearly a century (Eddington, 1928). The first measurements of the ISRF were performed by Habing (1968) who found an energy density of $\sim 4 \times 10^{-14}$ erg cm^{-3} for 12.4 eV photons. In later years, the UV portion of the ISRF was estimated based on the number and distribution of high mass stars combined with dust extinction models for the MW. The most commonly adopted form of the ISRF for UV wavelengths between 91.2 and 200 nm is presented in Draine (1978),

$$I(\lambda) = 3.2028 \times 10^{13}\lambda^{-3} - 5.1542 \times 10^{15}\lambda^{-4} + 2.0546 \times 10^{17}\lambda^{-5}, \qquad (1.7)$$

where $I(\lambda)$ is the intensity of radiation at wavelength λ in photons cm^{-2}s^{-1}nm^{-1}. The wavelength dependence of this equation, and previous theoretical and observa-

tional results, are shown in Figure 1.9. The resulting intensity is similar to a 20000 K, B-type star with some excess at smaller wavelengths. Variations in the local strength of the ISRF between factors of 2-3 can be expected as OB stars are born and subsequently die. Therefore, being able to accurately treat the formation of massive stars, and follow the propagation of their radiation through a GMC and the surrounding ISM, is vital to reconstructing the ISRF.

The physical, chemical, and thermal structure of the ISM is largely set through interactions with the ISRF. The ionization of diffuse interstellar material is driven by photoionization and photodissociation caused by the absorption of UV photons. The absorption by dust grains also leads to heating through the ejected photoelectons. UV photons also play a central role in controlling chemical reactions involving hydrogen, oxygen, carbon, and nitrogen-containing atoms and molecules, many of which are main cooling species in the ISM. The formation of ions through this process is often a precursor to the chemical reactions required to form larger species (Tielens & Hollenbach, 1985).

The diffuse ionized gas (DIG) layers that exist above and below the galactic plane also highlight the importance of clusters that host OB star formation. These layers have densities of $\sim$0.025 cm^{-3}, average temperatures of 8000 K, and a large scale height of $\sim$1 kpc (Reynolds, 1984, 1985). Massive OB stars are thought to be a main ionizing source for the DIG. The energy required to maintain the ionization state of the DIG is approximately 15% of the Lyman continuum photons produced by the sum total of MW OB stars (Reynolds, 1993). However, clusters containing OB type stars are restricted to the thin disk of the MW which only has a scale height of

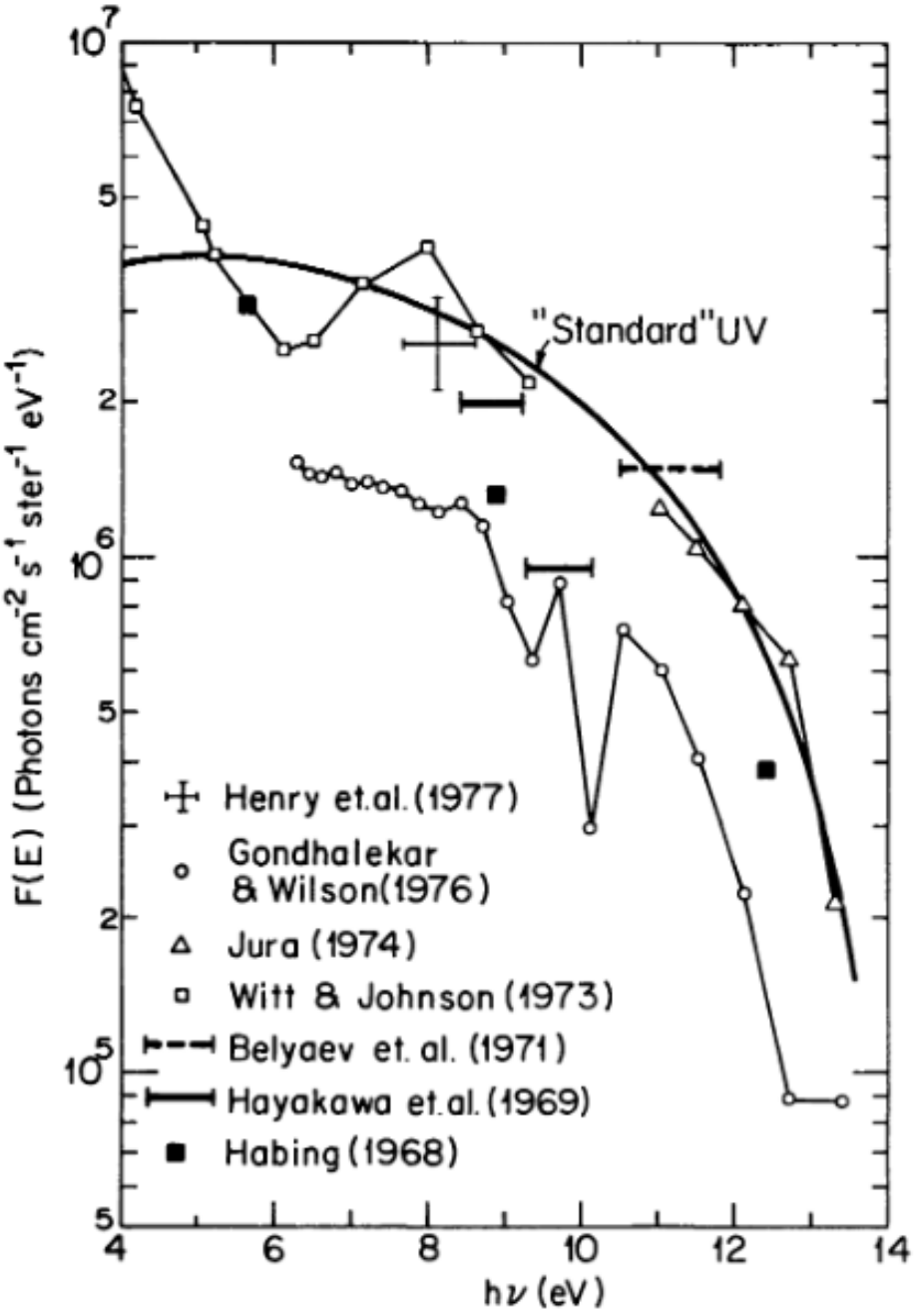

Figure 1.9: The wavelength dependence of the UV background up to 13.6 eV. Equation 1.7, expressed in terms of energy rather than wavelength, is plotted as a solid black line and is meant to represent the best fit to the previous theoretical and observational estimates shown by the points. *Figure adapted from Draine (1978) ©AAS. Reproduced with permission.*

300-400 pc (Carroll & Ostlie, 1996). Since the lifetime of the most massive stars can be 10 Myr or less, this suggests that photons must be escaping their host GMCs and interacting with the DIG. This is further supported by Hoopes & Walterbos (2000) who found that the field O star population in M33 is not sufficient to maintain the DIG. Instead, a significant portion must be contributed via HII regions that are leaking photons into the ISM. The fraction of UV photons escaping from a GMC (f_{esc}) is therefore crucial for galactic-scale modeling.

Despite the fundamental importance of f_{esc}, there have been few attempts to characterize and constrain it. Dale et al. (2012b) present f_{esc} from a suite of GMC models with masses of 10^4, 10^5, and 10^6 $M_\odot$ and find values that range from 7% to 90%. This large variation indicates that the properties of the host GMC, namely the porosity of the cloud, play a defining role in determining f_{esc}. The values quoted in Dale et al. (2012b), however, are only the final escape fractions from their models. The temporal variation of f_{esc} is not characterized. More recently, Rahner et al. (2017) measured f_{esc} from GMCs in the mass range 10^{5-8} $M_\odot$ under the influence of radiative feedback, stellar winds, and supernovae feedback. Again, f_{esc} is found to vary significantly depending on cloud mass with values between 0% and 90%. While more physical processes are included compared to Dale et al. (2012b), the setup is idealized in the sense that a cluster with a fixed mass is placed in the center of a uniform density cloud. The characterization of f_{esc}, and its temporal variations, in a suite of turbulent GMCs with a realistic prescription for cluster formation is a central goal of this thesis.

On scales larger than individual galaxies, UV photons contribute to cosmic reionization which refers to the complete ionization of the intergalactic medium (IGM). Observations of quasars at wavelengths smaller than the Lyα line indicate that cosmic reionization was complete by z$\sim$6 (Gunn & Peterson, 1965; Fan et al., 2006; Willott et al., 2007). While the sources of the UV photons needed for reionization are not completely understood, the rarity of massive quasars at high redshifts indicate that they cannot be the sole contributors (Grissom et al., 2014). Instead, the stars in the more numerous low mass ($\lessapprox 10^9$ $M_\odot$) dwarf galaxies are thought to provide the required photons. For the same reasons described above for the DIG, OB stars are likely a main contributor.

The UV escape fraction from these galaxies cannot be measured directly due to low luminosities and extreme distances. Instead, studies have attempted to observe the Lyman continuum (LyC) flux of local galaxies. In general, detections are unsuccessful and only place upper limits on f_{esc} of 2-10% (Hurwitz et al., 1997; Heckman et al., 2001; Deharveng et al., 2001; Grimes et al., 2007). LyC emission has been observed for individual galaxies at z$\sim$3. These studies find escape fractions of 4-20% depending on the galaxy (Shapley et al., 2006; Iwata et al., 2009). The positive detection of LyC photons at high redshifts suggests that the escape fractions of local galaxies may not be fitting proxies for studying cosmic reionization.

With advances in computing resources, radiation hydrodynamic simulations of galaxy formation and evolution have been completed. However, the resulting f_{esc} values from these simulations vary between works. For example, Wise & Cen (2009) find $f_{esc} > 30\%$ for isolated, irregular dwarf galaxies at z=8. While other works

have found similar results (Razoumov & Sommer-Larsen, 2010; Paardekooper et al., 2013), Gnedin et al. (2008) instead find $f_{esc} \sim$ 1-3% with no redshift dependence and a trend towards smaller escape fractions for lower mass galaxies, casting doubt on the ability of high redshift dwarfs to contribute to cosmic reionization.

As pointed out by Paardekooper et al. (2011), the main constraint on galactic scale simulations attempting to constrain f_{esc} is the treatment of the dense gas. The interplay between turbulence, star formation and its associated feedback, and the overall structure of the ISM need to be highly resolved. This can be computationally prohibitive. Like the ISRF, GMC scale simulations of star and cluster formation which include radiative transfer may be able to inform these larger scale models. While they would not include the larger structure of the ISM, they have the advantage of higher resolution over the length scales relevant for star formation and can provide valuable inputs for galactic scale estimates of f_{esc}.

1.4 Thesis Outline

The observational, theoretical, and numerical considerations described above lay the groundwork for the contributions made in this thesis. I attempt to answer several open questions related to cluster formation in GMCs and its potential impact on larger scales. More specifically, the questions I address can be summarized as follows:

- How do the initial conditions of GMCs affect the course of cluster formation? What initial conditions lead to the formation of clusters with realistic charac-

teristics such as SFRs, SFEs, and mass functions. Here, I am focusing on the gravitational boundedness and the mass of molecular clouds.

- What role does radiative feedback play in cluster formation? Is radiative feedback alone capable of stopping cluster formation and ultimately destroying a GMC? How does the answer to the previous question depend on the host GMC?

- What is the escape fraction of UV photons from individual GMCs with different initial conditions? How strongly does it vary as a function of time? What is the net escape fraction from a *population* of molecular clouds?

To address these questions, I turn to numerical simulations. I use the astrophysical code *FLASH* (Fryxell et al., 2000a) to model the process of cluster formation. *FLASH* is an Adaptive Mesh Refinement (AMR) code that contains modules to treat hydrodynamics, gravity, radiative transfer, star/cluster formation, and heating and cooling processes.

Two aspects of the code are particularly relevant to this work — cluster formation (represented through the use of sink particles), and radiative transfer. Firstly, the sink particle method from Federrath et al. (2010) is used for cluster formation in combination with the subgrid model in Howard et al. (2014) to represent unresolved star formation within the clusters. Since the details of the subgrid model are described in the following chapters, an overview will not be provided here. While the concept of the subgrid model is the same as in Howard et al. (2014), several adjustments have been made to increase the code's computational efficiency. Secondly, a hybrid-characteristics raytracing scheme is used to solve the radiative transfer equa-

tions. For a detailed description of this algorithm, I refer the reader to Rijkhorst et al. (2006).

Rather than providing a separate introduction for each chapter, which would repeat many of the points already discussed, a brief overview is outlined below. The chapters are reproductions of journal articles that have either been published, accepted, or are in preparation to be submitted. The state of each chapter is included in the overview.

- **Chapter 2**: *Simulating Radiative Feedback and Star Cluster Formation in GMCs: I. Dependence on Gravitational Boundedness*
  Authors: Corey Howard, Ralph Pudritz, William Harris
  Published in *Monthly Notices of the Royal Astronomical Society*, Volume 461, Issue 3, p.2953-2974 (September 2016)

  Description: We study the formation and early evolution (<5 Myr) of star clusters in massive, 10^6 $M_\odot$ GMCs with initial virial parameters of 0.5, 1, 2, 3, and 5. The clouds have diameters of 67.6 pc, the box sizes are 80 pc, and the maximum resolution is 0.13 pc. For each virial parameter, two simulations are completed — one purely hydrodynamic simulation, and one radiation hydrodynamic simulation — to characterize the role of radiative feedback. We find that varying the initial virial parameter results in SFEs in the range of 19-33% with the bound models having the highest efficiencies. The inclusion of radiative feedback only reduces the SFE by a maximum of ∼9% with 1%

being the typical value. We compare the resulting cluster properties to several observational results including SFRs, mass distributions, and stellar age spreads.

- **Chapter 3**: *Simulating Radiative Feedback and Star Cluster Formation in GMCs: II. Mass Dependence of Cloud Destruction and Cluster Properties*
  Authors: Corey Howard, Ralph Pudritz, William Harris
  Published in *Monthly Notices of the Royal Astronomical Society*, Volume 470, Issue 3, p.3346-3358

  Description: We present a follow up suite of GMC simulations with masses of 10^4, $5{\times}10^4$, 10^5, $5{\times}10^5$, and 10^6 $M_\odot$. The number of cloud masses simulated, in combination with using an identical initial virial parameter for all models, makes this the most comprehensive study aimed at isolating the role of GMC mass and radiative feedback in cluster formation simulations. We find that radiative feedback affects certain clouds more than others. In particular, the intermediate mass models are nearly fully ionized and disrupted by $\sim$5 Myr. We follow up with a discussion of an apparent relation between the host GMC mass and the most massive cluster it can form as well as the resulting cluster mass function obtained from combining the results from all simulations.

- **Chapter 4**: *Ultra Violet Escape Fractions from Giant Molecular Clouds During Early Cluster Formation*
  Authors: Corey Howard, Ralph Pudritz, Ralf Klessen
  Published in *The Astrophysical Journal*, Volume 834, Issue 1, article id. 40

(January 2017)

Description: We select a single GMC simulation from Chapter 2 and, for the first time, examine the full evolution of the UV photon escape fraction up to ∼4.5 Myr. Visualizations of the ionizing photon flux escaping the cloud show high variability in both time and space. We find an average escape fraction of 15% with factor of 2 variations that occur over very short timescales. These variations are attributed to the growth and collapse of HII regions caused by the turbulent nature of the gas in the GMC.

- **Chapter 5**: *Simulating the UV Escape Fractions from Star-forming Dwarf and Spiral Galaxies*

  Authors: Corey Howard, Ralph Pudritz, Bill Harris, Ralf Klessen

  In preparation for submission to *Monthly Notices of the Royal Astronomical Society*

  Description: We present the UV escape fractions from the suite of GMC masses, simulated in Chapter 3. The varying strength of radiative feedback in clouds of different masses has a direct impact on the escape fractions. The models that are disrupted by radiative feedback show escape fractions that approach 100% at late times. We then present a new model for combining our results to represent, for the first time, the escape fraction from populations of GMCs that are indicative of dwarf and spiral-type galaxies. While the typical escape fractions are low (<10%), values in the range 0-90% are observed. We compute

the resulting SFRs for the two galaxy models and compare to observational results.

Finally, I present my overarching conclusions, and how they fit in the context of star cluster formation, in Chapter 6. I also discuss possible future research directions that are natural extensions of the work presented in this thesis.

Chapter 2

Simulating Radiative Feedback and Star Cluster Formation in GMCs: I. Dependence on Gravitational Boundedness

2.1 Abstract

Radiative feedback is an important consequence of cluster formation in Giant Molecular Clouds (GMCs) in which newly formed clusters heat and ionize their surrounding gas. The process of cluster formation, and the role of radiative feedback, has not been fully explored in different GMC environments. We present a suite of

simulations which explore how the initial gravitational boundedness, and radiative feedback, affect cluster formation. We model the early evolution (< 5 Myr) of turbulent, 10^6 $M_\odot$ clouds with virial parameters ranging from 0.5 to 5. To model cluster formation, we use cluster sink particles, coupled to a raytracing scheme, and a custom subgrid model which populates a cluster via sampling an IMF with an efficiency of 20% per freefall time. We find that radiative feedback only decreases the cluster particle formation efficiency by a few percent. The initial virial parameter plays a much stronger role in limiting cluster formation, with a spread of cluster formation efficiencies of 37% to 71% for the most unbound to the most bound model. The total number of clusters increases while the maximum mass cluster decreases with an increasing initial virial parameter, resulting in steeper mass distributions. The star formation rates in our cluster particles are initially consistent with observations but rise to higher values at late times. This suggests that radiative feedback alone is not responsible for dispersing a GMC over the first 5 Myr of cluster formation.

2.2 Introduction

The modern paradigm for star cluster formation suggests that clusters are born from dense clumps ($n > 10^4$ cm^{-3}) which form in supersonically turbulent, filamentary molecular clouds (Lada & Lada, 2003; Mac Low & Klessen, 2004; Bertoldi & McKee, 1992; Kruijssen, 2012). Recent observations show that young stellar clusters tend to form at the intersection of filaments in regions that are fed by higher than average accretion rates (Schneider et al., 2012; Kirk et al., 2013; Balsara et al., 2001;

Banerjee & Pudritz, 2006). These overdense regions may then fragment further, resulting in highly subclustered objects which undergo mergers (Megeath et al., 2012; Kuhn et al., 2012).

The question of how the high accretion flow onto dense, star-forming clumps is halted is of particular importance. The mass accretion history of these objects has implications for the final cluster mass and, hence, the observed cluster mass function. Moreover, the overall conversion of molecular gas to stars is inefficient (Lada & Lada, 2003; Murray, 2011). Understanding what processes limit the star formation efficiency in molecular clouds is key to a complete star formation theory as well as underpinning all discussions of simulations and theories of galaxy formation and evolution.

Several mechanisms have been proposed to explain the low star formation efficiency observed in molecular clouds. For example, turbulent velocity fields have been shown to lower the overall star formation rate per freefall time (Klessen et al., 2000; Bate et al., 2003; Bonnell et al., 2008). This cannot be the sole mechanism at work, however, since, given enough time, all of the gas will be converted to stars. The added pressure support via magnetic fields can also lower the overall star formation efficiency (Myers & Goodman, 1988; Tilley & Pudritz, 2007; Federrath & Klessen, 2012). While magnetic fields may play an important role in limiting cloud fragmentation, they also contribute to the dispersal of gas within individual star forming cores by means of hydromagnetic bipolar outflows and jets that are associated with young stars of all masses (Matzner & McKee, 2000; Federrath et al., 2014).

The process of feedback from newly-formed stars can both limit the star formation efficiency and disperse the surrounding gas, thereby halting the star formation process. Feedback comes in various forms: protostellar jets (Li & Nakamura, 2006; Maury et al., 2009; Federrath et al., 2014), stellar winds (Dale & Bonnell, 2008), ionization and heating of the gas (Dale et al., 2005; Peters et al., 2010a; Klassen et al., 2012b), and radiation pressure (Krumholz & Thompson, 2012; Murray et al., 2010). Radiative feedback has been suggested as being the most important form of feedback in clusters which host massive star formation (Murray et al., 2010; Dale et al., 2012b; Bate, 2012). The ionizing radiation released from newly-formed stars heats the gas to approximately 10,000 K and can drive the expansion of massive HII regions. The direct input of momentum via high energy photons interacting with surrounding dust grains can also drive strong outflows.

Previous studies of radiative feedback on both small and large spatial scales have shown that the star formation efficiency can be significantly reduced (Dale et al., 2007; Peters et al., 2010a; Dale et al., 2012b; Bate, 2012; Klassen et al., 2012b; Kim et al., 2012). Studies which model the formation of individual stars, however, are typically limited to the clump scale or low mass molecular clouds. These studies therefore neglect the impact of radiative feedback on the global structure of massive GMC's. Since cluster formation can be broadly distributed throughout a cloud, cluster interactions over the entire range of the GMC must be considered. There have been studies of radiative feedback in massive GMCs (10^6 $M_\odot$) (Dale et al., 2012b). Due to numerical constraints, the supergiant molecular cloud regime ($>$ 10^6 $M_\odot$) has not been examined nor do most models follow the cloud's evolution

up to the point of dispersal which is crucial to placing constraints on the lifetime of molecular clouds. Recent results suggest that radiation feedback alone is not effective in accounting for low star formation rates in galaxy formation simulations (Agertz & Kravtsov, 2015).

The lifetimes of molecular clouds, and the processes responsible for destroying them, are challenging to measure. Estimates of GMC lifetimes range from a single freefall time (Elmegreen, 2000; Hartmann et al., 2001), τ_{ff}, up to tens of freefall times (Scoville & Hersh, 1979; Scoville & Wilson, 2004). Recent observations of the deuterium fraction in both massive, starless cores and Infrared Dark Clouds (IRDCs) indicates ages within a range of 6 to 10 local freefall times (Kong et al., 2015; Barnes et al., 2016), corresponding to $\sim$3 Myr for IRDCs. We note that direct measurements of the lifetimes of molecular clouds out to a redshift of 4 are now possible with ALMA (Atacama Large Millimeter Array) and the method outlined in Kruijssen & Longmore (2014). Theoretical estimates suggest that radiative feedback, in particular radiation pressure, is the most important physical process responsible for destroying massive GMC's (Murray et al., 2010) but numerical simulations of star formation in GMC's which include radiative feedback are required to validate these claims.

The role of radiative feedback in different molecular cloud environments has also not been explored in detail. The observed clouds in the Milky Way and extragalactic sources show a wide range of properties. More specifically, molecular clouds have been observed to have a range of virial parameters, defined as the ratio of the cloud's kinetic energy to gravitational potential energy. This ratio may vary from 0.5 up to

10 with the mean being approximately 1 (Solomon et al., 1987; Rosolowsky, 2007; Hernandez & Tan, 2015). Simulations have shown that dense, self-gravitating clumps can still fragment out of clouds that are globally unbound (Clark et al., 2005; Clark & Klessen, 2008; Bonnell et al., 2011). Furthermore, the star formation efficiency is naturally lowered in unbound clouds (Padoan et al., 2012). Radiative feedback may play a stronger role in lowering the star formation efficiency in unbound versus bound clouds since the added energy and momentum can more easily disperse the surrounding, unbound gas.

To investigate these questions, we have chosen to simulate the formation of young stellar clusters in molecular clouds with a range of properties while including detailed radiative feedback. As described above, we focus on varying the initial virial parameter in turbulent, 10^6 $M_\odot$ GMCs. We are focusing on this mass because the majority of star formation in the Milky Way is hosted in these clouds (Murray, 2011).

In order to simulate the long term evolution of these clouds, we use sink particles to represent young clusters and combine this with a subgrid model to track star formation within the clusters. In Section 2.3, we describe the details of this subgrid model and the initial conditions used in our simulations. In Section 2.4, we describe the evolution of clouds with varying initial virial parameters, discuss the role of radiative feedback, and compare cluster properties across clouds. We find that radiative feedback has only a slight effect on the star formation efficiency. We find, in fact, that efficiencies are dominated by the gravitational binding of the cloud and that virial and sub virial initial cloud models do not show the low efficiencies that observations demand. In Section 2.5, we discuss how our results compare to

recent observations of local star forming regions, followed by our conclusions in the final section.

2.3 Numerical Methods

We perform numerical simulations using version 2.5 of the hydrodynamical code FLASH (Fryxell et al., 2000a). FLASH is an adaptive mesh refinement code (AMR) which integrates the compressible gas dynamic equations on a Eulerian grid and includes modules to treat self-gravity, radiative transfer, and star formation. We include cooling via molecular lines and dust (Banerjee et al., 2006), and use a simple ideal gas law equation of state with an adiabatic index of 1.67.

Radiative transfer is handled via a hybrid-characteristics raytracing scheme developed by Rijkhorst et al. (2006) and adapted for star formation simulations by Peters et al. (2010a). This scheme follows the propagation of both ionizing and non-ionizing radiation and makes use of the DORIC routines (Frank & Mellema, 1994; Mellema & Lundqvist, 2002). The DORIC package is an iterative scheme used to calculate the ionization, heating, and cooling rates of a large number of species (Frank & Mellema, 1994). For simplicity, however, hydrogen is used as the only gas component. Peters et al. (2010a) have shown that the code can accurately reproduce the analytic solution for the expansion of a D-type ionization front from Spitzer (1978), and Iliev et al. (2006) have shown the code accurately treats R-type fronts. The opacity to the non-ionizing radiation is represented by the Planck mean opacities from the dust model of Pollack et al. (1994). The Planck mean opacities are used because the

raytracer has no frequency dependence apart from ionizing versus non-ionizing radiation. Radiation pressure is included by adopting a single UV opacity of 775 cm^2 g^{-1} from Li & Draine (2001). The associated radiative force per unit mass is given by,

$$F = \frac{L}{c} \frac{e^{-\tau}}{4\pi r^2} \tag{2.1}$$

where L is the source luminosity, c is the speed of light, and τ and r are the optical depth and distance between the source and the target cell.

To represent the formation of star clusters, we make use of Lagragian sink particles (Banerjee et al. 2009; Federrath et al. 2010). In order to form a particle, a region of gas in the simulation volume must meet the following conditions:

- At the highest level of refinement
- The divergence is less than zero (ie. converging)
- At a local gravitational minimum
- The region is Jeans unstable
- The region is gravitationally bound
- Not within the radius of another particle.

These particles were designed to represent stars but the above conditions also model the formation of a dense clump which hosts cluster formation.

In order to examine the impact of radiative feedback from stellar clusters, we require a subgrid model for the radiative output of a cluster as it evolves over time. Below, we provide a brief summary of this model. A more detailed description can be found in Howard et al. (2014).

2.3.1 Subgrid model for cluster formation: Cluster sinks

One of the most important aspects of radiative feedback of a young forming cluster on its surrounding host GMC is the shutting off of the accretion flow into the cluster forming region. A cluster must therefore be assigned the correct, combined radiative output of all its member stars as star formation proceeds. Here, we provide a brief description of the subgrid model we use to form stars within a cluster particle.

In order for cluster formation to begin, the host clump must reach sufficient density in order to fragment and collapse. The threshold density for cluster formation has been observationally measured by Lada & Lada (2003) who found that the transition from starless to star forming clumps, in local star forming regions, occurs at a density of $\sim 10^4$ cm^{-3}. This number has also been quoted by other authors (Lada et al., 2010; Heiderman et al., 2010) who found that the SFRs in molecular clouds are well correlated to the dense ($>10^4$ cm^{-3}) gas mass. More recent work by Kainulainen et al. (2014), aimed at producing probability density functions for gas density from column density observations, found a density threshold of 5×10^3 cm^{-3}. Analytical models for the density threshold, which also account for environmental effects, find a threshold of 1.5×10^4 cm^{-3} when adopting Solar neighbourhood parameters

(Krumholz & McKee, 2005; Padoan & Nordlund, 2011; Kruijssen et al., 2014). We have therefore chosen to use a fiducial density threshold for cluster formation of 10^4 cm^{-3}. We report on several simulations in which we vary this value by an order of magnitude.

Once this critical density threshold is reached, as well as the other conditions outlined above, a cluster, represented by a sink particle in this work, forms. Star formation then proceeds within this cluster as gas accretes onto this dense region.

With this general framework in mind, we use our subgrid model for the formation, radiative feedback, and evolution of a cluster that addresses how the original gas reservoir (ie. clump) is divided into stars over time and how accreted gas is handled (Howard et al., 2014). We refer the reader to that paper for the details, which we now briefly summarize.

To treat the conversion of reservoir mass into stars, we divide it into main sequence stars at a prescribed efficiency according to an IMF. We use a star formation efficiency of 20% per freefall time (Lada & Lada, 2003), where the freefall time is given by

$$t_{ff} = \sqrt{\frac{3\pi}{32Gn\mu m_H}} \tag{2.2}$$

where n is the number density, μ is the mean molecular weight, and m_H is the mass of hydrogen. As discussed above, our fiducial value for n is taken to be 10^4 cm^{-3}. The resulting freefall time is 0.36 Myr.

We use the Chabrier IMF, given by

$$\xi(log\ m) = \begin{cases} 0.093 \times exp\{\frac{-(log\ m - log\ 0.2)^2}{2\times(0.55)^2}\}, & \text{m} \leq 1\ \ \text{M}_\odot \\ 0.041 m^{-1.35\pm0.3}, & \text{m} > 1\ \ \text{M}_\odot, \end{cases} \tag{2.3}$$

as the probability distribution from which we draw our stars (Chabrier, 2005). We chose to sample the Chabrier IMF every tenth of a freefall time, or 3.6×10^4 years. As shown in Howard et al. (2014), this sampling frequency allows cluster properties to evolve smoothly over time while still accurately reproducing the IMF from which the stars are drawn.

The masses of all stars formed in a cluster are recorded, meaning that its stellar content is known at all times. Using the analytic fits for the luminosity of main sequence stars provided by Tout et al. (1996), we know the luminosity of each star within the cluster. The total luminosity, and ionizing photon rate, of each cluster is the sum of the stellar components. These quantities are then used by the raytracer to treat the radiative transfer.

Gas accreted by a cluster is simply added to the gaseous reservoir. Since we are sampling an IMF in order to get our final stellar masses, we do not need to treat accretion onto individual stars. The accreted gas can then be used to form new stars at a later time.

We do not include mass loss from the cluster particle because we assume that the reservoir gas remains gravitationally bound to the cluster over long timescales, even in the presence of stellar feedback. Earlier simulations by Dale et al. (2005, 2007) found that the inclusion of radiative feedback was *not* sufficient to unbind the majority of the clump mass. The reason for this is collimated ionized outflows which are released into low density regions perpendicular to the dense filaments out of which the stars form. We therefore assume our gas reservoir is in a similarly filamentary state, preventing its disruption via stellar feedback. Furthermore, recent numerical works (Kruijssen et al., 2012; Dale et al., 2015), both with and without feedback mechanisms, and observational studies (Ginsburg et al., 2016) suggest that cluster formation proceeds via gas exhaustion rather than gas expulsion. This further justifies the use of cluster particles which do not lose mass.

We note that, when performing a simulation, we apply a mass threshold below which particles do not radiate. This was implemented in order to reduce the computational time. The raytracing scheme is computationally expensive so by allowing only massive particles to radiate, the total time spent during the raytracing step can be greatly reduced. We have chosen a threshold of 1000 $M_\odot$ contained in *stars*. Note that this is not the *total* mass of the cluster particle, but rather the stellar mass. We have chosen this threshold because it is approximately the mass at which the first O stars are expected to appear (Howard et al., 2014). We have verified that, at any given time, particles above this mass dominate the total luminosity budget so we are therefore confident that the application of a mass threshold should not impact our results significantly.

We have performed tests of the raytracing scheme similar to Peters et al. (2010a), except with our cluster sink particles, as described at the beginning of this Section. These were low resolution simulations, with 128 grid cells along each simulation axis, where a cluster sink particle was placed at the center of a uniform medium with a number density of 10^3 cm^{-3}. We allowed the cluster particle to sample the IMF once at the beginning of the simulation, after which no new stars were added to the cluster, and compared the resulting HII region to the analytical expression for the expansion of a D-type ionization front from Spitzer (1978). We find that, during expansion, the size of the HII region does not differ by more than 15% from the analytical solution. This error is reduced to less than 9% if we instead compare to the analytical expression presented in Raga et al. (2012), as was done in the radiative transfer code comparison project *STARBENCH* (Bisbas et al., 2015).

The addition of radiation pressure produces an HII region that is $\sim$10% larger compared to the test without radiation pressure. Additionally, the central density inside the HII region is significantly lower when radiation pressure is included, differing by approximately two orders of magnitude compared to the test without radiation pressure.

2.3.1.1 Cluster Sink Mergers

The sink particle routines in FLASH allow for particle mergers (Federrath et al., 2010). In order for a merger to occur, several conditions must be met. Firstly, the particles must be closer than an accretion radius, defined to be 2.5 cells at the highest

level of refinement. Secondly, the particles must be approaching one another. Lastly, the particles must be gravitationally bound to one another. More specifically, the total gravitational potential energy of the particle pair, at a distance of an accretion radius, must be greater than the total kinetic energy. When all of these conditions are met, the smaller mass particle is merged to the more massive particle. The new position is taken to be the center of mass position and the resulting particle velocity is determined via momentum conservation.

We have made custom modifications to the merging routines in order to better represent the merging of cluster sink particles. As mentioned above, cluster sink particles have their mass divided between fully-formed stars and the gaseous reservoir. When a cluster particle merger occurs, we combine the reservoir masses and the total stellar mass. Since we track the masses of all stars formed in each particle, the total stellar content remains the same after merging. We emphasize that, while we will be using merger to describe the joining of two cluster sink particles, this differs from the dynamical mergers associated with fully formed clusters that are devoid of gas. In our context, a merger is more aptly defined as the coalescence of a central stellar cluster as well as the envelope of surrounding gas.

Recent studies indicate that gas poor clusters may form before feedback starts acting since the local freefall time in these dense regions is the highest (Kruijssen et al., 2012; Dale et al., 2015). This means that the stellar cluster within our particles may be spatially segregated from the surrounding gas reservoir. Therefore, the merger of the stellar component in our particles may be thought of in the traditional way, namely a dynamical merger of gas poor stellar clusters. The reservoir can be

interpreted as the cocoon of gas which surrounds the central cluster, which is also joined during the merger. We do not resolve the structure of the gas reservoir, however, so we cannot distinguish between the merger of gas rich clusters and gas poor clusters with a surrounding envelope of gas.

2.3.2 Initial Conditions

We simulate the formation of stellar subclusters in collapsing GMC's with different initial properties and examine the role of radiative feedback in these environments. The clouds have the same initial average of $n = 100$ cm^{-3} and masses of 10^6 M$_\odot$. The radius of all clouds is 33.8 pc, corresponding to a minimum cell size of 0.13 pc. This results in a particle accretion radius of 0.325 pc (ie. 2.5 cells at the highest level of refinement). We have chosen an initial density profile which is uniform in the inner half of the cloud and decreasing as r$^{-3/2}$ in the outer half of the cloud. A quadratic fit is applied in the transition from uniform to decreasing density to ensure a continuous and smooth function.

We use outflow conditions at the boundary of the simulation volume. The total mass in our simulations is therefore not conserved but can decrease over time as gas escapes the domain. This is particularly relevant to the discussion in the next Section.

The cloud is overlaid with a Kolomogorov turbulent velocity spectrum. The turbulence is not driven after it is initially imposed and its strength is determined via the virial parameter.

The virial parameter relates the total kinetic energy to the total gravitational potential energy in a cloud. It is defined as (Bertoldi & McKee, 1992),

$$\alpha = 2\frac{E_{kin}}{|E_{grav}|} \approx \frac{5\sigma^2 R}{GM} \tag{2.4}$$

where E_{kin} is the total kinetic energy, E_{grav} is the total gravitational potential energy, σ is the velocity dispersion, R is the cloud radius, and M is the cloud mass. Equation 2.4 is exact for a uniform density cloud. The velocity dispersion can be expressed as $\sigma = M_a \times c_s$ where M_a is the Mach Number and c_s is the sound speed, which is taken to be $2.3{\times}10^5$ cm/s at 10 K. For a uniform density cloud without magnetic fields, a virial parameter of 1 corresponds to virial equilibrium and $\alpha > 2$ represents gravitationally unbound clouds. We use the first relation in Equation 2.4 since the kinetic and gravitational potential energies are easily measurable in our simulations.

We have chosen to examine initial virial parameters, defined as α_0 henceforth, ranging from 0.5 to 5, which covers both bound, virialized, and unbound clouds. This range of virial parameters is within the range of observed GMC's (Solomon et al., 1987; Rosolowsky, 2007; Hernandez & Tan, 2015). The corresponding Mach Numbers can be found in Figure 2.1.

The models are evolved to $\sim$5 Myr, at which point supernovae are expected to inject large amounts of energy into the surrounding gas (Leitherer et al., 1999). Since the physics of Supernovae are not handled in the present code, we do not evolve the models past this point.

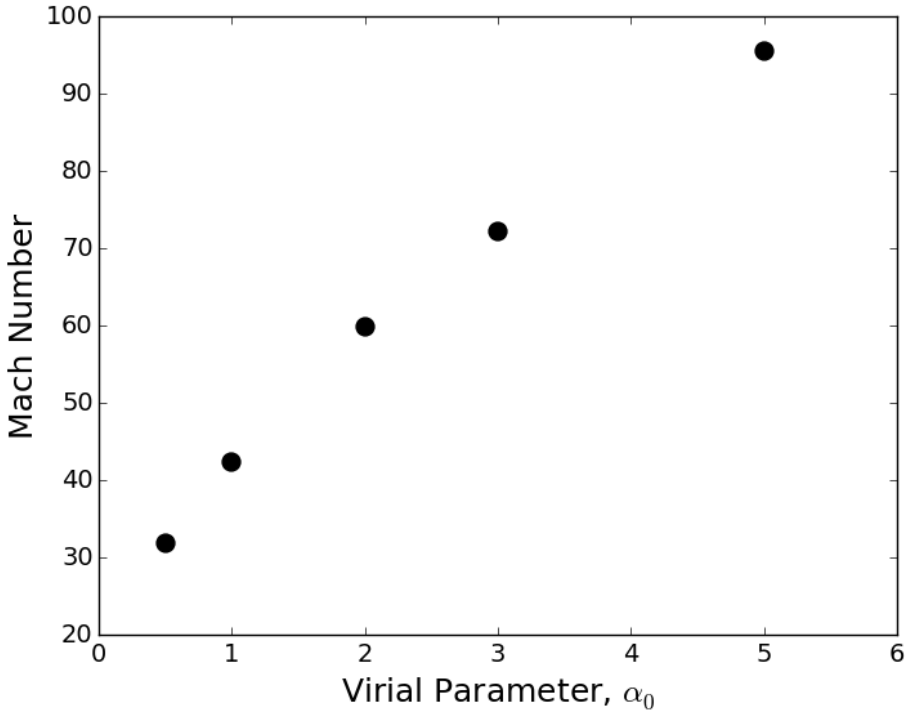

Figure 2.1: The Mach numbers corresponding to the initial virial parameters.

2.4 Results

2.4.1 Global Evolution and Gas Properties

A three-dimensional view showing the evolution of the virialized simulation (α_0 = 1) at three different times can be seen in Figure 2.2. Three different density contours are plotted with densities ranging from 1.0×10^{-23} to 3.0×10^{-20} g·cm^{-3}. These specific densities were chosen to highlight the sparse, low density gas, the

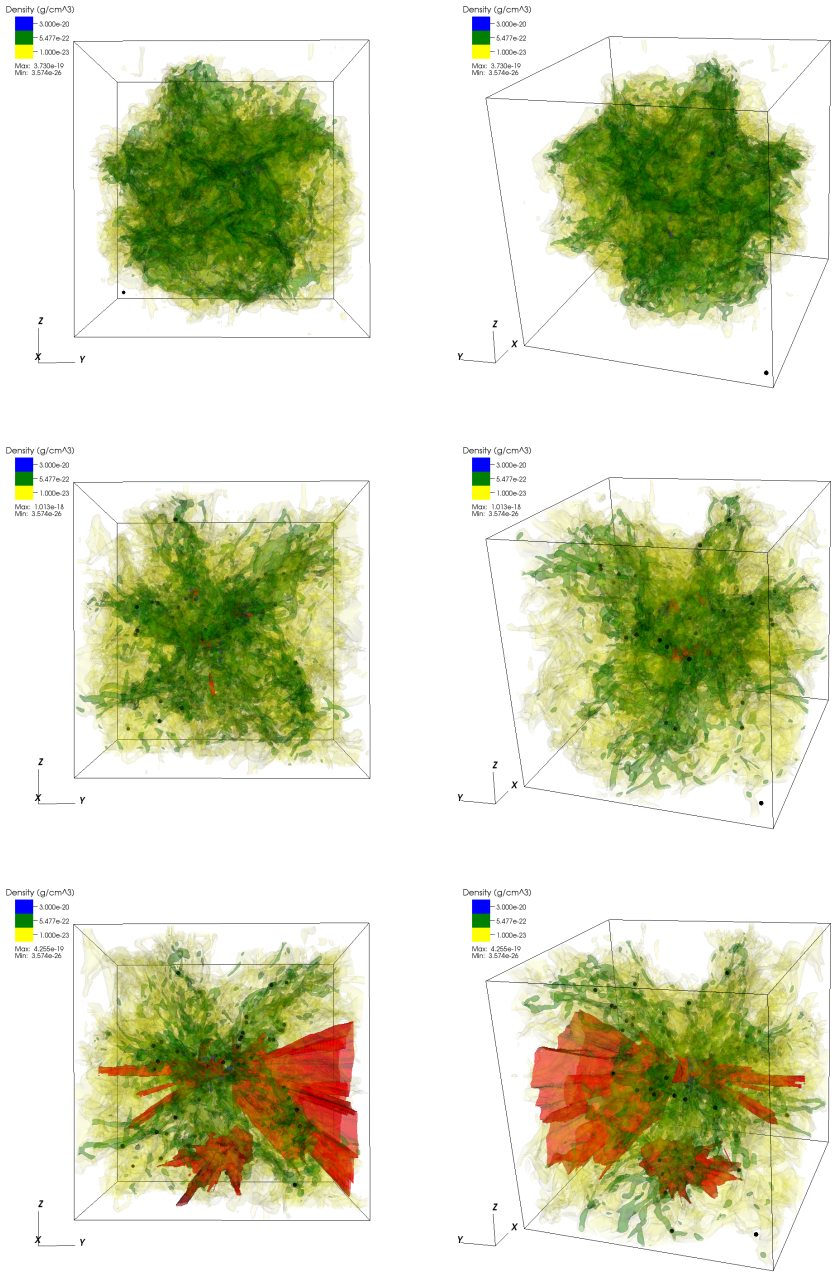

Figure 2.2: A three-dimensional view of the $\alpha_0 = 1$ simulation. The density contours are shown in yellow, green, and blue and the ionized regions are shown in red. The black circles represent cluster particles. Rows show two different views at the same time and columns show the state of the simulation at 0.97, 2.68, and 3.65 Myr from top to bottom.

intermediate density filaments, and the dense cores which form primarily in the center of the simulation. The bounding box has a side length of 80.2 pc and the location of the cluster particles are overplotted with black circles. The red regions in Figure 2.2 represent gas which has an ionization fraction greater than 95%, highlighting the HII regions produced by the cluster particles.

The first panel in Figure 2.2 shows that the gas quickly breaks up into filaments. A total of 17 cluster particles have formed by this time but have not produced enough stars to produce HII regions. The second panel, plotted at 2.68 Myr, still shows a filamentary network of gas but one which is more centrally condensed compared to the previous panel due to the global collapse of the gas. Dense cores are also now visible, scattered throughout the central region of the box where filaments intersect. A total of 84 particles are present at this time, some of which have produced enough stars to begin feeding back on their environment to produce small, localized HII regions. The total number of cluster particles remains roughly the same with a total of 88 particles at 3.65 Myr, shown in the bottom panel of Figure 2.2, but the stellar content in these clusters has grown significantly, allowing larger HII regions to form which cover a large fraction of the box. One region in particular has expanded outward from the central region into low density gas and extends to the edge of the simulation volume.

To give a complementary view to Figure 2.2, we show density slices through the center of the z-axis and column density projections in Figure 2.3, for $\alpha_0 = 1$, and Figure 2.4, for $\alpha_0 = 3$. The corresponding temperature slices are in Figure 2.5. We show an example of a bound and unbound ($\alpha_0 = 3$) simulation illustrate the effects

that initial boundedness plays on the evolution of the cloud. The locations of the cluster particles are projected onto the viewing plane in all images.

Like the three-dimensional images discussed above, both clouds quickly break up into filaments by ∼0.5 Myr. Since the unbound cloud has a higher Mach number, the filaments are more pronounced with more low density gas filling the voids between the filaments. The temperature profiles look similar at this point, with cold 10 K gas in the center surrounded by warmer ∼300 K gas. There are visible shocks, however, in only the unbound simulation, along the periphery of the cloud. Comparing the two simulations at the earliest times also shows that only the unbound cloud has formed cluster particles. This can again be attributed to its higher Mach number, leading to stronger density enhancements which fragment into particles.

The middle panels of Figure 2.3, 2.4, and 2.5, plotted at ∼2.5 Myr, show that both simulations have produced many clusters, totalling 81 and 107 for the bound and unbound simulation, respectively. The clusters are grouped more heavily towards the centre of the volume for the bound run, indicative of collapsing gas resulting in higher central densities and a more centrally condensed grouping of clusters. An HII region is also visible in the middle panel of Figure 2.5. The corresponding density slice shows that the HII region has disrupted the filaments, effectively smearing them out to a more uniform medium with density enhancements around the edges.

The final panel, shown at ∼4 Myr, shows more marked differences between the initially bound and unbound clouds. The bound cloud is now even more centrally condensed due to global collapse, with one dense central core from which filaments

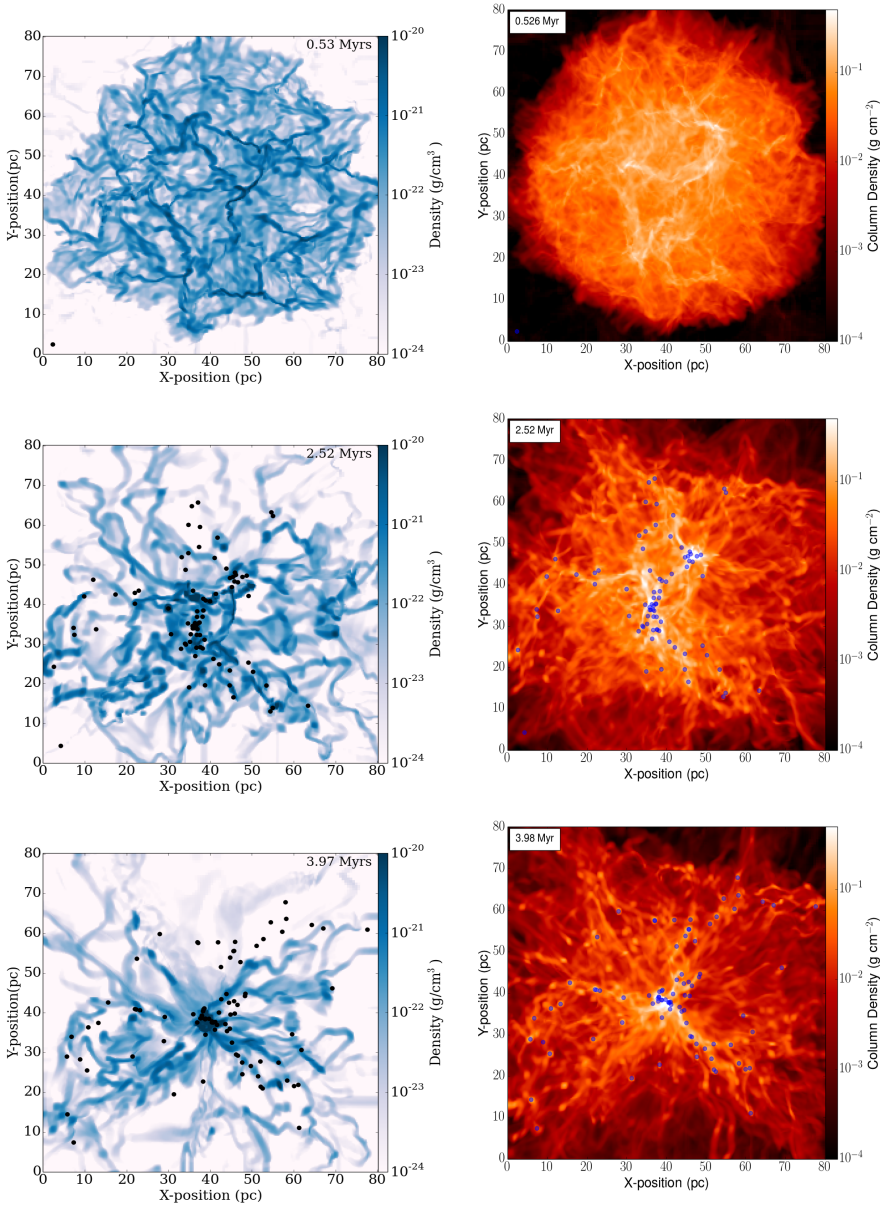

Figure 2.3: Density slices through the centre of the z-axis (left) and column density projections (right) for the simulation with $\alpha_0 = 1$. Cluster locations are projected onto the viewing plane and are plotted as black circles for the slice plots and blue circles for the column density plots.

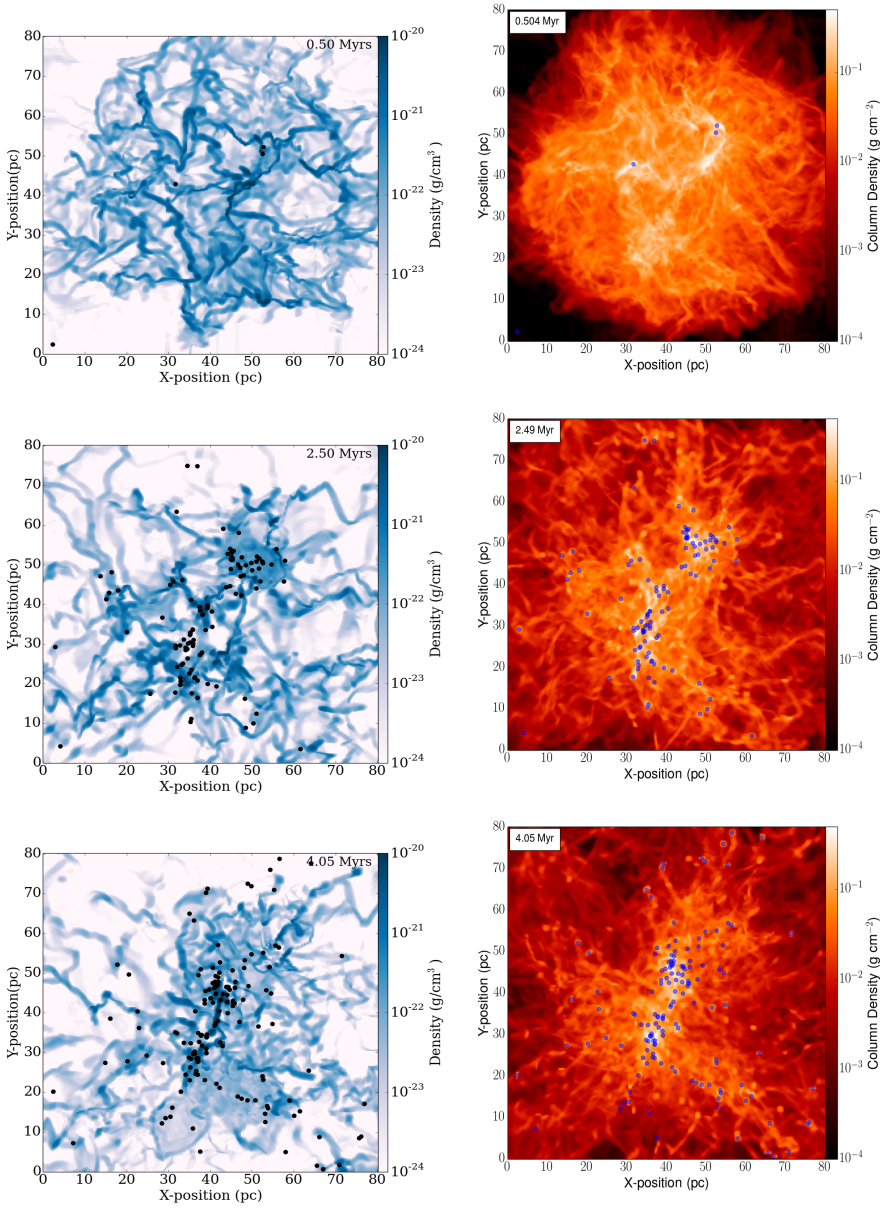

Figure 2.4: Density slices through the centre of the z-axis (left) and column density projections (right) for the simulation with $\alpha_0 = 3$. Cluster locations are projected onto the viewing plane and are plotted as black circles for the slice plots and blue circles for the column density plots.

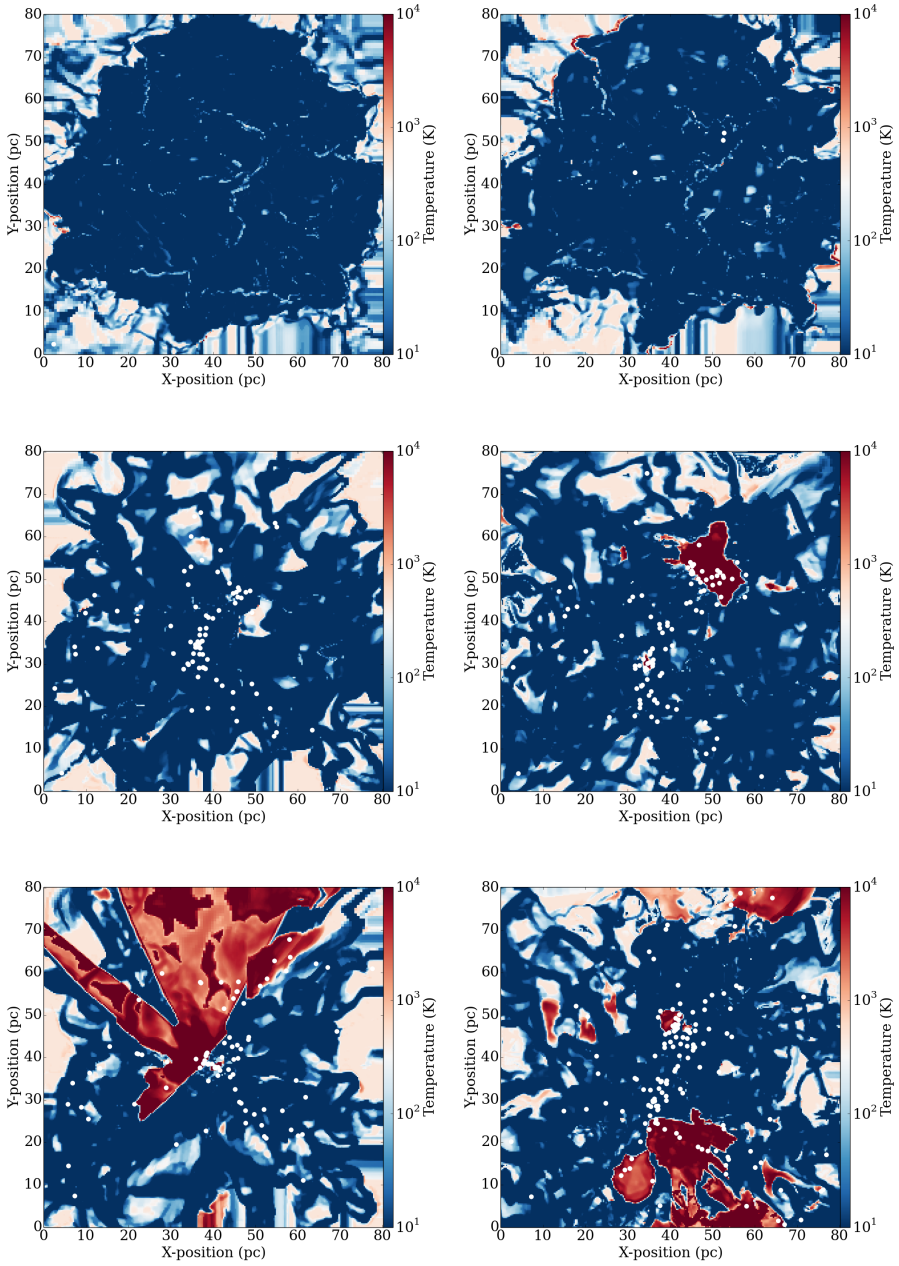

Figure 2.5: The corresponding temperature slices to Figure 2.3 (left) and Figure 2.4 (right). Cluster particles are now shown in white for ease of viewing.

radiate outwards. A large grouping of clusters remains in the center, allowing further accretion. The outskirts are devoid of dense gas, which has allowed a large HII region to extend northwards, away from the central condensation, where there is less gas to shield these regions from the ionizing photons produced by massive stars in the central grouping. The unbound simulation, on the other hand, has dense gas pervading a large fraction of the box and lacks a dense, central core. The number of clusters has grown slightly for a total of 87 and 140 for the bound and unbound run, respectively. This suggests that the majority of cluster formation occurs during the early evolution of the clouds.

The above visualizations provide a qualitative description of the evolution of a small subset of the completed simulations. A quantitative comparison showing both the gas and cluster particle evolution for all simulated clouds, with radiative feedback included, can be seen in Figure 2.6. The total mass in cluster particles is shown by the dashed lines, the total gas mass present in the simulation volume is shown by the dotted lines, and their sum is the shown by the solid lines. Since outflow boundary conditions are present, the solid lines do not remain constant at 10^6 $M_\odot$ because gas can leave the simulation volume. The total amount of mass lost from the simulation depends heavily on α_0. From Figure 2.6, it can be seen that the initially bound runs lose a negligible amount of mass. The unbound runs, on the other hand, lose a significant amount. For example, the case with an initial virial parameter of 5 loses $\sim$30% of the total mass by the end of the simulation.

Clearly α_0 plays an important role in the long term evolution of the cloud. However, the virial parameter does not remain constant over the course of the simulation

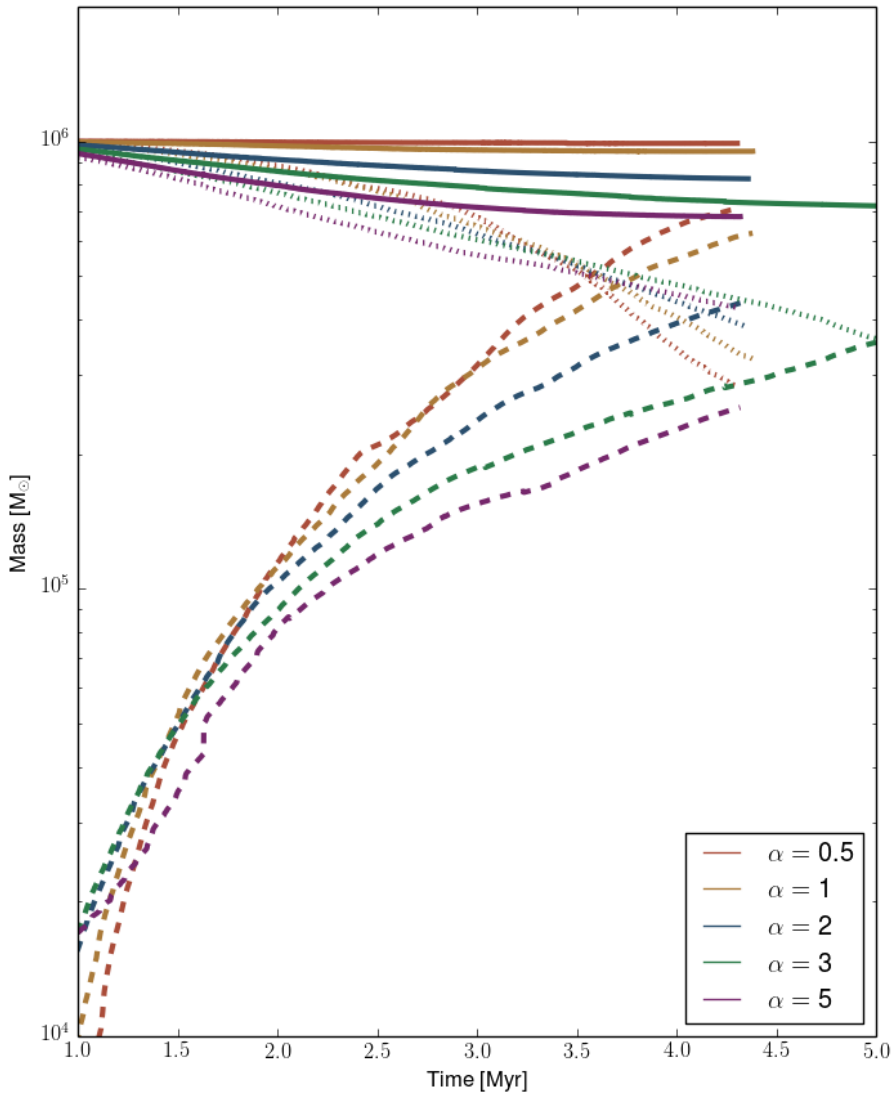

Figure 2.6: Mass components in 5 simulations with different α_0's. The dashed lines show the total mass in cluster particles. The dotted lines show the total gas mass in the simulation volume. The total mass in the simulation is the sum of gas and particles and is shown by the solid lines. Note that mass is lost from the simulations, particularly in the unbound cases, because outflow conditions are present.

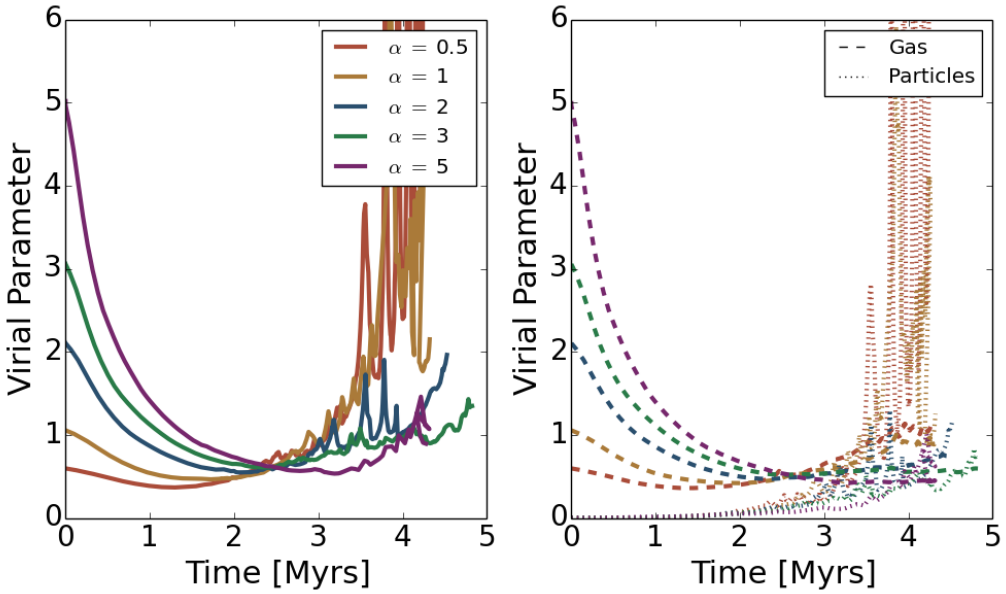

Figure 2.7: Left: Evolution of the virial parameter over time including both gas and particles. Right: Individual contributions to α from the gas (dashed) and the cluster particles (dotted). See text for more detail on how the virial parameter was split.

because the initial supersonic turbulence is damped via shocks. As the turbulence is damped, the velocity dispersion of the gas decreases which results in a decreasing α. The loss of high velocity gas from the simulation volume and the formation of cluster particles further modifies α.

In Figure 2.7, we plot the global virial parameter as a function of time on the left, and the contributions to α by the gas and cluster particles on the right. The global virial parameter, and the contributions from particles and gas, are expressed via,

$$\alpha = 2\frac{E_{kin}}{|E_{grav}|} = 2\frac{E_{kin,p}}{|E_{grav}|} + 2\frac{E_{kin,g}}{|E_{grav}|} = \alpha_p + \alpha_g \tag{2.5}$$

where E_{kin} is the kinetic energy, E_{grav} is the gravitational potential energy, and the subscripts g and p refer to gas and particles.

We see from Figure 2.7 that α initially decreases as the turbulence damps. The rate at which α decreases is greater for unbound simulations. All simulations tend towards a virial state (ie. $\alpha = 1$), and cross at approximately 2.3 Myr. The tendency towards a virial state is likely due to gravitational collapse after the decay of the initial turbulence which, in turn, drives enough internal turbulence to maintain α at 1 (Ballesteros-Paredes et al., 2011; Heitsch, 2013). Because the virial parameters intersect at similar times, the simulations with higher α_0 decrease more rapidly compared to lower α_0 simulations. This is attributed to the turbulent decay time, τ_{dec}, which is given by $\tau_{dec} \sim L/(Mc_s)$ (Tilley & Pudritz, 2004), where L is the box size, M is the turbulent Mach number, and c_s is the sound speed. Measuring the turbulent decay times from Figure 2.7 shows a relation that is roughly inversely proportional to the initial Mach number, as suggested by τ_{dec}. The relation is not exact, however, due to varying degrees of mass loss from bound and unbound models.

The right hand panel shows that this early phase, characterized by a decreasing α, is dominated almost exclusively by the gas energetics. A significant number of cluster particles have formed by this time (eg. $\sim$10% of all mass is in the form of cluster particles by 2.3 Myr for the simulation with $\alpha_0 = 0.5$), but they contribute negligibly to the overall α. After approximately 3 Myr, however, particle dynamics

begin to play a significant role in the energetics, leading to a rise in α. The cluster particle contribution even outweighs the gaseous contribution for the initially bound runs.

The role of the particle contributions to the global energetics points towards interesting dynamical differences between the simulations. We find that, in the bound simulations, the cluster particles are more centrally condensed relative to unbound simulations. This tighter grouping leads to stronger two-body interactions which result in velocities in excess of 50 km/s. These large particle velocities are responsible for the dominant contribution to α. For comparison, the velocities in unbound simulations do not exceed 20 km/s. We leave the discussion of particle dynamics, and its connection to α_0, to a later paper.

2.4.2 Formation Efficiencies and Particle Evolution

The discussion so far has been focused on global properties, such as the total mass in cluster particles, rather than the properties of individual objects. We move now to a discussion of the cluster particles themselves. The top panel of Figure 2.8 shows the time evolution of the two most massive cluster particles that survive to the end of the simulation for all clouds. Since the particles are not allowed to lose mass, these curves are monotonically increasing as a function of time. All curves also show a series of discrete jumps in mass. These jumps are due to merging events, as described in Section 2.3. It can be concluded from these curves that *merging plays a significant role in determining the mass of the most massive particles in*

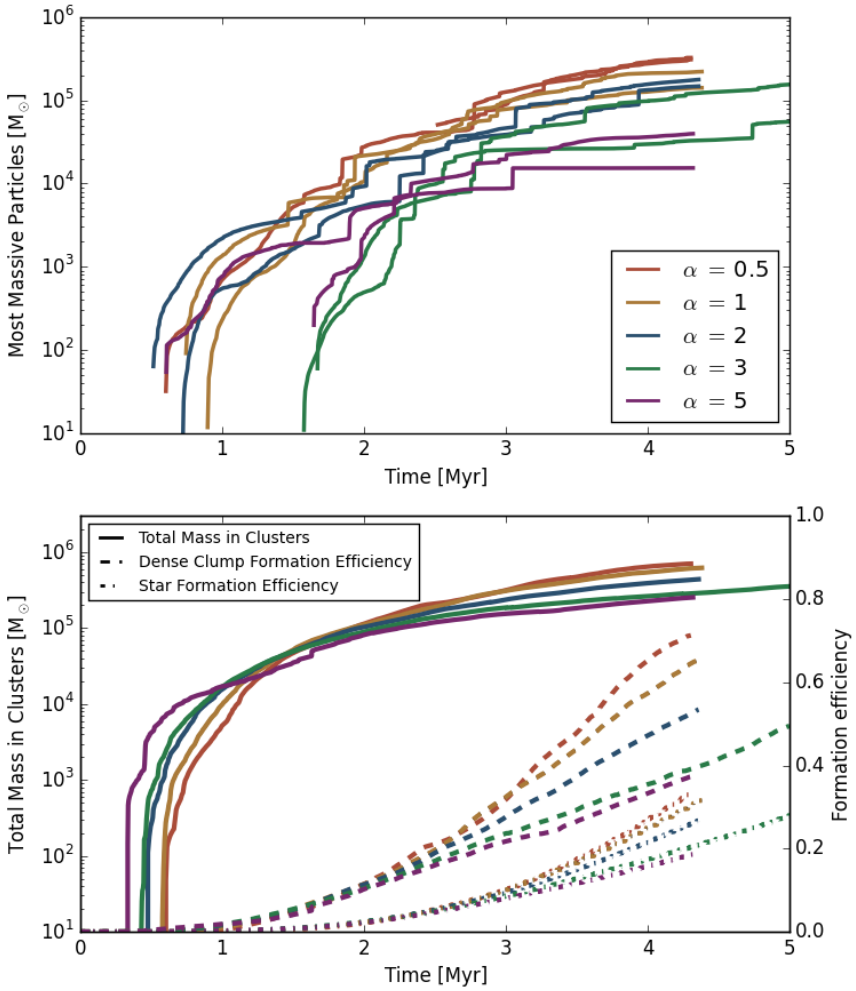

Figure 2.8: Top: The evolution of the total mass for the two most massive cluster particles that survive until the end of the simulation. Discrete jumps in total mass are due to cluster particle merging. Bottom: Solid lines represent the total mass contained in cluster particles and corresponds to the left axis. Dashed lines represent the dense clump formation efficiency, ϵ_{cl}. Dashed-dotted lines represents the star formation efficiency, ϵ_{sf}.

these simulations. This behaviour has also been observed in cluster-scale simulations (Maschberger et al., 2010).

An interesting trend is noted in the top panel of Figure 2.8, namely that the simulations with a lower α_0 tend to produce more massive cluster particles. The maximum mass cluster particles, including the mass of gas and stars, range from 3.26×10^4 $M_\odot$ to 3.27×10^5 $M_\odot$ for simulations with an α_0 of 5 and 0.5, respectively. This trend can be attributed to the central concentration of dense gas that forms as a result of gravitational collapse in the bound simulations, allowing the most massive particles to continue accreting strongly from their surroundings. This suggests that the distribution of cluster particle masses depends on α_0, which is discussed further below.

The solid lines in the bottom panel of Figure 2.8 show the total mass of all cluster particles (shown on the left y-axis). There is a spread between simulations in both the total mass in cluster particles, and the time at which cluster formation begins. There is a spread of $\sim$260 kyr between when the most unbound cloud ($\alpha_0 = 5$) and the most bound cloud ($\alpha_0 = 0.5$) begin to form particles.

While the unbound simulations form the first cluster particles, the bound simulations have more mass contained in particles overall. This can be seen by the dashed lines in the bottom panel of 2.8. We refer to these lines as the "dense clump formation efficiency", hereafter ϵ_{cl}, and are calculated by dividing the total mass in cluster particles over the initial mass of the cloud, ie.

$$\epsilon_{cl} = \frac{\sum_i M_i}{M_{total}} = \frac{\sum_i M_i}{10^6 M_\odot} \tag{2.6}$$

where M_i is the mass of the ith particle and the total cloud mass of 10^6 $M_\odot$ has been shown for clarity. We have chosen the nomenclature of "dense clump formation efficiency", rather than a cluster formation efficiency, because the mass contained in these particles is not solely in stars, but also a reservoir of unused gas which may be used for future star formation.

Since ϵ_{cl} closely follows the total mass contained in particles, we see a similar spread between simulations. The early evolution is similar, until about 2 Myr, when the dense clump formation efficiencies begin to diverge. The final efficiencies cover a range of 37%, for an α_0 of 5, to 71%, for an α_0 of 0.5 with the unbound runs ending up less efficient than the bound runs. This is consistent with earlier simulations which demonstrated that particle formation efficiencies, over a fixed time, are significantly reduced as the Mach number is increased (Klessen et al., 2000).

Our ϵ_{cl} values can be compared to the observationally measured "dense gas mass fractions" (DGMFs) in nearby molecular clouds. Recent work by Abreu-Vicente et al. (2015) has measured the fraction of dense gas, defined to be gas above an extinction of $A_V > 7$ corresponding to gas at densities of $n > 10^4$ cm^{-3}, in local molecular clouds with masses ranging from 200 to $2{\times}10^5$ $M_\odot$. We note that our simulations have greater masses than the clouds presented in Abreu-Vicente et al. (2015), but the observations still provide a useful point of comparison. The observed clouds span a range of evolutionary stages from starless clouds to star forming clouds

with well developed HII regions. They find that the DGMF covers a large range, with a maximum value of ∼0.8. The average DGMF over the entire mass range is found to be 0.39 with a cloud-to-cloud scatter of 0.28, and the higher mass clouds have DGMFs close to the maximum value. We see that our own DGMFs, as measured by the total mass in cluster particles, fall within the observed range. The simulation having the closest DGMF to the observational average is the unbound simulation α_0 = 3. This suggests that initially unbound molecular clouds more closely reproduce the properties of locally observed clouds.

This point can be elaborated further by examining the dash-dotted lines in Figure 2.8. These lines represent the star formation efficiency of the clouds (ϵ_{sf}), defined as the total mass in stars within cluster particles divided by the initial cloud mass. These curves show similar trends to ϵ_{cl} in the sense that higher initial virial parameters correspond to lower efficiencies. The curves take longer to diverge, however, as a consequence of our subgrid model which converts the cluster mass to stars gradually over time. The final ϵ_{sf} ranges from 18% to 34%. These values are higher than the global ϵ_{sf} in observed molecular clouds which typically span a range of 1-5% (eg. Duerr et al. (1982)). Since the highest virial parameter produces the lowest efficiency which is close to the observed values, this again suggests that a high initial virial parameter, in combination with radiative feedback, is required to match observations. There are, however, other forms of feedback that this work neglects which could also play a role in reproducing observed ϵ_{sf} values.

When discussing cluster particles properties up to this point, we have focused solely on mass. To fully understand the resulting mass distributions, however, the

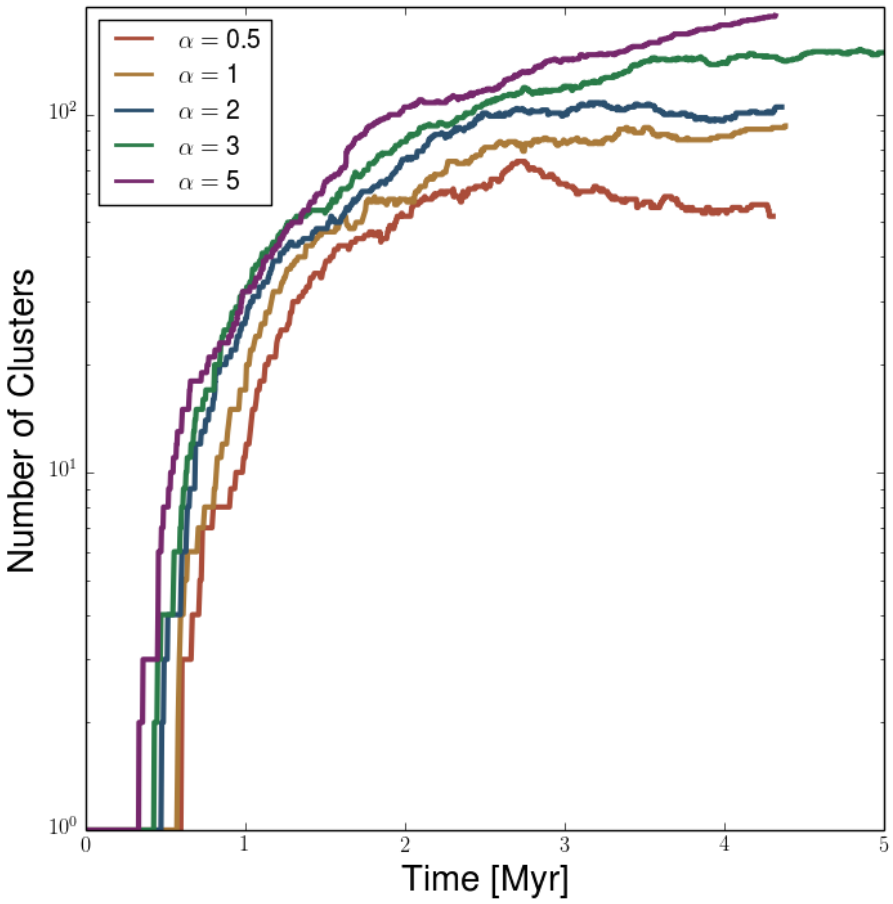

Figure 2.9: The total number of cluster particles as a function of time. The total number can increase via forming new particles, and decrease via mergers or particles leaving the simulation volume.

total number of cluster sink particles needs to be discussed. In Figure 2.9, we show the total number of cluster particles as a function of time. The number of particles can either increase via formation, or decrease via mergers or particles leaving the simulation volume. It can be seen that a large burst of cluster formation occurs early but levels out to roughly constant values around 2 Myr. The final number of clusters ranges from 52 for $\alpha_0 = 0.5$ to 189 for $\alpha_0 = 5$. As noted earlier, we see that initially unbound simulations begin to form cluster particles earlier. These curves do not cross, however, which is in contrast to the mass curves discussed in Figure 2.8. This means that while the bound simulations contain the most mass in cluster particles, they have the lowest number of particles overall. The bound simulations are therefore expected to have more massive particles, on average, than unbound simulations. This has will be discussed further in the following section.

2.4.3 Radiative Feedback Effects

The above discussion has been focused on the role that α_0 plays in shaping cloud properties and the resulting efficiencies. We now move on to discuss the impact of radiative feedback on these properties. To do this, we have completed an additional five simulations which are identical to those presented above but with radiative feedback not included. We refer to the simulations with radiative feedback included as "RHD" (Radiation Hydrodynamics) and the simulations with radiative feedback turned off as "HD" (Hydrodynamics).

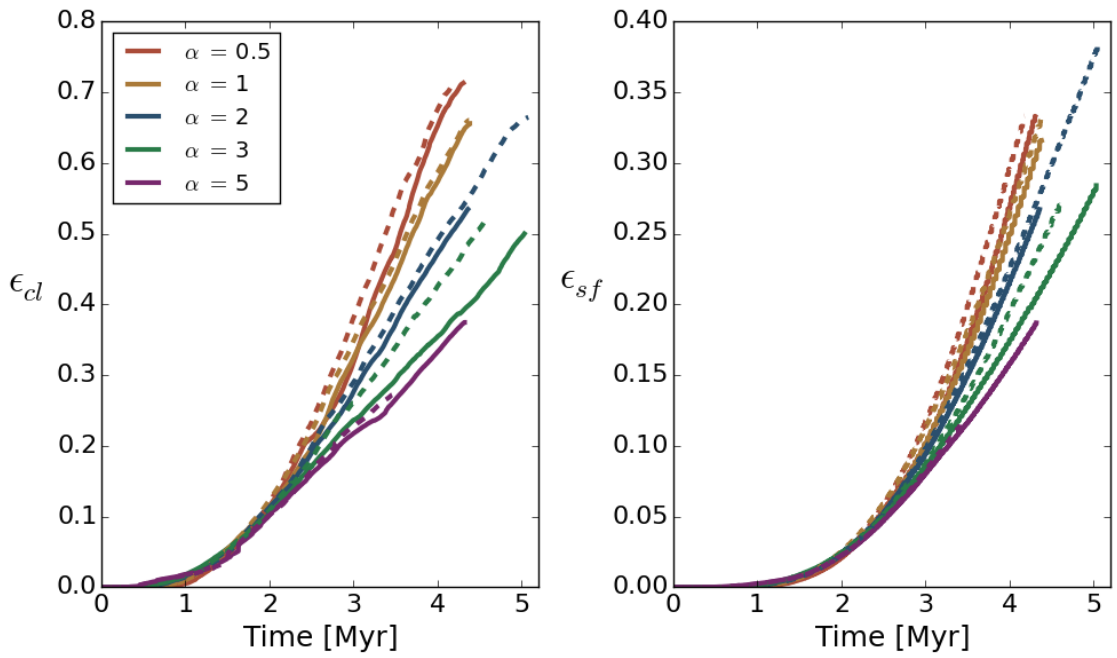

Figure 2.10: The dense clump formation efficiency (left) and the star formation efficiency (right) for simulations with radiative feedback included, shown by solid lines, or not included, shown by the dashed lines.

The main effect of radiative feedback is the suppression of star, or cluster, formation via the heating and ionization of the gas surrounding the newly formed stars. The strength of this suppression, however, is not fully understood and depends on the environment being modelled. For example, Dale et al. (2005) found that ionization feedback had a negligible effect on global SFEs in initially gravitationally bound clouds. In contrast, later work by Dale et al. (2012a) showed that ionization feedback can reduce the SFE by up to 50% in smaller, 10^4 $M_\odot$ clouds. Since it is clear that the GMC environment is a crucial component in determining the role of radiative feedback, we examine whether this role differs in 10^6 $M_\odot$ GMCs with various α_0. We

have also included a rudimentary treatment of radiation pressure in our radiative transfer scheme which was not included in these previous works.

We compare the dense clump formation efficiencies, ϵ_{cl}, and star formation efficiencies, ϵ_{sf}, between RHD and HD simulations in Figure 2.10. Solid lines represent the RHD simulations and dashed lines represent the HD simulations. We see that the inclusion of radiative feedback plays a small role in determining ϵ_{cl} and ϵ_{sf} in the early evolution of a GMC, regardless of initial boundedness. The largest difference in ϵ_{cl} occurs in the simulation with an α_0 of 3, with a difference of $\sim$10% between the RHD and HD simulation. The other simulations show that radiative feedback does suppress ϵ_{cl} but only by $<$3%. Since ϵ_{sf} closely mirrors the evolution of ϵ_{cl} but with a time delay, the difference in SFEs between RHD and HD simulations is less noticeable.

Overall, these results suggest that radiative feedback plays a minimal role in the early evolution of a massive GMC. Comparing these results to those presented in Figure 2.8, it is clear that α_0 is the major contributing factor to the final efficiencies. Visual examination of Figure 2.5, however, shows that radiative feedback is producing large scale HII regions which are evidently not strongly suppressing the global efficiencies in the cloud. The filamentary and porous nature of the cloud is likely limiting the role of radiative feedback.

It is possible that if we followed the evolution of the cloud over longer timescales, we would see a larger suppression in efficiencies due to the lower overall density of the cloud which can be more easily disrupted by radiative feedback. Since we did

not follow the cloud evolution to >5 Myr, at which point Supernovae are expected to begin injecting significant amounts of energy and momentum into the surrounding gas (Leitherer et al., 1999), we can only conclude that radiative feedback does not greatly suppress cluster and star formation in the early evolution of a GMC.

To show in which ways radiative feedback is suppressing the formation of particles, we focus on the simulation which had the largest difference between the RHD and HD simulations, namely the simulation with an α_0 of 3. The observed difference in efficiency could either be due to radiation unbinding gas which then leaves the simulation volume, or through the heating and ionization of gas locally which prevents future particle formation and limits the accretion rate onto existing particles. To see which of these scenarios is more likely, we examine how the mass is divided among gas and particles in Figure 2.11.

Figure 2.11 shows that the RHD simulation has comparably less mass contained in particles and more gas mass than the HD simulation. However, the sums of these components, shown by the solid lines, are nearly identical, indicating that the RHD and HD runs have lost the same amount of mass from the simulation volume. From this we can conclude that radiative feedback is not driving outflows from the GMC, but is instead suppressing the formation and accretion of cluster particles. We note that this may be a product of our large cloud masses (10^6 $M_\odot$) which have correspondingly deep potential wells which can trap the gas even under the influence of radiative feedback. Outflows may be more relevant in the early evolution of less massive GMCs where the energy and momentum input from stars may be sufficient to unbind the cloud.

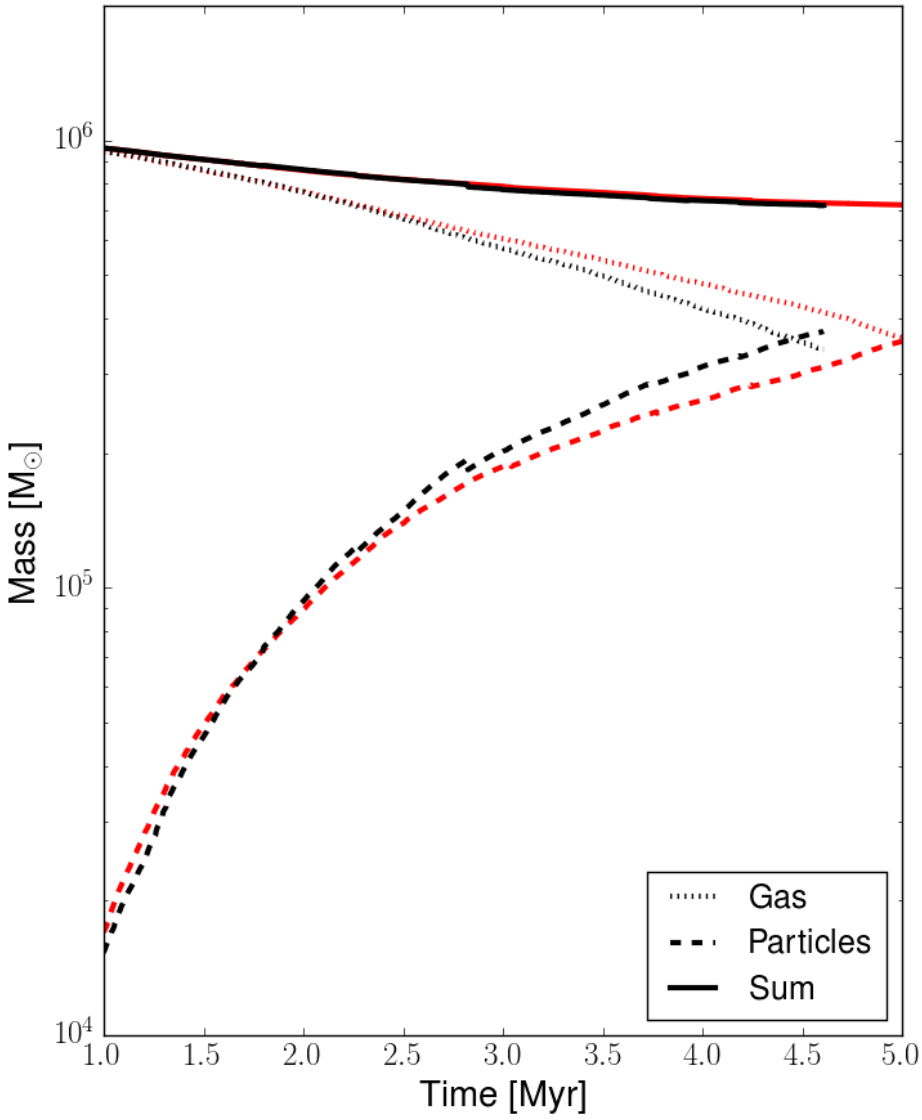

Figure 2.11: Mass components in the $\alpha_0 = 3$ simulations (similar to Figure 2.6). Red lines represent the RHD simulations including radiative feedback, while the black lines represent the HD simulations not including radiative feedback.

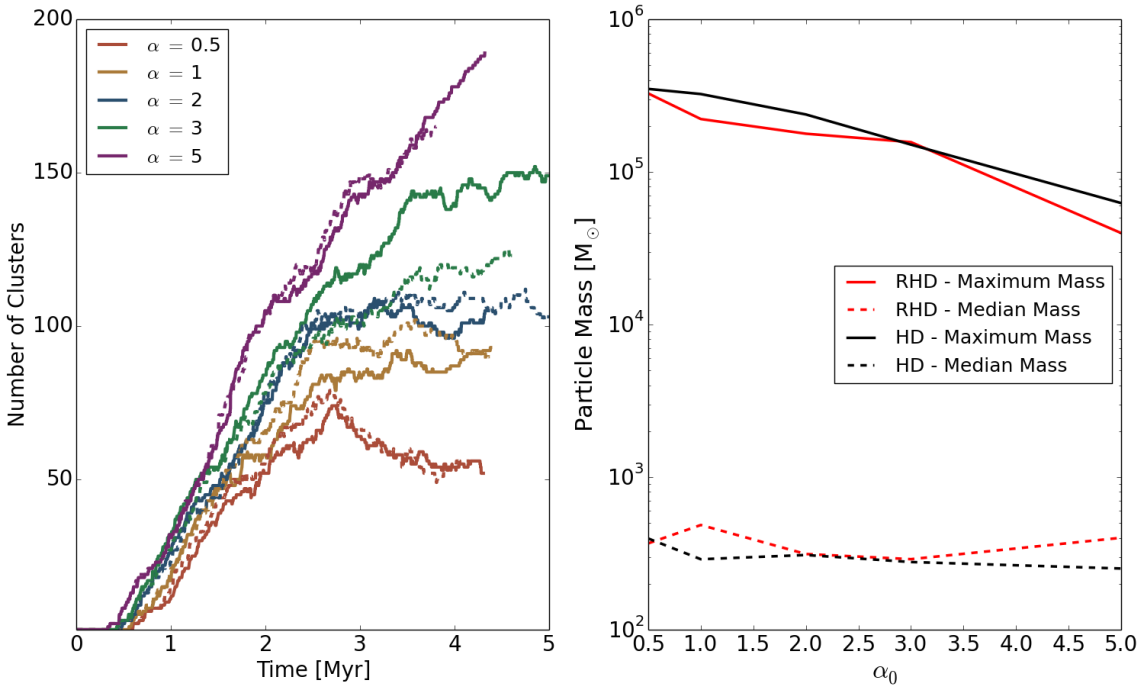

Figure 2.12: Left: The number of cluster particles as a function of time for RHD simulations, shown by the solid lines, and HD simulations, shown by the dashed lines. Right: The maximum and median mass cluster particles for simulations with different α_0 values.

While global efficiencies are not greatly influenced by the inclusion of radiative feedback, it is possible that the cluster properties formed in an RHD versus an HD simulation may differ. In Figure 2.12, we plot cluster properties for HD and RHD simulations to examine differences that arise. On the left, we show the total number of particles in all simulations. On the right, we plot the maximum and median mass cluster particles as a function of α_0.

The left hand panel of Figure 2.12 shows no clear trend in the number of cluster particles in RHD versus HD simulations. The simulations with an α_0 of 0.5 and 5 show no difference between the number of particles with radiative feedback included. The simulations with an α_0 of 1 and 2 show an excess of clusters in the HD simulations at intermediate times but the difference becomes negligible at late times. Only the simulations with an α_0 of 3 have different numbers of clusters at late times, with the RHD simulation forming $\sim$30 more cluster particles than the HD simulation.

The right hand panel of Figure 2.12 shows the maximum and median mass cluster particles versus α_0 in both HD (black) and RHD (red) simulations. The maximum mass curves (solid lines) indicate that, except for the $\alpha_0 = 3$, HD simulations tend to produce more massive cluster particles than their RHD counterparts. This effect has been observed in other simulations of radiative feedback in which the distribution of particle masses is shifted to lower values (Dale et al., 2012a). The median mass clusters show the opposite trend, with the RHD median masses being greater than the HD median masses. This indicates that the mass distribution is not simply being shifted to lower masses since the same trend would be seen in the median mass clusters as in the maximum mass clusters. It should be noted that since our subgrid model only includes radiative feedback from massive clusters ($M_* > 1000$ $M_\odot$), the median mass clusters in the RHD simulations are not outputting radiation which may account for the observed trend reversal.

2.4.4 Cluster Formation Thresholds

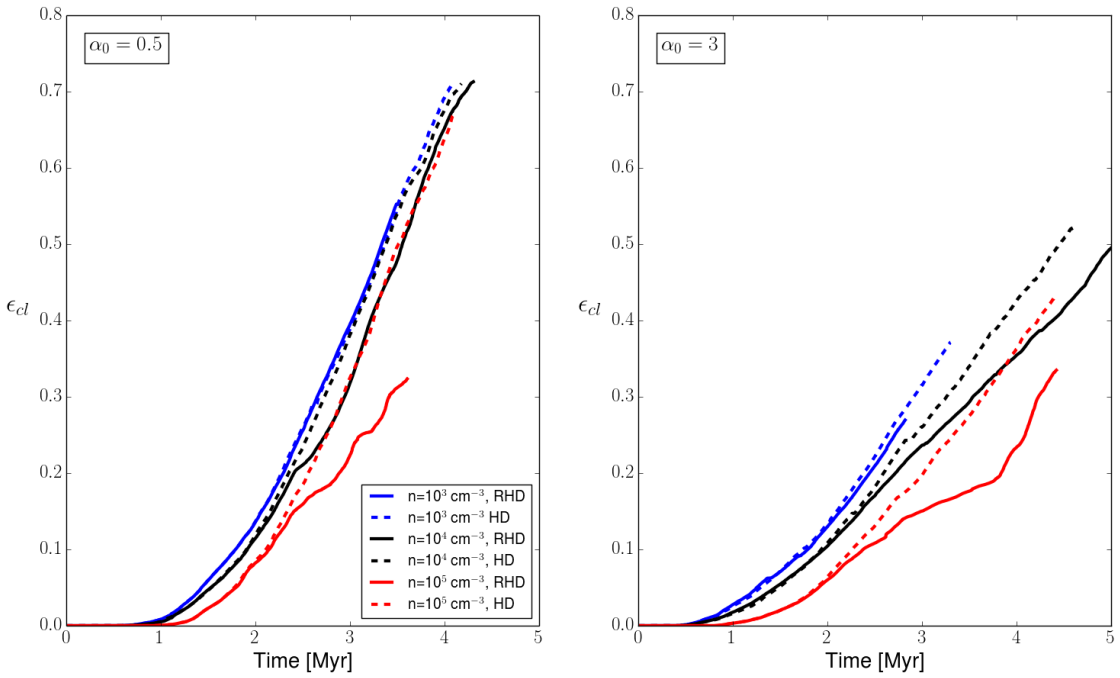

Figure 2.13: The effects of radiative feedback on ϵ_{cl} from varying the particle formation threshold in a bound ($\alpha_0 = 0.5$, left) and an unbound simulation ($\alpha_0 = 3$, right). As described in Section 2.3, the fiducial value we have used throughout is 10^4 cm^{-3}.

As discussed above, recent studies suggest that the strength of radiative feedback in different GMC environments may vary. We have shown that this is not the case for 10^6 M$_\odot$ clouds which have different initial virial parameters. Another parameter, however, which also affects a cluster particle's local environment is the threshold density for formation. We have chosen a fiducial value of 10^4 cm^{-3} (see Section 2.3) motivated by observations of cluster forming regions. If, for example, a higher threshold density were chosen, the global GMC environment would be denser at

the time of cluster formation and the radiation released by these clusters would be propagating into denser gas. This may have an important impact on the strength of radiative feedback. To examine the role that radiative feedback plays in clouds with different formation thresholds, we have resimulated a bound ($\alpha_0 = 0.5$) and an unbound ($\alpha_0 = 3$) cloud with formation thresholds of 10^3 and 10^5 cm^{-3}. The results of these simulations are presented in Figure 2.13.

The onset of cluster formation differs among simulations with different formation thresholds. As expected, simulations with higher thresholds begin to form clusters later since the cloud has to collapse to higher densities before particles form. Comparing HD simulations, shown by dashed lines, and RHD simulations, shown by solid lines, we see that lower formation thresholds mirror the results presented in Figure 2.10 in the sense that radiative feedback plays a minor role in controlling ϵ_{cl}. In fact, the differences in efficiency between RHD and HD simulations are reduced even further in the case of a low formation threshold.

For the case of a high formation threshold, we see that the strength of radiative feedback is enhanced. The final efficiencies between RHD and HD simulation differ by 21% and 10% compared to 2% and 8% at the same time for the fiducial formation threshold of 10^4 cm^{-3}. These comparisons were at the time corresponding to the end of the shortest running simulation. The higher density immediately surrounding particles efficiently couples the radiation to the gas rather than the radiation streaming to low density voids perpendicular to filaments. The impact of radiative feedback on filaments is significantly more pronounced. This clearly indicates that the strength of radiative feedback is not a constant, but instead varies depending on the GMC

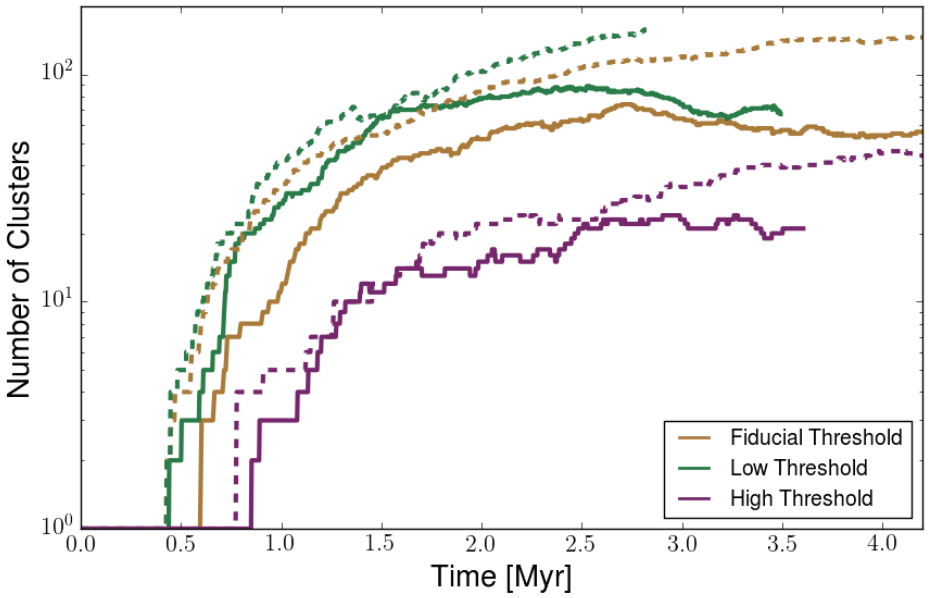

Figure 2.14: The number of cluster particles versus time for different formation thresholds. Simulations with an α_0 of 0.5 and 3 are shown by the solid and dashed lines, respectively.

environment. This may have important consequences for star formation in clumps and cores which are the densest regions in a molecular cloud. Indeed, observations of cores show that the densest cores ($n \sim 10^6$ cm^{-3}) have lifetimes of approximately a freefall time while less dense cores ($n \sim 10^{3-4}$ cm^{-3}) have lifetimes that are roughly ten times as long (André et al., 2014). This may be due, in part, to the increased strength of radiative feedback in denser regions.

The most significant difference between simulations with different particle thresholds is the number of cluster particles that form, as shown in Figure 2.14. As the particle formation threshold increases, the number of particles decreases. For exam-

ple, changing the formation threshold from 10^3 to 10^5 cm^{-3} in the simulation with an α_0 of 3 reduces the number of particles from 167 to 26. This trend is expected since the regions which form particles need to reach higher densities in the case of a higher threshold, and these regions become increasingly rare as the threshold increases.

While the particle formation efficiency is reduced in the case of a high formation threshold, it is not reduced by the factor of $\sim$6 that is seen in the particle number (for $\alpha_0 = 3$). This is because the particles which form in the high threshold cases are, on average, more massive. Since a particle has a fixed size, and the regions out of which the particles form have higher densities for higher threshold cases, this result is expected.

The combination of fewer particles which are, on average, more massive for higher threshold cases could have a significant impact on the cluster particle mass distribution. This is discussed briefly in the next Section. In the remainder of this Section, however, we will continue to focus on simulations with the fiducial value of the formation threshold because it is observationally motivated, and a full exploration of the formation threshold parameter space is beyond the scope of this paper.

2.4.5 Cluster Properties

We now move to discuss cluster properties in more detail with a focus on mass distributions and stellar content.

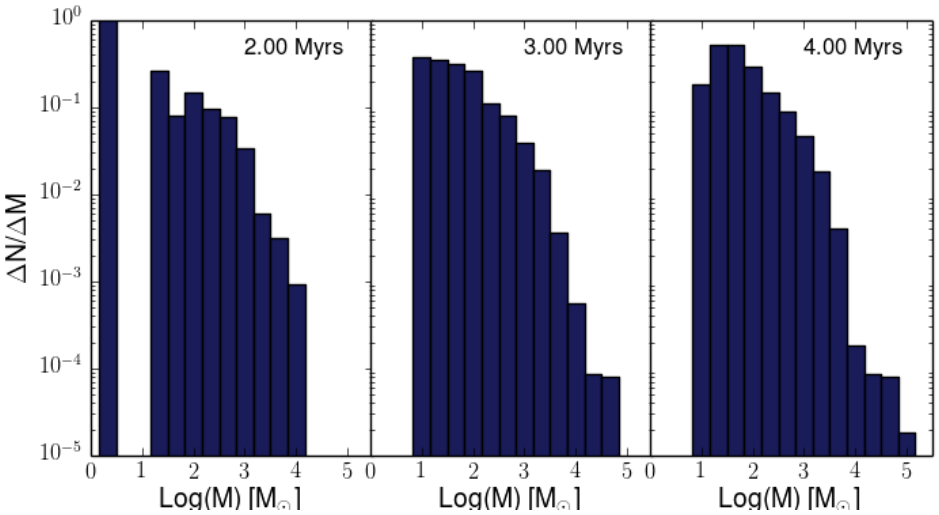

Figure 2.15: Representative snapshots of the cluster mass function at various times (2, 3, and 4 Myr from left to right, respectively) for the simulation with an initial virial parameter of 3.

In Figure 2.15, we show representative snapshots of the normalized cluster particle mass function at 2, 3, and 4 Myr for the simulation with $\alpha_0 = 3$. The other simulations show similar evolution, and a comparison between simulations is made below. The early evolution is dominated by low mass particles with the maximum particle mass reaching 10^4 $M_\odot$ by 2 Myr. While massive particles are present, the majority have masses on the order of Solar masses.

As time progresses, as shown in the middle panel of Figure 2.15, the distribution shifts to higher masses because of both ongoing gas accretion and particle mergers.

This same trend is evident in moving from 3 to 4 Myr. The highest mass particles have grown to approximately 10^5 $M_\odot$. The lowest bins have been depopulated, resulting in a turnover in the distribution just below 100 $M_\odot$.

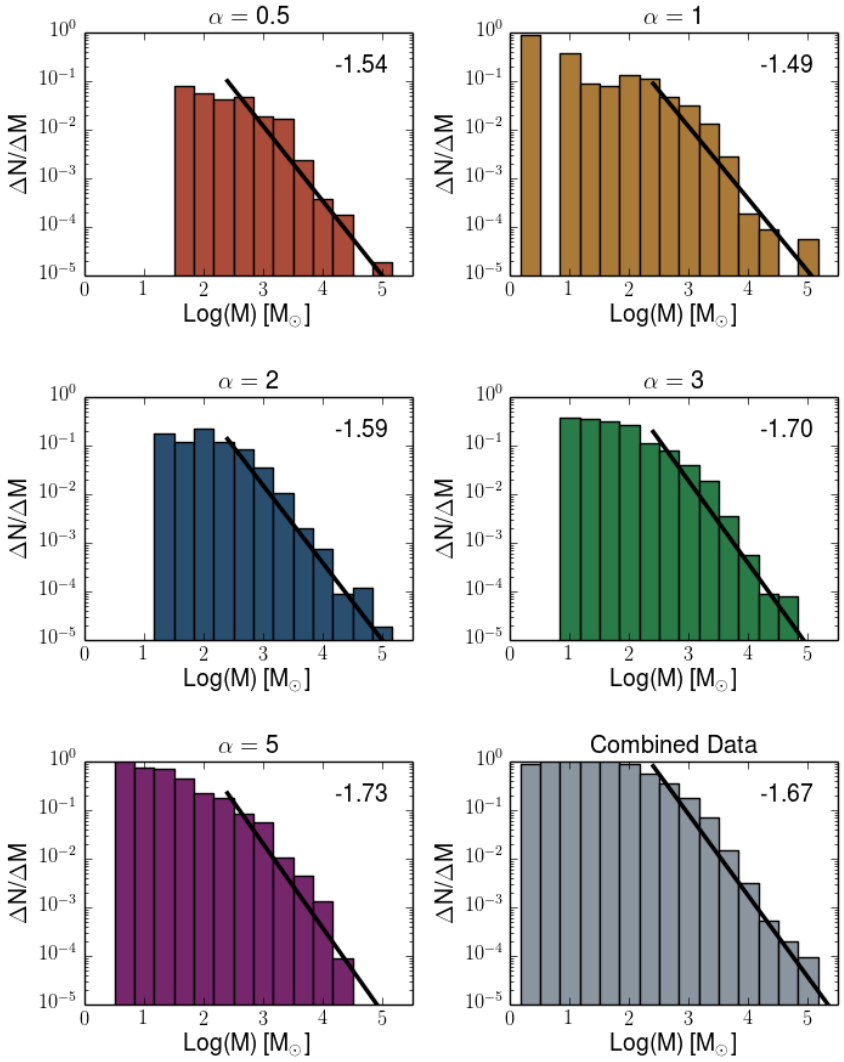

Figure 2.16: The final cluster particle mass distributions for all simulations. The initial virial parameter is shown an the top of each panel. The final panel shows the mass function for all of the data combined. The data is fit with a straight line for masses greater than log(M) > 2.4, following the work of Moore et al. (2015), and the resulting slope is shown in top right of each panel.

We compare the final total (ie. stellar content and gas reservoir) cluster particle mass distributions across simulations in Figure 2.16. In order to compare to the results presented in Moore et al. (2015), who measured the clump mass function in W43 using JCMT, we fit the distributions with a line for masses greater than $\log(M) > 2.4$ $M_{\odot}$. We discuss the observational results and the connection to our simulations in Section 2.5.

The resulting slopes are shown in the upper right hand side of each panel. The fits range from -1.49 to -1.73 for simulations with an α_0 of 1 and 5, respectively. The slope for all combined data, shown in the lower right panel, is -1.67. There is a slight trend towards steeper slopes as α_0 increases. Since the lower α_0 clouds have the most massive particles, more mass in cluster particles as a whole, and a smaller number of particles, this trend is easily understood. In other words, the mass distributions shift to higher masses as α_0 decreases, which manifests as a steepening slope when fitting over a fixed range.

The mass of individual cluster particles is of two types: the cumulative mass distribution of stars as determined by generations of random sampling of the IMF from the available gas reservoirs, and the current gas reservoir. The mass in each type depends on several factors. Firstly, the age of the particle determines how long it has been forming stars suggesting that older clusters may, on average, contain a larger fraction of mass in stars relative to younger clusters. Secondly, the accretion histories of individual clusters affect the division of mass. As mentioned in Section 2.3, any accreted mass is added directly to the gas reservoir. Therefore, if a cluster is undergoing strong accretion, the gas reservoir may dominate over the stellar mass.

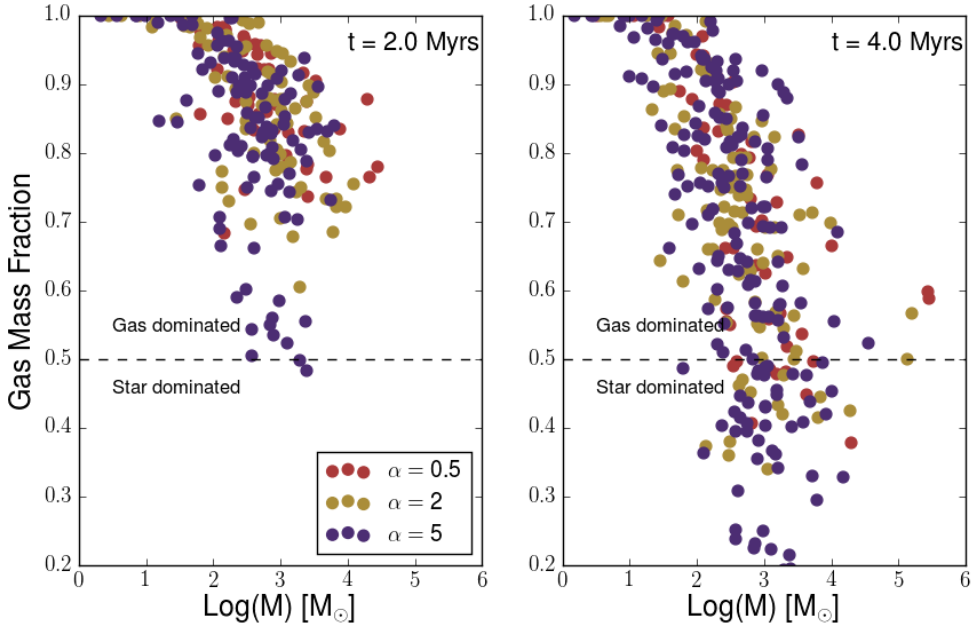

Figure 2.17: The particle gas mass fractions, defined as the total mass in the gas reservoir divided by the total cluster particle mass, of individual particles for simulations with different initial virial parameters, shown at 2 Myr (left) and 4 Myr (right). We only show three simulations for readability. Note that the gas reservoir refers to the gas which has been incorporated into the particle, and therefore resides within the particle radius of 0.325 pc.

We examine the division of particle mass into stars and the gas reservoir in Figure 2.17. We plot the gas mass fraction, defined as the ratio of the gas reservoir to the total mass, for each particle versus the total particle mass. The line at a gas mass fraction of 0.5 delineates clusters which are gas dominated from clusters which are stellar dominated. We show the gas mass fractions at 2 Myr, on the left, and 4 Myr, on the right. We only show three simulations, those with α_0 of 0.5, 2, and 3, for readability.

Figure 2.17 shows that the majority of cluster particles are still dominated by the gas reservoir at 4 Myr. These clusters are either undergoing strong accretion, or have not had enough time to convert their mass into stars. High gas mass fractions within clusters at late times appears to contradict observations which suggest that massive clusters are completely devoid of gas by 4 Myr (Hollyhead et al., 2015). Our subgrid model does not allow for gas expulsion from cluster sink particles which may explain the high gas mass fractions still present at late times. Even without gas expulsion from cluster particles, however, radiative feedback could conceivably halt further gas accretion which would naturally produce lower gas mass fractions at late times. Since this is not observed, it suggests that radiative feedback is not the only process responsible for producing gas free clusters by $\sim$4 Myr. Stellar winds (Dale & Bonnell, 2008) and protostellar jets (Federrath et al., 2014) may play a role in clearing young, star-forming regions of gas.

The overall spread in gas mass fractions shows differences among the simulations. The unbound simulation (ie. virial parameter of 5) contains the largest number of stellar dominated clusters. This is likely tied to the dynamical histories of individual particles. The higher gas velocities present in the high α_0 simulations can result in cluster particles drifting away from their local gas sources, thereby shutting off future accretion and producing stellar dominated clusters. This is less pronounced in the lower α_0 simulations because of the global collapse of both gas and particles which facilitates ongoing accretion.

The progression from a gas to a stellar dominated cluster particle is inherently a time driven process as cluster particles convert their mass into stars. This would

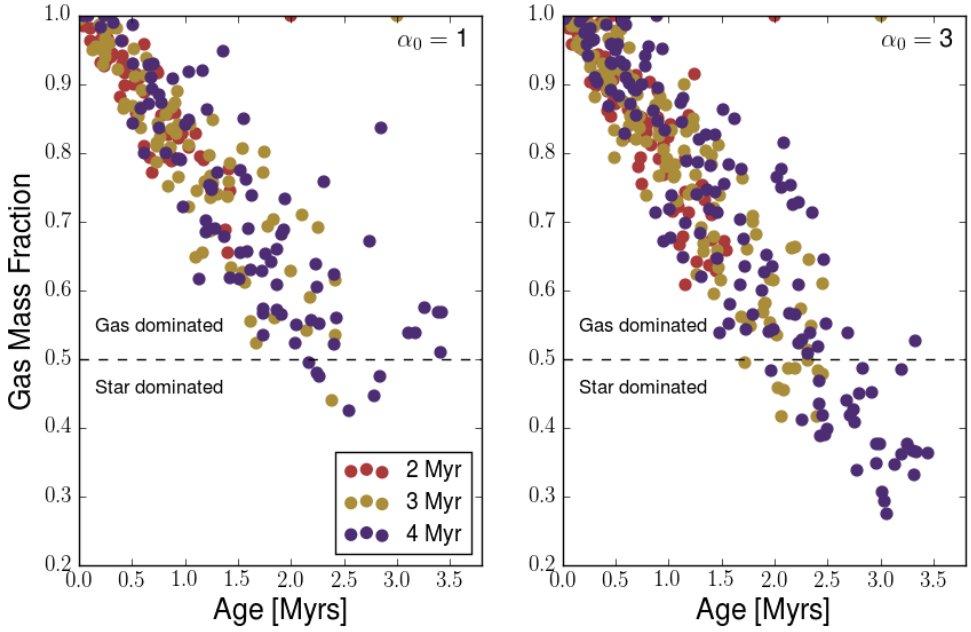

Figure 2.18: The particle gas mass fractions as a function of cluster age for a bound ($\alpha_0 = 1$) and an unbound ($\alpha_0 = 3$) simulations. The colours are now used to represent different times.

suggest that the oldest clusters should have the lowest gas mass fractions. This may not be case, however, because ongoing accretion can supply the clusters with a fresh gas supply. To visualize this interplay, we plot the gas mass fraction as a function of cluster age, instead of mass, in Figure 2.18. We show the results from two simulations, with α_0 values of 1 and 3, to show the difference between bound and unbound simulations. We plot the gas mass fractions of all particles present at 2, 3, and 4 Myr.

We see from Figure 2.18 that, generally speaking, older cluster particles have lower gas mass fractions (ie. a higher fraction of stars) than younger clusters. We do,

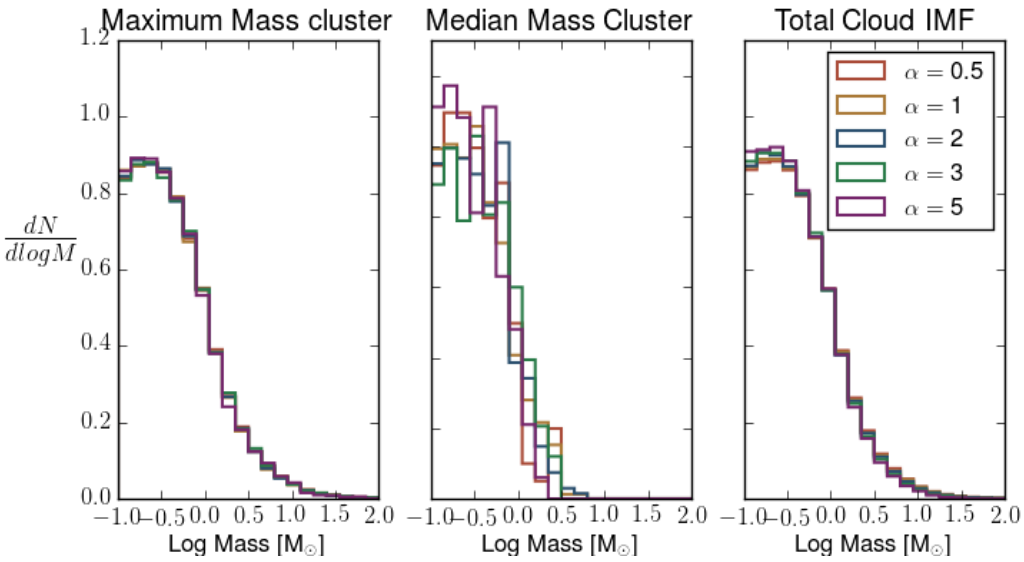

Figure 2.19: The stellar mass distributions within the maximum mass cluster particle (left), the median mass cluster particle (middle), and the total cloud (right). See Table 2.1 for the masses of the cluster particles being shown.

however, see significant outliers with some old clusters having high gas mass fractions. This highlights the importance of the local environment on star formation, suggesting that, even within one GMC, there can be distinct subclustered regions which can have very different star formation histories in comparison to their neighbours.

2.4.6 Stellar Content

The stellar mass distribution within individual cluster particles is partially determined by the subgrid model for star formation. A sufficiently massive particle with a large reservoir of mass to draw from will produce an IMF which is fully sampled. From Howard et al. (2014), particles with masses of ∼5000 M$_\odot$ are sufficiently mas-

sive to form O stars. For smaller clusters, however, the amount of mass available at sampling may not be sufficient to form massive stars.

For this reason, we examine the stellar mass distribution within individual cluster particles, as well as the total cloud, in Figure 2.19. We show the stellar mass distribution in both the maximum mass cluster particle, in the left panel, and the median mass particle, in the middle panel, to illustrate the variations between different star forming regions. The right hand panel of Figure 2.19 shows the stellar mass distribution of the entire cloud. For reference, the mass of the the maximum and median mass cluster for all simulations is shown in Table 2.1.

As expected, the most massive particles show a fully sampled IMF with stars covering the entire mass range. There is little cluster to cluster variation among the most massive particles. We see markedly different distributions for the median mass clusters, however, which vary in mass between 290 to 485 $M_{\odot}$. Because these clusters have significantly smaller masses, they rarely form stars with masses greater than $\sim$5 $M_{\odot}$. Moreover, the distributions show stronger variations among clusters. Because these particles form a small number of stars, the effects of randomly sampling an IMF become more apparent. Overall, these distributions highlight the importance that the accretion histories play in subclustered regions and how this impacts the type of stars that are able to form.

	Initial Virial Parameter (α_0)				
	0.5	**1**	**2**	**3**	**5**
Maximum Total Mass ($M_\odot$)	3.27×10^5	2.22×10^5	1.78×10^5	1.57×10^5	3.26×10^4
Median Total Mass ($M_\odot$)	368	485	313	290	318
Maximum Stellar Mass ($M_\odot$)	1.50×10^5	1.13×10^5	8.58×10^4	8.70×10^4	1.26×10^4
Median Stellar Mass ($M_\odot$)	144	107	103	91	97

Table 2.1: Particle masses in models with varying α_0 values.

2.4.7 Star Formation Rates

We conclude this Section with a discussion of the star formation rates within entire clouds and individual cluster particles, and relate this to the resulting stellar age spreads.

First, in Figure 2.20, we plot the total star formation rates from our simulations. As a consequence of our subgrid model for star formation, which only forms new stars at prescribed time intervals after a particle is formed, there are large, instantaneous jumps in the star formation rate. Since all particles do not form at the same time, the times at which particles sample the IMF are staggered. This means that, in a given timestep, there may be no particles which form new stars resulting in a SFR of zero. In other timesteps, the opposite may be true resulting in a large, instantaneous SFR. To aid in readability, the SFR curves presented in Figure 2.20 have been smoothed using a sliding average window. While this helps significantly in interpreting the Figure, there are still some spikes in the SFR that remain.

The curves show qualitatively similar trends across simulations. There is a rapid onset of star formation, beginning around 0.5 Myr, which rises up to a roughly

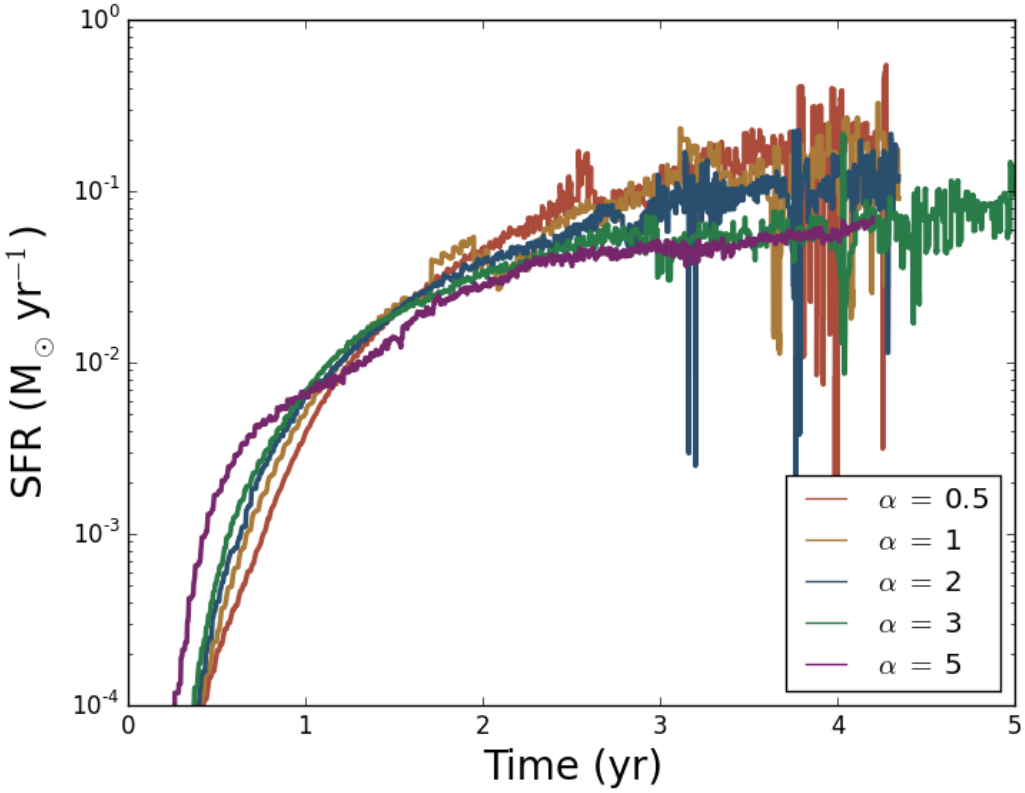

Figure 2.20: The global star formation rates over time for the 5 simulations including radiative feedback. The curves were smoothed using a sliding average window for readability.

constant value. We do not see a turnover in the SFR. We do not expect to see a complete halting of star formation as a consequence of our subgrid model in which dense gas is assumed to remain bound within the gravitational potential well of the cluster. As shown in Howard et al. (2014), however, the SFR will decrease for particles which are no longer accreting. This suggests that radiative feedback is not sufficient to halt the accretion onto a large number of particles and create a turn over in the SFR.

At late times, the variation in the SFR increases. This is likely due to the reason discussed above, namely that the formation of new stars in cluster particles is staggered. The variation becomes more pronounced at late times because there are more particles overall, and the particle masses increase as the simulation evolves meaning there is more mass out of which new stars can form. Additionally, the particle accretion rates become more variable at late times due to large velocities (see Figure 2.7) which can either disconnect a particle from its host filament or move it to a gas rich region where strong accretion is possible. Since the SFR is intimately tied to the accretion rate of particles, this is likely contributing to the variable SFR at late times.

The final, approximately constant, SFRs cover roughly a range of $4{\times}10^{-2}$ to $2{\times}10^{-1}$ $M_{\odot} \cdot yr^{-1}$, with variations of greater than an order of magnitude seen in some simulations.

The evolution of the global SFR is directly tied to the resulting stellar age distributions within the simulations. We compare the age spreads in the entire cloud,

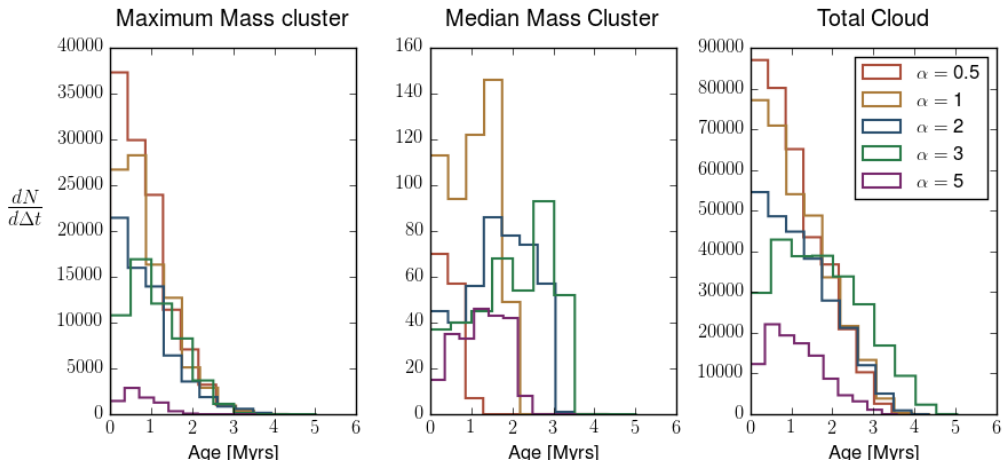

Figure 2.21: Stellar age distributions for the maximum mass cluster particle, median mass cluster particle, and the global age distribution from left to right, respectively.

as well as the maximum mass and median mass cluster particle, in Figure 2.21. The right panel, which shows the age spread of all stars in the respective simulations, mirrors the global SFR. The majority of stars are newly formed with a rapid decline in the amount of older stars. We do not see a turn over in the distribution since star formation is still occurring at high rates.

The age distributions within the maximum mass clusters are also strongly peaked towards young ages. This is not surprising since these clusters have a significant gas reservoir to continue forming stars. The median mass clusters show more variations between simulations. Some clusters, the median cluster in the simulation $\alpha_0 = 1$ for example, are newly formed and as a consequence the age distribution is narrow, $\sim$1 Myr, and peaked at young ages. The older median mass clusters, like in the simulation with $\alpha_0 = 2$, show much broader distributions with age spreads up to $\sim$3

Myr which also have a turnover at intermediate ages. This shows that the formation of a stellar population in a molecular cloud is not a uniform process with distinct regions forming stars at the same time. Instead, different subcluster regions have separate star formation histories tied to their local environments.

2.5 Comparison to Observations

2.5.1 Mass Distributions

We refer back to Figure 2.16 and discuss the connection to observed clump mass function. We focus on the recent results presented in Moore et al. (2015) who measured masses for 1029 clumps in W43. We have chosen this dataset in particular because W43 is one of the most massive cloud complexes in the Milky Way , with a total mass of $\sim 7\times10^6$ $M_\odot$ of which $\sim 8.4\times10^6$ $M_\odot$ is contained in dense clumps (Nguyen Luong et al., 2011), providing a good comparison to our simulated dataset.

The results presented in Moore et al. (2015) for W43 show a clump mass distribution with a high mass slope of -1.87$\pm$0.05, which is consistent with the results presented in Urquhart et al. (2014). This slope is inconsistent with our results, which range from -1.49 to -1.73, and suggests that our simulations have either overproduced very massive particles, under produced low mass particles, or is a combination of both effects. There are examples of clump mass functions which have smaller slopes (eg. Gómez et al. (2014) and discussions therein), but these studies have different cut off masses for the fits making comparisons difficult to make. Moreover, Reid & Wilson

(2005, 2006) measured the slope of the clump mass function in NGC 7538 and M17 and found inconsistent results between the two regions, suggesting that there may not be a universal clump mass function. As a final remark, we note that the slopes of our particle mass functions are consistent with those measured for entire GMC's by Solomon et al. (1987), who found a slope of -1. 50±0.36

The above discussion has focused on simulations which use a particle formation threshold of 10^4 cm^{-3}. As discussed in Section 2.4.4, we have also completed a subset of simulations which increase and decrease the formation thresholds by an order of magnitude. In the discussion surrounding Figure 2.14, we noted that increasing the formation threshold significantly reduces the number of cluster particles while increasing the average particle mass. The will clearly impact the resulting particle mass distributions.

We find that the resulting high mass slope, analyzed in the same way as above, differs dramatically for the high formation threshold of 10^5 cm^{-3}. For an α_0 of 0.5, the resulting slopes are -1.58, -1.54, and -1.05 for low, fiducial, and high thresholds, respectively. The corresponding slopes for the $\alpha_0 = 3$ simulations are -1.81, -1.7, and -1.09. The combination of less particles and higher average masses, in the case of a high formation threshold, results in significantly shallower slopes which are less consistent with observations. This provides further justification for the choice of 10^4 cm^{-3} as our formation threshold. Not only is this value observationally motivated, it results in particle mass distributions which are closer to measured values.

2.5.2 Star Formation Rates in Molecular Clouds

The SFRs discussed earlier were measured globally for each simulation. In order to make comparisons to observations, we plot the SFR of individual cluster particles in Figure 2.22. We again only show the simulations with an α_0 of 0.5, in red, 2, in blue, and 5, in purple for readability. We have over plotted the observational results from Lada (2010) in black crosses. These observations used 2MASS data to catalog the young stellar objects (YSOs) in 11 local star forming regions within 450 pc of the sun. The observed clouds are the Pipe Nebula, the Ophiuchus cloud, the Lupus cloud complex, Taurus, Perseus, the California clouds, RCrA, and the Orion cloud complex. How measurements of the YSO content in these clouds are used to estimate SFRs is described below.

The black triangles in Figure 2.22 represent the dataset from Heiderman et al. (2010) who also measured SFRs in local regions, some of which are the same regions as in Lada (2010). The solid line represents the SFR-mass relation measured for extragalactic sources by Wu et al. (2005). These observations measured the IR and HCN luminosity in the star forming cores of nearby galaxies, and used these measurements as proxies for the SFR. The resulting SFR-mass relation is given by,

$$SFR(M_{\odot}yr^{-1}) \sim 1.2 \times 10^{-8} M_{dense}(M_{\odot}) \tag{2.7}$$

where M_{dense} is the mass of dense gas ($n > 10^4$ cm^{-3}) traced by IR emission. We have extrapolated this relation to molecular cloud masses in Figure 2.22.

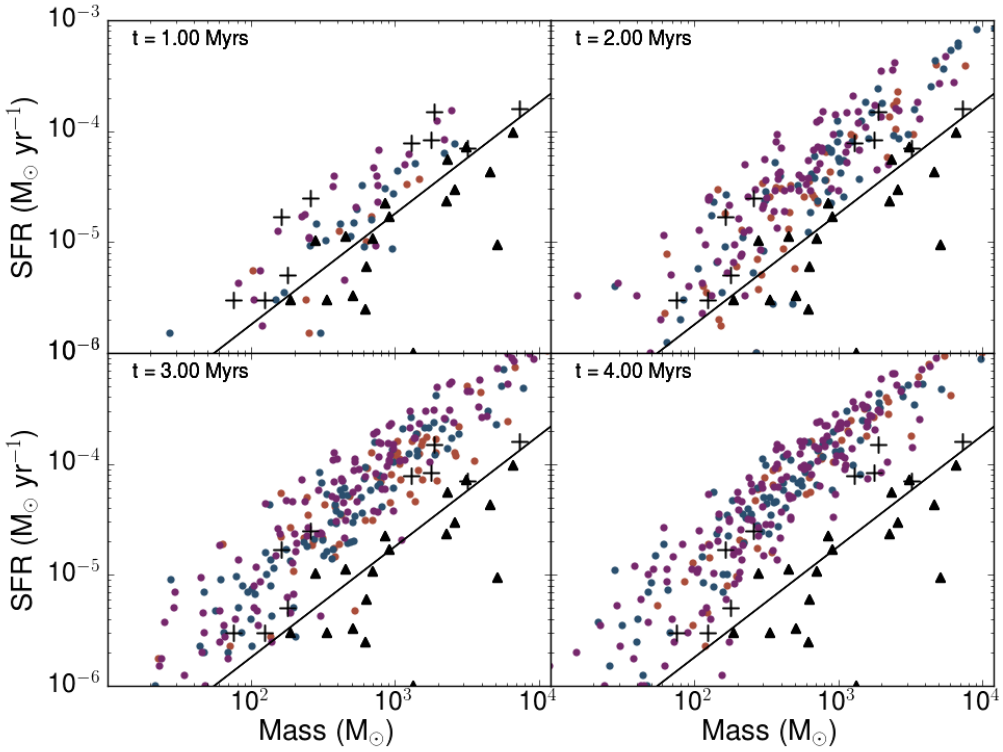

Figure 2.22: The SFR of individual cluster particles at various times in simulations with an initial virial parameter of 0.5 (red), 2 (blue), and 5 (purple). The crosses represent the SFRs measured in local star forming regions from Lada (2010). The black triangles represent another dataset presented by Heiderman et al. (2010). The solid line is an extrapolation to smaller masses from extragalactic SFR measurements performed by Wu et al. (2005).

In order to make a comparison to the observations, we have measured the SFR in each cluster particle in an identical manner to Lada (2010). The following formula was used to estimate the SFR in each region,

$$SFR = \frac{N\bar{M}}{\tau_{YSO}} = 0.25N \times 10^{-6} M_{\odot} yr^{-1} \tag{2.8}$$

where N is the total number of young stellar objects (YSOs) in each region, $\bar{M}$ is the median mass of a YSO in $M_{\odot}$, and τ_{YSO} is the average lifetime of a YSO. The median mass, $\bar{M}$, was taken to be 0.5 $M_{\odot}$, consistent with the IMF and therefore consistent with the stellar distributions within our cluster particles. An average YSO lifetime of 2 Myr was assumed. While we do not have prestellar evolution in our subgrid model, and therefore do not know the exact number of YSOs, we do know the formation times for all stars. When solving for the SFR via equation 2.8, we therefore take N to be the cumulative number of stars formed within the last 2 Myr to make the comparison to observations as consistent as possible.

At early times, the SFRs agree well with the measured values, in particular the Lada (2010) values. As time progresses, the SFRs in our simulations shift to higher values while following the same slope. This is consistent with the global picture presented earlier, where the global SFR rises rapidly to a roughly constant value producing age spreads which are heavily peaked at early times. While low to intermediate masses fall roughly in the range of the observations, the disparity between the observations and our results is particularly pronounced at high masses. At late times, the SFRs in the most massive cluster particles approach an order of

magnitude greater than the observations. Since these massive clusters contain the most stars, this again suggests that radiative feedback is not the sole form of feedback necessary to halt the star forming process.

The high SFRs of massive clusters in our simulations are not just a product of the local environment and accretion rate, but also a product of subcluster merging which can provide these massive clusters with fresh supplies of gas to continue forming stars at high rates.

We show this in Figure 2.23 which plots the fraction of mass obtained via mergers. The percentage of surviving clusters which underwent at least one merging event varies from 9.6% to 15.2% for α_0 values of 5 and 2, respectively, with no discernible trend as α_0 changes. All values are shown in the legend of Figure 2.23. Figure 2.23 shows that merging is not a significant form of mass accretion for the majority of cluster particles. This is particularly true for low mass clusters which grow solely via gas accretion, as shown by the large grouping of particles at zero. Above roughly 10^3 $M_\odot$, however, merging becomes a significant source of mass accretion with some particles obtaining more than half of their total mass via merging. This highlights the role that subcluster merging plays in the build up of young stellar clusters. High mass clusters in particular are not formed solely via gravitational fragmentation but rather through the merging of multiple, lower mass subclusters. Based on our simulations, we can conclude than subcluster merging plays a significant role in the early development of clusters with mergers producing large clusters within ~ 4 Myr.

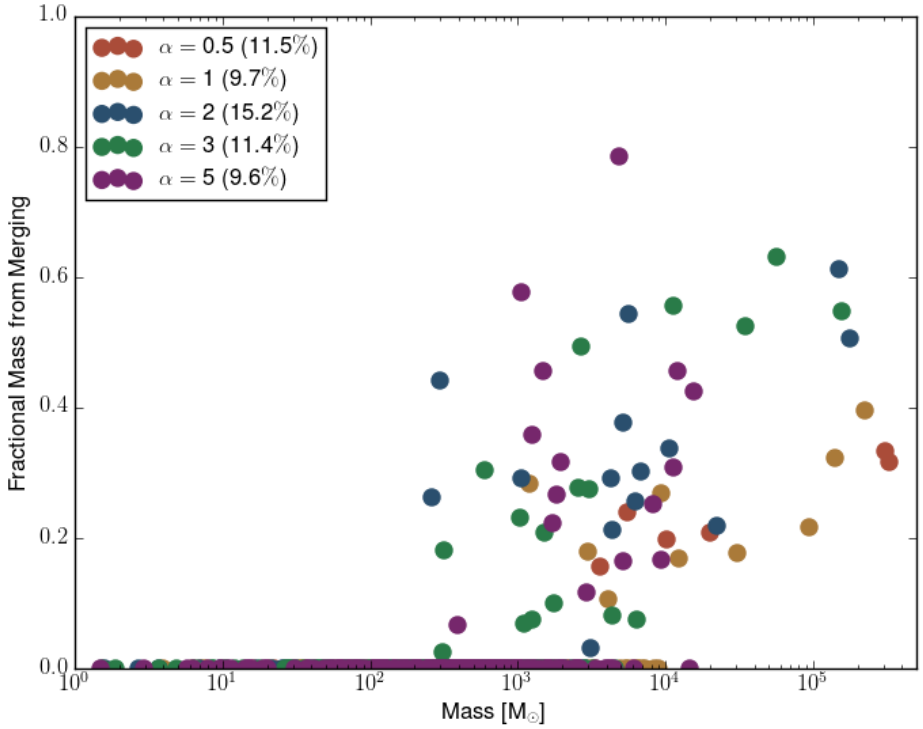

Figure 2.23: The fraction of total cluster particle mass obtained via merging events. Clusters with fractions greater than 0.5 have grown primarily through accreting other clusters. The legend shows the percentage of surviving particles that have undergone at least one merger in its history.

2.6 Conclusions

We have simulated a suite of turbulent, 10^6 $M_\odot$ GMCs using FLASH which have initial virial parameters in the range of 0.5 to 5. Using these, we explore the role that radiative feedback and gravitational boundedness play in the formation of star clusters and the early evolution (< 5 Myr) of a GMC. To do this, we have used sink particles to represent star clusters and implemented a subgrid model to populate

clusters with stars gradually over time via randomly sampling the IMF. The radiative output of these evolving clusters was then coupled to a raytracing scheme to treat the radiative transfer. The main conclusions of this work are as follows:

- The initial virial parameter, α_0, strongly influences the dense clump formation efficiency, ϵ_{cl}, and the star formation efficiency, ϵ_{sf}, during the early evolution of the GMCs. Models that are more bound (ie. lower α_0) have higher efficiencies in comparison to unbound models despite a delayed onset of cluster formation. This is tied to the global gas evolution of the cloud which becomes strongly centrally condensed in bound clouds, which can prolong gas accretion onto newly formed clusters, and the strong mass loss from unbound clouds. The final ϵ_{cl} values range from 37% to 71% and the final star formation efficiencies range from 19% to 33% for virial parameters of 5 and 0.5, respectively.

- Radiative feedback does not strongly affect formation efficiencies over the range of time simulated. The inclusion of radiative feedback reduced ϵ_{cl} by only $\sim$1%, except in the case of an $\alpha_0 = 3$, in which ϵ_{cl} was reduced from 52% to 41%. This reduction was not due to radiation unbinding gas and driving outflows, but instead by suppressing cluster formation and accretion locally via heating and ionization.

- The strength of radiative feedback is enhanced if a higher formation threshold for cluster particle formation is used. We have chosen a fiducial value of 10^4

cm^{-3} and explored using thresholds that are an order of magnitude smaller and larger than this value for a bound ($\alpha_0 = 0.5$) and an unbound ($\alpha_0 = 5$) cloud. In both cases, the higher threshold simulations showed larger differences in ϵ_{cl} between runs with and without feedback. A higher threshold of 10^5 cm^{-3} for the $\alpha_0 = 0.5$ model produced a difference in ϵ_{cl} between the HD and RHD simulations of 21% compared to 2% in the fiducial threshold simulations. The difference between the HD and RHD simulations for the $\alpha_0 = 3$ model was 10% compared to 8% with the fiducial threshold. Since the average density of the cloud is naturally higher when clusters form in the higher threshold case, this shows that the strength of radiative feedback can be enhanced in clouds with higher density. This may have important implications for Globular Cluster formation (Kruijssen, 2015) which is thought to occur in high density, high pressure environments.

- Cluster properties are sensitive to the initial virial parameter of the cloud out of which they form. The total number of clusters formed increases as α_0 increases, with the final number of clusters being 52 for the most bound simulation and 189 for the most unbound simulation. This, in combination with the result that bound clouds produce more massive clusters than unbound clouds, produces increasingly steeper cluster mass distributions as the initial virial parameter increases. This is a product of the mass distributions shifting to higher masses as α_0 decreases, resulting in a steeper slope when fitting over a fixed range. The high mass slopes of our cluster mass distributions range

from -1.54 to -1.73 which is only slightly shallower than the mass function presented in Moore et al. (2015) who measured a value of -1.87 for clumps in W43. We also find that there are more gas poor, star rich cluster particles formed in unbound simulations compared to bound simulations. While we do not have a prescription for mass loss from cluster particles, this highlights the role that dynamics plays in the early evolution of clusters. The gas poor clusters in bound simulations have been ejected from their host filaments effectively halting further gas accretion. In contrast, clusters formed in bound clusters are centrally condensed and continue to accrete, resulting in gas rich clusters.

- We have compared the SFRs of our cluster particles to observations of local star forming regions. The SFRs in our simulations agree with observations at early times but are higher at late times, particularly for the most massive cluster particles. This is related to the global SFRs in our models which show a sharp rise in star formation which levels out to a constant value. We see no evidence for a turnover in the global SFRs which suggests that, at least in the early evolution of a GMC, radiative feedback alone is not responsible for halting star formation and dispersing the cloud. Other forms of feedback, such as protostellar jets, stellar winds, and supernovae, should be included to fully understand the cluster formation process.

We plan to extend our work by exploring different cloud properties such as magnetic field strengths and metallicity. We will also be exploring radiative feedback

in cloud with masses 10^{4-7} $M_{\odot}$. The highest mass clouds will probe the Supergiant Molecular Cloud regime in which Globular Cluster mass objects may form (Harris & Pudritz, 1994). We will also model clouds with a range of initial densities because, as our results show, the density structure of a cloud can alter the strength of radiative feedback.

2.7 Acknowledgments

We thank an anonymous referee for a useful report which improved the quality of this paper. We thank Ralf Klessen and Mordecai Maclow for their invaluable input on numerics and theory, and Henrik Beuther and Jouni Kainulainen for interesting discussions of observations. C.S.H. and R.E.P gratefully acknowledge KITP, Santa Barbara, for their support and hospitality while participating as an affiliate (C.S.H) and an invited participant (R.E.P.) in the program "Gravity's Loyal Opposition: The Physics of Star Formation and Feedback". We thank Norm Murray, Andre Kravstov, and Christoph Federrath for interesting discussions during this time about simulations and theory. C.S.H. and R.E.P. also thank MPIA and the Institut für Theoretische Astrophysik (ITA) in the Zentrum für Astronomie der Universität Heidelberg for their generous support during R.E.P's sabbatical leave (2015/16) and C.S.H.'s extended visit (Oct. - Nov., 2015).

R.E.P. and W.E.H. are supported by Discovery Grants from the Natural Sciences and Engineering Research Council (NSERC) of Canada. C.S.H. acknowledges financial support provided by the Natural Sciences and Engineering Research Coun-

cil (NSERC) through a Postgraduate scholarship. The FLASH code was in part developed by the DOE-supported Alliances Center for Astrophysical Thermonuclear Flashes (ASCI) at the University of Chicago. This work was made possible by the facilities of the Shared Hierarchical Academic Research Computing Network (SHARCNET: www.sharcnet.ca) and Compute/Calcul Canada.

Chapter 3

Simulating Radiative Feedback and Star Cluster Formation in GMCs: II. Mass Dependence of Cloud Destruction and Cluster Properties

3.1 Abstract The process of radiative feedback in Giant Molecular Clouds (GMCs) is an important mechanism for limiting star cluster formation through the heating and ionization of the surrounding gas. We explore the degree to which ra-

diative feedback affects early ($\lesssim$5 Myr) cluster formation in GMCs having masses that range from 10^{4-6} $M_\odot$ using the *FLASH* code. The inclusion of radiative feedback lowers the efficiency of cluster formation by 20-50% relative to hydrodynamic simulations. Two models in particular — 5×10^4 and 10^5 $M_\odot$ — show the largest suppression of the cluster formation efficiency, corresponding to a factor of $\sim$2. For these clouds only, the internal energy, a measure of the energy injected by radiative feedback, exceeds the gravitational potential for a significant amount of time. We find a clear relation between the maximum cluster mass, $M_{cl,max}$, formed in a GMC of mass M_{GMC}; $M_{cl,max} \propto M_{GMC}^{0.81}$. This scaling result suggests that young globular clusters at the necessary scale of $10^6 M_\odot$ form within host GMCs of masses near $\sim 5\times10^7 M_\odot$. We compare simulated cluster mass distributions to the observed embedded cluster mass function ($dlog(N)/dlog(M) \propto M^\beta$ where β = -1) and find good agreement (β = -0.99$\pm$0.14) only for simulations including radiative feedback, indicating this process is important in controlling the growth of young clusters. However, the high star formation efficiencies, which range from 16-21%, and high star formation rates compared to locally observed regions suggest other feedback mechanisms are also important during the formation and growth of stellar clusters.

3.2 Introduction

The formation of star clusters takes place within dense (n > 10^4 cm^{-3}) clumps of molecular gas embedded in Giant Molecular Clouds (GMCs) (Lada & Lada, 2003; Mac Low & Klessen, 2004; Bertoldi & McKee, 1992; Kruijssen, 2012). These clouds

are supersonically turbulent and highly filamentary with the most massive clusters forming at the intersection of these filaments (Balsara et al., 2001; Banerjee & Pudritz, 2006; Schneider et al., 2012; Kirk et al., 2013). Since star clusters are almost exclusively formed in GMCs, understanding the processes that lead to their formation and destruction is vital for a complete understanding of galaxy evolution over cosmic time.

The properties of GMC within a galaxy — such as the mass and virial parameter (Solomon et al., 1987; Rosolowsky, 2007; Hernandez & Tan, 2015; Howard et al., 2016) — vary from cloud to cloud. Within the Milky Way (MW), the typical size of a GMC ranges from 50 pc to several hundreds of parsecs with masses in the range of $\sim 10^{4-7}$ $M_\odot$ (Fukui & Kawamura, 2010). More specifically, the mass distribution of clouds within the inner disk of the MW follows a power law $dN/dM \propto M^\alpha$ where $\alpha \sim$ -1.5 (Sanders et al., 1985; Solomon et al., 1987; Rosolowsky, 2005). The power law index for the GMC mass distribution in other Local Group galaxies is found to be significantly steeper, ranging from -1.7 for the LMC to -2.5 for M33 (Blitz et al., 2007; Rosolowsky, 2005).

The mass of a GMC has a direct impact on a cluster that forms within it. Both simulations (Fujii & Portegies Zwart, 2015) and observations (Hughes et al., 2013) indicate a relation between the mass of a GMC (M_{GMC}) and the maximum mass cluster ($M_{c,max}$) it produces of the form $M_{c,max} \propto M_{GMC}^{0.5}$. Based on the similarity of the mass scaling of GMCs and star clusters, Harris & Pudritz (1994) proposed that Globular Clusters (GCs) originated in Supergiant Molecular Clouds ($\geq 10^7$ $M_\odot$). Overall, these results suggest that the massive stellar content should increase with

GMC mass. This is indeed borne out in observations of the LMC (Kawamura et al., 2009; Fukui & Kawamura, 2010) which show that GMCs with large HII regions, indicating the presence of massive stars, are typically more massive than GMCs with no, or low luminosity, HII regions.

The overall conversion of molecular gas into stars, regardless of cloud mass, is an inherently inefficient process. Typical estimates of the star formation efficiency over the lifetime of an individual GMC in the MW range from 2-5% (Lada & Lada, 2003; McKee & Ostriker, 2007; Murray, 2011).

The question of what limits star formation in a GMC to such low values, and ultimately disrupts the cloud, is debated. Both turbulence (Klessen et al., 2000; Bate et al., 2003; Bonnell et al., 2008) and magnetic fields (Myers & Goodman, 1988; Tilley & Pudritz, 2007; Federrath & Klessen, 2012) can provide added pressure support against gravitational collapse and lower the star formation rate per freefall time, but cannot completely disperse the GMC. Alternatively, feedback from newly-formed stars can both limit the star formation efficiency and destroy the GMC via the input of energy and momentum into the gas.

The goal of this paper is to explore how cluster formation and radiative feedback affect GMCs and ultimately star cluster properties. For this purpose, we present the results from a suite of simulations which examine the role of radiative feedback in 5 clouds ranging from 10^{4-6} $M_{\odot}$. The initial average density and the initial virial parameter are identical for all models in order to ensure all observed differences are due solely to varying the mass.

Stellar feedback comes in many forms — protostellar jets (Li & Nakamura, 2006; Maury et al., 2009; Federrath et al., 2014), stellar winds (Dale & Bonnell, 2008; Gatto et al., 2017), ionization/heating of the gas (Dale et al., 2005; Peters et al., 2010a; Klassen et al., 2012b), radiation pressure (Krumholz & Thompson, 2012; Murray et al., 2010), and supernovae feedback (Rogers & Pittard, 2013; Fierlinger et al., 2016; Keller et al., 2014; Gatto et al., 2015; Walch & Naab, 2015). Of these mechanism, radiative feedback has been suggested as being most important during the early phases of cluster formation, particularly in clusters which are hosting massive star formation (Whitworth, 1979; Matzner, 2002; Murray et al., 2010; Dale et al., 2012b; Bate, 2012). The heating and ionization of the gas surrounding star-forming clusters prevents further fragmentation, and expanding HII regions can drive further turbulence (Gritschneder et al., 2009; Boneberg et al., 2015). Direct radiation pressure from high energy photons interacting with dust grains can also drive strong outflows.

Previous studies which examine the impact of radiative feedback on both small (individual cluster) scales and large (entire GMC) scales show that the overall star formation efficiency can be reduced (Dale et al., 2007; Peters et al., 2010a; Dale et al., 2012b; Bate, 2012; Klassen et al., 2012b; Walch et al., 2012). In particular, the work of Dale et al. (2012b) showed that radiative feedback produces large scale HII regions which drive significant gas outflows from the cloud. This is especially important in low mass ($\sim 10^4$ $M_\odot$) clouds. Despite the production of these large features, the influence on star formation efficiencies and rates was small. Their models, however, were limited to gravitationally bound clouds.

Our own work (Howard et al., 2016) also showed that the inclusion of radiative feedback did reduce the efficiency of cluster formation, but only by a maximum of $\sim$10%. This study was limited to a single GMC mass (10^6 $M_\odot$) which, while present in the MW, are not typical of the average GMC as illustrated by the powerlaw mass distribution discussed above. Moreover, since the properties of the population of clusters formed in a GMC depends on its initial mass, the effects of radiative feedback can possibly differ when considering a spectrum of cloud masses.

We evolve all models to $\sim$5 Myr, at which point supernovae are expected to become a significant factor in the cloud's evolution. To make this computationally feasible, we make use of sink particles to represent star clusters in combination with a custom subgrid model to follow the formation of stars within the cluster. We discuss the details of this model, our numerical methods, and the GMC initial conditions in Section 3.3.

In Section 3.4, we discuss the global evolution of our cloud models and the role that radiative feedback plays on the final cluster and star formation efficiencies. We find that feedback reduces these efficiencies for all clouds, but it is most significant in the 5×10^4 and 10^5 $M_\odot$ clouds which have the efficiency of cluster formation reduced by approximately a factor of 2. We show that this is the result of a trade off between the energy injected by radiative feedback and the gravitational potential energy of the cloud. GMCs in this particular mass range are massive enough to form a population of massive stars but have a small enough gravitational potential to become unbound under the influence of radiative feedback.

In Section 3.5, we compare our star formation rates and initial cluster mass function to their observed counterparts. We find that the slope of our cluster mass function over the range of masses observed for embedded clusters is consistent with observations only when radiative feedback is included. However, the combination of high SFRs at late times and star formation efficiencies which range between 16 and 21% suggest that radiative feedback alone is not responsible for limiting early star and cluster formation.

3.3 Numerical Methods

Here, we provide a brief description of the numerical methods employed in our simulations. For more detail, we refer the reader to Howard et al. (2016).

We perform numerical simulations using the Adaptive Mesh Refinement (AMR) code FLASH (version 2.5) (Fryxell et al., 2000a) which solves the compressible gas dynamic equations on a Eulerian grid. FLASH also includes modules to treat self-gravity, radiative transfer, star formation, and cooling via molecules and dust.

Gas cooling is treated using the methods from Banerjee et al. (2006) which handles cooling via gas-dust interactions, H_2 dissociation, and molecular line emission. The cooling rates for molecular line emission and gas-dust transfer are taken from Neufeld et al. (1995) and Goldsmith (2001), respectively.

The hybrid-characteristics raytracing scheme developed by Rijkhorst et al. (2006), and expanded for astrophysical use by Peters et al. (2010a), is used to treat radiative

transfer. This scheme follows the propagation of ionizing and non-ionizing radiation and uses the DORIC routines (Frank & Mellema, 1994; Mellema & Lundqvist, 2002) to calculate the ionization state of the gas. The DORIC routines consider hydrogen to be the only gas species when calculating the absorption of ionizing photons. We adopt the temperature dependent Planck mean opacities from Pollack et al. (1994) for non-ionizing radiation which were calculated for a mixture of gas, silicates, ices, and organics. The absorption of non-ionizing radiation acts as a source term when calculating the temperature of the gas.

Radiation pressure is included by adopting a single UV opacity of $\kappa = 775$ cm^2 g^{-1} (Li & Draine, 2001) which is scaled by the neutral fraction of the gas such that fully ionized regions have zero opacity. The radiative force per unit mass is calculated via,

$$F = \frac{L}{c} \frac{e^{-\tau_{uv}}}{4\pi r^2} \tag{3.1}$$

where c is the speed of light, L is the source luminosity, r is the distance between the source and the cell, and τ_{uv} is the optical depth between the source and the cell calculated using the raytracer. We note that the scattering and absorption of infrared (IR) photons is not included in our radiation pressure calculation. The trapping of IR photons in high density regions would introduce an additional factor of τ_{IR} — the optical depth to IR radiation — in Equation 1. For typical MW cluster forming regions, this additional contribution is thought to be negligible (Murray et al., 2010).

The formation of star clusters is represented by the sink particle methods from Federrath et al. (2010). A custom subgrid model is used to model star formation within these clusters (see Howard et al. (2014) for a full description of this model). When a particle is formed above the adopted density threshold of 10^4 cm^{-3}, which is based on observations of star-forming clumps (Lada & Lada, 2003), its mass is divided into two components; mass available for star formation during this timestep, and the remaining gas mass (referred to as the 'reservoir'). The mass available for star formation is drawn from the available gas reservoir and randomly distributed into stars using a Chabrier (2005) IMF. The reservoir gas is converted to stars with an efficiency of 20% per freefall time, where the freefall time is taken to be 0.36 Myr (ie. the freefall time of gas at 10^4 cm^{-3} with a mean molecular weight of 2.14), and the IMF is sampled every tenth of a freefall time to ensure cluster properties evolve smoothly over time. The efficiency per freefall time was chosen to be consistent with observations of star-forming clumps which are estimated to range from 10-30% (Lada & Lada, 2003).

The masses of all stars formed in each cluster are recorded and analytic fits from Tout et al. (1996) are used to obtain each star's temperature from its mass. We neglect the effects of protostellar evolution and assume each star to be radiating as a blackbody at its corresponding temperature. The total luminosity of each star is calculated by integrating the entire blackbody spectrum and the ionizing luminosity is calculated using the same method but only considering photon energies greater than 13.6 eV. The total ionizing luminosity of each cluster is then the sum of its constituent stars which is used by the radiative transfer scheme.

We allow our cluster sink particles to merge under the conditions that they are separated by less than a particle radius, their relative velocities are negative, and they are gravitationally bound to one another. When a merger occurs, all mass (including both the stellar mass and reservoir mass) is transferred to the more massive particle and the smaller particle is deleted. The total number of clusters may therefore either increase or decrease as the simulations evolves.

We employ a stellar mass threshold for our clusters, below which the clusters do not radiate. This was included in order to reduce the computational time, since the radiative transfer scheme is expensive. Clusters below this threshold continue to form stars, accrete gas, and interact gravitationally with their surroundings, but they are not included in the radiative transfer calculation. We discuss the specific thresholds we used for each simulation below.

3.3.1 Initial GMC Conditions

We simulate a suite of GMCs that have masses of 10^4, $5{\times}10^4$, 10^5, $5{\times}10^5$, and 10^6 M$\odot$. Two simulations were completed for each cloud mass — one with radiative feedback included, and one without radiative feedback (ie. purely hydrodynamic). The clouds are initially spherical, with a density profile which is uniform in the inner half of the cloud and decreases as $r^{-3/2}$ in the outer half. A quadratic fit is applied at the transition between these two profiles to ensure the density is smooth and continuous. The radius of each cloud is chosen such that the average density is $n = 100$ cm^{-3}.

Mass ($M_\odot$)	Radius (pc)	Virial Parameter	Initial Mach Number	Resolution (pc)	Particle Radius (pc)	Radiative Threshold ($M_\odot$)
10^4	7.67	3	13.6	0.13	0.33	100
5×10^4	13.1	3	23.3	0.23	0.58	100
10^5	16.5	3	36.2	0.29	0.73	1000
5×10^5	28.3	3	50.3	0.25	0.62	1000
10^6	33.8	3	73.1	0.31	0.78	1000

Table 3.1: Summary of parameters for each simulation. Note that two simulations were completed for every entry in the table — one including radiative feedback and one without radiative feedback.

Each GMC is initially overlaid with a Burgers turbulent velocity spectrum, as in Girichidis et al. (2011), after which the turbulence is not driven and allowed to decay. The strength of the turbulence varies between simulations but is chosen such that each cloud has the same initial virial parameter, α_0, defined by (Bertoldi & McKee, 1992),

$$\alpha_0 = 2\frac{E_{kin}}{|E_{grav}|} \tag{3.2}$$

where E_{kin} is the cloud's total kinetic energy, and E_{grav} is the total gravitational potential energy. We have chosen an initial virial parameter of 3 (ie. unbound) since it resulted in more realistic formation efficiencies compared to bound clouds in Howard et al. (2016). As shown in that work, the turbulence decays rapidly and becomes virialized at $\sim$2.5 Myr regardless of α_0.

We use outflow boundary conditions for all simulations. The total mass in the simulation volume is therefore not conserved, and can decrease over time due to gas leaving the domain. This is relevant to the discussion that follows in the next Section.

Since the radius, initial Mach number, resolution, particle size (given by 2.5 times the smallest cell size), and the threshold for radiating differ between clouds of different mass, we summarize these parameters in Table 3.1.

3.4 Results

3.4.1 Global Evolution and Cluster Properties

To visually compare the evolution of GMCs with different initial masses, we show density slices through the center of the simulation volumes in Figure 3.1. The columns, from left to right, show GMC masses of 10^4, 10^5, and 10^6 $M_\odot$ respectively. All simulations shown in Figure 3.1 include radiative feedback. The rows are plotted at different times, ranging from 1.5 to 5 Myr. The black dots represent the locations of clusters which have been projected onto the slice plane. The corresponding temperature slices are shown in Figure 3.2. It is very important to note that cloud sizes and simulation boxes are very different for these three GMCs: 10x10 pc, 20x20 pc, and 40x40 pc, respectively.

The first row shows the state of the simulation shortly after the formation of the first clusters. The gas has already broken up into filaments due to the turbulent nature of the gas. The 10^6 $M_\odot$ simulation has formed significantly more clusters by this time, totaling 37 compared to the 7 that have formed in the 10^4 $M_\odot$ cloud. Despite clusters being present, they have not grown to high enough masses to influence their environment via heating or ionization. This can be seen in the first row of Figure

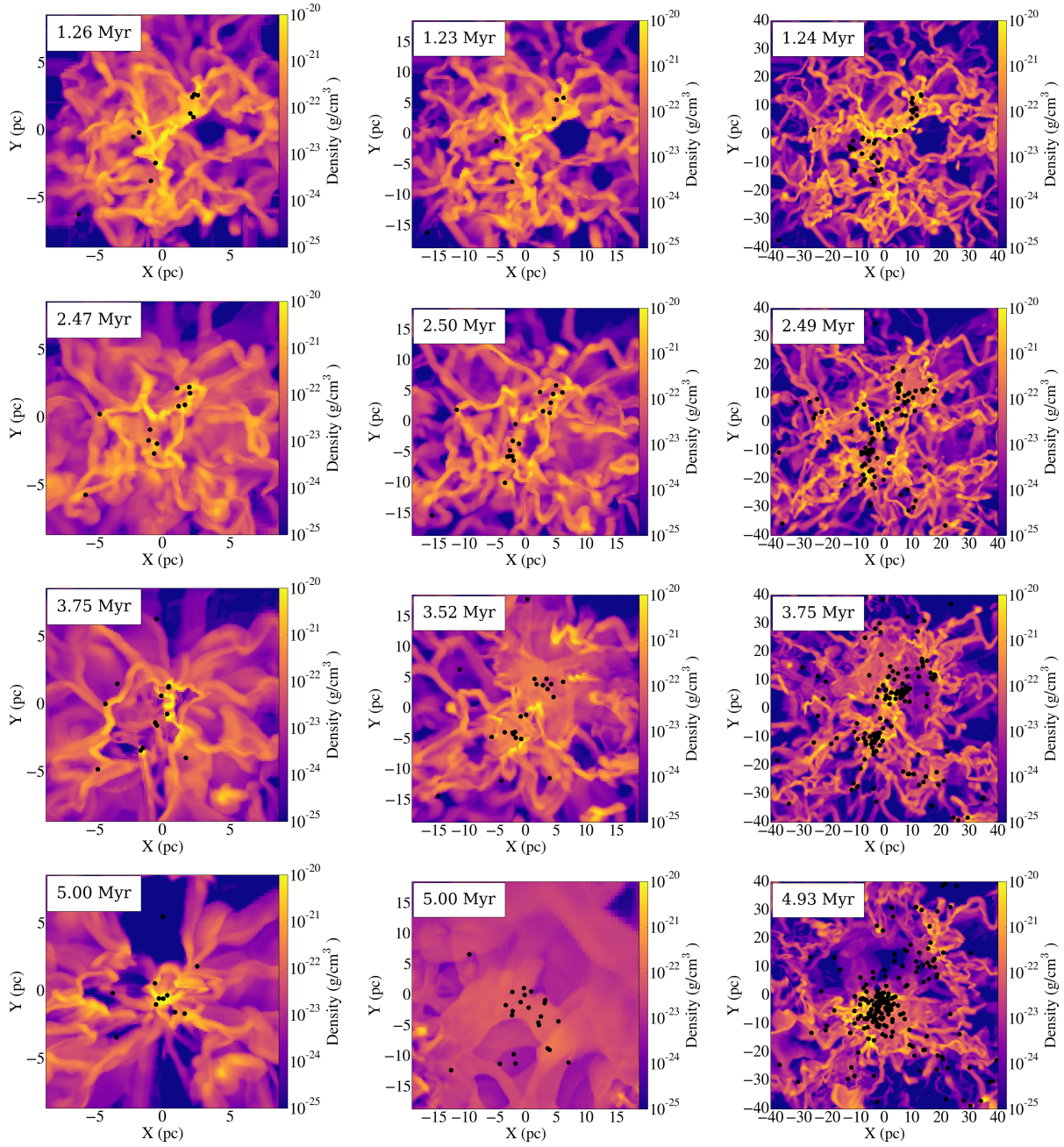

Figure 3.1: Density slices through the center of the simulation volume for the 10^4 (left), 10^5 (center), and 10^6 (right) $M_\odot$ GMCs. Time, shown in the top left of each panel, increases from top to bottom. Cluster locations are projected onto this slice and shown by black circles. Note that the physical (xy) scales change with cloud mass (10x10 pc, 20x20 pc, and 40x40 pc from left to right).

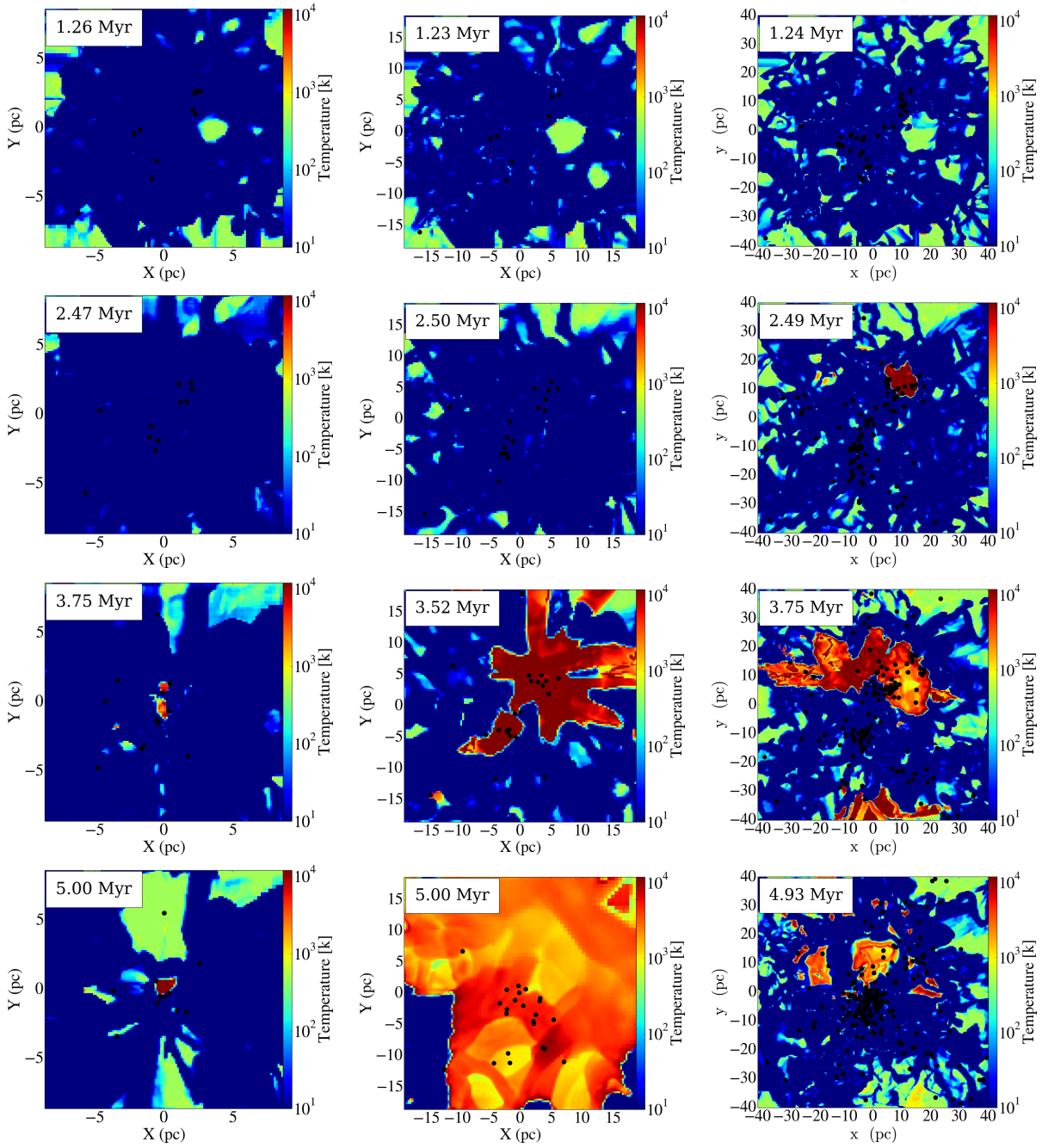

Figure 3.2: The corresponding temperature slices to the panels shown in Figure 3.1.

3.2 which shows that the majority of the gas still remains at 10 K, with ∼300 K gas filling the low density voids between filaments.

As the simulation progresses to 2.5 Myr, the clusters in the 10^6 $M_\odot$ cloud have become sufficiently populated with massive stars to begin ionizing their surroundings. This results in a hot (∼10,000 K) bubble of gas near the center of the simulation shown in Figure 3.2. The corresponding density slice shows that filaments in this region have been destroyed due to the high temperatures. The 10^4 and 10^5 $M_\odot$ clouds, in contrast, have not produced enough massive stars for radiative feedback to have any effects.

At 3.75 Myr, Figure 3.2 clearly shows that radiative feedback is active in all clouds. The 10^5 $M_\odot$ and 10^6 $M_\odot$ clouds in particular show extended HII regions centered on a group of massive clusters. The corresponding density images show that radiative feedback is in the process of destroying the filaments in the vicinity of these HII regions due to the expansion of the hot gas which smears out overdense regions.

The final panels of Figures 3.1 and 3.2 show marked differences between the three simulations. The gas in the 10^4 $M_\odot$ cloud is centrally condensed with the majority of clusters existing in this central region. This allows these clusters to continue accreting from their surroundings.

The 10^5 $M_\odot$ cloud has been effectively destroyed by radiative feedback. The entire cloud is nearly fully ionized and the resulting expansion of gas has caused a

large fraction of the initial mass to leave the simulation volume. The cloud remains fully ionized after this point and the accretion of gas by the clusters has been halted.

While there are large voids produced by HII regions in the 10^6 $M_\odot$ cloud, little mass loss has occurred. The clusters are also dispersed more evenly throughout the cloud, some of which are still actively accreting gas. Large scale filamentary structures are still present at 5 Myr.

To compare cluster formation across different clouds, we plot the total mass contained in clusters (top panel) and the total number of clusters (bottom panel) in Figure 3.3.

Since all GMCs were initialized with the same average density and virial parameter, the onset of cluster formation is comparable, ranging from 0.39 Myr for the 10^5 $M_\odot$ cloud to 0.59 Myr at 10^4 $M_\odot$. The clusters then rapidly grow in mass via gas accretion with the higher mass clouds containing more mass in clusters at any given time, as expected. At 5 Myr, the total mass contained in clusters, in order of lowest to highest initial cloud mass, is 4.1×10^3, 2.3×10^4, 2.3×10^4, 1.8×10^5, and 2.8×10^5 $M_\odot$. Note that the total cluster mass does not scale directly with the initial cloud mass. This will be relevant to the discussion of formation efficiencies which follows.

The number of clusters formed also does not scale directly with the initial cloud mass. The numbers of clusters at 5 Myr in the 10^4, 10^5, and 10^6 $M_\odot$ simulations are 11, 22, and 199, respectively. Note that we allow our clusters to merge so the number of clusters can decrease. Since mass is conserved in the merger, however, the total mass in clusters cannot decrease unless a cluster leaves the simulation volume

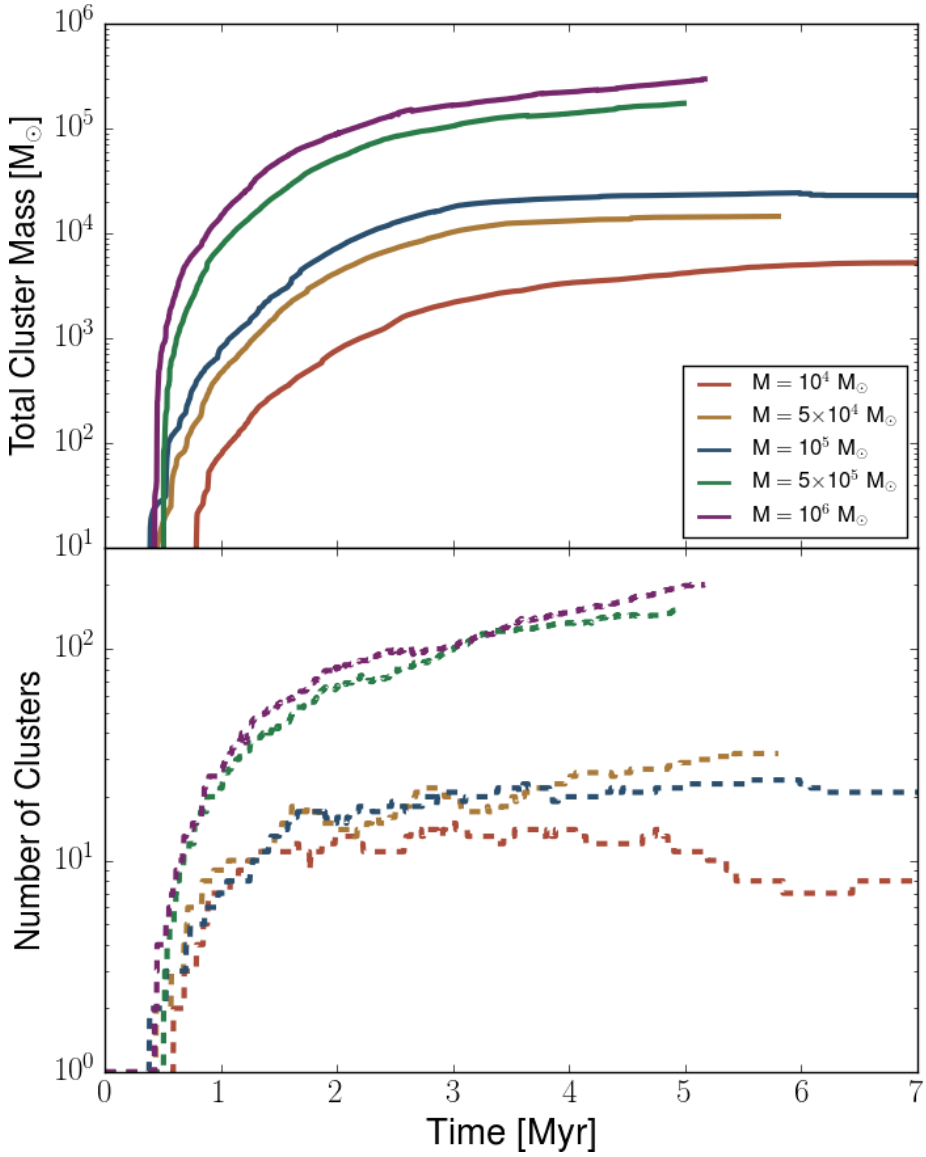

Figure 3.3: The total mass contained in clusters (top) and the total number of clusters (bottom) in our five GMC models including radiative feedback. Note that the total mass contained in clusters can decrease over time due to clusters leaving the simulation volume, and the number of clusters can decrease both through escaping clusters and merging events.

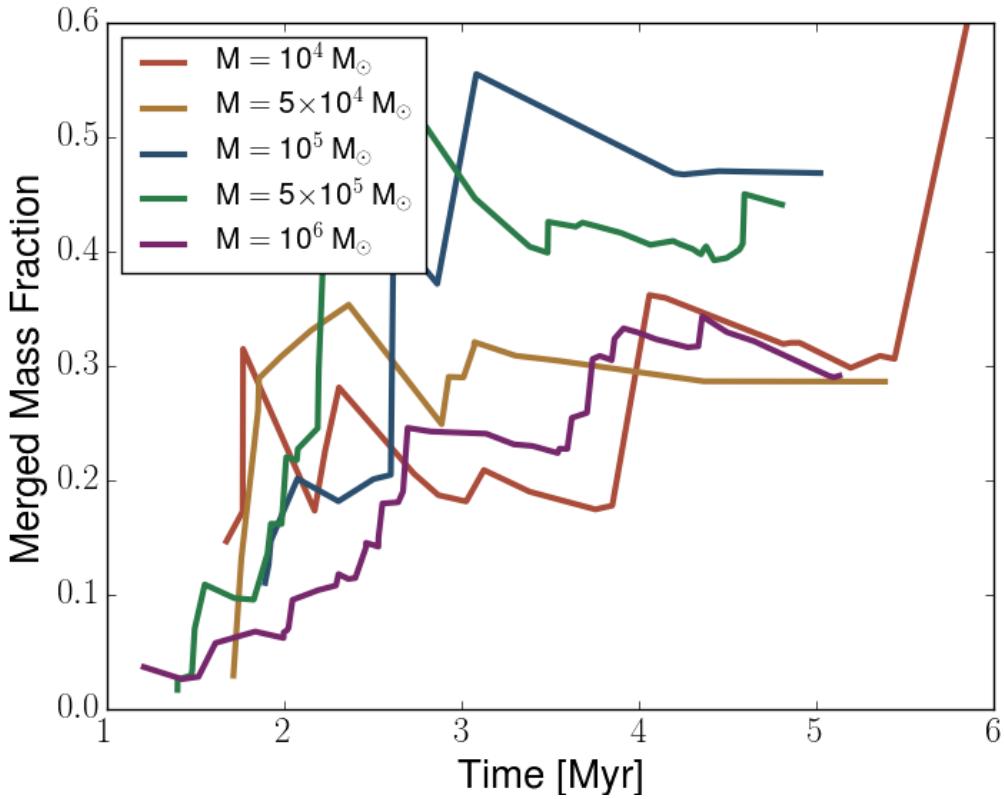

Figure 3.4: The merged mass fraction, defined as the total cluster mass that has participated in at least one merging event divided by the total mass contained in all clusters, versus time for the 5 GMCs including radiative feedback.

entirely which does not play a significant role. Only the 5×10^5 $M_\odot$ and 10^6 $M_\odot$ GMCs are still forming clusters in significant numbers at the end of the simulation.

Cluster merging plays a significant role in the growth of clusters. We demonstrate this in Figure 3.4 which plots the merged mass fraction versus time. We define the merged mass fraction as total amount of cluster mass that has participated in a merger event up until a given time divided by the total mass contained in clusters

at that same time. A merged mass fraction of 0.5, for example, means that half of the mass contained in clusters has participated in at least one merger.

While there does not appear to be a trend with GMC mass, it is clear that significant numbers of mergers are occurring in all clouds. At $\sim$5 Myr, the merged mass fractions range from 0.28 to 0.47. A fraction of 0.28 indicates that cluster growth is dominated by gas accretion while a fraction of 0.47 represents comparable contributions from gas accretion and cluster mergers. This highlights the importance of cluster merging during the early phases of star formation and suggests that a combination of both gravitational fragmentation (ie. top down cluster formation) and hierarchical merging (ie. bottom up cluster formation) are needed to fully understand the formation and evolution of young stellar clusters.

Lastly, we compare the star formation rates (SFR) in our GMC models in Figure 3.5. Note that this refers to the formation of stars *within* the clusters and not the formation of new clusters.

As a product of our star formation subgrid model which samples the IMF to form new stars at prescribed intervals, there are timesteps in which no new stars formed and others which have a burst of star formation. We have therefore smoothed these plots using a sliding average window to assist in readability. This leads to a highly variable SFR, particularly at late times when there are many clusters forming stars at staggered times.

All curves show a sharp rise in SFR following the onset of cluster formation. For the 10^4, 5×10^5, and 10^6 $M_\odot$ GMCs, the SFR levels out to approximately constant

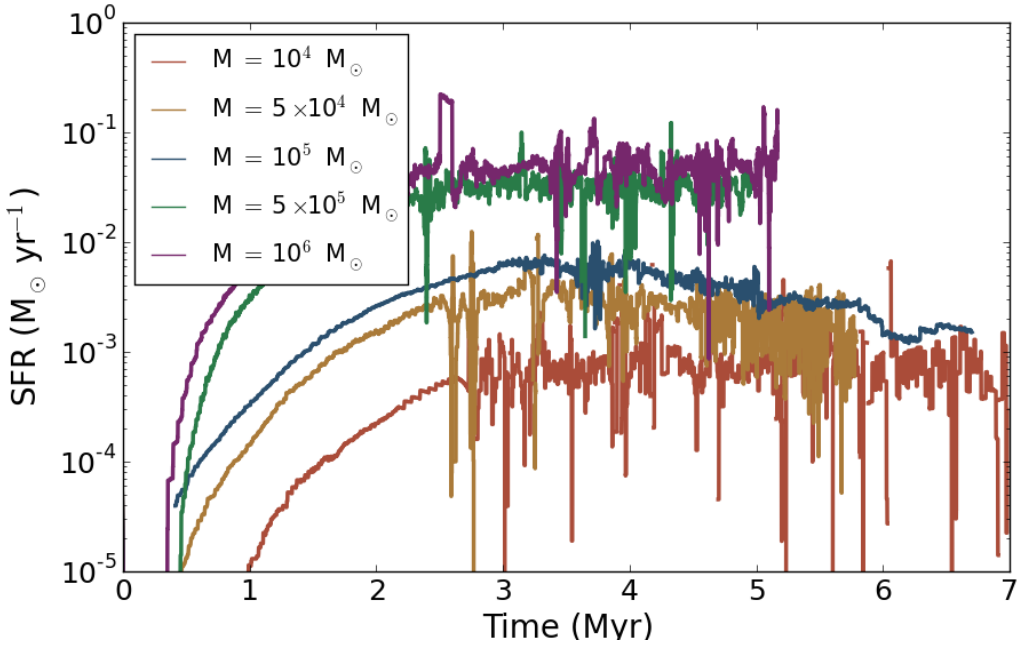

Figure 3.5: The total star formation rates (SFRs) for the 5 simulated GMCs which include radiative feedback. Note that this plot has been smoothed for readability (see text).

values of 6×10^{-4}, 3×10^{-2}, and 5×10^{-2} respectively. These values are consistent with a SFR that scales directly with the initial GMC mass, assuming similar density structures, as found in observations of local GMCs by Lada et al. (2010).

The other two GMC models (5×10^4 and 10^5 $M_\odot$) instead show a SFR rate which decreases at late times. As shown in Howard et al. (2014), which examined the properties of our adopted subgrid model for star formation, a decreasing SFR is indicative of a population of clusters which have completely stopped accreting and are simply using up the rest of their gaseous reservoir. The images for the 10^5 $M_\odot$ GMC in Figures 3.1 and 3.2 are consistent with this picture since they demonstrate that the cloud has been almost fully ionized and destroyed by 5 Myr. This suggests the

impact radiative feedback has on the formation and evolution of clusters is stronger in these clouds. We compare the effects of radiative feedback between cloud models below.

3.4.2 The role of radiative feedback

To understand the role of radiative feedback in GMCs with different initial masses, we computed a grid of complementary simulations which have radiative transfer turned off. We will refer to simulations with radiative feedback included as "RHD" (Radiation Hydrodynamics) simulations and "HD" (Hydrodynamics) simulations are those with radiative feedback not included.

How much the efficiency is suppressed when including radiative feedback is still debated. Howard et al. (2016) showed that it depends on the initial gravitational boundedness of the molecular cloud, as measured by the virial parameter. Here, we find that radiative feedback does indeed limit star cluster formation but, more importantly, the strength of this suppression depends on the cloud's initial mass.

We show this in Figure 3.6, which plots the cluster particle formation efficiency (ϵ_{cl}) and the star formation efficiency (ϵ_*) for both the RHD simulations, shown by the solid lines, and the HD simulations, shown by the dashed lines. We define ϵ_{cl} as the total mass in cluster particles divided by the initial cloud mass. The star formation efficiency, ϵ_*, is defined as the total mass of stars within the clusters divided by the initial cloud mass. Note that an entire cluster's mass is not necessarily only

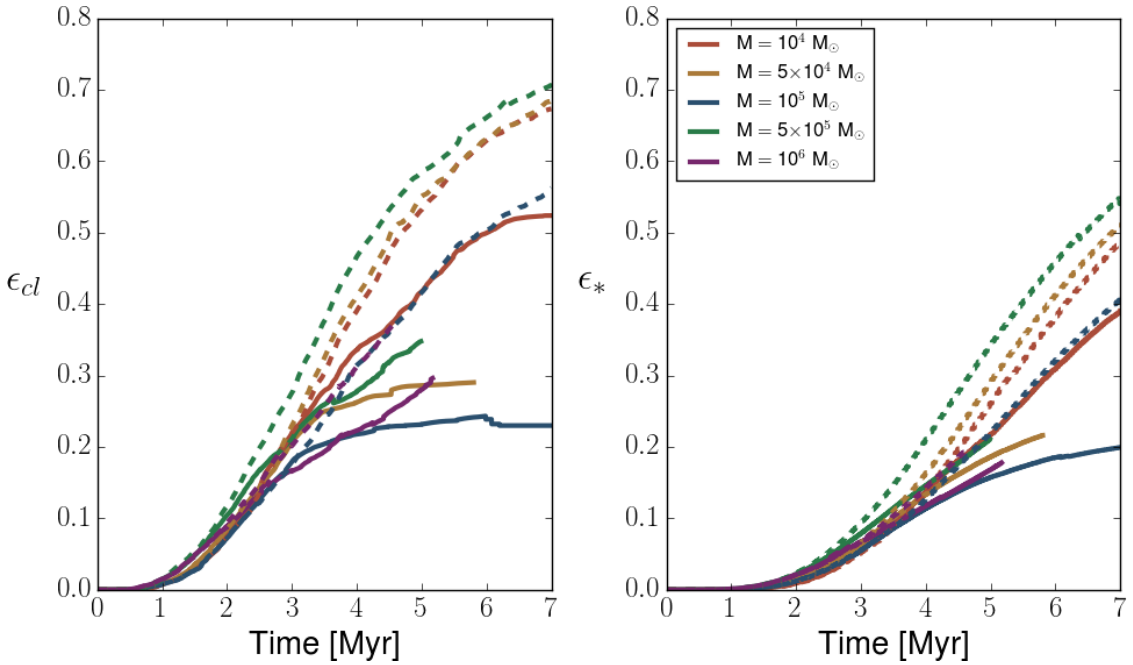

Figure 3.6: Left: The cluster particle formation efficiency (ϵ_{cl}, defined as the total mass in cluster particles divided by the GMC's initial mass) for our 5 RHD simulations (shown by solid lines) and the 5 HD simulations (shown by dashed lines). Right: Identical to the left panel except the star formation efficiency (ϵ_*, total mass of stars within clusters divided by the initial GMC mass) is plotted.

in stars, but can also be part of the gas reservoir which is available for future star formation.

When comparing the RHD and HD simulations, we see that star and cluster formation start at similar times and evolve identically for ∼2.5 Myr. At this point, ϵ_{cl} in the HD and corresponding RHD runs begin to diverge, with the HD simulations having the higher efficiency in all cases. This trend continues to the end of the simulation and the difference between the HD and RHD formation efficiencies grows. Choosing a time of 5 Myr to compare ϵ_{cl}, the efficiencies in the lowest to highest mass clouds are 43%, 29%, 23%, 35%, and 28%. At the same time, ϵ_* ranges from

16% to 21%. Note that these values are higher than the measured values from GMC observations (eg. Lada & Lada (2003); McKee & Ostriker (2007); Murray (2011)) which suggests that while radiative feedback does lower ϵ_* relative to HD runs, other pieces of physics such as stellar winds are required to lower these values further.

Both ϵ_{cl} and ϵ_* are the highest for the lowest mass (10^4 $M_\odot$) GMC. This is consistent with the results from Ochsendorf et al. (2017) who found evidence of a decreasing ϵ_* with increasing cloud mass in the LMC. While we reproduce their results for the 10^4 $M_\odot$ cloud, we do not see clear evidence for a trend with increasing GMC mass.

It is clear from Figure 3.6 that radiative feedback plays a stronger role in suppressing star and cluster formation in some clouds more than others. To make this clear, we plot the fractional reduction in efficiencies when including radiative feedback in Figure 3.7. This Figure shows that difference in formation efficiencies is largest for the 5×10^4 and 10^5 $M_\odot$ GMCs. Focusing on these two simulations at 5 Myr, the difference between ϵ_{cl} for the HD and RHD run is 27% and 18% for initial masses of 5×10^4 and 10^5 $M_\odot$ GMCs, respectively. This corresponds to approximately a factor of two reduction in both cases. The inclusion of radiative feedback in the 10^4, 5×10^5, and 10^6 $M_\odot$ GMCs reduced ϵ_{cl} by 21%, 40%, and 33% relative to the HD simulations, respectively.

This is consistent with the density and temperature visualizations discussed in Figures 3.1 and 3.2. It was clear from those images that the 10^5 $M_\odot$ simulation is more globally impacted by radiative feedback than the other two cases, as evidenced

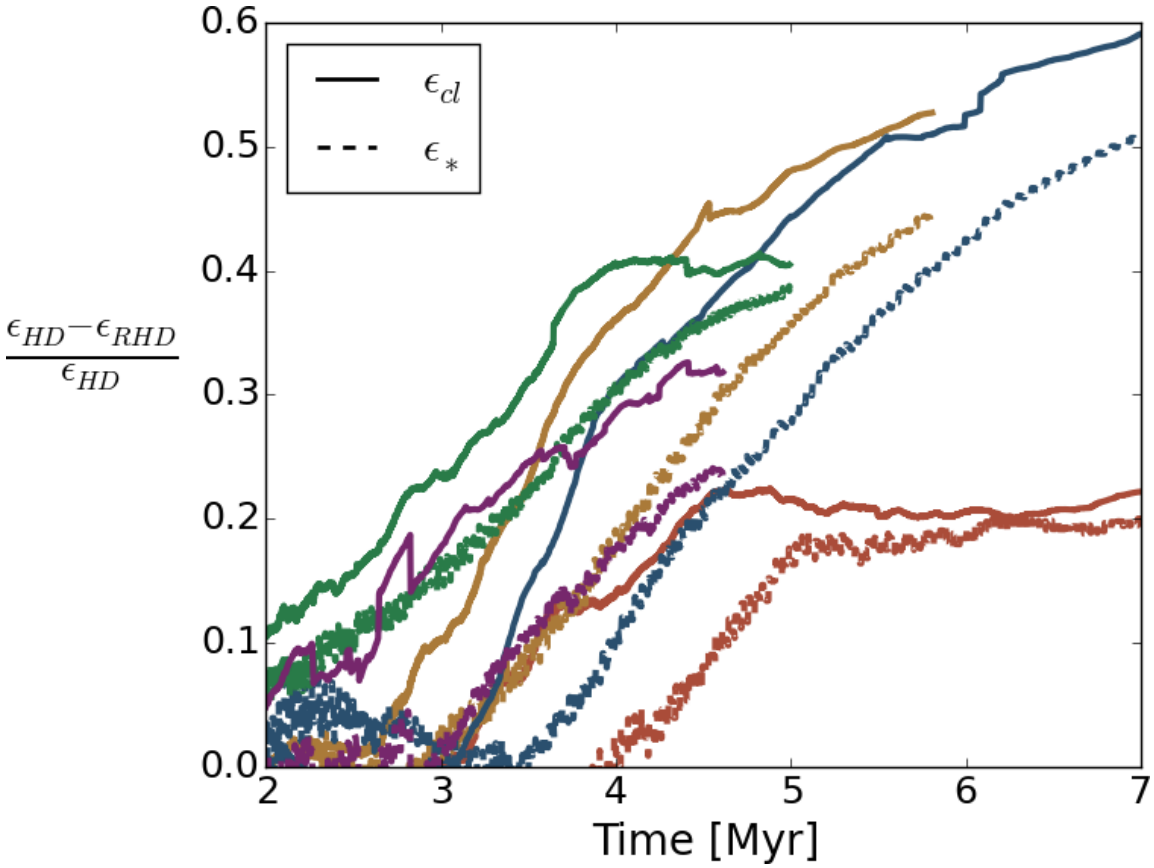

Figure 3.7: The fractional reduction of ϵ_{cl} (left) and ϵ_* (right) when including radiative feedback into a simulation, relative the HD formation efficiencies.

by the nearly fully ionized simulation volume. In contrast, the 10^4 and 10^6 $M_\odot$ GMCs showed small HII regions which may stop the accretion onto local clusters but not the entire population.

These results suggest there is something unique happening in clouds between $5{\times}10^4$ - 10^5 $M_\odot$ which make them more susceptible to radiative feedback effects. We propose that clouds lower than this mass are not able to form enough massive stars and therefore cannot completely ionize the cloud. Indeed, the 10^4 $M_\odot$ GMC did

not produce any O-stars throughout its evolution. On the other hand, clouds above this mass range are capable of producing O-stars but have too much gas mass, and therefore a higher column density to ionizing radiation, to be fully ionized during the early stages of cluster formation. The overall gravitational potential of these massive clouds is also deeper, meaning they are harder to unbind overall.

We can demonstrate this balance between gravity and the energy injected by radiative feedback by comparing the total gravitational potential energy to the total internal energy of the gas at any given time. The internal energy is calculated from the gas temperature and ionization fraction and is therefore a proxy for the energy injected by radiation. We plot the ratio of the total internal energy to the total gravitational potential energy in Figure 3.8.

All models start with a ratio less than 1, indicating that gravitational potential energy dominates during early times. At approximately 3.5 and 3.8 Myr, the ratio rises above one for the 10^5 $M_\odot$ and 5×10^4 GMCs, respectively. This indicates that the amount of radiation being injected into the gas is sufficient to unbind the cloud globally, resulting in the larger suppression of cluster formation under the influence of radiative feedback in these clouds. While internal energy does dominate over gravitational potential energy for the 10^4 $M_\odot$ GMC, it only does so at late times and therefore does not influence the early stages of cluster formation as significantly. In contrast, the more massive models (5×10^5 and 10^6 $M_\odot$) are always dominated by gravitational potential energy.

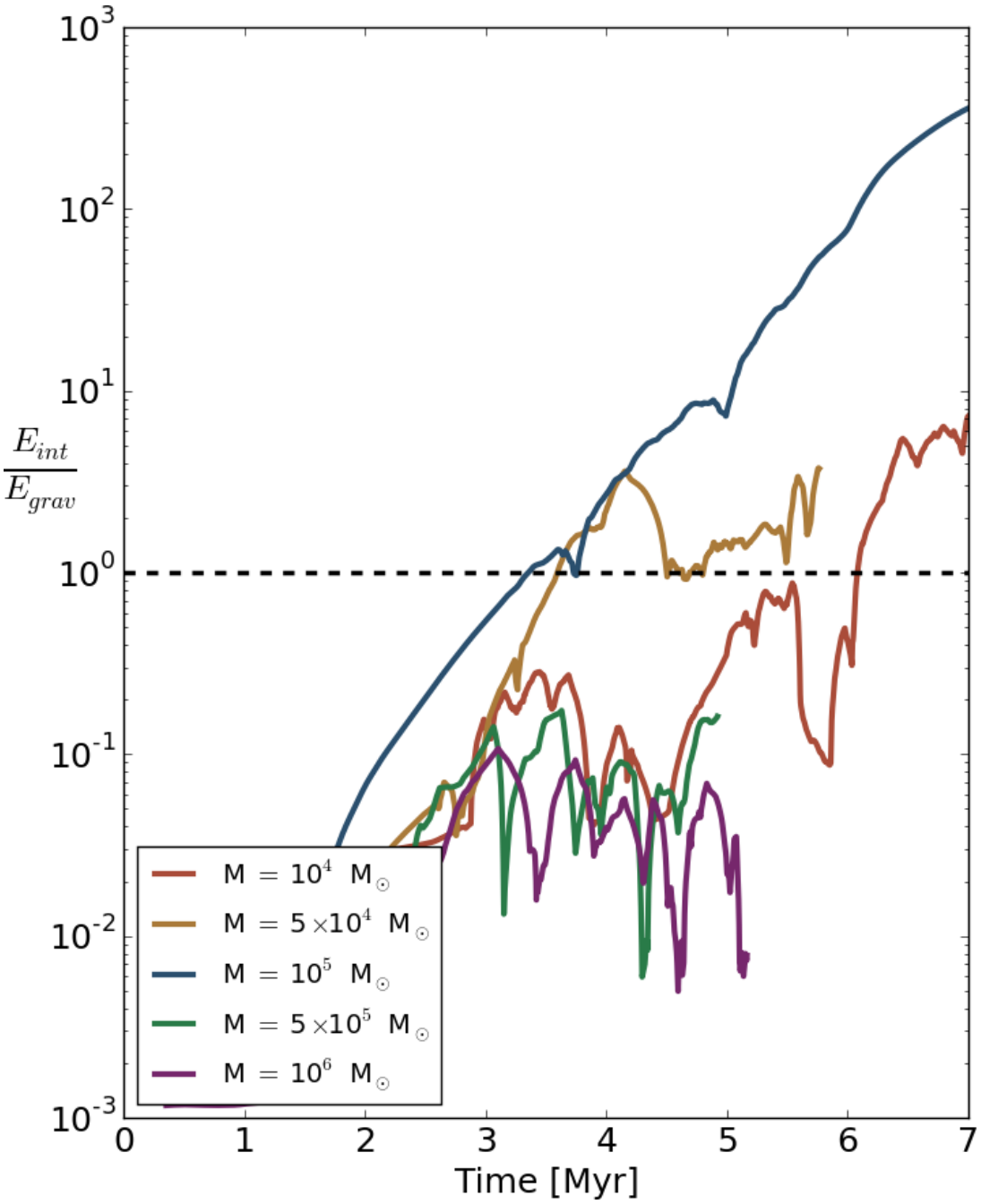

Figure 3.8: The ratio between the total internal energy of the gas to the global gravitational potential energy of the cloud. A lower ratio suggests a higher suppression of cluster and star formation.

These results explain why, in Figure 3.6, ϵ_{cl} begins to flatten around 3 Myr for the 5×10^4 and 10^5 $M_\odot$ clouds. As a larger volume of gas becomes hot and ionized, the formation of new clusters, and the accretion onto existing clusters, is suppressed. A similar result is not seen for ϵ_* due to our subgrid model. Since we do not allow unused gas to leave the clusters, star formation can proceed regardless of whether accretion is still taking place. As shown in Howard et al. (2014), cluster masses are typically dominated by the reservoir of gas, especially at early times.

The varying strength of radiative feedback may have important implications for the growth and evolution of GMCs if we assume they form through a bottom up process, such as spiral arm induced collisions, as suggested by Dobbs & Pringle (2013). Our results indicate that once a cloud reaches $\sim5\times10^4$ $M_\odot$, it should be destroyed via radiative feedback. This may act as a bottleneck for the growth of GMCs and could be partly responsible for their observed mass distribution.

The cluster formation efficiency is essentially a normalized measure of how much mass is present in clusters at any given time. To understand how this mass is distributed, we also need to know the total number of clusters. We examine how the number of clusters is affected by radiative feedback in Figure 3.9. This is similar to the plot shown in the previous section, except the results from the HD simulations are included as dashed lines. We see that the early evolution of the RHD and HD simulations are similar, but at late times there are more clusters present in the RHD cases. This will impact the distribution of cluster masses. Since the HD simulations have more mass contained in clusters (as illustrated in Figure 3.6) but fewer clusters overall, the average cluster mass will be higher than cases which include radiative

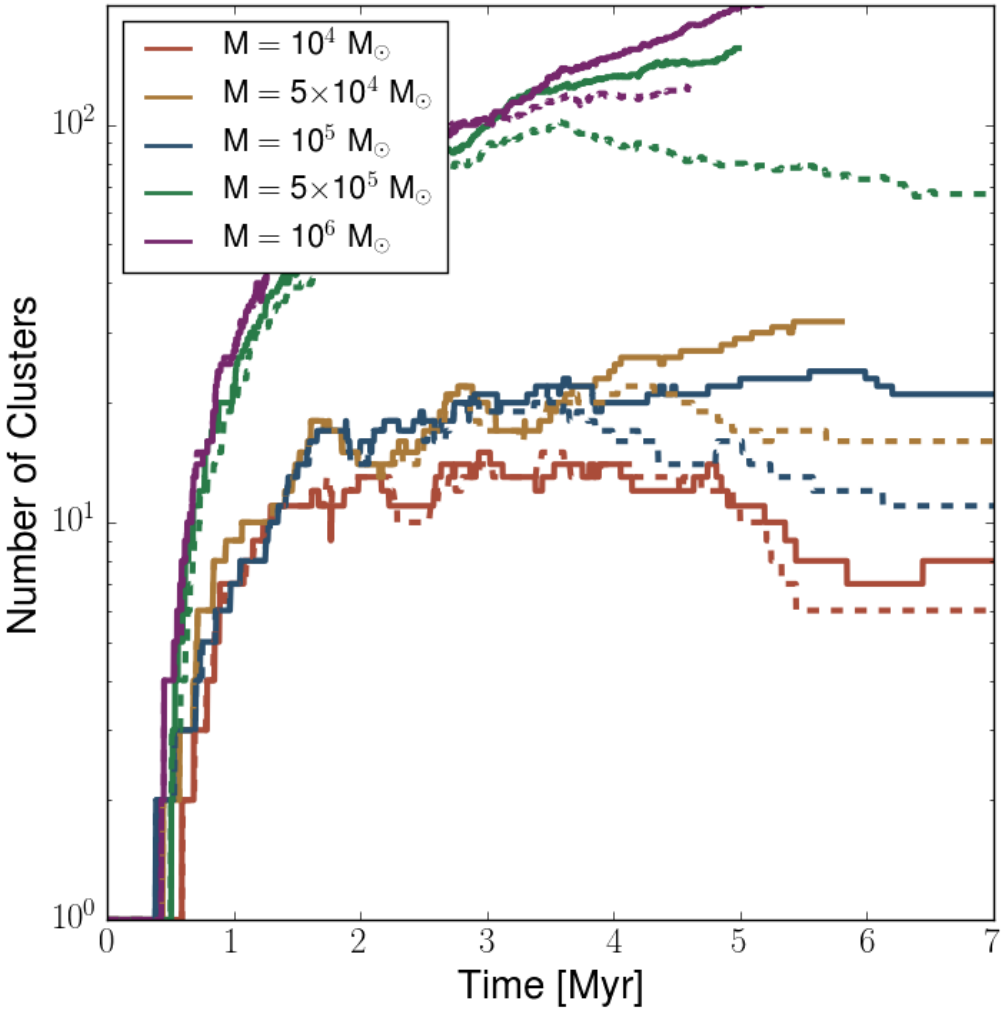

Figure 3.9: The number of clusters as a function of time (as seen in Figure 3.3) including both RHD (solid) and HD (dashed) simulations.

feedback. Taking, for example, the 5×10^4 $M_\odot$ cloud, the final average cluster mass is decreased from 2046 $M_\odot$ to 468 $M_\odot$ when including radiative feedback.

3.5 Observational Comparisons

3.5.1 The Initial Cluster Mass Function

The mass function of star clusters has been characterized observationally. As discussed in Fall & Chandar (2012), the mass function for embedded clusters (Lada & Lada, 2003) and extragalactic clusters taken from the Magellanic Clouds, M83, M51, and Antennae are all consistent with a powerlaw mass distribution of the form dlog(N) $\propto$ M^βdlog(m) where β $\sim$-1. Here, we compare the mass functions of our simulated clusters to these results.

The cluster mass functions for the 10^4, 10^5, 10^6 $M_\odot$ GMCs are shown in Figure 3.10. The data is plotted at 5 Myr, corresponding to the approximate end of the 10^6 $M_\odot$ simulation. The mass values represent only the *stellar* mass contained in each cluster and therefore do not include the unused gas reservoir.

As the initial mass of the GMC increases, the total number of clusters formed also increases (see Figure 3.3) and so the plot is consequently more populated. The cluster mass distributions also shift to higher masses as the initial GMC mass increases.

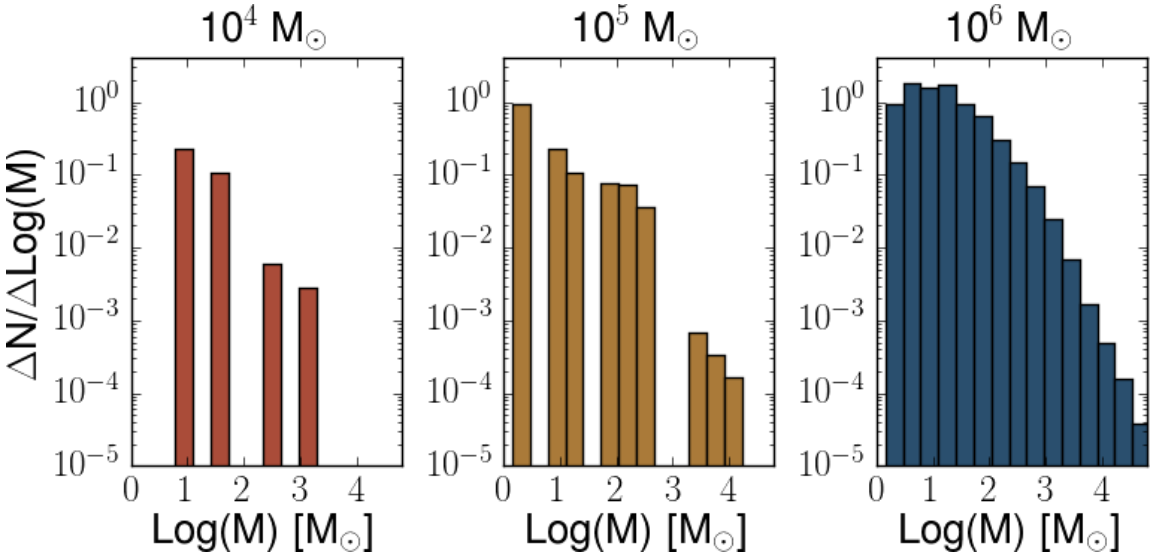

Figure 3.10: The cluster mass function for the 10^4 (left), 10^5 (center), 10^6 (right) $M_\odot$ GMCs, plotted at 5 Myr.

3.5.2 Cloud Mass - Maximum Cluster mass Relation

The previous results suggest a relation between the maximum mass cluster produced in a star-forming event and the mass of the GMC out of which it forms. This relation has been found in both observations (Hughes et al., 2013) and simulations (Fujii & Portegies Zwart, 2015) to take the form $M_{c,max} \propto M_{GMC}^{0.5}$, where $M_{c,max}$ is the maximum mass cluster that forms out of a GMC of mass M_{GMC}.

We plot the maximum cluster mass obtained from our 5 RHD GMC models in Figure 3.11, shown by the filled circles. We plot the relation at two times — 3 Myr (gold) and 5 Myr (black). Here, the maximum cluster mass includes only its stellar mass and not the unused reservoir of gas.

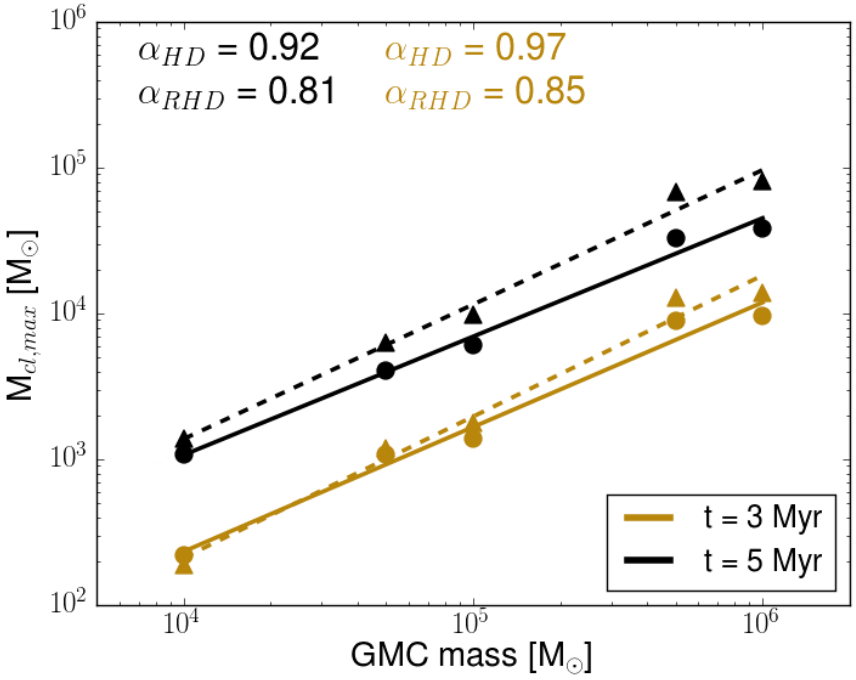

Figure 3.11: The maximum mass cluster produced in our 5 RHD models (circles) and the 5 HD simulations (triangles) as a function of the initial cloud mass. The results are plotted at 3 Myr (gold) and 5 Myr (black). The slope of the distributions are shown at the top of the plot and are colored based on the times they represent. Fits to the HD data are shown by the dashed lines, and fits to the RHD data are shown by solid lines.

At 5 Myr, we find a relation between the maximum cluster mass and the host GMC mass given by,

$$M_{c,max} \propto M_{GMC}^{0.81\pm0.09}. \tag{3.3}$$

While this does not agree with the relation above, it is roughly consistent with the relation between the maximum mass star formed in a given cluster proposed by observations from Pflamm-Altenburg et al. (2007) and the theoretical model of

Elmegreen (2002) that have powerlaw indices of 0.67 and 0.74, respectively. This seems to suggest that there may be self-similar star formation processes ranging from GMC masses down to protostellar core masses. In order to verify this claim, a fully consistent simulation of a GMC which resolves the formation of individual stars, in combination with a cluster finding algorithm, would be required.

Using the HD simulations at 5 Myr instead, we find a steeper slope of 0.93 and all points are higher than their RHD counterparts. Radiative feedback is clearly limiting the growth of the most massive clusters regardless of initial GMC mass. The separation between the HD and RHD maximum cluster masses is, however, more pronounced for the larger GMCs. This is likely due to the large population of massive stars in these clusters that can more effectively heat and ionize their surroundings and suppress further gas accretion.

Figure 3.11 shows that the slope of these distributions hardly vary with time. At 3 Myr, the slopes of the RHD and HD simulation are 0.85 and 0.97 (compared to 0.81 and 0.92 at 5 Myr), respectively. The intercept, however, does change from 3 to 5 Myr due to the growth of the stellar populations in these clusters. The separation between the HD and RHD clusters is also less pronounced compared to 5 Myr because radiative feedback has not been active for as long.

The insensitivity of the slope with time is likely due to two reasons. Firstly, we are plotting the clusters with the largest stellar content and therefore the highest luminosity. For the RHD simulations, these clusters significant affect their local surroundings and suppress their own growth in similar ways. Secondly, our subgrid

model for star formation prescribes the rate at which stars form in the clusters. Once the most massive clusters accrete a significant amount of gas, the total stellar mass will increase at the same rate.

We can estimate the mass of the host GMCs out of which Globular Clusters (GCs) ought to form by extrapolating our relation to larger cluster masses. We note that we have not yet completed any GMC simulations greater than 10^6 $M_\odot$ and, as shown in this work, the effects of radiative feedback are a clear function of cloud mass. It is therefore possible that the relation displayed in Figure 3.11 does not extend to higher masses. Assuming it does, a GMC of $\sim 4.5 \times 10^7$ $M_\odot$ is required in order to form a GC of mass 10^6 $M_\odot$. This is consistent with Harris & Pudritz (1994) who argued that Supergiant molecular clouds ($>10^7$ $M_\odot$) are the hosts to GC formation.

3.5.3 Combined Cluster Mass Function

To make an accurate comparison with the observed cluster mass function, we need to consider the relative number of GMCs with different mass. The powerlaw index for the GMC mass distribution in the inner Milky Way is approximately -1.5 (Sanders et al., 1985; Solomon et al., 1987; Rosolowsky, 2005). Taking the GMC mass distribution to be

$$\frac{dN}{dM} \propto M^{-1.5} \tag{3.4}$$

in the range 10^4 - 10^6 $M_\odot$, we combine the cluster data from our 5 RHD GMCs at 5 Myr, weighted by the relative numbers of the clouds in which they were born

In Figure 3.12 we show the resulting, computed cluster mass function that arises from the Milky Way cloud mass function. This can then be compared to the observed mass distribution which is a collection of distinct clusters in forming in different regions. Note that we only include the stellar mass of each cluster when producing this distribution. The Figure shows that the cluster mass function peaks at $\sim$10 $M_\odot$ corresponding to a small stellar group. The peak cluster mass is on the same order of magnitude as the 50 $M_\odot$ turnover found in Lada & Lada (2003).

We make a further comparison to the results of Lada & Lada (2003) who measured the embedded cluster mass function of nearby star-forming regions and found $dlog(N)/dlog(M) \propto M^\beta$, where $\beta \sim$ -1. The cluster mass function has been measured for extragalactic clusters (see Fall & Chandar (2012) for comprehensive overview) and the same functional form is also found which, in some galaxies, extends to $>10^5$ $M_\odot$ clusters. Embedded clusters of this mass are not seen in the MW.

Motivated by the observational data and a cluster mass function which appears consistent with a broken powerlaw, we provide two fits to our data — one covering the range of observed, embedded clusters in the MW (solid line), and one for the higher mass clusters (dashed line). We only include cluster masses greater than 10 $M_\odot$ in the calculation.

Fitting over the range of embedded clusters in the MW — $1 \leq \log(M/M_\odot) \leq 3.3$ (Lada & Lada, 2003) — results in a slope of β = -0.99 $\pm$ 0.14. This is consistent

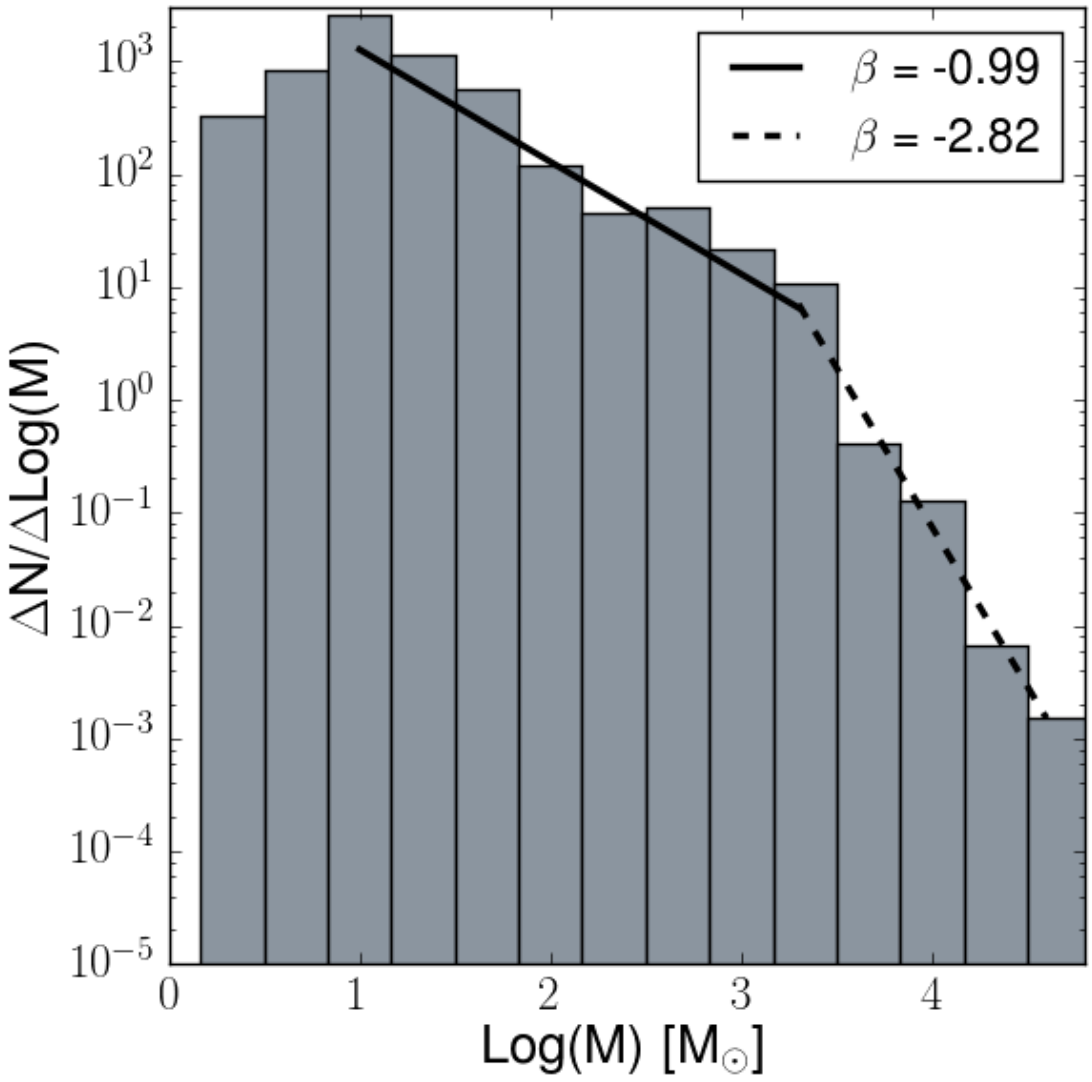

Figure 3.12: The combined cluster mass function obtained from all 5 RHD simulations. The relative abundance of each parent cloud has been included via the GMC mass function in order to compare directly to observations. Fits to the mass range of observed embedded clusters (solid) and the high mass regime (dashed) are also included.

with the observed slope. Performing the same analysis for the HD simulations, we find a slope of -0.83 that is significantly shallower than observed. This clearly shows that radiative feedback is playing some role in limiting the growth of clusters since there are a relatively larger amount of high mass clusters in the HD simulations.

A slope of β = -2.82 is found for cluster masses greater than $\sim$2000 $M_\odot$. One reason for the steeper slope at high masses is that the largest GMCs — the source of the most massive clusters — are not disrupted at the end of the 5 Myr simulation. This suggests that these clusters will continue to grow and accrete gas, leading to more clusters populating the high mass end of the distribution.

3.5.4 Star Formation Rates

We plot the SFRs of our individual clusters versus the cluster mass at various times in Figure 3.13. We only show the 10^4, 10^5 and 10^6 $M_\odot$ for clarity.

We have over plotted the results from Lada (2010), shown by black squares, who measured the SFRs of local star forming regions by counting Young Stellar Objects (YSOs) and adopting a star formation timescale to estimate the SFR. In order to make an accurate comparison to these results, we adopt the same model parameters as Lada (2010) and estimate the SFR via recently formed stars. We direct the reader to Howard et al. (2016) which plotted the SFRs in the same way and contains more detail about this procedure. We also include the results from Heiderman et al. (2010) who also measured the SFRs of local regions, some of which are also included in the Lada (2010) dataset.

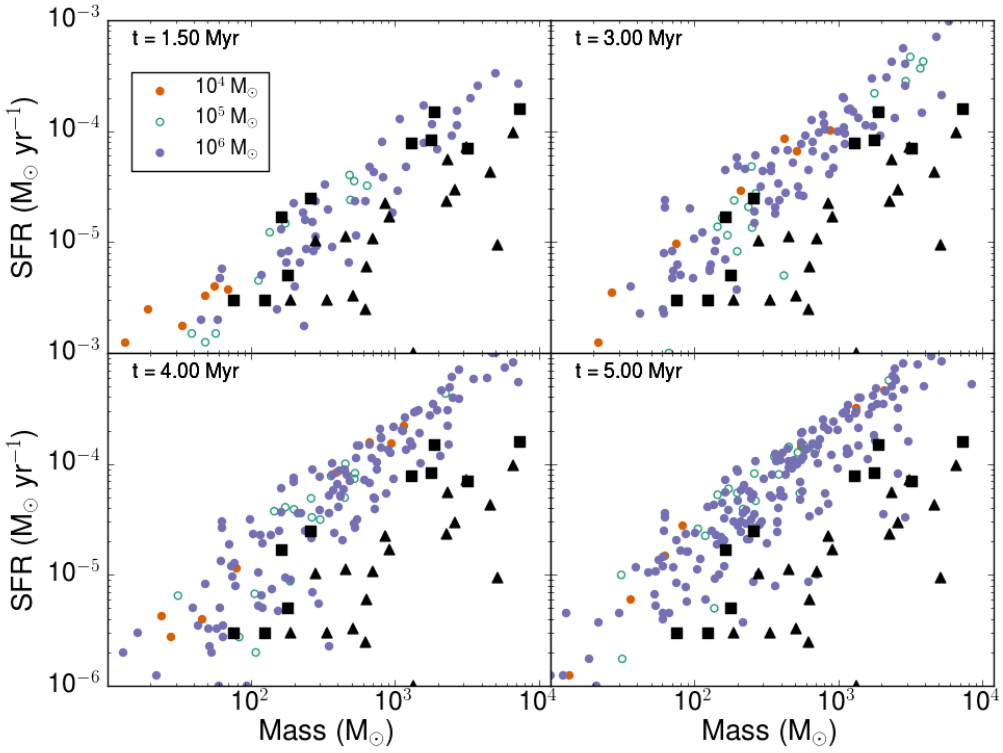

Figure 3.13: The SFR of individual cluster particles at various times for the 10^4, 10^5, and 10^6 $M_\odot$ GMCs. The squares are the observational results from Lada (2010) and the black triangles are a similar data set from Heiderman et al. (2010).

Our simulated SFRs agree well with the observed values at early times, particularly with the Lada (2010) results. At 3 Myr, the low to intermediate mass clusters are still consistent with the measured SFRs, but the high mass clusters are overproducing stars. This is strong evidence that radiative feedback alone is not sufficient for limiting the SFR (and therefore the SFE) since these high mass clusters have the highest ionizing luminosity and should be influencing their surroundings the strongest.

The trend of high SFRs extends to all mass regimes past 4 Myr. While the slope of the SFR-mass relation is consistent with the observations, the normalization is not. This is also true for the 10^5 $M_\odot$ GMC which, as shown in Section 3.4.2, had a large reduction in ϵ_{cl} when including radiative feedback and a globally decreasing SFR at late times. This also supports the claim that other feedback mechanisms, such as stellar winds, are required to explain the SFRs of young, nearby star-forming regions (Gatto et al., 2017).

We note that high SFRs may also be due, in part, to our adopted subgrid model for star formation. We do not include feedback on scales smaller than our cluster particles, and so any accreted gas will inevitably be converted to stars over a long enough timescale. We refer the reader to Section 2.1 of Howard et al. (2016) for a detailed discussion of this point.

If our cluster SFRs are artificially high, the total luminosity will also be too high. This means that the impact radiative feedback has on each cloud, as discussed above, should be considered an upper limit. This lends further support for the need of other feedback mechanisms during the early phases of cluster formation since the maximum suppression of ϵ_{cl} relative to HD simulations was approximately a factor of two.

3.6 Discussion and Conclusions

We examine the early phases of cluster formation and the role of radiative feedback in a suite of GMCs that have masses in the range of 10^{4-6} $M_\odot$. To isolate

the role of GMC mass, we use the same initial density and virial parameter across clouds. Sink particles are used to represent the formation of a cluster and a custom subgrid model is used for star formation within the clusters. The properties of the stellar population in each cluster is tracked and, combined with a raytracing radiative transfer scheme, is used to compute the radiative feedback.

The main result of this work is that the strength of radiative feedback depends on the initial GMC mass. The fractional reduction in the cluster formation efficiency, ϵ_{cl}, when including radiative feedback is the largest for the 5×10^4 and 10^5 $M_\odot$ GMCs. Both of these models had ϵ_{cl} reduced by a factor of $\sim$2 relative to purely hydrodynamical simulations. The star formation efficiency in these clouds was reduced by 30-40%. In contrast, the lowest mass model (10^4 $M_\odot$) showed a only $\sim$20% reduction in ϵ_{cl}.

The variation in the impact radiative feedback has on the cluster and star formation efficiencies is attributed to the balance between how much radiation energy is absorbed by the GMC and the gravitational potential energy of the cloud. The smallest GMC is not massive enough to form a population of massive stars and therefore cannot effectively limit early star and cluster formation. The highest mass objects, on the other hand, do produce massive stars but their corresponding gravitational potential is too large for the cloud to be globally unbound. The regime between these two limits (5×10^4 to 10^5 $M_\odot$) balances these two effects, leading to a larger suppression in ϵ_{cl} and ϵ_*. We have shown this by plotting the ratio of the internal energy, a proxy for the amount of absorbed radiation energy injected by the star-forming clusters, to the gravitational potential energy of the cloud. This ratio

exceeds one, indicating the cloud has been globally unbound, for the 5×10^4 and 10^5 $M_\odot$ clouds at 3.5 and 3.8 Myr. respectively. The higher mass GMCs always have a ratio below 1, indicating that gravity dominates, and the ratio for the 10^4 $M_\odot$ only exceeds 1 at late times at which point the majority of star and cluster formation has already occurred.

The other important conclusions of this work can be summarized as follows:

- The cluster formation efficiency (ϵ_{cl}) and the star formation efficiency (ϵ_*) vary significantly across different mass GMCs. At 5 Myr, ϵ_{cl} is 43%, 29%, 23%, 35%, and 28% for the 10^4, 5×10^4, 10^5, 5×10^5, and 10^6 $M_\odot$ GMCs, respectively. At the same time, ϵ_* ranges from 16%-21%.

- The high SFEs found in all models, even when including radiative feedback, suggests that other forms of feedback, such as stellar winds, are required to limit early star formation in GMCs (Gatto et al., 2017). This is further supported by the comparison between our clusters and the SFRs of local star-forming regions. We find good agreement with observed SFR-mass relation at early times, but by $\sim$3 Myr our clusters are systematically overproducing stars. The slope of our SFR-mass relation, however, is consistent with observed star-forming clusters at all times.

- We produced an initial cluster mass function by combining the results from all RHD simulations weighted by the Galactic GMC mass function. The resulting slope of the powerlaw distribution ($dlog(N)/dlog(M) \propto M^\beta$) over the range of embedded cluster masses in the MW ($\log(M/M_\odot) < 3.3$) is β = -

0.99±0.14. This is consistent with the observed slope. Performing the same analysis for the HD simulations results in a shallower slope of -0.83, indicating that radiative feedback does contribute to limiting the growth of star-forming clusters. An apparent break in the powerlaw above $\log(M/M_{\odot}) = 3.3$ is attributed to the 5 Myr timescale of our simulations. The most massive GMCs are not yet disrupted and, given more time, will fill out the high mass end of the distribution.

- The limiting of cluster growth by radiative feedback is also supported by the relation between the host GMC mass (M_{GMC}) and the maximum mass cluster it forms ($M_{c,max}$). Using the RHD data, we find that $M_{c,max} \propto M_{GMC}^{0.81}$. The HD simulations always form higher mass clusters and the relation is instead $M_{c,max} \propto M_{GMC}^{0.93}$. The steeper slope for the HD simulations indicates that the largest clusters in the highest mass GMCs are more strongly limiting their growth via radiative feedback compared to those formed in smaller clouds.

3.7 Acknowledgements

We thank the anonymous referee for useful suggestions. C.S.H. acknowledges financial support provided by the Natural Sciences and Engineering Research Council (NSERC) through a Postgraduate scholarship. R.E.P. and W.E.H. are supported by Discovery Grants from the Natural Sciences and Engineering Research Council (NSERC) of Canada. The FLASH code was in part developed by the DOE supported Alliances Center for Astrophysical Thermonuclear Flashes (ASCI) at the University

of Chicago. Computations were performed on the gpc supercomputer at the SciNet HPC Consortium. SciNet is funded by: the Canada Foundation for Innovation under the auspices of Compute Canada; the Government of Ontario; Ontario Research Fund - Research Excellence; and the University of Toronto.

Chapter 4

Ultra Violet Escape Fractions from Giant Molecular Clouds During Early Cluster Formation

4.1 Abstract

The UV photon escape fraction from molecular clouds is a key parameter for understanding the ionization of the Interstellar Medium (ISM), and extragalactic processes, such as cosmic reionization. We present the ionizing photon flux and the corresponding photon escape fraction (f_{esc}) arising as a consequence of star cluster formation in a turbulent, 10^6 $M_\odot$ GMC, simulated using the code FLASH. We make use of sink particles to represent young, star-forming clusters coupled with a radia-

tive transfer scheme to calculate the emergent UV flux. We find that the ionizing photon flux across the cloud boundary is highly variable in time and space due to the turbulent nature of the intervening gas. The escaping photon fraction remains at ∼5% for the first 2.5 Myr, followed by two pronounced peaks at 3.25 and 3.8 Myr with a maximum f_{esc} of 30% and 37%, respectively. These peaks are due to the formation of large HII regions, that expand into regions of lower density and some of which reach the cloud surface. However, these phases are short lived and f_{esc} drops sharply as the HII regions are quenched by the central cluster passing through high-density material due to the turbulent nature of the cloud. We find an average f_{esc} of 15% with factor of two variations over 1 Myr timescales. Our results suggest that assuming a single value for f_{esc} from a molecular cloud is in general a poor approximation, and that the dynamical evolution of the system leads to large temporal variation.

4.2 Introduction

The escape of UV photons from massive stars in young star clusters within molecular clouds drives many critical processes in the Interstellar and Intergalactic Medium. The radiation released by stars contributes to the Interstellar Radiation Field (ISRF) which has the highest energy densities at optical and UV wavelengths (Draine, 2011), the strength of which was first estimated by Habing (1968) to be $\sim 4\times10^{-14}$ erg cm^{-3} for 12.4 eV photons. Later authors have further characterized the

strength of the UV portion of the ISRF by including wavelength dependence (Draine, 1978; Mathis et al., 1983).

The ISRF, and its interactions with gas and dust, is responsible for determining the chemical, thermal, and ionization state of the Interstellar Medium (ISM) via photoionization, photodissociation, photoelectric heating, and absorption and re-emission by dust grains (Draine, 2011). Since most UV photons are generated by massive stars in the range 10-100 $M_{\odot}$, they contribute significantly to the strength of the ISRF and significantly alter the state of the ISM in their vicinity, even when considering their short lifetimes.

It has also become clear in recent years that UV ionizing photons from galaxies hosting Active Galactic Nuclei (AGN) are not sufficient to completely reionize the Intergalactic medium (IGM) by z=6 (Fan et al., 2006; Robertson et al., 2013). Instead, fainter dwarf galaxies, with masses as low as $\sim 10^8$ $M_{\odot}$, are needed to provide the remaining UV photons via their stellar content (Wise et al., 2014; Xu et al., 2016). These low mass galaxies may contribute up to ∼40% of the total ionizing photons required for reionization (Wise et al., 2014).

In order to contribute to reionization, ionizing photons produced in these galaxies must escape into the intergalactic medium (IGM) (Robertson et al., 2010). The exact fraction of photons, f_{esc}, which escape their host galaxies, however, is a debated topic. For bright, high redshift galaxies, measured via the Lyman continuum, f_{esc} ∼7% (Siana et al., 2015) but this number can be as high as ∼30% for fainter Lyman-α emitting galaxies (Nestor et al., 2013). Estimates of f_{esc} from the Large Magellanic

Cloud (LMC) and the Small Magellanic Cloud (SMC) based on HII region mapping suggest global escape fractions of 4% and 11% respectively (Pellegrini et al., 2012).

Simulations which attempt to quantify f_{esc} for both high and low mass galaxies have been performed, but these results often vary by orders of magnitude. For example, Paardekooper et al. (2011) found f_{esc} <1% for high redshift dwarf galaxies, while later numerical works have found f_{esc} >10% (Razoumov & Sommer-Larsen, 2010; Ferrara & Loeb, 2013; Paardekooper et al., 2015). Moreover, f_{esc} can vary by orders of magnitude over the lifetime of the galaxy (Paardekooper et al., 2011).

As illustrated by the numerical simulations in Paardekooper et al. (2011), the distribution of dense gas in star forming regions is one of the main constraints on f_{esc} from a galaxy. This suggests that detailed modeling of f_{esc} from dense regions *within* galaxies is required to fully understand the trends observed in more global simulations. Giant molecular clouds (GMC) are the densest regions of the galactic ISM, and they are the sites where all known star formation takes place. Studying the escape of UV photons from GMCs is therefore also important for a better understanding of cosmological reionization.

The GMC environment is complex, consisting of filaments produced by supersonic turbulence out of which stars, and clusters, ultimately form (Bertoldi & McKee, 1992; Lada & Lada, 2003; Mac Low & Klessen, 2004; McKee & Ostriker, 2007; André et al., 2014; Klessen & Glover, 2016). Stars which form in this environment can then alter their surroundings via the emission of radiation, producing HII regions. The complexity of this problem necessitates the use of numerical simulations. While

simulations of GMCs which include star formation and radiative transfer have been completed (Dale et al., 2005; Murray et al., 2010; Peters et al., 2010a; Krumholz et al., 2010; Bate, 2012; Klassen et al., 2012b; Walch et al., 2013), these studies do not examine the fraction of photons that escape the cloud.

In this paper, we address the critical question of UV escape fractions from turbulent molecular clouds by computing f_{esc} from 10^6 $M_\odot$ GMCs. We employ our suite of simulations which simulated star cluster formation and radiative feedback within young, 10^6 $M_\odot$ GMCs which have varying initial virial parameters (Howard et al., 2016). We model the early evolution of star clusters, defined here as less than 5 Myr, since the effects of supernovae are not included. We found that, despite producing large HII regions, the inclusion of radiative feedback only suppressed the formation of clusters by a few percent. In comparison, varying the initial virial parameter from 0.5 to 5 (ie. bound to unbound) reduced the efficiency of cluster formation by $\sim$34%. The high final star formation efficiencies (SFEs), which range from 18% to 34%, suggest that radiative feedback alone is not responsible for limiting star formation but that initially unbound clouds better reproduce locally observed GMCs.

Given that we have computed the structure and dynamics of cluster forming clouds undergoing radiative feedback, we can now address the question of what fraction of the UV photons produced by the massive stars in clusters escapes the molecular cloud.

We present maps of the ionizing photon flux escaping the cloud to demontrate its highly nonuniform nature in space. We also present f_{esc} (used hereafter to represent

the escape fraction from a GMC) during the first 4 Myr of the GMC's evolution which is shown to be highly variable in time and peaks at ∼35% with a long term average value of ∼15%. The variable nature of f_{esc} is attributed to HII regions which dramatically vary in both shape and size due to the dynamical nature of the gas and embedded clusters.

4.3 Method

Below, we provide a brief description of our numerical methods and subgrid model for star cluster formation.

We have simulated a 10^6 $M_\odot$ GMC using the Adaptive Mesh Refinement (AMR) code FLASH (Fryxell et al., 2000a) which includes self-gravity, radiative transfer, star cluster formation, and cooling processes (see Howard et al. (2016) for more detail). This cloud mass was chosen in particular because high mass GMCs contain most of the molecular mass in the Milky Way and are host to the most massive stellar clusters (Mac Low & Klessen, 2004; McKee & Ostriker, 2007; Klessen & Glover, 2016).

The cloud is initially overlaid with a turbulent velocity field which is composed of a mixture of solenoidal and compressive turbulence with a Burgers spectrum (as in Girichidis et al. (2011)). We selected a configuration with an initial virial paramater of 3, corresponding to an initial Mach number of 73. We chose this simulation in particular out of the suite presented in Howard et al. (2016) because we found that initially unbound clouds best reproduce the properties of massive GMCs in the Milky Way. The radius of the cloud is 33.8 pc. The initial average density of the GMC is

$n = 100$ cm^{-3}, with a density profile which is uniform in the inner half of the cloud and decreases as r$^{-3/2}$ in the outer half.

The package PARAMESH is used for the adaptive mesh portion of FLASH Fryxell et al. (2000a). The grid is refined at locations with sharp density or temperature contrasts to improve the resolution near filaments and HII regions. The minimum cell size in our simulation is 0.13 pc.

To model gas cooling, we employ the method from Banerjee et al. (2006) which treats cooling via molecular line emission, gas-dust interactions, H_2 dissociation, and radiative diffusion in the optically thick limit. The cooling rates from Neufeld et al. (1995) are used to treat molecular line emission, while the treatment in Goldsmith (2001) cools the gas via gas-dust transfer.

Radiative transfer is treated via a hybrid-characteristics raytracer developed by Fryxell et al. (2000b) and adapted for astrophysical use by Peters et al. (2010a). This scheme treats both ionizing and non-ionizing radiation and makes use of the DORIC package (Mellema & Lundqvist, 2002) to solve the ionization equations. While the DORIC package is capable of treating a large number of species, we consider hydrogen to be the only gas component for simplicity. The flux of ionizing photons, F_* from an individual source is given by,

$$F_* = \frac{S_*}{4\pi r^2} e^{-\tau} \tag{4.1}$$

where S_* is the cluster's ionizing photon rate in s^{-1}, r is the distance between the source and cell of interest, and τ is the intervening optical depth. The opacity to non-ionizing radiation is represented by the Planck mean opacities from Pollack et al. (1994), which are used because the raytracer has no frequency dependence. We adopt a single UV opacity in neutral gas of $\kappa = 775$ cm^2 s^{-1} from Li & Draine (2001). This opacity is scaled by the neutral fraction of the gas, so completely ionized regions have an opacity of zero.

We make use of sink particles (Federrath et al., 2010) to model star cluster formation with a custom subgrid model to represent star formation within the clusters (Howard et al., 2014). We adopt a threshold density for formation of 10^4 cm^{-3} which is based on observations of star-forming clumps (Lada & Lada, 2003). Our subgrid model within cluster sink particles (henceforth referred to as clusters), divides the cluster mass into two types; stars, and the remaining gas mass (denoted as the reservoir). We convert the reservoir to stars by randomly distributing the mass into main sequence stars via a Chabrier (2005) IMF with an efficiency of 20% per freefall time, where the freefall time is taken to be 0.36 Myr. The IMF is sampled every tenth of a freefall time to allow cluster propeties to evolve smoothly over time. Newly accreted gas is added to the reservoir (ie. gas which available for star formation during the next IMF sampling step). The masses of all stars formed in the cluster are recorded, and analytical fits provided by Tout et al. (1996) are used to determine each star's total and ionizing luminosity. The cluster's luminosity is then the sum of its consituents, which is then used by the raytracer.

In order to reduce the computational time, we apply a mass threshold of 1000 $M_\odot$ in *stars* (which typically have ∼1 O star), below which clusters do not radiate. Clusters below the threshold continue to accrete gas and form new stars but they are not included in the radiative transfer calculation.

4.4 Results

To study the spatial distribution of the escaping UV flux from the cloud, we produce maps of the ionizing flux across a spherical surface which are presented in Figure 4.1. The radius of this sphere corresponds to the intial cloud radius of 33.8 pc and all clusters are contained within the surface. The maps were made using a Hammer projection which was chosen because it is an equal area projection. We also include the locations of the 10 most luminous clusters (accounting for 93% of the final ionizing luminosity), projected to the closest location on the sphere, in white circles. Note that the clusters are not actually located on this spherical surface, but are contained within its volume.

The first panel, plotted at 1.5 Myr, shows the ionizing flux shortly after the first clusters begin to radiate. A large fraction of the surface is not receiving any ionizing photons, shown by the white patches. This is because at this time, the clusters have only recently formed (meaning that their total ionizing luminosity is low compared to their final values).

In the same panel, the regions that are receiving ionizing photons are concentrated in the upper right quadrant. Note that the most luminous clusters appear in

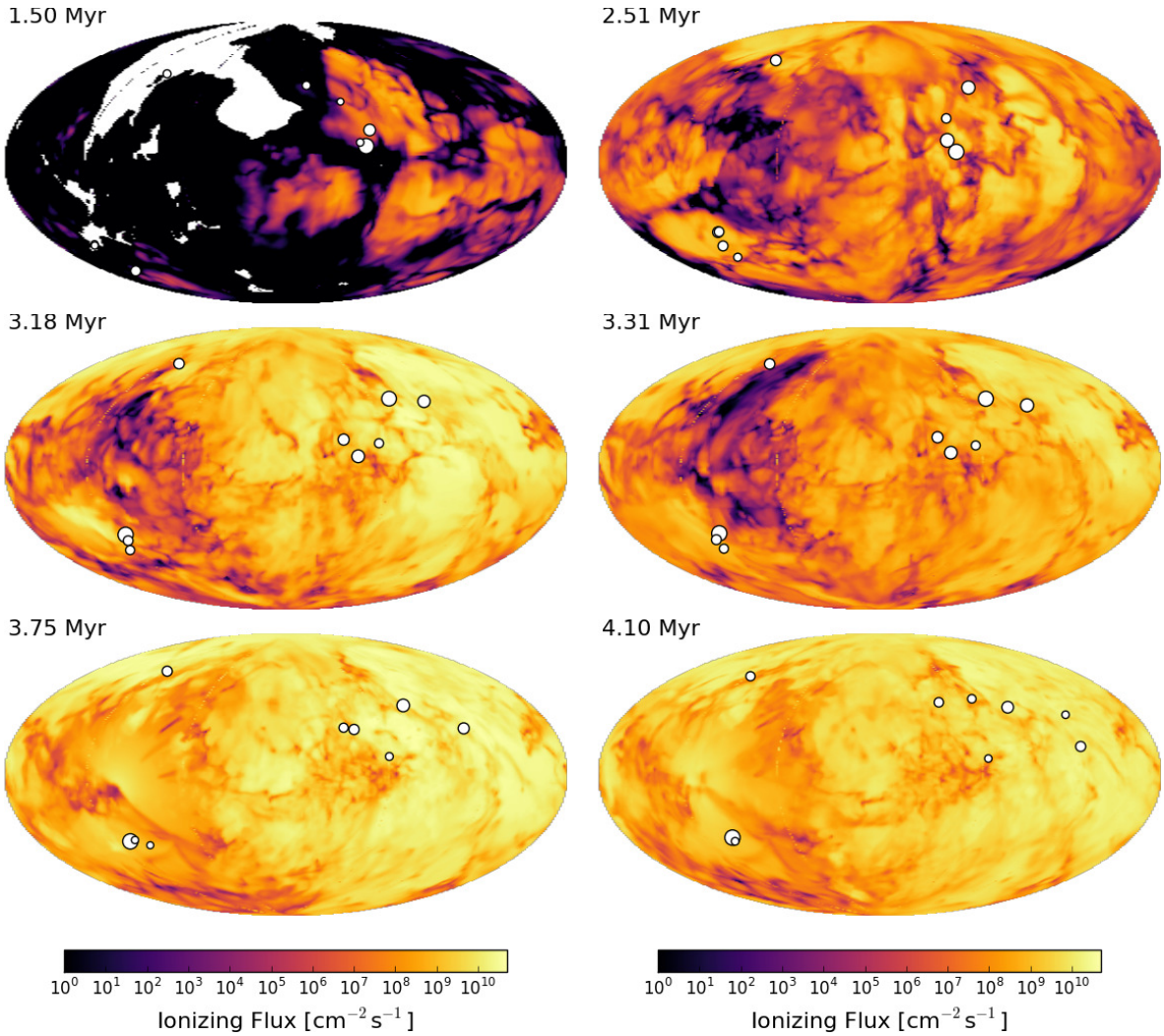

Figure 4.1: Maps of the ionizing photon flux across a spherical surface of radius 33.8 pc (corresponding to the initial GMC radius) shown at 6 different times. White circles represent the closest location of the 10 most luminous clusters to the sphere. More luminous clusters are shown by larger circles. The maps were produced using a Hammer projection, which is an equal area projection.

a grouping towards the right side as well, suggesting that these clusters are responsible for much of the emission observed outside the cloud. There is also some flux associated with the cluster in the bottom left quadrant of this panel.

At 2.5 Myr, we see that the entire surface is now being traversed by UV photons from the clusters. The flux of photons, however, is not spatially uniform. Since the flux on the sphere's surface depends on the intervening column density, the presence of dense clumps and filaments manifests itself as regions with lower flux. We note that the simulation has virialized ($\alpha = 1$) at 2.5 Myr, so any further turbulence is driven by gravitational collapse of the gas (see Howard et al. (2016) for details and Klessen & Hennebelle (2010) for a more general discussion of accretion driven turbulence).

As the total ionizing luminosity increases and the total mass in gas decreases, the presence of these dark filaments becomes less pronounced. At 3.18 Myr, only the left side of Figure 4.1 shows regions with low flux. The grouping of clusters on the right of this Figure is likely responsible for the higher flux in that region. From 3.75 Myr onwards, the flux is more spatially uniform due to increased cluster luminosities and lower total gas mass.

The above visualizations show that the ionizing flux can vary significantly over both space and time within a GMC.

In Figure 4.2, we focus on the evolution of f_{esc} from the cloud. We define f_{esc} as the total number of photons crossing the spherical surface previously discussed in Figure 4.1, divided by the summed total of all photons being generated by the

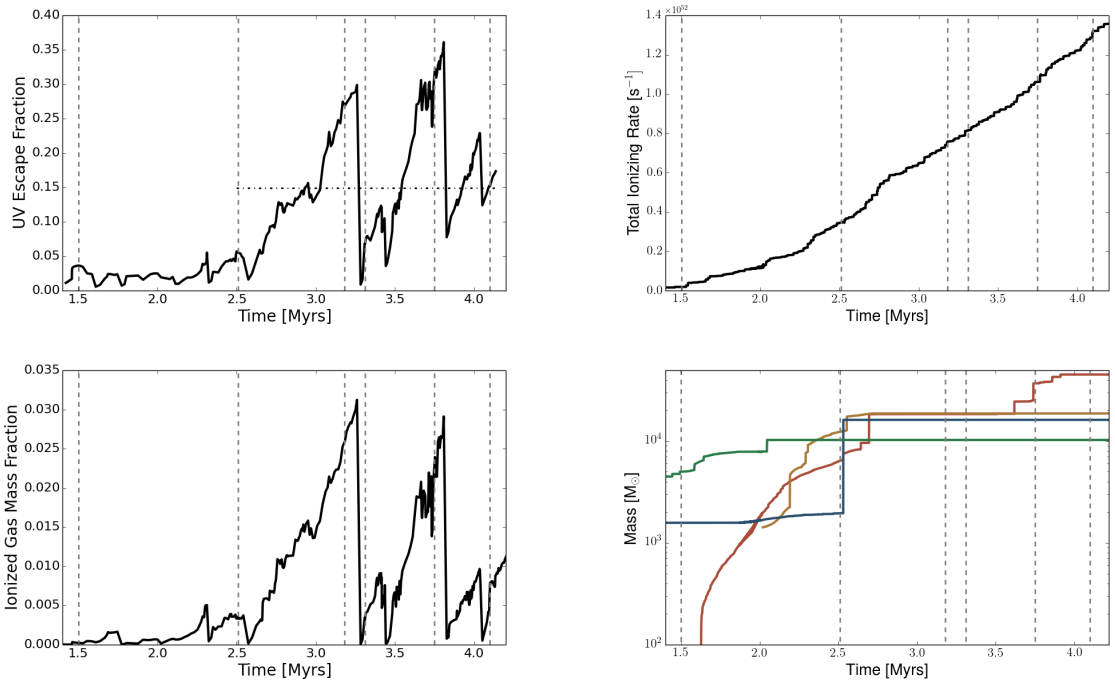

Figure 4.2: Top Left: The total UV escape fraction across the spherical surface presented in Figure 4.1. The vertical lines, shown in all panels, correspond to the times shown in Figure 4.1 (1.50, 2.51, 3.18, 3.31, 3.75, and 4.10 Myr). The horizontal line shows the average f_{esc} from 2.5 to 4.2 Myr. The escape fraction is defined here as the total number of photons crossing the surface divided by the total number of photons being produced by the clusters. Note that we only include clusters above the mass threshold described in Section 4.3, since clusters below this threshold are not included in the radiative transfer calculations. Top Right: The total ionizing photon rate produced by clusters above the mass threshold for radiation. Bottom Left: The fraction of gas, by mass, which has an ionization fraction of greater than 95%. Bottom Right: The mass evolution of the four most massive clusters, shown for reference. Discrete jumps in mass are due to cluster merging events. The complete mass evolution tracks can be found in Howard et al. (2016).

clusters. Its time evolution is shown in the top left panel of Figure 4.2. Note that we only include the clusters which are above the mass threshold discussed in Section 4.3, since these are the clusters that are used by the radiative transfer scheme.

The total escape fraction remains low at approximately 3% between 1.5 and 2.5 Myr. After 2.5 Myr, f_{esc} rises to a peak of 30% at 3.25 Myr, followed by a sudden drop. The escape fraction begins to rise again, reaching a peak of 37% at 3.8 Myr. The average f_{esc} from the first rise at 2.5 Myr to the end of the simulation, shown by the horizontal line, is 15%.

The rising f_{esc} and subsequent rapid drops are not due to changes in the ionizing photon output from the clusters, which is shown in the top right panel of Figure 4.2. These clusters are accreting new gas vigourously from their surroundings and building new, massive stars as time progresses. The increase in the ionizing photon output is steady and shows no distinct features which correspond to the features seen in f_{esc}.

Rather, the ionization structure of the gas is responsible for the variable f_{esc}. In the bottom left panel of Figure 4.2, we plot the fraction of gas mass which has an ionization fraction of greater than 95%. This Figure clearly mirrors the features seen in f_{esc}, with an increasing f_{esc} corresponding to an increase in the mass fraction of ionized gas. Recall that UV opacity in ionized regions is significantly lower than in neutral regions.

While the change in the ionized mass fraction is low, peaking at $\sim$3%, the HII regions can spatially occupy a significant fraction of the simulation volume, typically

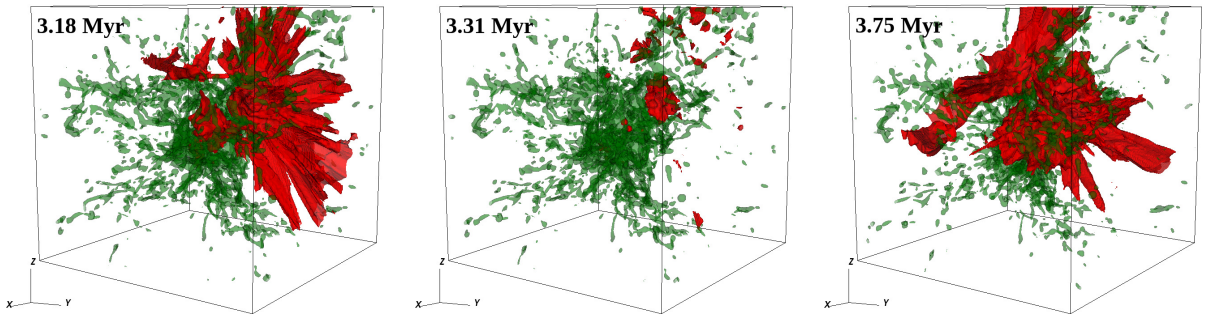

Figure 4.3: 3d images of the density (shown in green) and ionized regions (shown in red) at 3.18, 3.31, and 3.75 Myr from left to right, respectively. These images correspond to the first peak in f_{esc} in Figure 4.2, the trough at 3.31 Myr, and the second peak at 3.75 Myr. The density contours represent densities of $\sim$30 cm^{-3} and the box side length is 80 pc.

filling large voids that are interspersed between dense filaments. Since clusters are the source of radiation and, therefore, tend to exist in HII regions, photons can travel large distances due to the reduced opacity resulting in higher photon fluxes near the boundary of the simulation volume.

However, the size and shape of HII regions is not constant. Both observations (De Pree et al., 2014, 2015) and simulations (Peters et al., 2010a,b; Galván-Madrid et al., 2011; Klassen et al., 2012a) show that the size of an HII region can flucuate on short timescales, a phenomenon described as "flickering". The dynamic and anisotropic nature of the gas, in combination with dynamic clusters, can result in HII regions becoming shielded to radiation due to changes in density between the source and the ionized regions. The formerly irradiated gas then recombines, causing the HII to flicker.

A visual demonstration of this flickering is displayed in Figure 4.3, which shows 3-dimensional images of density, in green, and HII regions, in red. The green density

contours show gas at $\sim$100 cm^{-3} which is the typical density of the filaments out of which the clusters form. The entire simulation volume is shown and the box side length is 83 pc.

The left most panel of Figure 4.3 shows the state of the simulation at 3.18 Myr, corresponding to the first pronounced peak in f_{esc}. A large HII region has developed on one side of the cloud which extends away from the dense, central gas to the boundary of the simulation volume. The middle panel, shown at 3.31 Myr, shows the decrease in the size of the HII region which is responsible for the deep trough in f_{esc} at 3.25 Myr. The right most panel of Figure 4.3, plotted at the second peak of f_{esc} at 3.75 Myr, shows that the HII region has expanded again to a similar size as seen in the first panel.

To investigate the cause of the variable HII region size, we focus our analysis on one luminous cluster which is associated with the HII region. This cluster is the second most luminous in the simulation with a final ionizing luminosity of 1.40×10^{51} s^{-1}. The most luminous cluster was not chosen because it is deeply embedded in the dense, central gas and therefore its associated HII region is small in comparison to the one which extends to the boundary of the simulation volume, as seen in Figure 4.3.

We drew lines of sight which originate at the cluster's position and extend a distance of 20 pc through the large HII region. This was done at two times, one just before the HII region collapses for the first time (at 3.25 Myr) and one immediately after the collapse ($\sim$35,000 yr after the first image). We can then examine how the

density and the recombination rate differ before and after the HII region collapse along these lines of sight.

We find that the radiative recombination rate along the lines of sight increases significantly immediately after the HII region collapses, increasing from $\sim 5\times10^{-8}$ to 1×10^{-6} cm^{-3} s^{-1}. The radiative recombination rate is given by αn^2, assuming an ionization degree of 100%, where α is the radiative recombination coefficient and n^2 is the square of the number density. The recombination coefficient varies with temperature as,

$$\alpha = 2.59 \times 10^{-13} \left(\frac{T}{10^4 K} \right)^{-0.7} \tag{4.2}$$

where T is the gas temperature in Kelvin.

The radiative recombination rate increases after the collapse for two reasons. Firstly, the density immediately surrounding the cluster increases, likely due to the turbulent nature of the surrounding gas. Secondly, as the region cools, the recombination coefficient increases.

We also examined the quantity $\alpha x^2 n^2$, where x is the ionization fraction of the gas, which removes the assumption of a 100% ionization fraction. In this case, we see the opposite trend and the recombination rate drops from 5×10^{-8} to 2×10^{-13} cm^{-3} s^{-1}. Despite the increase in density and the recombination coefficient, the recombination rates decrease significantly due to the low ionization fraction of the gas after the HII region collapses.

We find that n^2 increases by a factor of $\sim$1.5 - 4 along the lines of sight within a 1 pc radius of the clusters location. This increased density limits the amount of radiation that propagates to larger radii. The gas can then recombine and cool from $\sim 10^4$ K, typical of HII regions, to $\sim$10 K which is the temperature floor adopted in the simulation.

This can be visualized by examining the neutral column density from the luminous cluster through the HII region, as shown in Figure 4.4. The top panels show a slice of density (left) and ionization fraction (right) centered on the luminous cluster associated with the HII region which collapses at 3.25 Myr. These images are plotted before the HII region collapses. At this time, the cluster is no longer deeply embedded in the massive cold filament out of which it formed in the first place. The bottom panels of Figure 4.4 shows a Hammer projection of the neutral gas column density across a spherical surface of radius 20 pc centered the same cluster before the HII region collapse (left) and after the collapse (right). A 20 pc radius circle is shown in the density and ionization fraction slices for reference. The column density projections clearly show that the region which was previously ionized has increased in column density after the HII region collapses.

The increase in density surrounding the massive cluster can be understood through turbulent shocks in the surrounding ionized gas. We measured the local gas velocity dispersion at the location of the cluster immediately before the HII region collapse to be 10.1 km s^{-1} (corresponding to a Mach number of 1.14). Thus a density fluctuation can cross the cluster's radius of 0.78 pc in $\sim$76,000 years. This is comparable to the $\sim$35,000 years it takes for the HII region to collapse. A passing shock could

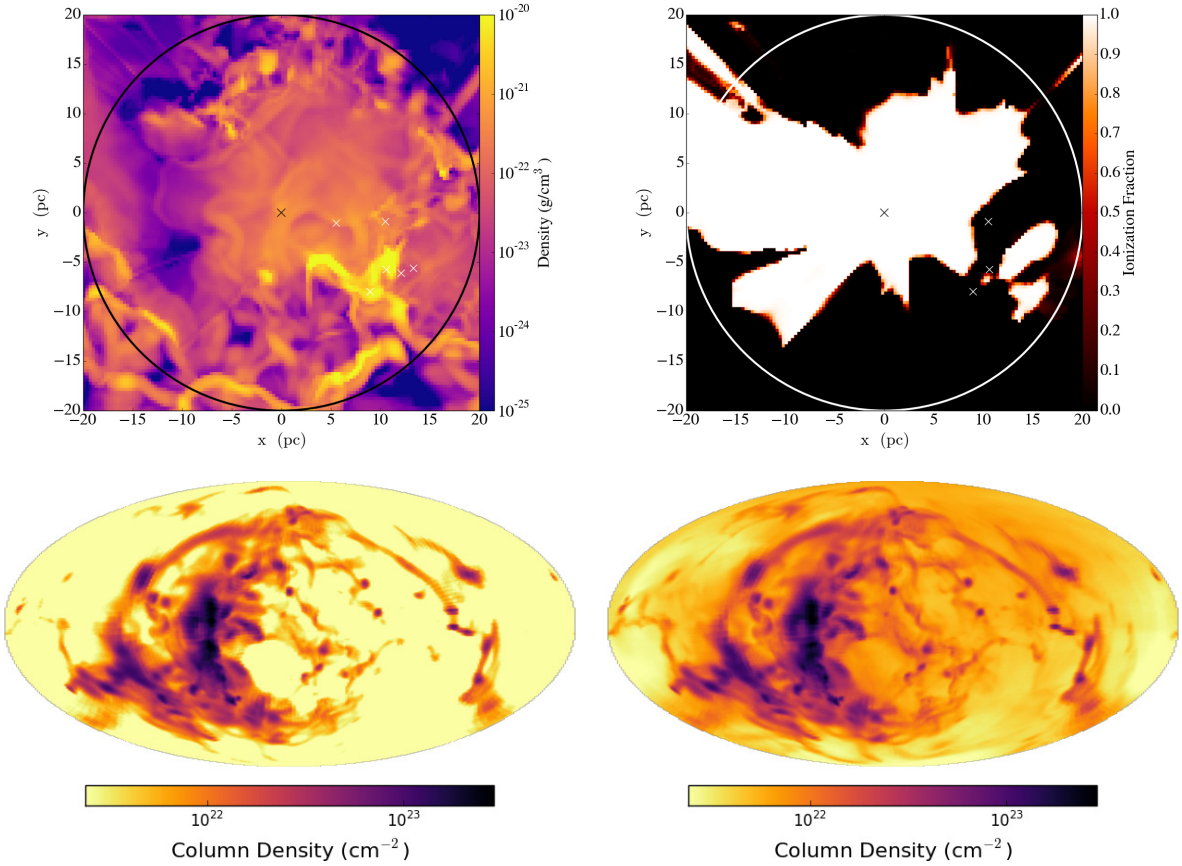

Figure 4.4: Top Left: A slice of density centered on the location of the most luminous cluster associated with the collapsing HII region at 3.25 Myr. Top Right: The same slice in the previous panel except the ionization fraction of the gas is displayed. Bottom Left: A Hammer projection of the neutral gas column density at a 20 pc spherical surface centered on the same cluster, plotted before the HII region collapses at 3.25 Myr. Bottom Right: The same but ∼35,000 yr after the Bottom Left panel. The HII region has collapsed by this time.

therefore lead to a local density enchancement causing the HII region to collapse in the observed time. As the gas recombines, it cools and shields regions further along the line of sight.

This further analysis supports our claim that the dynamic nature of the gas, which at this point in time causes the density to increase within the HII region, is responsible for the strong fluctuations in the size of the HII regions being produced by luminous clusters, and hence in the value of f_{esc}.

The above discussion has focused on f_{esc} from the entire molecular cloud which is a useful quantity when studying the build-up of the ISRF or estimating the global escape fraction from a galaxy as a whole. We may instead investigate the escape fraction from smaller regions surrounding luminous clusters to follow the evolution of f_{esc} as a function of distance from the cluster. We are limited in this regard due to the fact that the raytracer used to compute the radiative transfer only tracks the total flux in each grid cell with no directional information about the incoming rays. This means that if we calculate the flux across a small spherical surface centered on a luminous cluster, it will likely include contributions from sources outside the sphere.

Still, we can calculate f_{esc} across a surface if the majority of the total ionizing luminosity is being generated within its volume. This minimizes the contribution to the total flux from outside sources. We find that the 10 most luminous clusters generate 90% of the total ionizing luminosity and are located a maximum of 24.3 pc from the simulation center. We therefore repeat the f_{esc} calculation for a sphere of radius 25 pc instead of 33.8 pc, which was presented in Figure 4.2.

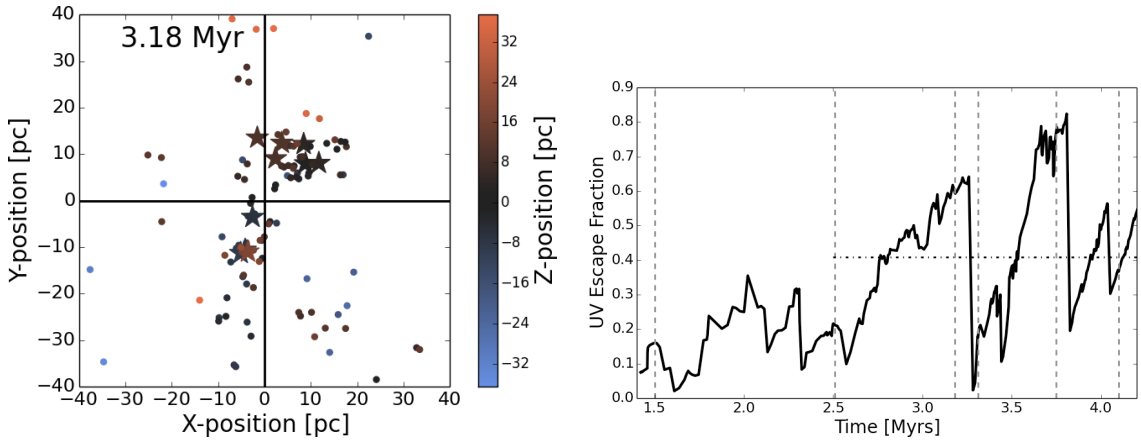

Figure 4.5: Left: The positions of all clusters plotted at 3.18 Myr. The stars represent the locations of the 10 most massive clusters and colours represent Z-position. Right: The escape fraction, f_{esc}, across a spherical surface of radius 25 pc. This is the smallest possible radius which contains 90% of the total ionizing luminosity within its volume and therefore minimizes the contribution to the flux across the surface from outside sources.

For reference, we show a 2-dimensional projection of the position of all clusters in the left panel of Figure 4.5. The 10 most luminous clusters are shown by the stars, and all clusters are colored by their Z-position in the cloud. We only show the positions at one time, 3.18 Myr which corresponds to the first peak of f_{esc} in Figure 4.2, to illustrate that the clusters are not strongly grouped together but instead cover the cloud's entire extent.

The right panel of Figure 4.5 shows f_{esc} across a spherical surface of radius 25 pc. Comparing to the top left panel of Figure 4.2, we see that f_{esc} across the smaller surface well within the cloud has a similar temporal evolution with pronounced peaks at 3.25 and 3.75 Myr, but the values are $\sim$2 times larger. The average f_{esc} from 2.5 to 4.2 Myr is 41%, compared to 15% for ionizing radiation that escapes from the surface of the cloud. The early evolution (ie. less than 2.5 Myr) of f_{esc} is also significantly

enhanced, likely due to the generation of small HII regions surrounding the luminous clusters which are not large enough to extend to the edge of the simulation volume.

Overall, these results suggest that f_{esc} decreases with cloud radius as one moves through the cloud and out its surface. This trend has been found observationally by Pellegrini et al. (2012) who noted that the global f_{esc} from the LMC and SMC is estimated to be 4% and 11% respectively, while f_{esc} from individual star-forming regions can be as high as ∼60%.

The values presented in Figure 4.2 are particularly important for the global ISRF and ISM structure since they represent the escape fraction from the surface of an entire 10^6 $M_\odot$ GMC. Clouds of this mass are host to the most massive stellar clusters which dominate the stellar feedback and overall luminosity of a galaxy (Harris & Pudritz, 1994; Mac Low & Klessen, 2004; McKee & Ostriker, 2007; Klessen & Glover, 2016).

4.5 Discussion and Conclusions

We computed the UV photon escape fraction from a turbulent, 10^6 $M_\odot$ GMC using the astrophysical code FLASH. The cloud, taken from Howard et al. (2016), is initially unbound with a virial parameter of 3 and sink particles are used to model the formation of star clusters. Our simulations end just before supernovae explosions could disrupt the star clusters and remove surrounding gas.

Our analysis indicates that the flux is both highly anisotropic due to the filamentary and clumpy nature of the intervening turbulent gas as well as highly variable in time. As time progresses, the flux naturally increases since the clusters contain more massive stars.

The integrated escape fraction, defined as the total number of photons leaving the cloud divided by the total number of photons being produced by all clusters, also varies significantly over time. For the first 2.5 Myr of evolution, f_{esc} remains low at $\sim$5%. There are two distinct peaks in the escape fraction at 3.25 and 3.8 Myr, with a maximum escape fraction of 30% and 37% at the two peaks. The average f_{esc} from the onset of large HII regions at 2.5 Myr to the end of the simulation is 15%. The average f_{esc} increases to 41% if we instead consider a smaller surface well inside the cloud at a radius of radius 25 pc, as compared to the GMC's surface which is at a radius of 33.8 pc.

The peaks of f_{esc}, and subsequent troughs, are tied to the local gas density structure surrounding the luminous clusters which determines the size of the HII region they produce. At a peak, the HII is large and extends towards the boundary of the simulation volume. At a trough, the HII region is only a small fraction of its previous size. The collapse of the HII region is tied to the turbulent nature of the gas surrounding the luminous clusters which causes the density to vary with time. As it increases, so does the recombination rates and the HII regions shrinks.

We argue that calculations of the photon escape fraction on galactic scales require knowledge of f_{esc} for individual GMCs and for the star forming complexes in their

interior. For many applications (eg. cosmic reionization), this is computationally prohibitive and we suggest to use an average value of $f_{esc} = 15\%$ for a 10^6 $M_\odot$ GMC with fluctuations of a factor of two superimposed on timescales of about 1 Myr.

4.6 Acknowledgements

We thank Bill Harris and Eric Pelligrini for interesting discussions.

C.S.H. and R.E.P. thank the the Zentrum für Astronomie der Universität Heidelberg (ZAH), Institut für Theoretische Astrophysik (ITA), as well as the Max-Planck-Institut für Astronomie (MPIA), for their generous support during R.E.P's sabbatical leave (2015/16) and C.S.H.'s extended visit (Oct. - Nov.,2015).

R.E.P. is supported by Discovery Grants from the Natural Sciences and Engineering Research Council (NSERC) of Canada. C.S.H. acknowledges financial support provided by the Natural Sciences and Engineering Research Council (NSERC) through a Postgraduate scholarship. The FLASH code was in part developed by the DOE supported Alliances Center for Astrophysical Thermonuclear Flashes (ASCI) at the University of Chicago. This work was made possible by the facilities of the Shared Hierarchical Academic Research Computing Network (SHARCNET:www.sharcnet.ca) and Compute/Calcul Canada.

R.S.K. acknowledges support from the European Research Council under the European Communitys Seventh Framework Programme (FP7/2007-2013) via the ERC Advanced Grant 'STARLIGHT: Formation of the First Stars' (project number

339177). R.S.K. further thanks for funding from the Deutsche Forschungsgemeinschaft (DFG) in the Collaborative Research Center SFB 881 The Milky Way System (subprojects B1, B2, and B8) and in the Priority Program SPP 1573 Physics of the Interstellar Medium (grant numbers KL 1358/18.1, KL 1358/19.2).

Chapter 5

Simulating the UV Escape Fractions from Star-forming Dwarf and Spiral Galaxies

5.1 Abstract

The escape of ultraviolet photons from the densest regions of the interstellar medium (ISM) — Giant Molecular Clouds (GMCs) — is a poorly constrained parameter which is vital to understanding the ionization of the ISM and the intergalactic medium. We characterize the escape fraction, f_{esc}, from a suite of GMC simulations with masses in the range 10^{4-6} $M_\odot$ using FLASH. We find significantly different f_{esc} depending on the GMC mass which can reach >90% for clouds of 5×10^4 and 10^5 $M_\odot$

or remain low at ∼5% for more massive GMCs. All clouds show fluctuations over short timescales produced by rapidly varying HII regions. We combine our results to represent f_{esc} from GMC populations in dwarf starburst and spiral-type galaxies by randomly drawing clouds from a GMC mass distribution ($dN/dM \propto M^{\alpha}$, where α is either -1.5 or -2.5) over fixed time intervals. We find typical f_{esc} values of 8% for both the dwarf and spiral models. The fluctuations of these escape fractions, however, are much larger for the dwarf models and can reach as high as 90%. The photons escaping from the 5×10^4 and 10^5 $M_{\odot}$ GMCs are the dominant contributors to f_{esc} in all cases. We also show that the resulting star formation rates (SFRs) of our model (2×10^{-2} and 1.77 $M_{\odot}yr^{-1}$) are consistent with observations of SFRs in dwarf starburst and spiral galaxies, respectively.

5.2 Introduction

The emission, absorption, and reprocessing of ultraviolet (UV) photons produced by massive stars are important processes both within a galaxy and in the intergalactic medium (IGM). On galactic scales, these photons contribute to the interstellar radiation field (ISRF), first characterized by Habing (1968). This field is responsible for the thermal, chemical, and ionization state of the interstellar medium (ISM) (Draine, 2011). Despite their short lifetimes, massive stars in the range of 10-100 $M_{\odot}$ are a strong contributor the ISRF due to their high UV luminosities. Moreover, it has been shown that the field O-star population of the Milky Way (MW) is not sufficient to maintain the ionization of the Diffuse Ionized Gas (DIG) layers above

and below the galactic plane (Reynolds, 1993). Instead, a significant portion must be contributed via HII regions that are leaking photons into the ISM. How, and the degree to which, UV photons propagate from massive stars out of their gaseous birth sites is therefore crucial for the large-scale structure of the ISM.

Once a photon escapes a galaxy, it can interact with the IGM and, at high redshifts (z$\geq$6), contribute to cosmic reionization (Robertson et al., 2010). However, the exact fraction of UV photons that escape from a galaxy, f_{esc}, is poorly constrained and is likely a function of the host galaxy's properties. For example, estimates of f_{esc} for high redshift galaxies measured via the Lyman continuum range from 7% (Siana et al., 2015) to 30% (Nestor et al., 2013). Recent estimates of f_{esc} calculated via HII region mapping for the Small Magellanic Cloud (SMC) and the Large Magellanic Cloud (LMC) suggest values of 4% and 11%, respectively (Pellegrini et al., 2012).

It has been shown that galaxies which host active galactic nuclei (AGN) are not sufficient to drive cosmic reionization (Fan et al., 2006; Robertson et al., 2013). Instead, dwarf galaxies are thought to be important contributors. Estimates suggest that $\sim$40% of the total ionizing photons required for cosmic reionization may be produced in dwarfs (Wise et al., 2014).

Since the masses of these dwarfs are small — as low as $\sim 10^8$ $M_\odot$ — they are not observable at high redshifts and, therefore, simulations are required to constrain f_{esc}. As with the observations mentioned above, there is a large variation between quoted values. For example, the predicted f_{esc} for high redshift dwarfs ranges from $<$1% (Paardekooper et al., 2011) to $>$10% (Razoumov & Sommer-Larsen, 2010; Ferrara

& Loeb, 2013; Paardekooper et al., 2015). Moreover, f_{esc} can vary by orders of magnitude throughout an individual galaxy's evolutionary history (Paardekooper et al., 2011).

The distribution of dense gas in a galaxy, and the treatment of star formation within that gas, is one of the main constraints on modeling f_{esc} (Paardekooper et al., 2011). Thus detailed studies aimed at modeling f_{esc} from Giant Molecular Clouds (GMCs) — the densest regions of the ISM and the hosts to massive star formation — can provide important constraints on the global f_{esc} from a galaxy. This problem is complicated, however, by the complex internal structure of GMCs, the variation in physical conditions from cloud to cloud, and the addition of several physical processes at the onset of star formation.

GMCs as a whole consist of dense filaments formed as a product of supersonic turbulence (Bertoldi & McKee, 1992; Lada & Lada, 2003; Mac Low & Klessen, 2004; McKee & Ostriker, 2007; André et al., 2014; Klessen & Glover, 2016). The mass of individual clouds, however, can vary over several orders of magnitude. Within the MW, GMCs range from 10^{4-7} $M_{\odot}$ (Fukui & Kawamura, 2010) with a powerlaw mass distribution of $dN/dM \propto M^{-1.5}$ (Solomon et al., 1987; Rosolowsky, 2005). The virial parameter of GMCs (ie. the ratio of internal kinetic energy to gravitational potential energy) also covers a wide range, from significantly bound to unbound (α = 0.5 - 5, Blitz et al. (2007)). As shown in Howard et al. (2016), the virial parameter plays a central role in determining the star formation efficiency (SFE) of a GMC.

At the onset of star formation — typically occurring at the intersection of filaments for massive clusters (Balsara et al., 2001; Schneider et al., 2012; Kirk et al., 2013) — energy and momentum are imparted to the gas by a variety of feedback processes from newly formed stars. Stellar winds (Dale & Bonnell, 2008; Gatto et al., 2017), protostellar jets (Li & Nakamura, 2006; Maury et al., 2009; Federrath et al., 2014), radiative feedback (Dale et al., 2005; Peters et al., 2010a; Klassen et al., 2012b; Howard et al., 2016), and supernovae feedback (Rogers & Pittard, 2013; Fierlinger et al., 2016) are several examples of these processes. Radiative feedback is particularly important for clusters hosting massive star formation (Murray et al., 2010; Bate, 2012). Ultraviolet photons produced by massive stars heat and ionize the surrounding gas resulting in the formation of HII regions. The interaction of photons with dust grains can also impart momentum into the gas and drive outflows.

In Howard et al. (2017a), we examined the role that radiative feedback plays in controlling the SFE and star formation rates (SFR) of young, filamentary GMCs over a mass range of 10^{4-6} $M_\odot$. We completed a suite of 5 simulations of turbulent GMCs using the code FLASH which combined sink particles to represent star-forming clusters and a raytracing scheme to complete the radiative transfer. We found that the inclusion of radiative feedback lowered the SFEs for all clouds, but GMCs in the range of 5×10^4 to 10^5 $M_\odot$ were affected the most. In that mass range, the energy injected by radiative feedback outweighs the gravitational potential energy of the cloud, resulting in nearly complete ionization by $\sim$5 Myr.

In this paper, we take the next step and compute the UV escape fraction from the same suite of simulations in order to put further constraints on the global escape

fraction from the observed mass spectrum of clouds in entire galaxies. In Section 5.3, we provide an overview of our numerical methods and the details of the f_{esc} calculation.

We first discuss (Section 5.4) the escape fractions from individual GMCs. We find that cloud mass plays an important role in determining f_{esc}. For clouds of mass $5{\times}10^4$ and 10^5 $M_\odot$, the final escape fractions are 90%, and 100% at 5 Myr. Still more massive clouds have correspondingly low escape fractions which do not exceed ∼12%. Regardless of GMC mass, there are large fluctuations in f_{esc} over short timescales due to dynamic HII regions which grow and shrink rapidly depending on the local conditions surrounding the luminous clusters embedded within the GMCs.

We then present a model (Section 5.5) for combining our results for individual GMCs in order to represent f_{esc} from a *population* of clouds. This model involves drawing clouds from a GMC mass distribution over fixed time intervals at random, evolving the clouds over 5 Myr, and calculating f_{esc} from the existing population. We present two realizations of this model — one representative of a dwarf starburst galaxy, and one for a normal spiral-type galaxy.

We find typical escape fractions of 8% for both the dwarf and spiral models. However, there are strong variations in f_{esc} with time, particularly for the dwarf models which cover the range of 0-90%. We also present the resulting SFRs and find typical values of $2{\times}10^{-2}$ and 1.77 $M_\odot yr^{-1}$ for the dwarf and spiral model which are consistent with observed values. We discuss the consequences of these results for galactic evolution.

5.3 Numerical Methods

5.3.1 Simulation Details

We briefly describe the details of our numerical methods and simulation suite below. For more detail, we refer the reader to Howard et al. (2017a).

We have completed a suite of GMC models having masses of 10^4, $5{\times}10^4$, 10^5, $5{\times}10^6$, and 10^6 $M_\odot$ using the Adaptive Mesh Refinement (AMR) code FLASH (Fryxell et al., 2000b). FLASH includes modules to treat self-gravity, cooling via molecular lines and dust (Banerjee & Pudritz, 2006), radiative transfer, and star formation — all of which are included in our simulations.

To isolate the effects of varying GMC mass, we fixed the initial average density to 100 cm^{-3} and the initial virial parameter ($\alpha = 2E_{kin}/E_{grav}$, where E_{kin} is the internal kinetic energy and E_{grav} is the gravitational potential energy) to 3 for all models. The density profile is uniform in the inner half of the cloud and decreases as $r^{-3/2}$ in the outer half. Following the method of Girichidis et al. (2011), we overlay the clouds with an initial Burgers turbulent velocity spectrum that is not driven and which decays with time. The Mach number of the turbulence varies depending on the cloud mass in order to keep the virial parameter constant across models. The resolution also depends on the GMC mass and ranges from 0.13 to 0.31 pc (see Table 1 of Howard et al. (2017a) for a full list of our model parameters).

A hybrid-characteristics raytracing method developed by Rijkhorst et al. (2006) and adapted for star formation simulations by Peters et al. (2010a) is used to treat radiative transfer. Both ionizing and non-ionizing radiation are included in this scheme. The ionization equations are solved via the DORIC package (Frank & Mellema, 1994) assuming hydrogen is the only gas component. The Planck mean opacities taken from Pollack et al. (1994) are used for non-ionizing radiation. We include radiation pressure by adopting a single UV opacity of $\kappa = 775$ cm^2 g^{-1} (Li & Draine, 2001) that is scaled by the neutral fraction of the gas such that fully ionized regions have zero opacity. The corresponding radiative force per unit mass is given by,

$$F = \kappa \frac{L}{c} \frac{e^{-\tau_{uv}}}{4\pi r^2} \tag{5.1}$$

where κ is the opacity to UV radiation, c is the speed of light, L is the source luminosity, r is the distance between the source and the cell, and τ_{uv} is the optical depth between the source and the cell calculated using the raytracer

The radiative transfer scheme is coupled to the sink particle method implemented by Federrath et al. (2010). We use these sink particles to represent star-forming clusters. A density threshold for cluster formation of 10^4 cm^{-3} is adopted in order to be consistent with observations of star-forming clumps (Lada & Lada, 2003).

We have developed a subgrid model for how star formation proceeds in these clusters (see Howard et al. (2014) for full details and tests of our model). We divide each cluster's mass into two components; the mass contained in fully formed stars,

and the remaining gas mass (referred to as the reservoir). Every 0.36 Myr, corresponding to the free fall time of the gas at our adopted threshold density, 20% of the reservoir mass is converted to stars by randomly sampling a Chabrier (2005) IMF. Any gas accreted by the cluster from the surrounding GMC in which it is forming is added to the reservoir and is then available for future star formation.

The stars formed in each cluster are recorded and the total luminosity of a cluster is the sum of its stellar components. We use analytic fits from Tout et al. (1996) to determine each star's total luminosity and ionizing luminosity. These fits were developed for main sequence stars so we therefore neglect the effects of protostellar evolution. The radiative properties of each cluster are passed to the raytracer to complete the radiative transfer.

We note that the radiative transfer scheme only tracks the total flux of ionizing photons in each cell and not the net direction of the flux. This leads to some approximations when calculating the f_{esc} from the cloud, as discussed below.

5.3.2 Escape Fraction Calculation

To calculate the escape fraction of UV photons from each GMC, we first extract a spherical surface with a radius corresponding to the initial radius of the cloud. We use the marching cube algorithm implemented in the YT analysis toolkit (Turk et al., 2011) to perform the surface extraction. This algorithm identifies isocontours of the provided quantity (in our case the distance from the center of the simulation volume) and represents these contours as a collection of triangles which, together,

represent the extracted surface. There can be multiple triangles within an individual grid cell depending on the geometry and the requested isocontour surface.

The total number of photons crossing the extracted surface is then calculated. The three dimensional positions of all surface triangles are known as well as the flux of photons through each element. In order to calculate the outward flux of photons, the direction of the flux is required. As mentioned above, the radiative transfer scheme only tracks the magnitude of the flux in each grid cell. We therefore make the assumption that all photons are generated at the center of luminosity (ie. the luminosity weighted average cluster position). The direction of the flux across each surface element is then known, and the total number of photons crossing the surface is given by

$$N = \sum_i \vec{F}_i \cdot d\vec{A}_i \tag{5.2}$$

where $\vec{F}_i$ is the vector flux of ionizing photons across surface element i, and $d\vec{A}_i$ is its corresponding area vector. The escape fraction of UV photons is then calculated by dividing N by the total number of UV photons being produced by all clusters.

We note that this method has been improved from what was presented in Howard et al. (2017b). In that work, we did not consider a direction for the flux and simply took $d\vec{A}_i$ to be the area of each grid cell viewed face-on. As we will show below, this led to an overestimate of f_{esc}, and when applied to our new suite of simulations resulted in clearly nonphysical escape fractions that were greater than 1. The improved

method results in more accurate results, and we quantify the errors introduced by our assumption that all radiation is generated at the center of luminosity in the next Section.

5.4 Individual GMC Escape Fractions

In this Section we present the results of the escape fraction calculations from clouds in a range of masses. We produce visualizations of the ionizing photon flux across our extracted surfaces using Hammer projection maps, described in Howard et al. (2017b), in Figure 5.1. Here, we only produce maps for the 10^4 and 10^5 $M_\odot$ clouds and refer the reader to Howard et al. (2017b) for the 10^6 $M_\odot$ model.

A Hammer projection, an equal-area projection which reduces the distortion in the outer regions of the map, was used to project the flux of photons across the extracted surface. We also include the positions of the luminous clusters as white circles, scaled in size by their ionizing luminosity, which are plotted at their closest position to the spherical surface. We note that there are more clusters present in the simulation but small clusters that do not produce significant UV flux are not included in the radiative transfer calculation to reduce the overall computational time. The physical sizes of the maps are also different between the 10^4 and 10^5 $M_\odot$ GMCs so a 5 pc scale bar is included for reference.

Starting at 3 Myr, both GMC models show regions of high and low flux separated by $\sim$8 orders of magnitude. This is due to the large amount of neutral gas still present in the simulation which absorbs photons as they propagate outwards to the surface.

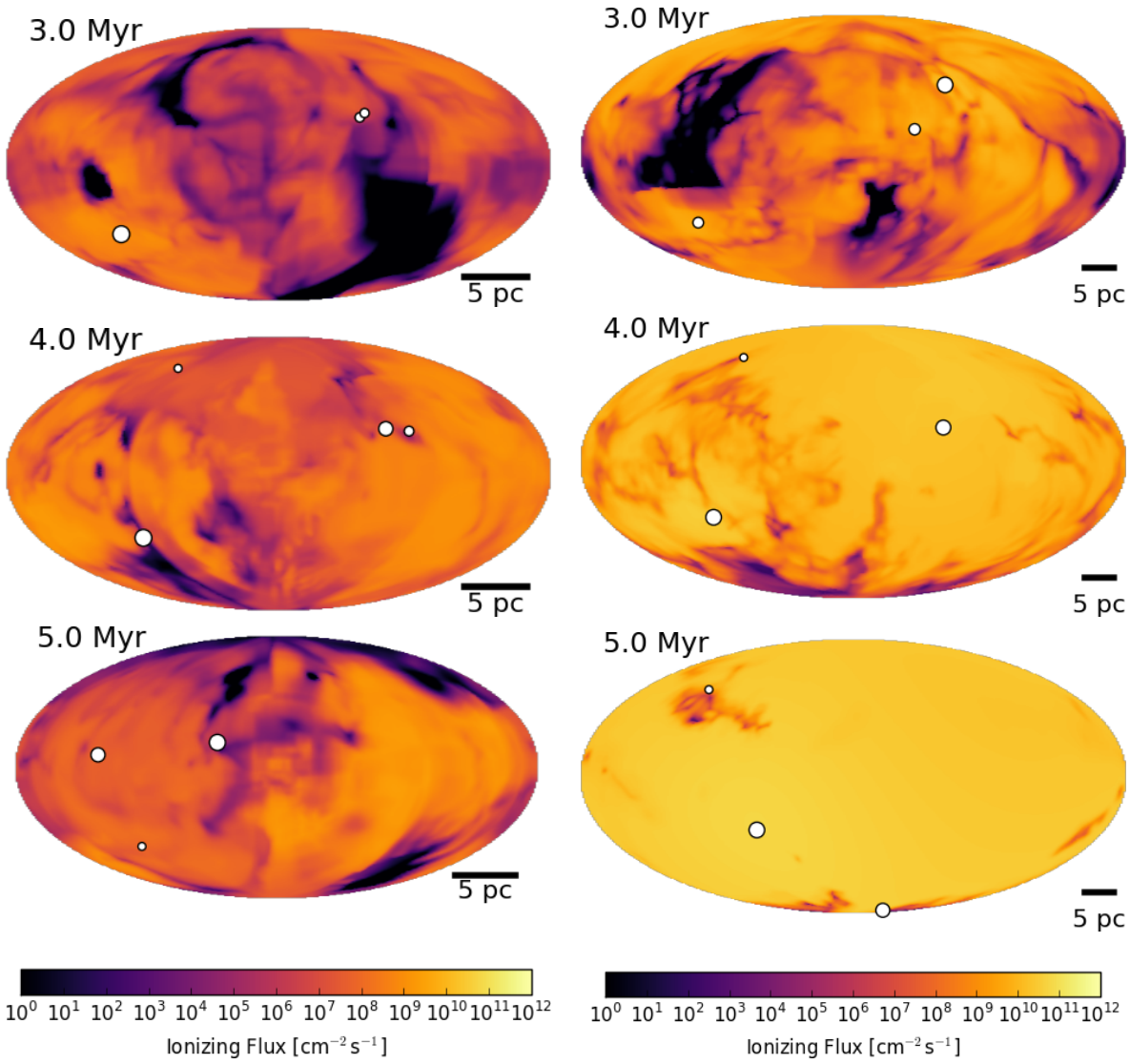

Figure 5.1: The flux of ionizing photons across the extracted spherical surface for the 10^4 (left) and 10^5 (right) $M_\odot$ GMCs. White circles represent the luminous clusters which are plotted at their closest location to the sphere and are scaled in size by their ionizing luminosity.

The clumpy and filamentary nature of the intervening neutral gas is responsible for the appearance of the dark regions.

Significant differences between the two simulations are clearly evident at 5 Myr. While the 10^4 $M_\odot$ simulation still has regions of low flux, the 10^5 $M_\odot$ GMC has a nearly uniform flux of $\sim 10^{11}$ cm^{-2}·s^{-1}. As discussed in Howard et al. (2017a), this is due to the cloud being nearly fully ionized at 5 Myr, meaning the opacity to ionizing luminosity is low and nearly all photons are crossing the plotted surface. The same is true for the 5×10^4 $M_\odot$ GMCs which is not plotted here.

The emergence of a fully ionized GMC by $\sim$5 Myr is unique to the 5×10^4 and the 10^5 $M_\odot$ model. For the lowest mass GMCs, there is not a large enough population of massive stars to appreciably affect the cloud. On the other hand, the largest clouds remain mostly neutral and bound throughout their evolution. The intermediate mass clouds produce enough massive stars to globally unbind the cloud via radiative feedback alone which results in a fully ionized cloud at late times.

We plot f_{esc} for our five simulated GMCs in Figure 5.2. For the reasons discussed above, the escape fraction is highest for the 5×10^4 and 10^5 $M_\odot$ GMCs. We can quantify our errors based on the 10^5 $M_\odot$ cloud which, at late times, has f_{esc} of 1.07 rather than unity. We can therefore quote the escape fractions to within 7%. As discussed in Section 5.3, the largest source of error is the assumption that all radiation originates at the center of luminosity.

The final (and average) escape fractions, in order of ascending GMC mass, are 31% (10%), 90% (38%), 100% (49%), 6% (2%), and 9% (6%). The peak escape

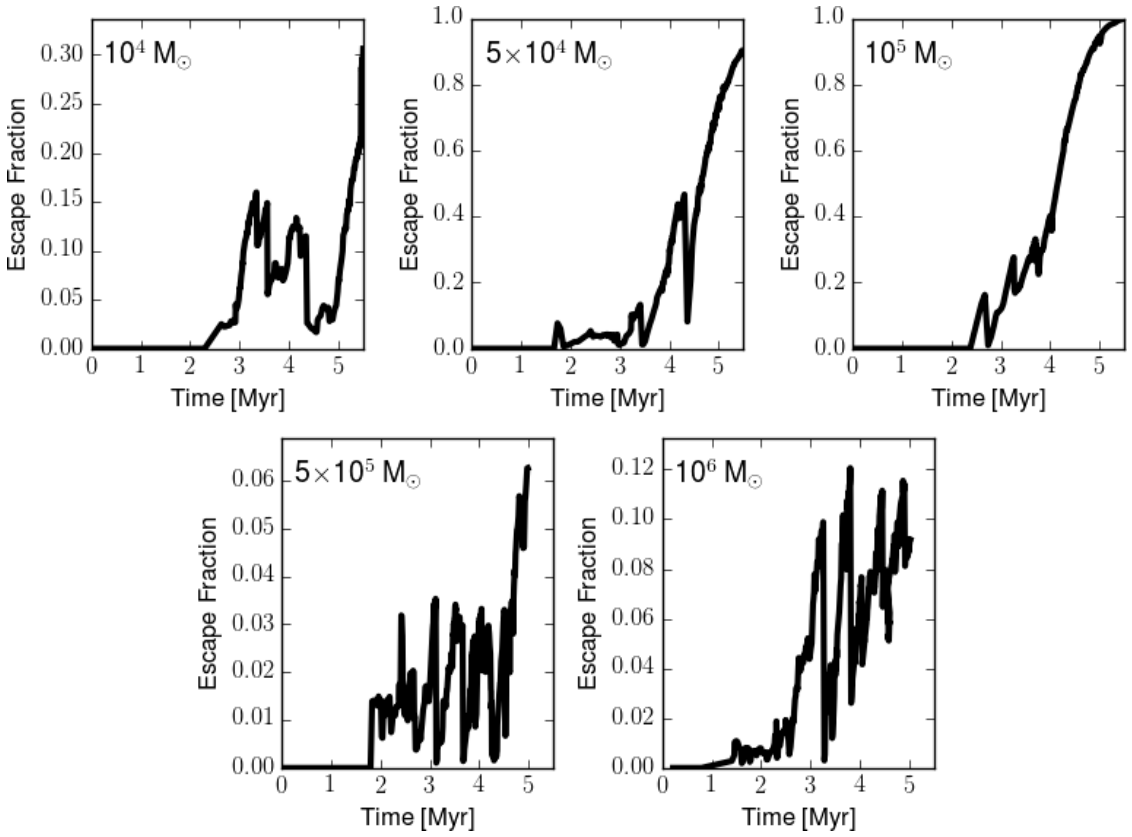

Figure 5.2: The escape fraction from our 5 GMC models of varying mass. The highest escape fractions are seen in the 5×10^4 and 10^5 $M_\odot$ clouds, both of which are nearly fully ionized at the end of the simulation.

GMC Mass [$M_\odot$]	**Average f_{esc} [%]**	**Peak f_{esc} [%]**	**Final f_{esc} [%]**
10^4	9.9	31	31
5×10^4	46	90	90
10^5	50	100	100
5×10^5	1.8	6.3	6.3
10^6	5.6	12	9.2

Table 5.1: Escape fraction results for individual GMCs of different masses.

fractions are also listed in Table 5.1. We note that the average escape fraction for the 10^6 $M_\odot$ GMC has dropped from 15% in Howard et al. (2017b) due to the newly implemented method.

All models show a high degree of variability. The origin of this variability, discussed in Howard et al. (2017b), is directly related to variable HII region sizes. As an HII region grows, the total column density of neutral material between the clusters and the extracted surface decreases resulting in a higher fraction of photons reaching the surface. Due to the turbulent nature of that gas combined with the dynamical motions of the clusters, the conditions locally surrounding the clusters can vary. When a cluster enters a region of high density, the HII region can be shielded from further radiation which leads to its collapse as the gas recombines. This leads to the sharp declines seen in f_{esc}. Fluctuating HII regions have been seen in both observations (De Pree et al., 2014, 2015) and other simulations (Peters et al., 2010a,b; Galván-Madrid et al., 2011; Klassen et al., 2012b).

Generally, the behaviour of f_{esc} follows one of two trends depending on GMC mass — a smoothly increasing f_{esc} at late times with large variations superimposed at early times, or a highly variable f_{esc} which oscillates around a mean value. A clear

example of the first trend is the 5×10^4 $M_\odot$ cloud. After approximately 3 Myr, f_{esc} begins to increase eventually reaching 90% at the end of the simulation. At ∼4 Myr, f_{esc} drops from 47% to 8% within 20 timesteps (or ∼6000 yrs) which is the frequency of data output used for the simulations. There are no further decreases in f_{esc} due to the HII region continually growing in size until it nearly fills the entire simulation volume.

On the other hand, the two highest mass clouds (5×10^5 and 10^6 $M_\odot$) are characterized by large variations throughout their entire evolution and show only a modest increase in f_{esc}. The 10^6 $M_\odot$ models shows two particularly large decreases in f_{esc} at 3 and 3.75 Myr, the first of which drops from 10% to <1%. Over the 5 Myr of evolution, f_{esc} only rises to a maximum of 12%. The 5×10^5 $M_\odot$ oscillates around an f_{esc} of 2% from 2 Myr to 4.5 Myr and only reaches a maximum of 6% in the last 0.5 Myr of evolution.

5.5 Escape Fraction from GMC Populations

The results presented above represent the escape fractions from individual GMCs only. Here, we present a simple model to calculate the f_{esc} from a population of GMCs that are at different stages in their evolution. We tailor our model to be representative of a dwarf starburst galaxy and regular spiral-type galaxy.

Broadly, our model assumes that a new star-forming cloud is birthed every time interval, Δt. The mass of this cloud is drawn randomly from a GMC mass distribution and corresponds to one of the 5 simulations presented above. The GMC is

evolved for an assumed lifetime, after which we consider the cloud destroyed. The net escape fraction and the total SFR of the GMC population at any given time is calculated by summing over the properties of the currently active clouds. The two main observational results used by the model are the mass of molecular gas and the depletion time of the galaxy. These are used to determine the appropriate Δt. We note that, over the timescales considered here, the total mass of molecular gas in each model galaxy is assumed to remain constant. This is a consequence of how we constructed our model and is described in more detail below.

We choose a molecular gas mass of 3×10^9 $M_\odot$, the approximate mass of molecular gas and the cold neutral medium in the Milky Way (Tielens, 2005), for the spiral galaxy model and a mass of 10^8 $M_\odot$ for the starburst dwarf model. This is consistent with local starburst dwarfs studied by McQuinn et al. (2010a).

We then assume that a new GMC becomes star-forming every time interval Δt. The mass of this cloud — which corresponds to one of our 5 models — is randomly drawn from a GMC mass spectrum given by,

$$dN/dM \propto M^\alpha, \tag{5.3}$$

where N is the number of clouds at a given mass, M. We consider two values of α. Exponents of -1.5 and -2.5 are consistent with the distribution of clouds in the inner MW and M33, respectively (Rosolowsky, 2005). These values were chosen not only because of observations, but because the shallower slope implies most of the total mass in GMCs is contained in high mass clouds and vice versa for the steeper

slope. Here, we only present the results of varying the GMC mass distribution for the dwarf galaxy model as the spiral galaxy model is significantly more computationally expensive.

In order to determine the main parameter of our model, Δt, we use the measured depletion time for our target galaxy types. The depletion time is given by,

$$\tau_{dep} = \frac{M_{H_2}}{\dot{M}_*}, \tag{5.4}$$

where M_{H_2} is the total mass of molecular gas in the galaxy, and $\dot{M}_*$ is the SFR. Physically, it represents the amount of time, given the current mass of H_2 and the current SFR, it would take to convert all the molecular gas into stars. A gas depletion time for spiral-type galaxies is typically $\sim$2.35 Gyr (Bigiel et al., 2011) while $\sim$1 Gyr is representative of dwarf starbursts (McQuinn et al., 2010a).

The appropriate Δt is found through the following steps: 1) We start with the total amount of molecular gas within the model galaxy, referred to as the 'reservoir'. 2) A new star-forming GMC appears every time interval Δt. We start with an estimate of this parameter. 3) We evolve each cloud for an assumed lifetime (see below) after which we consider the cloud destroyed. 4) Any gas in the cloud that has not been converted to stars is returned to the mass reservoir from which clouds are drawn. 5) We continue forming new clouds until the reservoir of molecular gas is exhausted.

Through trial and error, we are able to converge on the Δt that ensures the initial amount of molecular gas is converted to stars in one depletion time. We note that we are not suggesting that all the molecular gas is consumed in a depletion time in a real galaxy. Molecular gas is constantly being formed from atomic gas so this would therefore be an incorrect statement. We have adopted the above procedure to be faithful to the definition of the depletion time which is an *instantaneous* measurement of the time it would take to convert a galaxy's molecular gas to stars given the current SFR. Our method for determining Δt ensures we are consistent with this definition. Since Δt remains constant throughout the evolution of our models, we are inherently assuming that the depletion time, and therefore the molecular gas content and the global star formation properties, of the galaxies do not appreciably change.

The procedure outlined above results in Δt values of 0.75 Myr for the dwarf starburst model with α = -1.5, 0.18 Myr for the dwarf starburst model with α = -2.5, and 52 kyr for the spiral galaxy model.

With these values in hand, we complete the final model run by repeating many of the steps already described. Namely, new star-forming clouds are drawn from the adopted GMC mass distribution every time interval Δt and the clouds are evolved for an assumed lifetime after which we consider them destroyed. The length of time we evolve our model is a free parameter but overall its effect is minimal as long as it significantly exceeds the lifetime of our individual GMC models. This is because shortly after starting the model, an equilibrium is established between the number of clouds starting and stopping star formation resulting in a roughly constant number of GMCs with time. Since an element of stochasticity is introduced via randomly

sampling the mass distribution, we have chosen to evolve all models through one full depletion time. The figures presented below indicate that this is sufficient for capturing the behaviour of our model.

We take the lifetimes of the 10^4, 5×10^4 and 10^5 $M_\odot$ GMCs to be 5 Myr. As shown in Howard et al. (2017a), these clouds are nearly entirely disrupted by radiative feedback by this time. The more massive clouds, however, show no evidence of large-scale disruption. We therefore adopt a lifetime of 20 Myr for these clouds to be consistent with Murray et al. (2010) who estimated GMC lifetimes for massive ($\sim10^6$ $M_\odot$) clouds. This is also consistent with the estimated lifetimes of GMCs in M33 (Corbelli et al., 2017). The authors, using a sample of 566 GMCs complete down to $\sim5\times10^4$ $M_\odot$, were able to compare the relative frequencies of clouds with no evidence of star formation, clouds with evidence of embedded star formation, and clouds hosting HII regions. They found that the time between cloud assembly and when the first clusters break through the cloud is 14.2 Myr. They do not consider how long it takes to completely disperse the remaining gas, so the the time between cloud formation and destruction is likely longer. This justifies our use of a 20 Myr lifetime for the massive GMCs. Since our simulations only evolved for $\sim$5 Myr, we assume that the final escape fraction and SFR extends a further 15 Myr. We note that this assumption is only a placeholder until the simulations, which are in the process of completing now, evolve further in time.

At any given time, we know the total population of clouds, which were randomly drawn from an assumed GMC powerlaw mass distribution, and where they are in their respective evolutionary histories. Since the clouds are formed at different times,

the population of GMCs will necessarily contain clouds that are nearing the end of their lifetime while others will be just starting star formation. The instantaneous number of photons being generated by the clusters, and the fraction of those that escape the cloud, are known for each GMC at all times. The escape fraction from the ensemble of clouds is then the instantaneous number of photons escaping all clouds divided by the total number of photons being generated by all clusters. Mathematically, it is expressed as,

$$f_{esc} = \frac{\sum_i N_{esc,i}}{\sum_i N_{tot,i}}, \tag{5.5}$$

where $N_{esc,i}$ is the number of photons escaping from cloud i, and $N_{tot,i}$ is the total number of photons being produced by the stars in cloud i. The star formation rate (SFR) is also calculated by summing the instantaneous SFRs of the individual clouds.

We start by showing the evolution of the reservoir gas mass, used to determine the appropriate Δt values, in Figure 5.3. The dwarf starburst models begins with 10^8 $M_\odot$ which is fully converted to GMCs in 1.005 Gyr and 1.03 Gyr for the cases with α = -1.5 and -2.5 respectively. The spiral galaxy model (right) uses 3×10^9 $M_\odot$ in 2.24 Gyr.

The resulting f_{esc} for the two dwarf models (top and middle) and the spiral model (bottom) are shown as a function of time in Figure 5.4. The averages over a 100 Myr timescale are shown by the solid black points. The histogram represents the normalized distribution of f_{esc} over the entire history of each model. The vertical scale is identical for the time evolution plot and the histogram.

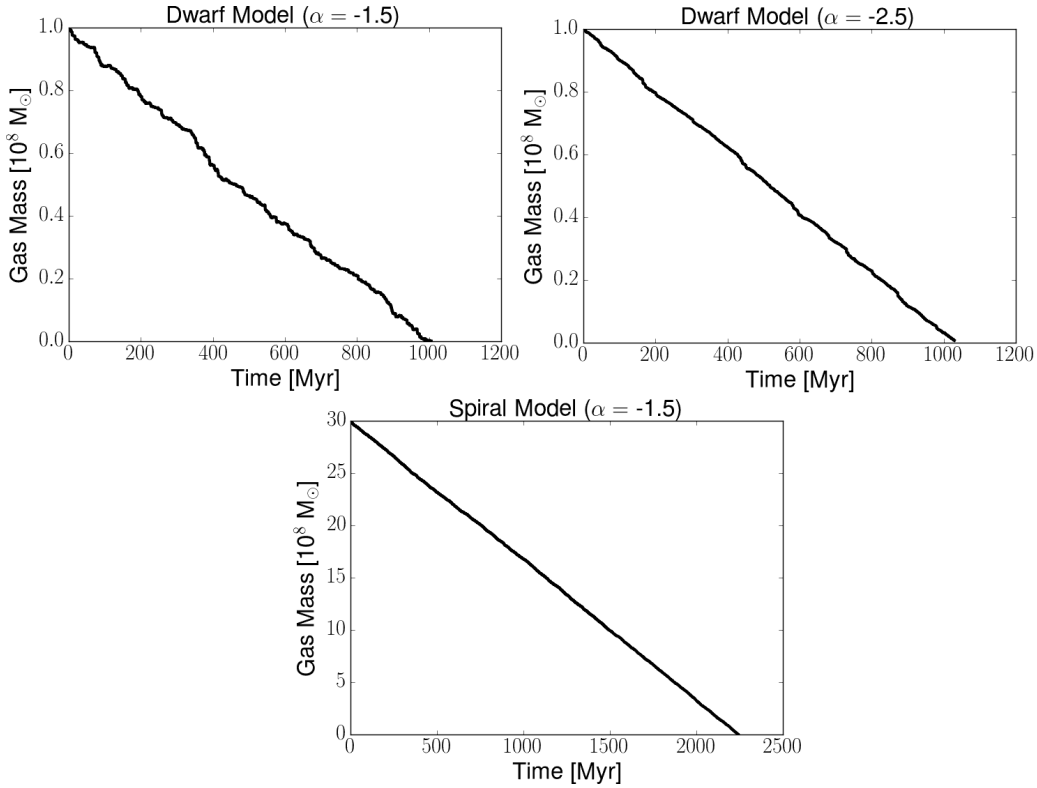

Figure 5.3: The evolution of the mass reservoir out of which GMCs are drawn to determine Δt for the dwarf model with α = -1.5 (top left), α = -2.5 (top right), and the spiral-type model (bottom). We choose the time between GMC formation such that the gas is exhausted after one gas consumption time of $\sim$1 Gyr for dwarf and $\sim$2.35 Gyr for the spiral model.

The dwarf model with α = -1.5 is characterized by a low escape fraction interspersed with infrequent but pronounced peaks that can reach as high as 90%. The histogram indicates that the most likely value of f_{esc} over the entire galaxy's history is 7.8%.

The middle panel of Figure 5.4 demonstrates that varying the slope of the GMC mass distribution can alter the time evolution of f_{esc}. While the most likely value of f_{esc} remains unchanged when considering α = -2.5, the probability of having higher

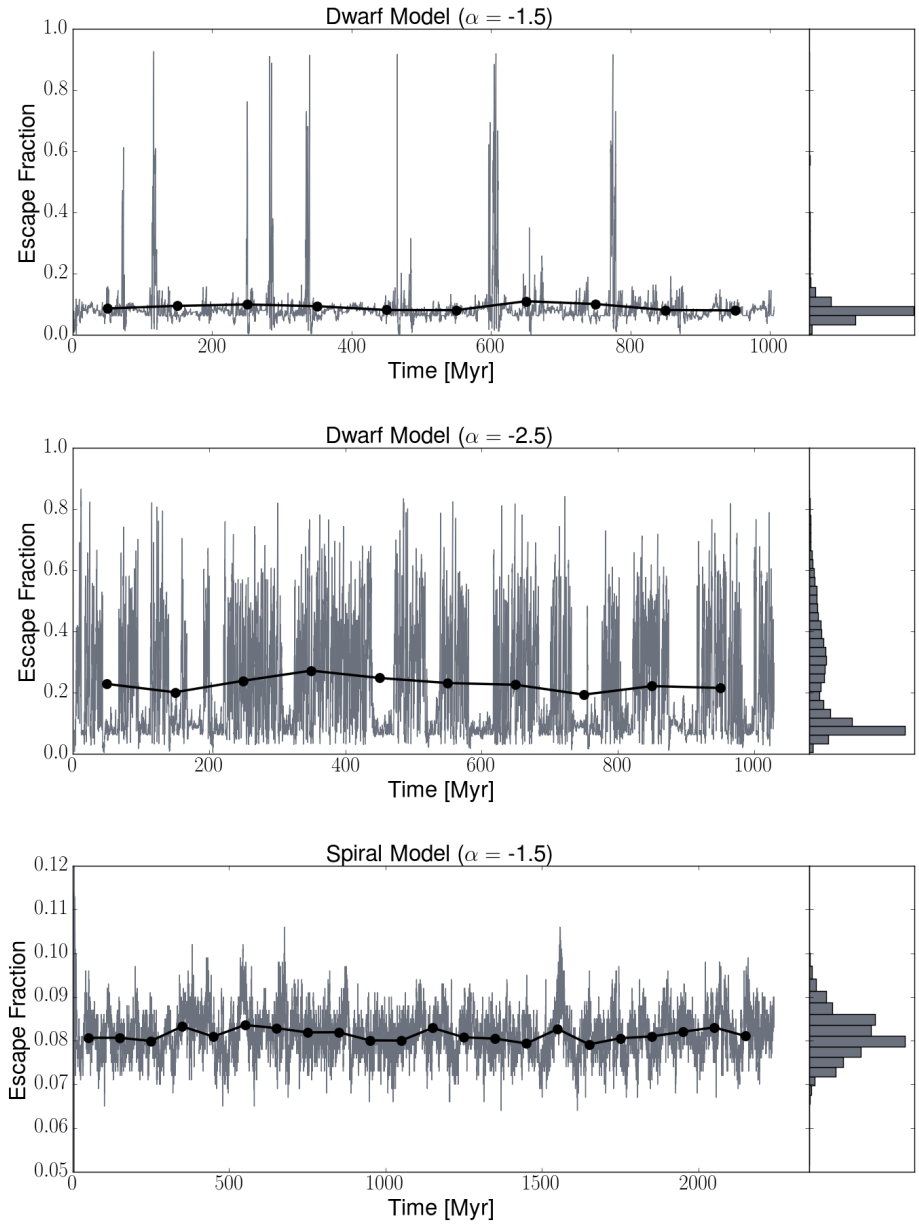

Figure 5.4: The escape fraction for the two starburst dwarf models (top and middle) and the spiral-type galaxy model (bottom) as it evolves over time. Black circles represent the average over 100 Myr timescales. The histogram, plotted with the same vertical scale as the left plot, represents the distribution of f_{esc} over each galaxy's history.

escape fractions at any given time is increased, as demonstrated by the tail of the histogram that extends to high f_{esc}. This is attributed to the different population of GMCs in each case. For the shallower slope (α = -1.5), more mass is contained in the most massive clouds which have correspondingly low escape fractions (see Figure 5.2). Therefore, high f_{esc} values only occur when a subset of the clouds are between 10^{4-5} $M_{\odot}$ and near the end of their lifetime. The case with α = -2.5, however, will have a more mass contained in these low to intermediate mass clouds and therefore a higher f_{esc}. Moreover, since Δt is smaller for α = -2.5 — a higher fraction of low mass GMCs means that clouds need to form more often in order to exhaust the gas reservoir in the same amount of time — there are more GMCs present at any given time which increases the likelihood of having 10^{4-5} $M_{\odot}$ clouds near the end of their life cycle.

Our claim that the intermediate mass clouds with high f_{esc} are responsible for the peaks seen in Figure 5.4 is verified by Figure 5.5. Here, we separate the total escape fraction into the contributions from the different GMC masses. The sum of these curves returns the total f_{esc} discussed above. It is clear from these Figures that the 5×10^4 and 10^5 $M_{\odot}$ GMCs are responsible for the peaks of f_{esc}. The more massive GMCs, on the other hand, only contribute up to 10% of total photons that are escaping from the population of molecular clouds despite hosting a larger stellar population. The low escape fraction from these clouds (see Figure 5.2), combined with their low frequency compared to less massive clouds, limits their contribution to the total f_{esc}.

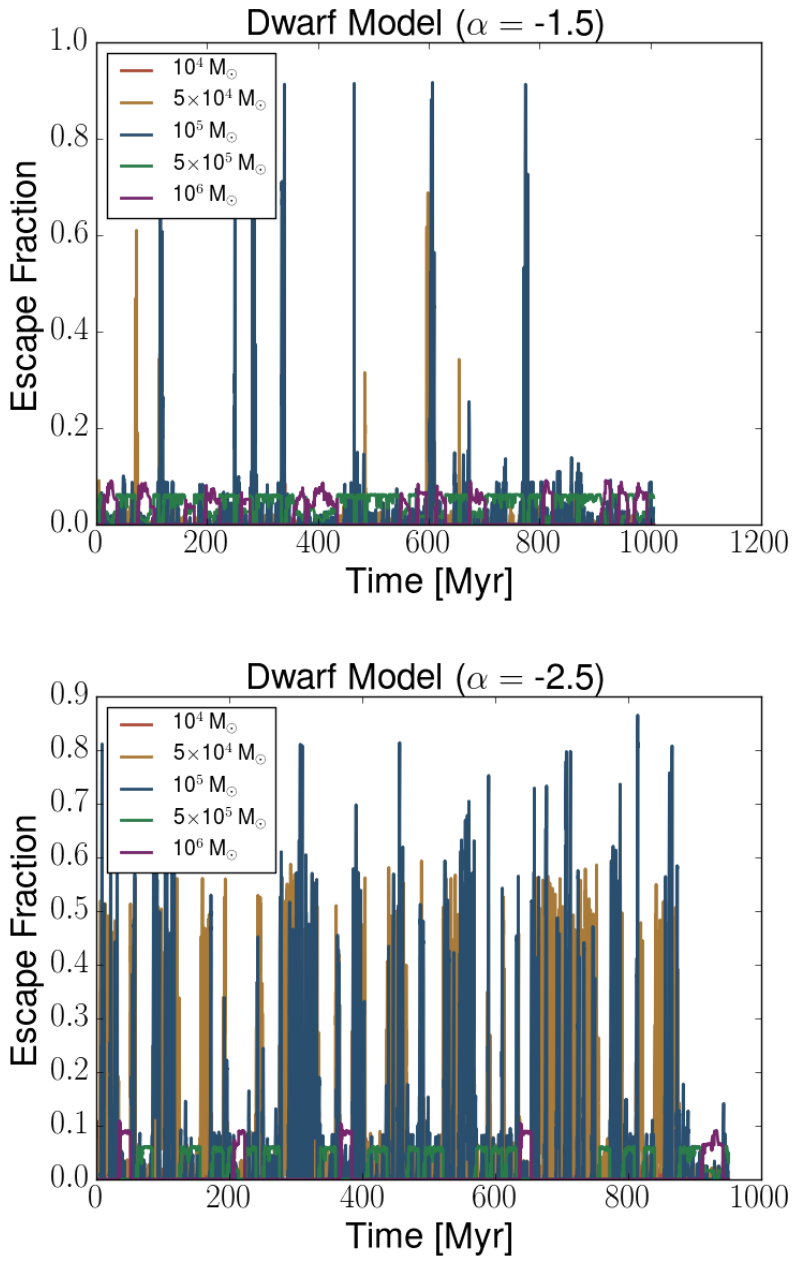

Figure 5.5: The contributions to the total f_{esc} by each of the 5 cloud masses. Note that there can be many GMCs with the same mass at any given time. The sum of these curves represents the total f_{esc} presented in Figure 5.4.

The lower panel of Figure 5.4 shows f_{esc} for the spiral model. Compared to the dwarf models, there is significantly less variation in f_{esc} which only ranges from ∼7-11%. The most common f_{esc} (ie. the peak of the histogram) is 8%. This is consistent with f_{esc} from both dwarf models, indicating that an escape fraction of 8% is a robust result regardless of galaxy type or GMC mass distribution. However, the larger variations in the dwarf models means an increased probability of observing a high f_{esc} at any given time.

The higher variation in the dwarf model is due to the larger Δt parameter. For the dwarf model with α = -1.5, we adopted a Δt value of 0.75 Myr so there will be only ∼7 star-forming GMCs at any given time. Due to the stochastic nature of our model, this will inevitably lead to times when several of the GMCs will be either 5×10^4 or 10^5 $M_\odot$ which have higher escape fractions relative to the other clouds. This will lead to the peak escape fractions of ∼90%. At other times, there will be high mass clouds present (5×10^4 and 10^5 $M_\odot$) that generate a large number of photons but have a low corresponding f_{esc}. This skews the overall escape fraction to small values.

In contrast, the shorter Δt value of 52 kyr for the spiral model means there will be at least ∼96 clouds present at a given time. This limits the impact of stochastic sampling and results in a more consistent mass distribution of GMCs. The significantly higher number of GMCs present at any time means the high escape fractions from 5×10^4 and 10^5 $M_\odot$ are less pronounced. Nonetheless, a similar analysis to Figure 5.5, which is not shown here due to its similarity to the Figures already presented,

indicates that these two clouds masses are still the dominant contributors to the total f_{esc} for the spiral model.

We note that the number of star-forming clouds in the spiral model is less than the number found in M33 by Corbelli et al. (2017). In that work, the authors identify a total of 566 GMCs in M33 which represents a complete sample down to $\sim 5 \times 10^4$ $M_\odot$. A large fraction (32%) of the GMCs, however, show no evidence for star formation. A total of 369 GMCs show either embedded star formation or contain visible HII regions. Our model, therefore, has approximately 4 times less star-forming clouds than their sample. This is attributed to the high SFEs of our individual GMC simulations which range from 16% to 21%. As discussed in (Howard et al., 2017b), this is likely due to not including other forms of feedback during the early phases of cluster formation (ie. stellar winds). Since our SFEs are higher than those observed in local GMCs, we require less clouds overall to fully convert the molecular gas to stars in one depletion time.

5.6 Comparison with Observations of Galactic Star Formation Rates

To compare with observations of starburst dwarf and spiral-type galaxies, we plot the SFRs, given by the summed instantaneous SFRs of the cloud population, in Figure 5.6. Figure 5.6 is plotted in the same manner as the escape fractions in Figure 5.4.

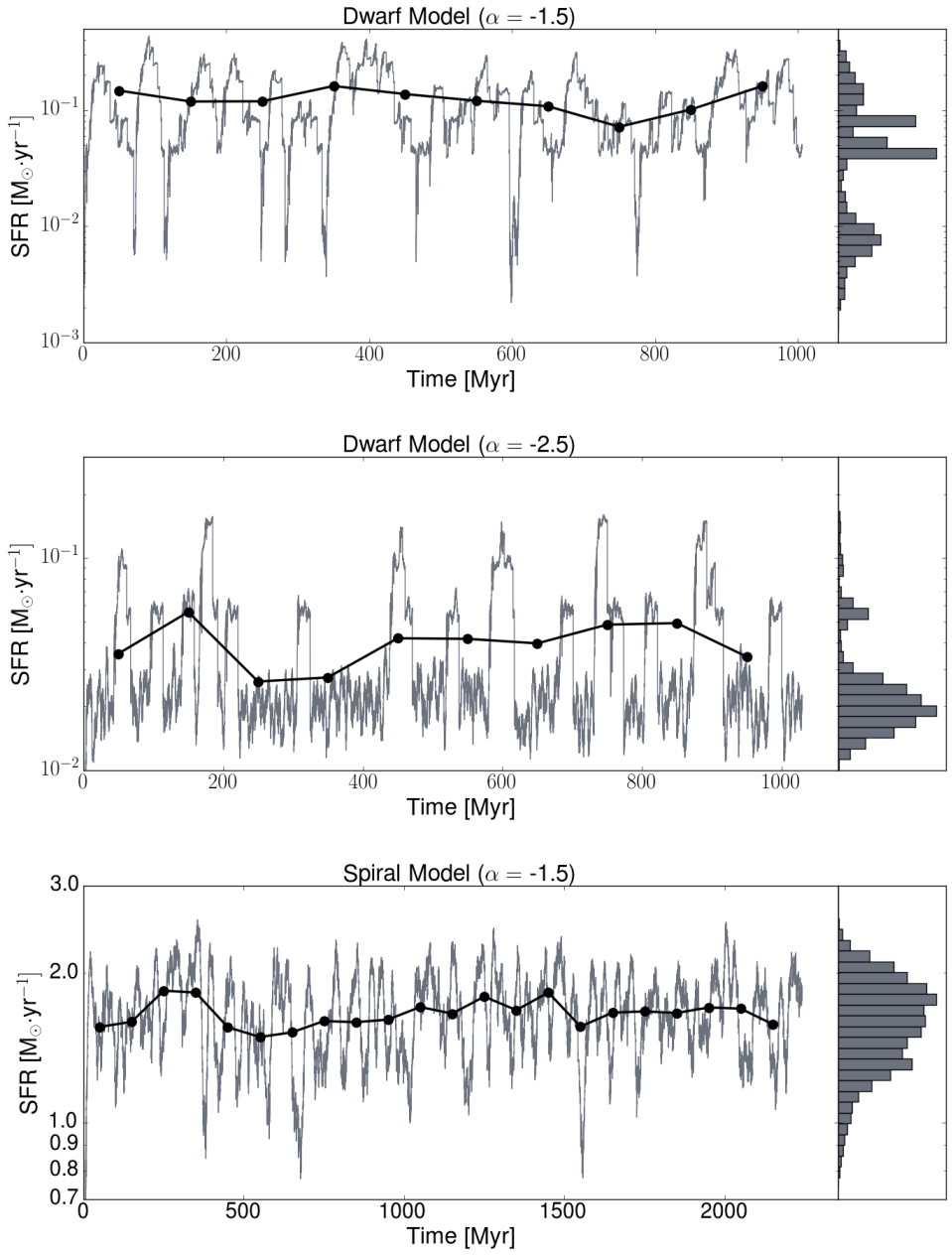

Figure 5.6: The evolution of the star formation rate (SFR) for the dwarf starburst models and the spiral-type galaxy model. As in Figure 5.4, the black dots represent the average values in 100 Myr bins and the histogram shows the overall distribution of SFRs over each model's history.

The SFR for the dwarf model with α = -1.5 varies between 2×10^{-3} and 0.4 $M_{\odot}yr^{-1}$. The most likely SFR from the histogram is 5×10^{-2} $M_{\odot}yr^{-1}$. Changing the GMC mass distribution slope to α = -2.5 results in a similar range (10^{-2} to 0.2 $M_{\odot}yr^{-1}$) and a slightly smaller peak value of 2×10^{-2} $M_{\odot}yr^{-1}$. We can directly compare to observed SFRs, and inferred star formation histories (SFHs), of starburst dwarfs from McQuinn et al. (2010a) who were able to reconstruct the SFHs of local dwarfs using a combination of stellar photometry and stellar evolution models. The results from this analysis indicate peak SFRs which range from 5.2×10^{-4} to 9.7×10^{-1} $M_{\odot}yr^{-1}$ depending on the galaxy studied. Their average peak SFR was 0.13 $M_{\odot}yr^{-1}$. The results presented here are consistent with several of their observed galaxies but we note that the star formation histories of dwarf starbursts vary significantly. Our results are also consistent with the observations of Weisz et al. (2011) who measured the average SFRs in dwarfs of various morphologies over their entire history. A similarly large spread in SFRs between galaxies is also found.

The temporal variation of the SFRs for the dwarf model is also consistent with the inferred SFHs. The results presented in McQuinn et al. (2010a) and McQuinn et al. (2010b) demonstrate variations of up to an order of magnitude in the SFRs of dwarf starbursts over timescales of 10-20 Myr. The combination of our GMC scale physics and the stochastic sampling of a GMC mass distribution naturally reproduce this feature.

Similar to the escape fraction presented in Figure 5.4, the spiral model shows less variation in the SFR compared to the dwarf model. The SFR varies from $\sim$0.8 to 2.5 $M_{\odot}yr^{-1}$. The peak of the SFR histogram occurs at 1.77 $M_{\odot}yr^{-1}$.

The SFR from our model is consistent with observations of local spiral galaxies. The SFR of the Milky Way, which was used as a basis for choosing the initial reservoir mass for the spiral model, is $\sim$1.65 $M_{\odot}yr^{-1}$ (Licquia & Newman, 2015). The SFRs measured for local, normal spiral galaxies are typically between 0.5-10 $M_{\odot}yr^{-1}$ (Gao & Solomon, 2004). Our results fall well within this observed range.

Therefore, by utilizing only a suite of 5 GMC mass models under the assumption of a constant GMC formation rate, we have been able to reproduce the behaviour of the SFRs in dwarfs and spirals. This is likely due to using the gas consumption time as a main observational constraint in our model since it inherently depends on the SFR.

5.7 Discussion and Conclusions

The escape of UV photons from GMCs which host massive stars drives many crucial astrophysical processes, from determining the chemical, thermal, and ionization state of the ISM by contributing to the ISRF (Draine, 2011) to participating in cosmic reionization (Wise et al., 2014). Estimates of the escape fraction from an entire galaxy vary significantly — the distribution of dense gas being a main factor in controlling f_{esc}.

In order to place constraints on f_{esc} from both individual and populations of molecular clouds, we present the UV photon escape fraction from a suite of GMC models simulated using the FLASH code. The simulations, taken from (Howard et al., 2017a), consisted of 5 GMCs with masses of 10^4, 5×10^4, 10^5, 5×10^6, and

10^6 $M_\odot$. All clouds had the same initial density of 100 cm^{-3} and an initial virial parameter of 3. Sink particles, coupled with a custom subgrid model, are used to model cluster formation and radiative transfer is included via a raytracing scheme.

We note that the escape fractions presented in this work should be interpreted as lower limits. We do not include the effects of stellar winds in our simulations which have been shown to significantly alter the density structure surrounding massive stars (Dale & Bonnell, 2008; Rahner et al., 2017). The momentum imparted by stellar winds can remove gas from a cluster's surroundings, resulting in low density regions which are easily ionized thereby allowing more UV photons to escape the cloud.

To represent f_{esc} from a population of GMCs, we develop a model which forms clouds by randomly sampling a GMC mass distribution over fixed time intervals. Two realizations of the model were completed to represent a dwarf starburst galaxy and a normal spiral-type galaxy.

The main inputs into this model are total molecular gas mass of the galaxy, and the time between cloud formation (Δt). Masses of 10^8 and 3×10^9 $M_\odot$ are used for the dwarf and spiral models, respectively. One of our simulated clouds is drawn randomly from a GMC mass distribution of $dN/dM \propto M^\alpha$, and the cloud is evolved for either 5 Myr for 10^{4-5} $M_\odot$ or 20 Myr for more massive objects. A new cloud is drawn every time interval Δt. The appropriate values for this parameter are determined by ensuring that the mass of molecular gas we have adopted is converted to stars in one depletion time — taken to be 1 Gyr for dwarfs (McQuinn et al., 2010a) and 2.35 Gyr for spirals (Bigiel et al., 2011). This process is repeated and the net f_{esc}

and SFR from the population of GMCs is calculated. For the spiral model, we fix α at -1.5 but complete two realizations — α = -1.5 and -2.5 — of the dwarf starburst model.

We stress that our model represents f_{esc} from a population of GMCs and not an entire galaxy. To fully constrain the latter problem, a full treatment of the ISM in galaxies is required, as well as the contribution from field stars. Nevertheless, the results from this work are valuable inputs for galactic scale modeling due to the increased resolution and the inclusion of physical processes (eg. radiative feedback) that are typically neglected in larger scale models.

The main conclusions of this work are summarized as follows:

- Escape fractions from individual clouds vary strongly with time. The final f_{esc} values for individual clouds, in order of ascending GMC mass, are 31%, 90%, 100%, 6%, and 9%. The high final f_{esc} for the 5×10^4 and 10^5 $M_\odot$ clouds is due to nearly complete ionization of the GMC at 5 Myr. All models show several large fluctuations (up to a factor of 6) over small timescales. These fluctuations are attributed to dynamic HII regions within the highly filamentary molecular clouds which grow and shrink rapidly depending on the local conditions surrounding the clusters.

- The escape fraction from our dwarf starburst models vary from values near zero to 90%. The typical value for f_{esc} is 8% for both values of α, but the model with α = -2.5 shows a higher degree of variation. The 5×10^4 and 10^5 $M_\odot$ GMCs, which have the highest f_{esc} at late times, are responsible for peaks

in the escape fraction. The corresponding SFRs are in the range of 10^{-3} and 0.4 $M_{\odot}yr^{-1}$ with typical values of $5{\times}10^{-2}$ and $2{\times}10^{-2}$ $M_{\odot}yr^{-1}$ for α of -1.5 and -2.5, respectively. These values are consistent with the reconstructed star formation histories of starburst dwarf galaxies. The observations of dwarfs also show rapid variations in the SFR over 10-20 Myr timescales which is recovered by our model.

- The spiral model shows significantly less variation in f_{esc} (7-11%) compared to the dwarf models. However, the most likely value of f_{esc} remains unchanged indicating that, to first order, the escape fraction of a GMC population can be taken to be 8% regardless of galaxy type. We find SFRs of $\sim$1.77 $M_{\odot}yr^{-1}$ with the highest values reaching 2.5 $M_{\odot}yr^{-1}$. This is comparable to the MW (1.65 $M_{\odot}yr^{-1}$ (Licquia & Newman, 2015)) and is consistent with nearby, spiral-type galaxies which typically have SFRs in the range of 0.5 to 10 $M_{\odot}yr^{-1}$ (Gao & Solomon, 2004).

  The success of our simple model in reproducing the properties of our target objects, in combination with our detailed treatment of GMC scale cluster formation, means our f_{esc} results can provide important constraints for galactic scale simulations. The variations in f_{esc} from one GMC, and from a population as a whole, also highlights the importance of a fully self-consistent and highly resolved treatment of star formation in simulations which study the escape fraction of UV photons from a galaxy. We will examine the implications of these UV escape fractions from GMCs in galaxies, to the question of cosmic reionization, in a future paper.

Chapter 6

Conclusions

6.1 Thesis Summary

The formation of star clusters is a hierarchical process that takes place in filamentary structures that are generated by supersonic turbulence within GMCs. This process is heavily influenced by the physical structure and dynamics of the host GMC which can differ widely between clouds. The masses of GMCs span several orders of magnitude (10^{4-7} $M_\odot$) and clouds can either exist in both bound and unbound states with virial parameters in the range of 0.5 to 5 (Rosolowsky, 2007). One consistent property of GMCs, however, is their low global SFE of $\sim$2% (Evans, 1991).

A mixture of radiative feedback — both radiation pressure, and the heating/ionization of the cluster-forming gas — and the pressure support from turbulent gas motions is one proposed mechanism to limit the SFE in molecular clouds. Radiative feedback

is one of the first forms of stellar feedback to activate in a star-forming region, and is therefore important to consider, but the inclusion of accurate radiation transfer is inherently difficult and computationally expensive. Previous studies of radiative feedback indicate that it plays only a minor role in suppressing star formation, but these works typically only consider a subset of GMC properties. Moreover, the effects of radiative feedback on the early evolution of cluster properties are not well constrained.

Star cluster formation, and the radiation produced by said clusters, also contributes to processes on scales larger than the GMC out of which they form. UV photons from young clusters contribute to the ISRF which sets the chemical, thermal, and ionization state of the ISM within galaxies. Stellar photons escaping from entire galaxies are also thought to be a main driver of cosmic reionization. Both of these problems rely on photons escaping from a molecular cloud and, therefore, depend intimately on the GMC scale physics of early cluster formation.

In this thesis, we address how cluster formation and evolution is tied to the problems of GMC initial conditions and structure, and radiative feedback. We also put important constraints on the escape fractions of UV photons from GMCs. We address these issues via numerical simulations with the AMR code *FLASH*.

The numerical methods utilized in our simulations represent a major leap forward in the accurate treatment of cluster formation and its link to radiative feedback. This is for two main reasons. Firstly, our subgrid model, the culmination of years of development, treats star formation within clusters in an observationally motivated

way. Unlike previous studies (Harper-Clark, 2011; Dale & Bonnell, 2011; Dale et al., 2012b) that instantly convert a newly formed cluster's mass into stars, we allow stars to form gradually within the cluster. As discussed in Chapter 1, the stars in a cluster are not necessarily coeval — an observation naturally reproduced by our model. Moreover, our clusters can accrete from the surrounding gas and grow in mass. Clusters are not instantaneously cut off from the surrounding medium at the onset of star formation, but this is often overlooked in previous numerical works.

The second main advantage of our numerical methods is the use of a raytracer. It treats many relevant physical processes including photoionization, photoionizational heating, a self-consistent treatment of the ionization state of the gas, and additional heating via non-ionizing radiation. We have also included the capability to treat the direct radiation pressure UV photons exert on dust grains — a key component missing from most radiative transfer schemes. This is all computed efficiently enough to treat multiple sources of radiation in a reasonable time. Similar simulations done previously to this thesis, for example Dale et al. (2012b) and all previous simulations from the same group, use simpler radiative transfer schemes that relies on identifying the locations of the Stromgen sphere around an ionizing source and simply setting the gas within that region to 10^4 K. Furthermore, the additional heating from non-ionizing radiation is neglected.

In Chapter 2, we presented a suite of turbulent, 10^6 $M_\odot$ GMCs with initial virial parameters that range from 0.5 to 5 (ie. bound to unbound). We found that the resulting SFE depends sensitively on the initial virial parameter. The final SFEs ranged from 19-33% with the most bound models being the most efficient star-

forming clouds. We conclude that the most significant factor in ensuring low SFEs in molecular clouds is that they begin as essentially unbound entities. Radiative feedback will not drastically reduce the SFE in bound clouds. The properties of the clusters themselves also depend on the initial virial parameter which is shown to alter both the total number and mass distribution of the clusters. Despite the production of pronounced HII regions, radiative feedback only limited the SFE by typically $\sim$1%. No large-scale outflows or unbinding of the gas are observed. This result, in combination with high SFRs compared to locally observed regions, suggests that alternate forms of feedback, in addition to starting with unbound clouds, are required to halt star formation and disperse massive, 10^6 $M_\odot$ GMCs.

We followed this up with the suite of simulations in Chapter 3 that instead fix the initial virial parameter and varied the GMC mass from 10^4 to 10^6 $M_\odot$. We chose an initial virial parameter of 3 because, as shown in Chapter 2, this results in lower SFEs and α quickly decays to 1 which is consistent with the average GMC in the MW. Contrary to the results for massive, 10^6 $M_\odot$ GMCs in Chapter 2, we find that radiative feedback globally unbinds GMCs with masses of 5×10^4 and 10^5 $M_\odot$ and lowers the SFE by a factor of two. This was attributed to the balance between the internal energy and the gravitational potential energy of the cloud. In this mass range, the internal energy, a proxy for the energy injected by feedback, is sufficient to destroy the GMC. We combined the results from all simulations to create an embedded cluster mass function which is shown to agree with observations only when radiative feedback is included. A clear relation is also found between the maximum mass cluster ($M_{c,max}$) and the mass of the host GMC (M_{GMC}) which scales

as $M_{c,max} \propto M_{GMC}^{0.81}$. A steeper slope is found for purely hydrodynamical simulations, indicating that radiative feedback plays a role in limiting the growth of the most massive star clusters. While the normalization of our SFRs is again high compared to observations, we show that we successfully reproduce both the trend in SFR with cluster mass and the scatter in the relation, indicating that our simulations capture a fundamental aspect of star cluster formation.

In Chapter 4, we presented a detailed analysis of f_{esc} from a single, 10^6 $M_\odot$ GMC. The flux of ionizing photons across the cloud surface is highly anisotropic in both time and space due to the filamentary and clumpy nature of the intervening gas. The escape fraction is similarly variable with average values of 15% overlaid with distinct peaks that can reach as high as ∼30% and subsequently drop over very short timescales. The variable nature of f_{esc} is tied to the size of the HII regions. Large HII regions which extend to the edge of the simulation boundary result in high escape fractions while low f_{esc} values are seen when the gas is mostly neutral. The collapse of the HII regions is directly related to the turbulent nature of the gas surrounding the luminous clusters which causes the local density, and therefore the recombination rate, to vary with time.

Finally, in Chapter 5, we presented f_{esc} from the complete range of cloud masses simulated in Chapter 3 and showed that low escape fractions do not characterize all GMCs. This is because the fractional volume of ionized gas varies between different mass molecular clouds. Due to the near full ionization of the 5×10^4 and 10^5 $M_\odot$ GMCs, f_{esc} approaches 100% by 5 Myr. We then presented a simple model for combining these results to represent the total f_{esc} from a population of GMCs in

dwarf starburst and spiral-type galaxies. We found that the typical f_{esc} from all model galaxies is ∼8%, however the escape fractions in the dwarf models can temporarily reach as high as 90%. The typical SFRs in the two dwarf models and the spiral model are 2×10^{-2}, 5×10^{-2}, and 1.77 $M_\odot$ yr^{-1}, respectively. These values are consistent with the SFRs of the objects they are meant to represent.

6.2 Broader Implications for Cluster Formation

The detailed numerical simulations presented in this thesis have several profound implications for cluster formation and evolution. Firstly, the physical conditions (eg. mass and boundedness) of the host GMC affect star cluster formation. Stated another way, the specific evolutionary history of an individual GMC can have lasting impacts on its cluster population. This is shown most clearly in Chapter 2, which demonstrated that the initial virial parameter controls the total number of clusters as well as their mass distributions. We also showed in that Chapter that, after ∼2.5 Myr of evolution, all clouds were globally virialized and therefore would appear similar observationally. There are, however, already marked differences in the cluster populations at this time. Therefore, not only are the instantaneous properties of a GMC relevant to star formation, but so are the evolutionary histories of these objects. This may be a possible explanation for the differences in SFRs and SFEs observed in local GMCs. Lada et al. (2010), for example, find a spread of up to an order of magnitude in the number of YSOs for clouds with the same amount of dense gas.

Differences in the assembly histories and early evolution of these GMCs may explain these variations.

In Chapter 2, we clearly demonstrated that the SFE of a GMC is inversely proportional to the initial virial parameter. This has important implications for star formation on both the GMC scale and galactic scales. Firstly, on GMC scales, this is likely an important contributor to the low observed SFEs of molecular clouds. Moving away from the paradigm that all clouds are bound, even for a portion of their lifetime, therefore reduces the overall role of feedback processes which, at least for radiative feedback as demonstrated here, may not be sufficient in limiting star formation to the observed values. On galactic scales, the presence of unbound clouds can possibly explain the low global SFRs — $\sim$1.65 $M_{\odot}yr^{-1}$ (Licquia & Newman, 2015) for the MW — compared to what would be expected if all the molecular gas in a galaxy was bound and undergoing freefall collapse (>200 $M_{\odot}yr^{-1}$, Evans (1999)). Additionally, working in a framework in which GMCs are unbound during their assembly and early evolution may illustrate why $\sim$32% of the observed molecular clouds in M33 show no evidence for current star formation (Corbelli et al., 2017). Detailed measurements of the virial parameter in such clouds, in combination with simulations modeling the formation of GMCs, should therefore be a driving scientific goal in future works.

It is also clear from this thesis that the formation of a star cluster cannot be considered in isolation. We demonstrate that the HII regions produced by young clusters are dynamic in both time and space. The flickering of HII regions is one of the most visually dramatic aspects of our simulations and its effects should be

considered in the global picture of cluster formation. It indicates that gas which is currently ionized is not necessarily restricted from participating in future star formation. In terms of implications for cluster formation, these HII regions can extend tens of parsecs through a GMC, enveloping clusters that otherwise would be free to accrete neutral gas. The effects of an external source of irradiation, as illustrated by Dale et al. (2007), can alter the course of cluster formation.

Even more important, however, is the role of star cluster merging. We show in Chapter 3 that up to 50% of the total mass contained in clusters has participated in at least one merger. This is true for all GMCs, regardless of mass. Cluster formation is therefore not solely a top-down (ie. gravitational fragmentation) or a bottom-up process but a combination of both — a fact often overlooked by star formation theorists. There is now observational evidence that young clusters are substructured, possibly a result of merging events (Kuhn et al., 2015).

Shifting to a paradigm in which clusters initially fragment out of dense filaments and grow via a mixture of accretion and mergers may be the key to understanding several outstanding questions relating to cluster properties. For example, the origin of the cluster mass function for young clusters is not understood. The merging of distinct star-forming regions may also explain the age spreads observed in young clusters (Da Rio et al., 2010).

Radiative feedback alone is clearly not sufficient to explain the low global SFEs of molecular clouds. In all our simulations, regardless of virial state or mass, we find SFEs that are higher than the average GMC. Therefore, some combination of

protostellar jets, stellar winds, and supernovae is required. Nevertheless, radiative feedback does play a role in the growth of clusters. In Chapters 2 and 3, we have shown that radiative feedback lowers the mass of the most massive clusters relative to purely hydrodynamical simulations. Since it also affects the number of clusters formed, radiative feedback is likely an important piece of the puzzle considering the origin of the cluster mass function.

Despite the limited role of radiative feedback in terms of global SFEs, it has important implications for the lifetimes of GMCs. Estimates span the range of timescales from a single free-fall time to upwards of 10 free-fall times (Elmegreen, 2000; Hartmann et al., 2001; Scoville & Wilson, 2004). Our results show that, for intermediate mass GMCs, radiative feedback can completely ionize and unbind the clouds by $\sim$5 Myr. This would place the lifetimes of these clouds between 1 and 2 free-fall times. The same behaviour is not observed for more massive clouds, however, implying that all GMCs do not have the same lifetime. Instead, it will be a function of GMC properties such as their mass.

In terms of processes on scales larger than GMCs, we have demonstrated that UV photons are capable, to some degree depending on the GMC mass, of escaping their host molecular clouds. This is a reflection of their internal filamentary structure. The results presented here represent the first attempt at characterizing the evolution of f_{esc} in GMCs. The highly spatiotemporal variation of both the ionizing flux and escape fraction — a product of internal GMC turbulence and the resulting filamentary structure of the gas — suggests that the strength of the ISRF should be equally variable. Therefore, the assumption of a Habing field, which is only a local

measurement of the UV background, present everywhere in a galaxy is likely a poor assumption. Instead, the local structure of the UV portion of the ISRF should have strong variations depending on the number of nearby, massive young clusters. This highlights the importance that GMC scale models, such as those presented in this thesis, play in understanding the global ISM structure.

The same variability extends to the global escape fraction from a population of GMCs, and therefore an entire galaxy. The detailed interplay among turbulence, star formation, and radiative transfer on these scales is likely responsible for the fluctuations in f_{esc} observed in galactic-scale simulations (Paardekooper et al., 2011). The result that, to first order, f_{esc} from a population of GMCs is well represented by a typical value of 8% regardless of galaxy type provides a valuable starting point for models of cosmic reionization.

6.3 Future Work

While the work presented in this thesis represents one of the most thorough examinations of radiative feedback in GMCs to date, the full parameter space of molecular cloud properties has not been explored. For example, magnetic fields are not included in our simulations. Magnetic fields are known to slow the collapse of molecular clouds and lower the SFE per freefall time of the cloud (Myers & Goodman, 1988; Tilley & Pudritz, 2007; Federrath & Klessen, 2012). The density structure of the filaments which host cluster formation is also affected (Kirk et al., 2015). It is therefore possible that a combination of turbulence, magnetic fields, and radiative feedback can

reproduce the SFEs observed in local star-forming clouds. *FLASH* includes magnetohydrodynamic solvers making the exploration of this problem extremely tractable. Preliminary simulations of supercritical 10^5 $M_\odot$ GMCs indicate that the presence of magnetic fields only delays the onset of cluster formation while the long term SFEs are not changed significantly.

The question of how our models extend to the high-redshift universe during the epoch of globular cluster formation is also of the utmost importance. As pointed out by multiple authors (Harris & Pudritz, 1994; Elmegreen & Efremov, 1997; Kruijssen, 2015), GCs are likely the product of "normal" cluster formation in high-redshift galaxies. The properties of the GMCs which host GC formation, however, are thought to differ significantly from present day molecular clouds. The high pressure environments in these galaxies likely result in clouds that are more massive than MW clouds and denser by several orders of magnitude. We have already shown that the local gas density surrounding clusters can strengthen the role of radiative feedback. Our own results also suggest 10^6 $M_\odot$ GC-like objects can form out of $\sim 5\times10^7$ $M_\odot$ GMCs, providing further motivation for extending our calculations to more massive clouds. Not only are the mass and density expected to vary in high redshift star-forming GMCs, the metallicity of the gas is also subsolar. The metallicity determines gas cooling rates as well as the gas opacity through which the radiation is coupled to star-forming gas. Therefore, simulating dense GMCs with subsolar metallicity with the inclusion of radiative feedback can help identify possible formation scenarios for GC formation. Moreover, the detailed merging histories of each cluster allow for the testing of possible enrichment scenarios that may give rise to the multiple stellar

populations within individual GCs. Such simulations are currently underway and early indications are that the role of metallicity, at least for values down to a tenth solar, in cluster formation is minimal.

One of the main advantages to isolated GMC simulations is the degree of control over the initial conditions. The role of different physical conditions, and how these conditions affect cluster formation, can be identified and thoroughly explored by such simulations. However, considering a GMC to be an isolated object neglects the effects of the large scale galactic potential, galactic shear, cloud-cloud collisions, the external properties of the ISM, and gas accretion onto the molecular cloud. One potential remedy to this problem is by extracting GMCs that form in galactic disk simulations and re-simulating with higher resolution. Such a methodology has been attempted previously (Rey-Raposo et al., 2015; Dobbs, 2015) but the results depend sensitively on the extraction and refinement process. This can potentially be alleviated by using *FLASH* for both the galactic disk simulation, for example those being completed by Koertgen, Banerjee, Pudritz and Schmidt (in prep.), and the GMC scale simulation to ensure a consistent treatment of the physics, extracting the clouds before the onset of star formation, and slowly increasing the refinement level to avoid numerical artifacts introduced by resolution changes.

As has been pointed out numerous times throughout this thesis, star formation is a multi-scale process. From stars to clusters, clusters to GMCs, GMCs to galaxies, and galaxies to the vast IGM pervading our universe, the processes occurring at one scale are intimately linked to those above and below it. Behind it all, however, is

star formation; the fundamental astrophysical process that makes this thesis, and your reading of it, possible.

Bibliography

Abreu-Vicente, J., Kainulainen, J., Stutz, A., Henning, T., & Beuther, H. 2015, A&A, 581, A74

Agertz, O. & Kravtsov, A. V. 2015, ApJ, 804, 18

Alves, J. & Bouy, H. 2012, A&A, 547, A97

André, P., Di Francesco, J., Ward-Thompson, D., Inutsuka, S.-I., Pudritz, R. E., & Pineda, J. E. 2014, Protostars and Planets VI, 27

Arzoumanian, D., André, P., Didelon, P., Könyves, V., Schneider, N., Men'shchikov, A., Sousbie, T., Zavagno, A., Bontemps, S., di Francesco, J., Griffin, M., Hennemann, M., Hill, T., Kirk, J., Martin, P., Minier, V., Molinari, S., Motte, F., Peretto, N., Pezzuto, S., Spinoglio, L., Ward-Thompson, D., White, G., & Wilson, C. D. 2011, A&A, 529, L6

Ballesteros-Paredes, J., Hartmann, L. W., Vázquez-Semadeni, E., Heitsch, F., & Zamora-Avilés, M. A. 2011, MNRAS, 411, 65

Ballesteros-Paredes, J., Klessen, R. S., Mac Low, M.-M., & Vazquez-Semadeni, E. 2007, Protostars and Planets V, 63

Balsara, D., Ward-Thompson, D., & Crutcher, R. M. 2001, MNRAS, 327, 715

Banerjee, R. & Pudritz, R. E. 2006, ApJ, 641, 949

Banerjee, R., Pudritz, R. E., & Anderson, D. W. 2006, MNRAS, 373, 1091

Barnes, A. T., Kong, S., Tan, J. C., Henshaw, J. D., Caselli, P., Jiménez-Serra, I., & Fontani, F. 2016, MNRAS

Bastian, N. & Silva-Villa, E. 2013, MNRAS, 431, L122

Bate, M. R. 2009, MNRAS, 392, 590

—. 2012, MNRAS, 419, 3115

Bate, M. R., Bonnell, I. A., & Bromm, V. 2003, MNRAS, 339, 577

Bertoldi, F. & McKee, C. F. 1992, ApJ, 395, 140

Bigiel, F., Leroy, A. K., Walter, F., Brinks, E., de Blok, W. J. G., Kramer, C., Rix, H. W., Schruba, A., Schuster, K.-F., Usero, A., & Wiesemeyer, H. W. 2011, ApJ, 730, L13

Bisbas, T. G., Haworth, T. J., Williams, R. J. R., Mackey, J., Tremblin, P., Raga, A. C., Arthur, S. J., Baczynski, C., Dale, J. E., Frostholm, T., Geen, S., Haugbølle, T., Hubber, D., Iliev, I. T., Kuiper, R., Rosdahl, J., Sullivan, D., Walch, S., & Wünsch, R. 2015, MNRAS, 453, 1324

Blitz, L., Fukui, Y., Kawamura, A., Leroy, A., Mizuno, N., & Rosolowsky, E. 2007, Protostars and Planets V, 81

Boneberg, D. M., Dale, J. E., Girichidis, P., & Ercolano, B. 2015, MNRAS, 447, 1341

Bonnell, I. A., Clark, P., & Bate, M. R. 2008, MNRAS, 389, 1556

Bonnell, I. A., Smith, R. J., Clark, P. C., & Bate, M. R. 2011, MNRAS, 410, 2339

Bosch, G., Terlevich, E., & Terlevich, R. 2009, AJ, 137, 3437

Brodie, J. P. & Strader, J. 2006, ARA&A, 44, 193

Brunt, C. M., Kerton, C. R., & Pomerleau, C. 2003, ApJS, 144, 47

Carroll, B. W. & Ostlie, D. A. 1996, An Introduction to Modern Astrophysics (Pearson)

Castor, J., McCray, R., & Weaver, R. 1975, ApJ, 200, L107

Chabrier, G. 2005, in Astrophysics and Space Science Library, Vol. 327, The Initial Mass Function 50 Years Later, ed. E. Corbelli, F. Palla, & H. Zinnecker, 41

Clark, P. C., Bonnell, I. A., Zinnecker, H., & Bate, M. R. 2005, MNRAS, 359, 809

Clark, P. C. & Klessen, R. S. 2008, Astronomische Nachrichten, 329, 960

Commerçon, B., Hennebelle, P., Audit, E., Chabrier, G., & Teyssier, R. 2010, A&A, 510, L3+

Corbelli, E., Braine, J., Bandiera, R., Brouillet, N., Combes, F., Druard, C., Gratier, P., Mata, J., Schuster, K., Xilouris, M., & Palla, F. 2017, A&A, 601, A146

Currie, T., Hernandez, J., Irwin, J., Kenyon, S. J., Tokarz, S., Balog, Z., Bragg, A., Berlind, P., & Calkins, M. 2010, ApJS, 186, 191

Da Rio, N., Robberto, M., Soderblom, D. R., Panagia, N., Hillenbrand, L. A., Palla, F., & Stassun, K. G. 2010, ApJ, 722, 1092

Dale, J. E. & Bonnell, I. 2011, MNRAS, 414, 321

Dale, J. E. & Bonnell, I. A. 2008, MNRAS, 391, 2

Dale, J. E., Bonnell, I. A., Clarke, C. J., & Bate, M. R. 2005, MNRAS, 358, 291

Dale, J. E., Clark, P. C., & Bonnell, I. A. 2007, MNRAS, 377, 535

Dale, J. E., Ercolano, B., & Bonnell, I. A. 2012a, MNRAS, 427, 2852

—. 2012b, MNRAS, 424, 377

—. 2015, MNRAS, 451, 987

Dame, T. M., Elmegreen, B. G., Cohen, R. S., & Thaddeus, P. 1986, ApJ, 305, 892

De Pree, C. G., Peters, T., Mac Low, M.-M., Wilner, D. J., Goss, W. M., Galván-Madrid, R., Keto, E. R., Klessen, R. S., & Monsrud, A. 2014, ApJ, 781, L36

De Pree, C. G., Peters, T., Mac Low, M. M., Wilner, D. J., Goss, W. M., Galván-Madrid, R., Keto, E. R., Klessen, R. S., & Monsrud, A. 2015, ApJ, 815, 123

Deharveng, J.-M., Buat, V., Le Brun, V., Milliard, B., Kunth, D., Shull, J. M., & Gry, C. 2001, A&A, 375, 805

Dobbs, C. L. 2015, MNRAS, 447, 3390

Dobbs, C. L., Burkert, A., & Pringle, J. E. 2011, MNRAS, 413, 2935

Dobbs, C. L. & Pringle, J. E. 2013, MNRAS, 432, 653

Draine, B. T. 1978, ApJS, 36, 595

—. 2011, Physics of the Interstellar and Intergalactic Medium (Princeton University Press)

Duerr, R., Imhoff, C. L., & Lada, C. J. 1982, ApJ, 261, 135

Eddington, A. S. 1928, MNRAS, 88, 352

Elmegreen, B. G. 2000, ApJ, 530, 277

Elmegreen, B. G. 2002, ApJ, 577, 206

Elmegreen, B. G. & Efremov, Y. N. 1997, ApJ, 480, 235

Evans, II, N. J. 1991, in Astronomical Society of the Pacific Conference Series, Vol. 20, Frontiers of Stellar Evolution, ed. D. L. Lambert, 45–95

Evans, II, N. J. 1999, ARA&A, 37, 311

Fall, S. M. & Chandar, R. 2012, ApJ, 752, 96

Fall, S. M., Krumholz, M. R., & Matzner, C. D. 2010, ApJ, 710, L142

Fan, X., Carilli, C. L., & Keating, B. 2006, ARA&A, 44, 415

Federrath, C., Banerjee, R., Clark, P. C., & Klessen, R. S. 2010, ApJ, 713, 269

Federrath, C. & Klessen, R. S. 2012, ApJ, 761, 156

Federrath, C., Schrön, M., Banerjee, R., & Klessen, R. S. 2014, ApJ, 790, 128

Ferrara, A. & Loeb, A. 2013, MNRAS, 431, 2826

Fiege, J. D. & Pudritz, R. E. 2000, MNRAS, 311, 85

Fierlinger, K. M., Burkert, A., Ntormousi, E., Fierlinger, P., Schartmann, M., Ballone, A., Krause, M. G. H., & Diehl, R. 2016, MNRAS, 456, 710

Frank, A. & Mellema, G. 1994, A&A, 289, 937

Fryxell, B., Olson, K., Ricker, P., Timmes, F. X., Zingale, M., Lamb, D. Q., MacNeice, P., Rosner, R., Truran, J. W., & Tufo, H. 2000a, ApJS, 131, 273

—. 2000b, ApJS, 131, 273

Fujii, M. S. & Portegies Zwart, S. 2015, MNRAS, 449, 726

Fukui, Y. & Kawamura, A. 2010, ARA&A, 48, 547

Galván-Madrid, R., Peters, T., Keto, E. R., Mac Low, M.-M., Banerjee, R., & Klessen, R. S. 2011, MNRAS, 416, 1033

Gao, Y. & Solomon, P. M. 2004, ApJ, 606, 271

Gatto, A., Walch, S., Low, M.-M. M., Naab, T., Girichidis, P., Glover, S. C. O., Wünsch, R., Klessen, R. S., Clark, P. C., Baczynski, C., Peters, T., Ostriker, J. P., Ibáñez-Mejía, J. C., & Haid, S. 2015, MNRAS, 449, 1057

Gatto, A., Walch, S., Naab, T., Girichidis, P., Wünsch, R., Glover, S. C. O., Klessen, R. S., Clark, P. C., Peters, T., Derigs, D., Baczynski, C., & Puls, J. 2017, MNRAS, 466, 1903

Ginsburg, A., Goss, W. M., Goddi, C., Galván-Madrid, R., Dale, J. E., Bally, J., Battersby, C. D., Youngblood, A., Sankrit, R., Smith, R., Darling, J., Kruijssen, J. M. D., & Liu, H. B. 2016, A&A, 595, A27

Girichidis, P., Federrath, C., Banerjee, R., & Klessen, R. S. 2011, MNRAS, 413, 2741

Gnedin, N. Y., Kravtsov, A. V., & Chen, H.-W. 2008, ApJ, 672, 765

Goldsmith, P. F. 2001, ApJ, 557, 736

Gómez, L., Wyrowski, F., Schuller, F., Menten, K. M., & Ballesteros-Paredes, J. 2014, A&A, 561, A148

Grimes, J. P., Heckman, T., Strickland, D., Dixon, W. V., Sembach, K., Overzier, R., Hoopes, C., Aloisi, A., & Ptak, A. 2007, ApJ, 668, 891

Grissom, R. L., Ballantyne, D. R., & Wise, J. H. 2014, A&A, 561, A90

Gritschneder, M., Naab, T., Walch, S., Burkert, A., & Heitsch, F. 2009, ApJ, 694, L26

Gunn, J. E. & Peterson, B. A. 1965, ApJ, 142, 1633

Habing, H. J. 1968, Bull. Astron. Inst. Netherlands, 19, 421

Harper-Clark, E. 2011, PhD thesis, University of Toronto (Canada

Harris, W. E. 1991, ARA&A, 29, 543

Harris, W. E. & Pudritz, R. E. 1994, ApJ, 429, 177

Hartmann, L., Ballesteros-Paredes, J., & Bergin, E. A. 2001, ApJ, 562, 852

Heckman, T. M., Sembach, K. R., Meurer, G. R., Leitherer, C., Calzetti, D., & Martin, C. L. 2001, ApJ, 558, 56

Heiderman, A., Evans, II, N. J., Allen, L. E., Huard, T., & Heyer, M. 2010, ApJ, 723, 1019

Heitsch, F. 2013, ApJ, 769, 115

Hennebelle, P. 2013, A&A, 556, A153

Hensler, G. 2011, in IAU Symposium, Vol. 270, Computational Star Formation, ed. J. Alves, B. G. Elmegreen, J. M. Girart, & V. Trimble, 309–317

Hernandez, A. K. & Tan, J. C. 2015, ApJ, 809, 154

Heyer, M. H., Carpenter, J. M., & Snell, R. L. 2001, ApJ, 551, 852

Hill, T., Motte, F., Didelon, P., Bontemps, S., Minier, V., Hennemann, M., Schneider, N., Andre, P., Men'shchikov, A., Anderson, L. D., Arzoumanian, D., Bernard, J.-P., di Francesco, J., Elia, D., Giannini, T., Griffin, M. J., Kirk, J., Konyves, V., Marston, A. P., Martin, P., Molinari, S., Nguyen Luong, Q., Peretto, N., Pezzuto,

S., Roussel, H., Sauvage, M., Sousbie, T., Testi, L., Ward-Thompson, D., White, G. J., Wilson, C. D., & Zavagno, A. 2011, ArXiv e-prints: 1108.0941

Hillenbrand, L. A. 1997, AJ, 113, 1733

Hollyhead, K., Bastian, N., Adamo, A., Silva-Villa, E., Dale, J., Ryon, J. E., & Gazak, Z. 2015, MNRAS, 449, 1106

Hoopes, C. G. & Walterbos, R. A. M. 2000, ApJ, 541, 597

Howard, C., Pudritz, R., & Harris, W. 2017a, preprint (arXiv:1706.00477)

Howard, C., Pudritz, R., & Klessen, R. 2017b, ApJ, 834, 40

Howard, C. S., Pudritz, R. E., & Harris, W. E. 2014, MNRAS, 438, 1305

—. 2016, MNRAS, 461, 2953

Hughes, A., Meidt, S. E., Schinnerer, E., Colombo, D., Pety, J., Leroy, A. K., Dobbs, C. L., García-Burillo, S., Thompson, T. A., Dumas, G., Schuster, K. F., & Kramer, C. 2013, ApJ, 779, 44

Hurwitz, M., Jelinsky, P., & Dixon, W. V. D. 1997, ApJ, 481, L31

Iliev, I. T., Ciardi, B., Alvarez, M. A., Maselli, A., Ferrara, A., Gnedin, N. Y., Mellema, G., Nakamoto, T., Norman, M. L., Razoumov, A. O., Rijkhorst, E.-J., Ritzerveld, J., Shapiro, P. R., Susa, H., Umemura, M., & Whalen, D. J. 2006, MNRAS, 371, 1057

Inutsuka, S.-i. & Miyama, S. M. 1997, ApJ, 480, 681

Iwata, I., Inoue, A. K., Matsuda, Y., Furusawa, H., Hayashino, T., Kousai, K., Akiyama, M., Yamada, T., Burgarella, D., & Deharveng, J.-M. 2009, ApJ, 692, 1287

Kainulainen, J., Beuther, H., Henning, T., & Plume, R. 2009, A&A, 508, L35

Kainulainen, J., Federrath, C., & Henning, T. 2014, Science, 344, 183

Kawamura, A., Mizuno, Y., Minamidani, T., Filipović, M. D., Staveley-Smith, L., Kim, S., Mizuno, N., Onishi, T., Mizuno, A., & Fukui, Y. 2009, ApJS, 184, 1

Keller, B. W., Wadsley, J., Benincasa, S. M., & Couchman, H. M. P. 2014, MNRAS, 442, 3013

Kim, J.-h., Krumholz, M. R., Wise, J. H., Turk, M. J., Goldbaum, N. J., & Abel, T. 2012, ArXiv e-prints

Kirk, H., Klassen, M., Pudritz, R., & Pillsworth, S. 2015, ApJ, 802, 75

Kirk, H., Myers, P. C., Bourke, T. L., Gutermuth, R. A., Hedden, A., & Wilson, G. W. 2013, ApJ, 766, 115

Klassen, M., Peters, T., & Pudritz, R. E. 2012a, ApJ, 758, 137

Klassen, M., Pudritz, R. E., & Peters, T. 2012b, MNRAS, 421, 2861

Klessen, R. S. & Glover, S. C. O. 2016, Star Formation in Galaxy Evolution: Connecting Numerical Models to Reality, Saas-Fee Advanced Course, Volume 43. ISBN 978-3-662-47889-9. Springer-Verlag Berlin Heidelberg, 2016, p. 85, 43, 85

Klessen, R. S., Heitsch, F., & Mac Low, M.-M. 2000, ApJ, 535, 887

Klessen, R. S. & Hennebelle, P. 2010, A&A, 520, A17

Kong, S., Tan, J. C., Caselli, P., Fontani, F., Pillai, T., Butler, M. J., Shimajiri, Y., Nakamura, F., & Sakai, T. 2015, ArXiv e-prints

Kritsuk, A. G., Norman, M. L., & Wagner, R. 2011, ApJ, 727, L20

Kruijssen, J. M. D. 2012, MNRAS, 426, 3008

—. 2015, MNRAS, 454, 1658

Kruijssen, J. M. D. & Longmore, S. N. 2014, MNRAS, 439, 3239

Kruijssen, J. M. D., Longmore, S. N., Elmegreen, B. G., Murray, N., Bally, J., Testi, L., & Kennicutt, R. C. 2014, MNRAS, 440, 3370

Kruijssen, J. M. D., Maschberger, T., Moeckel, N., Clarke, C. J., Bastian, N., & Bonnell, I. A. 2012, MNRAS, 419, 841

Krumholz, M. R., Cunningham, A. J., Klein, R. I., & McKee, C. F. 2010, ApJ, 713, 1120

Krumholz, M. R. & Matzner, C. D. 2009, ApJ, 703, 1352

Krumholz, M. R. & McKee, C. F. 2005, ApJ, 630, 250

Krumholz, M. R. & Thompson, T. A. 2012, ApJ, 760, 155

Kudryavtseva, N., Brandner, W., Gennaro, M., Rochau, B., Stolte, A., Andersen, M., Da Rio, N., Henning, T., Tognelli, E., Hogg, D., Clark, S., & Waters, R. 2012, ApJ, 750, L44

Kuhn, M. A., Baddeley, A., Feigelson, E. D., Getman, K. V., Broos, P. S., Townsley, L. K., Povich, M. S., Naylor, T., King, R. R., Busk, H. A., & Luhman, K. L. 2012, ArXiv e-prints

Kuhn, M. A., Feigelson, E. D., Getman, K. V., Sills, A., Bate, M. R., & Borissova, J. 2015, ApJ, 812, 131

Lada, C. J. 2010, Royal Society of London Philosophical Transactions Series A, 368, 713

Lada, C. J. & Lada, E. A. 2003, ARA&A, 41, 57

Lada, C. J., Lombardi, M., & Alves, J. F. 2010, ApJ, 724, 687

Larson, R. B. 1981, MNRAS, 194, 809

Lebouteiller, V., Bernard-Salas, J., Brandl, B., Whelan, D. G., Wu, Y., Charmandaris, V., Devost, D., & Houck, J. R. 2008, ApJ, 680, 398

Leitherer, C., Schaerer, D., Goldader, J. D., Delgado, R. M. G., Robert, C., Kune, D. F., de Mello, D. F., Devost, D., & Heckman, T. M. 1999, ApJS, 123, 3

Li, A. & Draine, B. T. 2001, ApJ, 554, 778

Li, Z.-Y. & Nakamura, F. 2006, ApJ, 640, L187

Licquia, T. C. & Newman, J. A. 2015, ApJ, 806, 96

Liu, H. B., Jiménez-Serra, I., Ho, P. T. P., Chen, H.-R., Zhang, Q., & Li, Z.-Y. 2012, ApJ, 756, 10

Longmore, S. N., Kruijssen, J. M. D., Bastian, N., Bally, J., Rathborne, J., Testi, L., Stolte, A., Dale, J., Bressert, E., & Alves, J. 2014, Protostars and Planets VI, 291

Mac Low, M.-M. & Klessen, R. S. 2004, Reviews of Modern Physics, 76, 125

Maschberger, T., Clarke, C. J., Bonnell, I. A., & Kroupa, P. 2010, MNRAS, 404, 1061

Massey, P. & Hunter, D. A. 1998, ApJ, 493, 180

Mathis, J. S., Mezger, P. G., & Panagia, N. 1983, A&A, 128, 212

Matzner, C. D. 2002, ApJ, 566, 302

Matzner, C. D. & McKee, C. F. 2000, ApJ, 545, 364

Maury, A. J., André, P., & Li, Z.-Y. 2009, A&A, 499, 175

McKee, C. F. & Ostriker, E. C. 2007, ARA&A, 45, 565

McQuinn, K. B. W., Skillman, E. D., Cannon, J. M., Dalcanton, J., Dolphin, A., Hidalgo-Rodríguez, S., Holtzman, J., Stark, D., Weisz, D., & Williams, B. 2010a, ApJ, 721, 297

—. 2010b, ApJ, 724, 49

Megeath, S. T., Gutermuth, R., Muzerolle, J., Kryukova, E., Flaherty, K., Hora, J. L., Allen, L. E., Hartmann, L., Myers, P. C., Pipher, J. L., Stauffer, J., Young, E. T., & Fazio, G. G. 2012, AJ, 144, 192

Mellema, G. & Lundqvist, P. 2002, A&A, 394, 901

Moore, T. J. T., Plume, R., Thompson, M. A., Parsons, H., Urquhart, J. S., Eden, D. J., Dempsey, J. T., Morgan, L. K., Thomas, H. S., Buckle, J., Brunt, C. M., Butner, H., Carretero, D., Chrysostomou, A., deVilliers, H. M., Fich, M., Hoare, M. G., Manser, G., Mottram, J. C., Natario, C., Olguin, F., Peretto, N., Polychroni, D., Redman, R. O., Rigby, A. J., Salji, C., Summers, L. J., Berry, D., Currie, M. J., Jenness, T., Pestalozzi, M., Traficante, A., Bastien, P., diFrancesco, J., Davis, C. J., Evans, A., Friberg, P., Fuller, G. A., Gibb, A. G., Gibson, S., Hill, T., Johnstone, D., Joncas, G., Longmore, S. N., Lumsden, S. L., Martin, P. G., Lu'o'ng, Q. N., Pineda, J. E., Purcell, C., Richer, J. S., Schieven, G. H., Shipman, R., Spaans, M., Taylor, A. R., Viti, S., Weferling, B., White, G. J., & Zhu, M. 2015, MNRAS, 453, 4264

Murray, N. 2011, ApJ, 729, 133

Murray, N., Quataert, E., & Thompson, T. A. 2010, ApJ, 709, 191

Myers, P. C. & Goodman, A. A. 1988, ApJ, 326, L27

Nestor, D. B., Shapley, A. E., Kornei, K. A., Steidel, C. C., & Siana, B. 2013, ApJ, 765, 47

Neufeld, D. A., Lepp, S., & Melnick, G. J. 1995, ApJS, 100, 132

Nguyen Luong, Q., Motte, F., Schuller, F., Schneider, N., Bontemps, S., Schilke, P., Menten, K. M., Heitsch, F., Wyrowski, F., Carlhoff, P., Bronfman, L., & Henning, T. 2011, A&A, 529, A41

Ochsendorf, B. B., Meixner, M., Roman-Duval, J., Rahman, M., & Evans, II, N. J. 2017, preprint (arXiv:1704.06965)

Offner, S. S. R., Clark, P. C., Hennebelle, P., Bastian, N., Bate, M. R., Hopkins, P. F., Moraux, E., & Whitworth, A. P. 2014, Protostars and Planets VI, 53

Offner, S. S. R., Klein, R. I., McKee, C. F., & Krumholz, M. R. 2009, ApJ, 703, 131

Ostriker, E. C., Stone, J. M., & Gammie, C. F. 2001, ApJ, 546, 980

Ostriker, J. 1964, ApJ, 140, 1056

Paardekooper, J.-P., Khochfar, S., & Dalla Vecchia, C. 2013, MNRAS, 429, L94

—. 2015, MNRAS, 451, 2544

Paardekooper, J.-P., Pelupessy, F. I., Altay, G., & Kruip, C. J. H. 2011, A&A, 530, A87

Padoan, P., Haugbølle, T., & Nordlund, Å. 2012, ApJ, 759, L27

Padoan, P. & Nordlund, Å. 2011, ApJ, 730, 40

Pellegrini, E. W., Oey, M. S., Winkler, P. F., Points, S. D., Smith, R. C., Jaskot, A. E., & Zastrow, J. 2012, ApJ, 755, 40

Peters, T., Banerjee, R., Klessen, R. S., Mac Low, M.-M., Galván-Madrid, R., & Keto, E. R. 2010a, ApJ, 711, 1017

Peters, T., Mac Low, M.-M., Banerjee, R., Klessen, R. S., & Dullemond, C. P. 2010b, ApJ, 719, 831

Pflamm-Altenburg, J., Weidner, C., & Kroupa, P. 2007, ApJ, 671, 1550

Pollack, J. B., Hollenbach, D., Beckwith, S., Simonelli, D. P., Roush, T., & Fong, W. 1994, ApJ, 421, 615

Porras, A., Christopher, M., Allen, L., Di Francesco, J., Megeath, S. T., & Myers, P. C. 2003, AJ, 126, 1916

Pudritz, R. E. & Kevlahan, N. K.-R. 2013, Philosophical Transactions of the Royal Society of London Series A, 371, 20120248

Pudritz, R. E., Ouyed, R., Fendt, C., & Brandenburg, A. 2007, Protostars and Planets V, 277

Raga, A. C., Cantó, J., & Rodríguez, L. F. 2012, Rev. Mexicana Astron. Astrofis., 48, 149

Rahner, D., Pellegrini, E. W., Glover, S. C. O., & Klessen, R. S. 2017, preprint (arXiv:1704.04240)

Razoumov, A. O. & Sommer-Larsen, J. 2010, ApJ, 710, 1239

Reid, M. A. & Wilson, C. D. 2005, ApJ, 625, 891

—. 2006, ApJ, 644, 990

Rey-Raposo, R., Dobbs, C., & Duarte-Cabral, A. 2015, MNRAS, 446, L46

Reynolds, R. J. 1984, ApJ, 282, 191

—. 1985, ApJ, 294, 256

Reynolds, R. J. 1993, in American Institute of Physics Conference Series, Vol. 278, Back to the Galaxy, ed. S. S. Holt & F. Verter, 156–165

Rijkhorst, E.-J., Plewa, T., Dubey, A., & Mellema, G. 2006, A&A, 452, 907

Robertson, B. E., Ellis, R. S., Dunlop, J. S., McLure, R. J., & Stark, D. P. 2010, Nature, 468, 49

Robertson, B. E., Furlanetto, S. R., Schneider, E., Charlot, S., Ellis, R. S., Stark, D. P., McLure, R. J., Dunlop, J. S., Koekemoer, A., Schenker, M. A., Ouchi, M., Ono, Y., Curtis-Lake, E., Rogers, A. B., Bowler, R. A. A., & Cirasuolo, M. 2013, ApJ, 768, 71

Rogers, H. & Pittard, J. M. 2013, MNRAS, 431, 1337

Rosolowsky, E. 2005, PASP, 117, 1403

Rosolowsky, E. 2007, ApJ, 654, 240

Salpeter, E. E. 1955, ApJ, 121, 161

Sanders, D. B., Scoville, N. Z., & Solomon, P. M. 1985, ApJ, 289, 373

Schneider, N., Csengeri, T., Hennemann, M., Motte, F., Didelon, P., Federrath, C., Bontemps, S., Di Francesco, J., Arzoumanian, D., Minier, V., André, P., Hill, T., Zavagno, A., Nguyen-Luong, Q., Attard, M., Bernard, J.-P., Elia, D., Fallscheer, C., Griffin, M., Kirk, J., Klessen, R., Könyves, V., Martin, P., Men'shchikov, A., Palmeirim, P., Peretto, N., Pestalozzi, M., Russeil, D., Sadavoy, S., Sousbie, T., Testi, L., Tremblin, P., Ward-Thompson, D., & White, G. 2012, A&A, 540, L11

Scoville, N. Z. & Hersh, K. 1979, ApJ, 229, 578

Scoville, N. Z. & Wilson, C. D. 2004, in Astronomical Society of the Pacific Conference Series, Vol. 322, The Formation and Evolution of Massive Young Star Clusters, ed. H. J. G. L. M. Lamers, L. J. Smith, & A. Nota, 245

Scoville, N. Z., Yun, M. S., Sanders, D. B., Clemens, D. P., & Waller, W. H. 1987, ApJS, 63, 821

Shapley, A. E., Steidel, C. C., Pettini, M., Adelberger, K. L., & Erb, D. K. 2006, ApJ, 651, 688

Siana, B., Shapley, A. E., Kulas, K. R., Nestor, D. B., Steidel, C. C., Teplitz, H. I., Alavi, A., Brown, T. M., Conselice, C. J., Ferguson, H. C., Dickinson, M., Giavalisco, M., Colbert, J. W., Bridge, C. R., Gardner, J. P., & de Mello, D. F. 2015, ApJ, 804, 17

Solomon, P. M., Rivolo, A. R., Barrett, J., & Yahil, A. 1987, ApJ, 319, 730

Spitzer, L. 1978, Physical processes in the interstellar medium (New York Wiley-Interscience)

Teixeira, P. S., Lada, C. J., Young, E. T., Marengo, M., Muench, A., Muzerolle, J., Siegler, N., Rieke, G., Hartmann, L., Megeath, S. T., & Fazio, G. 2006, ApJ, 636, L45

Tielens, A. G. G. M. 2005, The Physics and Chemistry of the Interstellar Medium (Cambridge University Press)

Tielens, A. G. G. M. & Hollenbach, D. 1985, ApJ, 291, 722

Tilley, D. A. & Pudritz, R. E. 2004, MNRAS, 353, 769

—. 2007, MNRAS, 382, 73

Tout, C. A., Pols, O. R., Eggleton, P. P., & Han, Z. 1996, MNRAS, 281, 257

Turk, M. J., Smith, B. D., Oishi, J. S., Skory, S., Skillman, S. W., Abel, T., & Norman, M. L. 2011, ApJS, 192, 9

Urquhart, J. S., Moore, T. J. T., Csengeri, T., Wyrowski, F., Schuller, F., Hoare, M. G., Lumsden, S. L., Mottram, J. C., Thompson, M. A., Menten, K. M., Walmsley, C. M., Bronfman, L., Pfalzner, S., König, C., & Wienen, M. 2014, MNRAS, 443, 1555

Vázquez-Semadeni, E. 1994, ApJ, 423, 681

Vázquez-Semadeni, E. & García, N. 2001, ApJ, 557, 727

Walch, S. & Naab, T. 2015, MNRAS, 451, 2757

Walch, S., Whitworth, A. P., Bisbas, T. G., Wünsch, R., & Hubber, D. A. 2013, MNRAS, 435, 917

Walch, S. K., Whitworth, A. P., Bisbas, T., Wünsch, R., & Hubber, D. 2012, MNRAS, 427, 625

Ward, R. L., Benincasa, S. M., Wadsley, J., Sills, A., & Couchman, H. M. P. 2016, MNRAS, 455, 920

Weisz, D. R., Dalcanton, J. J., Williams, B. F., Gilbert, K. M., Skillman, E. D., Seth, A. C., Dolphin, A. E., McQuinn, K. B. W., Gogarten, S. M., Holtzman, J., Rosema, K., Cole, A., Karachentsev, I. D., & Zaritsky, D. 2011, ApJ, 739, 5

Whitworth, A. 1979, MNRAS, 186, 59

Williams, J. P. & McKee, C. F. 1997, ApJ, 476, 166

Willott, C. J., Delorme, P., Omont, A., Bergeron, J., Delfosse, X., Forveille, T., Albert, L., Reylé, C., Hill, G. J., Gully-Santiago, M., Vinten, P., Crampton, D., Hutchings, J. B., Schade, D., Simard, L., Sawicki, M., Beelen, A., & Cox, P. 2007, AJ, 134, 2435

Wise, J. H. & Cen, R. 2009, ApJ, 693, 984

Wise, J. H., Demchenko, V. G., Halicek, M. T., Norman, M. L., Turk, M. J., Abel, T., & Smith, B. D. 2014, MNRAS, 442, 2560

Wu, J., Evans, II, N. J., Gao, Y., Solomon, P. M., Shirley, Y. L., & Vanden Bout, P. A. 2005, ApJ, 635, L173

Xu, H., Wise, J. H., Norman, M. L., Ahn, K., & O'Shea, B. W. 2016, ApJ, 833, 84